2015

Unsteady Physics and Aeroelastic Response of Streamwise Vortex-Surface Interactions

Caleb J. Barnes
Wright State University

Unsteady Physics and Aeroelastic Response of Streamwise Vortex-Surface Interactions

A dissertation submitted in partial fulfillment
of the requirements for the degree of
Doctor of Philosophy

By

CALEB JAMES BARNES
B.S., Wright State University, 2009
M.S., Wright State University, 2011

2015
Wright State University

WRIGHT STATE UNIVERSITY

THE GRADUATE SCHOOL

April 30, 2015

I HEREBY RECOMMEND THAT THE THESIS PREPARED UNDER MY SUPERVISION BY **Caleb James Barnes** ENTITLED **Unsteady Physics and Aeroelastic Response of Streamwise Vortex-Surface Interactions** BE ACCEPTED IN PARTIAL FULFILLMENT OF THE REQUIREMENTS FOR THE DEGREE OF **Doctor of Philosophy**.

George Huang, Ph.D.
Dissertation Director

Ramana V. Grandhi, Ph.D.
Director, Ph.D. in Engineering Program

Robert E. W. Fyffe, Ph.D.
Vice President for Research and
Dean of the Graduate School

Committee on Final Examination

George Huang, Ph.D.

Joseph Shang, Ph.D.

Zifeng Yang, Ph.D.

Miguel Visbal, Ph.D.

Aaron Altman, Ph.D.

Abstract

Barnes, Caleb James. Ph.D., Engineering Ph.D. Program, Wright State University, 2015. *Unsteady Physics and Aeroelastic Response of Streamwise Vortex-Surface Interactions.*

Streamwise vortex-surface interactions can occur in aviation intentionally in the context of formation flight as an energy saving mechanism, unintentionally in wake crossings when aircraft fly in close proximity, and as a consequence of aircraft design through the interaction of fluid dynamics between different aerodynamic surfaces. The bulk of past work on streamwise vortex-surface interactions has focused on steady inviscid analysis for optimizing aerodynamic loads in the context of formation flight or experimental analysis on fin buffeting problems. A fundamental understanding of the viscous and unsteady effects that may occur is both important and currently lacking in the literature. This dissertation seeks to fill this need by using a high-fidelity implicit large-eddy simulation approach coupled with geometrically non-linear finite elements to identify and analyze important physics that may occur. Simple, canonical configurations are employed in order help disentangle the many interrelated factors of a very complex problem. Analysis of a tandem wing configuration elucidated mutual induction between the incident vortex from the leader wing and tip vortex of the follower wing that resulted in a broad taxonomy of flow structure, wake evolution, and unsteady behaviors for several lateral impingement locations. Interaction of an isolated streamwise vortex with a wing revealed a robust helical instability develops when a strong vortex impinges directly with the leading-edge. This spiraling behavior was found to occur as a result of the upstream influence of adverse pressure gradients provided by the wing that drive the vortex into its linearly unstable regime allowing for the growth of shortwave perturbations. Stability can be augmented through vertical positioning of the vortex. A negative offset can enhance stability by providing a stronger adverse pressure gradient while a positive offset exploits a favorable gradient and removes the upstream instability altogether. The effects of wing compliance were

revealed through full aeroleastic simulations. Essentially static, vortex-induced bending deformations reposition the vortex and drive it further into its unstable regime. Static and dynamic components of the aeroelastic response were systematically isolated where the static deformations were shown to provide the greatest influence. Dynamic effects provide some influence to the incident vortex behavior but these are secondary to the static behavior.

Contents

List of Figures

List of Tables

Acknowledgements

I would like to offer my deepest gratitude to my dissertation advisor, Dr. George Huang. He has been an integral part of my academic career beginning with a study abroad program as an undergraduate and has persevered with me to the end of my doctorate. His challenging, yet encouraging, guidance has provided a fruitful and lasting impact to my personal and professional development for which I will forever owe a debt of gratitude. His love for engineering and computational fluid dynamics is contagious and has been a formative influence in my own path as a researcher.

Dr. Miguel Visbal, Dr. Joseph Shang, Dr. Aaron Altman, and Dr. Zifeng Yang deserve many thanks for serving on my dissertation committee, asking the tough questions, and holding me to a high standard. Their insightful feedback has without doubt improved the quality of my work. Dr. Joseph Shang deserves special mention. His mentoring and guidance during my time at WSU has shaped my habits and practices as a researcher for the best. I will never forget his many words of wisdom, his invaluable advice, nor the opportunities he has made for me.

I am extremely grateful toward Dr. Miguel Visbal who served as my technical supervisor and mentor during my time as a Ph.D. intern at the Air Force Research Laboratory (AFRL). His vast experience in unsteady fluid dynamics and high-fidelity numerical simulation has been an incredible fount of knowledge for me. I could not have done this work without his exceptional guidance. Dr. Donald Rizzetta, Dr. Raymond Gordnier, and Dr. Daniel Garmann at AFRL also deserve special thanks for sharing their expertise and providing continued encouragement during my time with them. I could not ask for better colleagues and friends.

Last, but certainly not least, my wife has served the most important role in my graduate studies. I would like to thank her for being an encouraging support and warm light through the most discouraging times. I look forward to spending much more of my time with both her and our daughter in the coming days.

Chapter 1

Introduction

Streamwise-oriented vortex interactions describe a class of flow-structure interaction in which swirling flow oriented perpendicular to an airfoil, blade, or fin impinges upon or passes close by the aerodynamic surface. The influence of streamwise vortices can be important in many aerodynamic applications. Trailing vortices that form as a consequence of spanwise flow over the tip of a finite wing can persist for several spans. Aircraft flying in close proximity might cross a trailing vortex resulting in a sudden change in flowfield creating a potentially dangerous flight environment. Alternatively, an aircraft may intentionally position itself in line with a trailing vortex in order to exploit the upwash field of the swirling flow region. This is known as formation flight and has become an attractive energy saving mechanism. Streamwise-oriented vortex interactions can also occur as a consequence of an aircraft's design as in a canard configuration or the separation of the leading-edge vortex from a slender wing. Tip vortices in rotating machinery are also known to interact with trailing blades.

It is easy to perceive a number of situations in which a perpendicular vortex might interact with a flying object and it has been shown these vortex-surface interactions can produce unsteady fluid dynamics. Further complicating the problem, energy efficiency trends might tend toward larger aspect-ratio wings and lighter-weight struc-

tures. Combining an unsteady vortex-surface interaction with airframes prone to aeroelastic effects could lead to a complex interrelationship between fluid and structural dynamics producing significant buffeting loads or catastrophic failure in the more extreme case.

While a significant body of work exists that explores the benefits and detriments of streamwise-oriented vortex interactions in several different contexts, very little is known about unsteady effects that may occur. This dissertation seeks to identify and address the need for detailed investigation of unsteady fluid dynamics in perpendicular vortex interactions with rigid and flexible structures. While motivated by the topic of formation flight, the work in this dissertation is intended to investigate the broader class of streamwise vortex interactions through detailed high-fidelity and aeroelastic numerical analysis of fundamental configurations.

1.1 Motivation

A primary inspiration for the current work stems from recent interests in energy efficiency benefits of formation flight. The following sections provide a general review on the state of research for this topic. As the genesis of drag reduction through wake interference stems from nature, the discussion on this topic will begin there.

1.1.1 Formation flight in nature

With many exceptionally successful examples of flight in nature it is only to be expected that insects, birds, and other biological fliers would serve as inspiration to overcome modern-day challenges. In the past, a number of researchers have studied the aerodynamic impact of birds that travel in flocks demonstrating numerous advantages of formation flight. Essentially, a bird trailing another is capable of riding the upwash induced by the trailing vorticies from a leader bird. This upwash, defined by

the periodic shedding of vortices from flapping wings, reduces the power required for the trailing bird to fly through a forward tilt of the lift vector, shown in Figure 1.1, and can even extend the range of the entire flock.

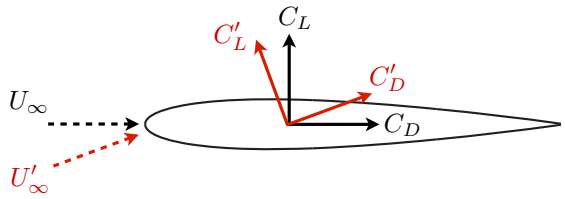

Figure 1.1: Tilt in lift and drag vectors due to trailing vortex upwash

It is now common knowledge that the migratory pattern of many avian species, such as the V-formation shown in Figure 1.2 for Canadian geese, provides energy-saving benefits. Among the first researchers to demonstrate this concept in the proper context was Wieselsberger[6] who in 1914 used horseshoe vortices to represent birds in formation flight. In his work, three bodies in a diagonal formation were demonstrated to utilize the updraft from the leading bird consequently reducing the induced drag for each member. However, the much simplified theory used in this study resulted in an unduly low power reduction estimate. Much later, Lissaman and Shollenberger[7] in 1970 used more accurate aerodynamic theory to investigate numerous arrangements of birds in flight. The most optimal configurations resulted in close to a 27% range increase for 3 birds and a 71% range increase for a formation of 25 members compared to that of a single bird.

Several works by Hummel[8, 9] have employed classical aerodynamic theory to investigate the benefits of birds in close-formation flight and demonstrated several aspects of formation spacing. For instance, Hummel[8] showed that longitudinal spacing of birds does not affect the total power reduction, but does influence the distribution of this power reduction among members in the formation. Lateral spacing was shown to be of more critical importance on the aerodynamic benefit for a particular member. Additionally, calculations of heterogenous formations demonstrated the stronger up-

wash induced by larger members produces a greater influence on the younger, smaller birds in the flock[9].

Figure 1.2: Canadian geese in a typical V-formation

Badgerow and Hainsworth[10] showed that a wingtip overlap in formation positioning is necessary to achieve the most benefit due to wake roll-up. Later, Hainsworth[11] used the methods of Lissaman and Schollenberger[7] to predict the power savings for formations measured from a photographic study of Canadian geese in formation. The median spacing for a formation of 55 geese was fairly close to that predicted by simple aerodynamic theory resulting in a 35% power reduction compared to a single bird demonstrating the spacing of actual avian formations resembles beneficial configurations suggested by previous works. Similarly, Cutts and Speakman[12] used a theoretical model to analyze observed formations of pink-footed geese finding a 14% induced power savings. This value was determined to be well below the optimum predicted in Ref. [7] due to the tendency of this particular species to fly outboard of the ideal position. They hypothesized that it was difficult for the geese to maintain the most favorable placement alternatively erring on the side of a more conservative outboard wingtip spacing. Despite this departure from the most beneficial configuration, formation flight in the natural world appears to be relatively forgiving. More recently, biologists have shown the power reducing capability of flocks using direct measurements from pelicans in flight[13]. In this study, measurements for both the

heartbeat and wing-beat frequency decreased for the birds when in formation revealing a reduced and therefore demonstrated energy savings. This finding lends further credence to previous claims by providing a direct link between theoretical performance benefits and experimental measurements obtained directly from biological formation flight.

Frazier and Gopalarathnam[14] theorized that biological fliers are capable of exploiting their variable-geometry wings to improve spanwise lift-distributions, even when not in the optimal configuration predicted by aerodynamic theory. It is possible that natural fliers actively exploit wing geometry to better harness wake features. Though beyond the scope of the current investigation, this concept would be an interesting topic for future study especially in the context of harnessing wake interference in aviation.

Indeed, a growing body of evidence strongly points to the fact that the natural world has already learned how to fly more efficiently. Additional details of the mechanics of formation flight in a biological context are well-summarized in Ref. [9]. The next section surveys formation flight in the context of aviation.

1.1.2 Formation flight in aviation

Recent interests in formation flight for aviation stem from an increased need to extend operating range and improve fuel efficiency. As with birds, the exploitation of aircraft positioning is particularly attractive due its ability to produce favorable aerodynamic effects without much change to existing air vehicles. A follower aircraft would only need to be carefully placed in the upwash portion of the leader aircraft's wake profile, as shown in Figure 1.3. Such advantages, even if minor, can compound to large benefits. For instance, a 1% reduction in drag may result in as much as 100,000 lb per year in fuel consumption for a single large aircraft annually[15].

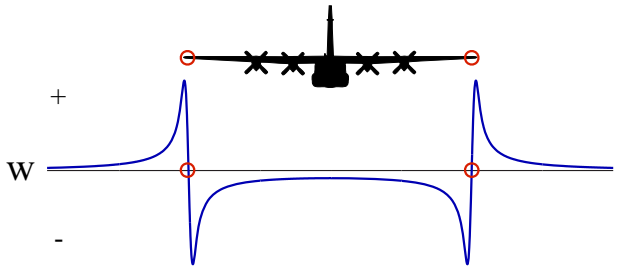

Figure 1.3: Example up/down-wash profile behind an aircraft as predicted by Lamb-Oseen vortices

Commercially, passenger and cargo aircraft could exploit formation flight as an energy-saving mechanism. One study[16] investigated formations of passenger aircraft revealing a 60% reduction in lift-induced drag. A more recent work[17] on commercial formation flight examined potential fuel savings for cargo aircraft utilizing configurations based upon realistic scenarios. Two aircraft were shown to reduce total fuel burn up to 10% and three aircraft produced savings up to 16%. Difficulties regarding passenger comfort relative to unsteady loading in commercial formations are actively being addressed[18].

The advantages of wake interference are not just limited to commercial fuel savings alone. Small aircraft tend to have a shorter operating range which can be extended through aerial refueling or directly through power-reduction imposed by the upwash of trailing vortices. In both cases, the wake-interaction between vehicles is an important consideration. Larger aircraft have been shown to produce a stronger upwash and therefore a greater induced drag reduction on trailing aircraft[8]. Smaller short-range wingmen following a larger mothership could receive a significant drag reduction and hence an extension in operating range[19, 20]. In close formation configurations even the leader aircraft can recieve some benefit due to upstream influence of the follower aircraft[21].

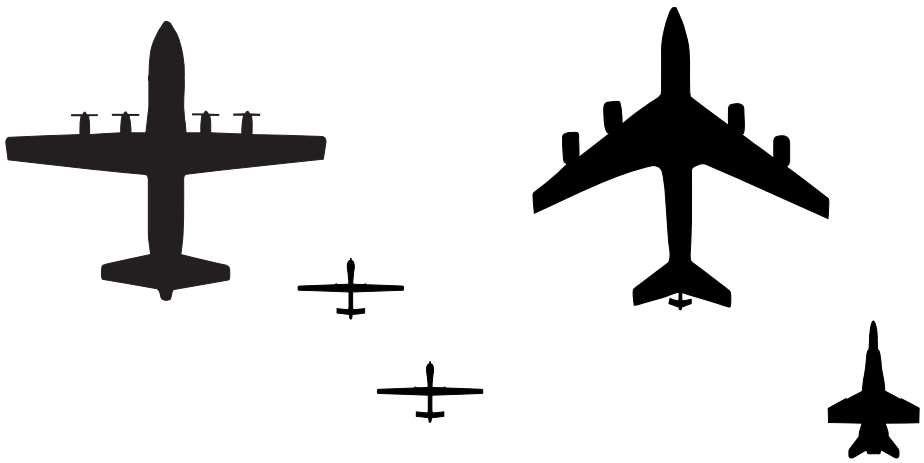

Figure 1.4: Examples of heterogenous formations

1.1.3 Flight testing

A number of flight tests have helped validate theoretical predictions for energy savings. Hummel[9] showed a drag reduction of around 15% for a two Do-28D1 aircraft and found the benefit was very sensitive to the lateral spacing. Following his previous analytical work, Wagner *et al.*[22] conducted flight tests for two T-38 aircraft in formation achieving an 8.8% fuel flow reduction. Around the same time, NASA's Autonomous Formation Flight Project[23] produced data for several flight tests using F/A-18 aircraft in close formation similar to that shown in Figure 1.5. Performance benefits were shown to compare well with those predicted by aerodynamic theory over a range of lateral, longitudinal, and vertical positions[24]. Analysis of the rolling moments showed that peak values coincided with the most beneficial positioning[25] which could pose control difficulty and reduce aerodynamic benefits due to trim penalties. However, through optimal positioning of the trailing vortex, drag was reduced by over 20% and an 18% fuel-flow reduction was achieved[26]. Furthermore, these optimal conditions were observed to occur at positions where flight was easily controlled in a manually piloted air vehicle. In fact, two F/A-18 aircraft in formation have achieved as much as a 20% fuel savings[27]. Pilots did note significant

difficulty maintaining position and sensitivity to rolling or pitching moment changes when in the range of optimal positioning[25] suggesting unsteady fluid dynamics can play a significant role.

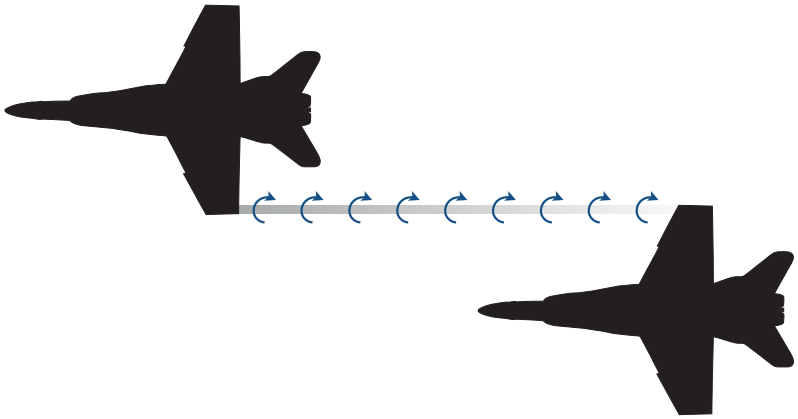

Figure 1.5: F/A-18 aircraft in a two member formation. The impingement of the trailing vortex on the follower aircraft is demonstrated

A more recent flight test by Pahle *et al.*[15] explored performance for larger transport-class C-17 aircraft in an extended ($\Delta x/c \approx 18$) formation. Performance was evaluated by measuring fuel-flow and thrust reduction to maintain level flight. Fuel flow for the trailing aircraft in this preliminary study was shown to reduce by 8% compared to solo flight with potential for savings greater than 10%.

1.1.4 Issues of practicality

Influence of the streamwise vortex from a leader wing can produce asymmetrical loading such as an unbalanced rolling moment or side force which must be overcome to maintain steady flight[28, 29, 30]. Typically the trail wing positions that produce the most drag reduction also tend to induce the largest rolling moments[25, 31]. These observations lead to the question: can unbalanced forces due to the vortex upwash be overcome without losing aerodynamic benefits? A number of methods to maintain steady flight in formation have been proposed such as morphing the wing[14], varying camber, the addition of winglets, or adjusting aircraft trim[16], to name a few. In fact,

a number of authors have investigated the practicality of countering these off-balance loads using aircraft trim.

In 1999, Gingras[32] used force measurements from experimental data in a six-degree-of-freedom (6-DOF) model to account for the trim penalties. Predictions based on these calculations did reveal a diminished benefit, but a 17% improved lift-to-drag ratio was still maintained. Wagner *et al.*[33] used a vortex lattice method to explore the drag reduction of multiple aircraft in close formation. Primarily, the influence of trimming the aircraft to overcome rolling moments induced by wake interference was demonstrated. Accounting for aircraft trim using aileron deflections inherently changed the optimal lateral position of the wingman (trailing) aircraft and somewhat reduced the energy saving benefit of the formation. Three T-38 aircraft in tight formation were predicted to increase the operating range of the entire formation by 11.5% and up to 67% for a single aircraft from the group. Despite roll trim-penalties, formations were shown to be favorable. An earlier flight test using two Dornier Do-28 by Beukenberg and Hummel[34] produced a 15% power reduction for the trailing aircraft and demonstrated the feasibility of control systems to maintain positioning in tight spacing. Pitch, roll, and yawing moment penalties were insignificant compared to the energy-saving mechanisms of formation-flight; even if the formation consists of only two planes. More recently, Kless *et al.*[35] performed a numerical study on the influence of aircraft in an extended-formation (around 30-span separation) configuration. The influence of trimming the aircraft to maintain position only reduced benefits at most by 5% for subsonic and 11% for transonic conditions returning a 54% and 35% drag decrease for subsonic and transonic conditions respectively. Indeed, the effects of trimming the aircraft to maintain steady level flight are important and change the optimal positioning, but much of the aerodynamic benefits can be maintained.

Past analysis of formation positioning has shown that benefits are particularly sensitive to lateral and vertical positioning of the aircraft, particularly near the locations

of maximum benefit. Without going into too much detail on this topic, a number of researchers have worked toward developing tools to assist in station-keeping for formation flight, such as Refs. [36, 37, 38, 39, 40] to name a few. NASA's autonomous flight project [23] demonstrated the feasibility of manual control with cues on the heads-up display to guide the pilot's actions. In the case of larger cargo and passenger aircraft in which extended-formations are more practical the longer distances can render station keeping a difficult task. Advanced collaborative positioning technology could be useful[41] in commercial applications. Furthermore, atmospheric disturbances can make the trailing vortex position difficult to predict. In this case it makes more sense to position the follower air vehicles based upon the wake rather than its position relative to other aircraft in formation. To this end, wake sensing techniques have also recently been under development[42]. As positioning and station-keeping technology become more advanced, the feasibility of practically applying formation flight concepts improves as well.

1.2 Streamwise vortex-surface interaction

Although motivated by the concept of formation flight, the work contained in this dissertation is intended to improve the understanding of the viscous and unsteady physics related to the broader class of streamwise vortex-surface interactions on a more fundamental level. This branch of flow-structure interaction can be further divided into three categories:

1. Wake-vortex interaction
2. Blade-vortex interaction (BVI)
3. Vortex-fin interaction

Each of these fields reveal unique perspectives of the general problem that provide a more comprehensive understanding of the topic when considered together. A review of the most relevant works is provided in the following sections organized according to the aforementioned classification.

1.2.1 Wake-vortex interaction

This branch of perpendicular vortex encounters can include aircraft flying in close proximity, unintentional wake crossings, or formation flight. As will become apparent through the following overview, this branch is dominated by research on the optimization of inviscid aerodynamic loading in the context of formation flight. However, there are many potential issues related to viscous and unsteady effects not well addressed in the literature to date.

Theoretical analysis

A number of theoretical analyses have investigated the optimum loading imposed by streamwise vortex interactions. Probably one of the earliest works on drag reduction in the context of aviation was Schlichting[43] who used lifting-line theory to predict power reductions of symmetrical V-formations for multiple aircraft. Years later, in order to demonstrate the applicability of biologically inspired formation flight in aviation, Beukenberg and Hummel[34] used horseshoe vortex and rolled-up vortex sheet models to predict the power reduction for a two aircraft in formation. A 10% power reduction was shown for the formation with a 17% reduction for the trailing aircraft. Somewhat more recently, Blake and Multhopp[44] presented a series of calculations for aircraft in close proximity using both a vortex lattice method and a horseshoe vortex model with a viscous core. This work explored heterogeneous formations where aircraft weight was not evenly distributed among the formation. Their findings suggested that heavier aircraft should be placed in the middle of the

formation and favored the use of an echelon configuration with the lead aircraft periodically rotating to the back of the group. Later, Blake[45] extended this work to include a larger number of aircraft using vortex lattice methods and experimental results emphasizing the influence of aerodynamic coupling due to the wake interference of aircraft in close formation.

Several authors have used various inviscid techniques in order to characterize optimal loading in formation configurations. For instance, Iglesias and Mason[29] and Frazier and Gopalarathnam[14], while using different methods, both found identical lift distributions that minimized induced drag for the entire formation. Similarly both concluded that streamwise spacing of the wings has little influence on the optimal loading. Later, King and Gopalarathnam[46], showed that wings in formation with an elliptic lift distribution can produce the same induced drag benefits as the optimal loading. This elliptic distribution can be realized by adapting wing shape in flight, similar to birds.

Experimental analysis

Experimental works exploring the effects of wake interaction are few and mostly focus on an exploration of wing positioning to find the optimal drag reduction and lift to drag ratios. For instance, Gingras[32] analyzed a wind-tunnel experiment on scale models of fighter aircraft and found a 30% increase in lift-to-drag ratios which resulted from an increased suction on the upper surface. The uneven loading due to the vortex encounter produced asymmetrical side-force and moment coefficients. Later, Blake and Gingras[28, 47] performed several wind-tunnel tests to investigate a two-body formation of delta wings which returned a 25% reduction in induced drag for the trailing wing. The most significant changes with respect to lift and moments for the trail wing were found to correlate with changes in lateral spacing where optimal conditions coincide with a small wingtip overlap. A similar trend with lateral

spacing was observed when the vertical offset was changed, but attenuation of the aerodynamic benefits from the optimal condition was less dramatic. A comparison between the experimental results and a vortex lattice method calculation was generally favorable except when the wings were positioned in such a manner that they overlap. This discrepancy was attributed to upwash induced by the lead wing which increases separation at the trailing wingtip.

A more recent paper by Bangash *et al.*[48] presents a series of wind-tunnel tests and vortex-lattice simulations for echelon, inverted-V, and inline formation configurations, see Figure 1.6. The lead-wing angle of attack and lateral positioning of the wings produced the strongest influence on the trailing wing. The upwash/downwash induced by the trailing vortex significantly modified the effective angle of attack along the span and can cause sections of the wing to stall that would otherwise remain attached. They found a favorable increase in lift-to-drag ratios for both the inverted-V and echelon formations while the echelon formation exhibited an undesirable rolling moment. In general, the effective angle of attack of trailing wings increased proportionately to the circulation of the leader wing trailing vortex due to the change in induced upwash. Both of the previous papers found that viscous effects induced by the wake encounter, such as flow separation, can become important aspects.

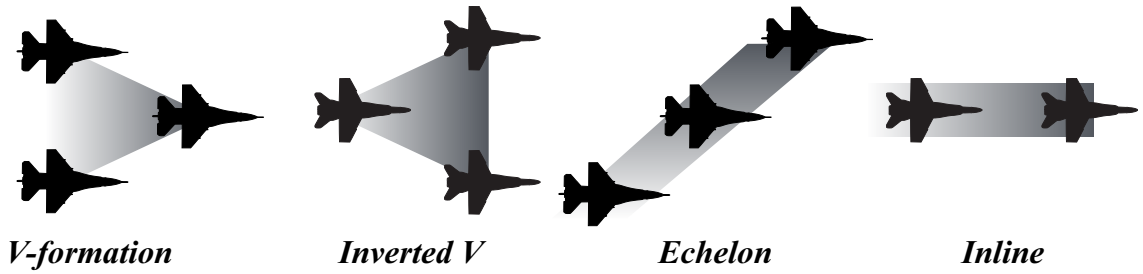

Figure 1.6: Formation configurations for two to three aircraft

Recently, Inasawa *et al.*[49] conducted wind-tunnel tests for two rectangular $\mathcal{R} = 5$ NACA 23012 wings in a close-formation. The maximum advantage of lift and drag was found at no vertical offset and a small positive lateral overlap of 5% of the

span producing a 24% increase in lift-to-drag ratio for the trail wing compared to an isolated wing at the same conditions. Particle image velocimetry (PIV) measurements elucidated the influence of the lead wing tip vortex encounter on the trail wing and several streamwise vortex interactions. For instance, at a small spanwise overlap, the lead wing trailing vortex was shown to interact with and reduce the circulation of the trail-wing tip vortex. This circulation reduction was found to be minimum (40% decrease) at the spacing that produces the optimal aerodynamic benefits.

Computational analysis

Due to the level of complexity and computational expense to model two wing bodies, numerical analysis of wings in formation flight has been almost exclusively limited to potential flow solutions. For instance, Refs. [44, 50, 40] employed various horseshoe vortex models. However, vortex lattice methods appear to have been the method of choice over the last several decades and have been used to find minimum drag[44, 28, 33, 30] and optimum span loads or downwash [29, 14] for a variety of configurations. Generally, the vortex lattice methods compare well with experimental results, except when the wings are close together[28, 50]. This discrepancy has been attributed to flow separation and the flat-wake model assumption used in these works[28, 47].

Several authors have incorporated relaxed-wake schemes such as Refs. [30, 20]. More recently, Bramesfeld and Maughmer[21] used a relaxed-wake model to investigate the effects of wake rollup which showed small improvement in aerodynamic predictions. While these simple numerical techniques are efficient to utilize and mostly match well with experimental data, they are limited to steady analysis and do not account for viscous effects shown in several of the experimental works[47, 19, 48]. Vortex lattice methods are not capable of predicting viscous effects which could be important in formation flight. For instance, Bangash[48] showed vortex induced separation due

to the trailing vortex upwash.

Based on Munk's stagger theorem[51], one would expect the total induced drag of the formation should not change as the streamwise separation is increased. Indeed, this appears to be a consistent observation among the potential flow solutions for close-formation configurations available in the literature[8]. However, in the large separation distances of an extended-formation, in which there are roughly 10-40 spans of streamwise separation, several important effects neglected by Munk's theorem become important. Ning *et al.*[52] developed an analytical approach which included several aspects relevant to extended formations such as the the effects of wake roll-up, vortex decay, vortex instabilities, vortex motion, and atmospheric turbulence. This work demonstrated the practicality of extended formation configurations which are more practical for larger cargo and passenger aircraft. They showed that a two-aircraft formation within 20 spans can reduce induced drag by 26-31% and three aircraft experiences a 38-45% reduction. Longer streamwise separations of roughly 40 spans resulted in degraded performance due to an increased influence of turbulent gusts.

A limited number of detailed numerical analyses is available due to the complexity and scale of this problem. Computations involving a just single body in flight can be rather complex. Including a second aircraft into numerical simulation can more than double the problem scale due to requiring two fully-resolved near-body regions and preservation of the lead-aircraft wake. Only in the last several years have detailed CFD (computational fluid dynamics) simulations been performed on a full formation configuration. For instance, a series of papers[31, 53, 35] explored steady, inviscid, extended formation flight (10-40 spans of streamwise separation between aircraft) building upon the previous analytical work in Ref. [52]. For instance, Ning and Kroo[53] used an Euler solver and wake propagation model in order to investigate the influence of two aircraft in extended-formation and evaluated the effects of

compressibility. They found that formation flight at the drag divergence Mach number, results in vortex-induced shocks on the follower aircraft which could cause flow separation and buffeting. This issue was alleviated by reducing the Mach number by 2-3% or flying at a 5% higher lift coefficient. A similar Euler/vortex-propagation model simulation by Kless *et al.*[35] followed this analysis in which both subsonic and transonic cases were considered. Overall, a 54% subsonic and 35% transonic induced drag reductions were found for the trailing aircraft which was appropriately trimmed to maintain positioning. Steady Reynolds-averaged Navier-Stokes (RANS) computations coupled with a wake propagation model have been recently reported by Slotnick *et al.*[54] as part of the Surfing Aircraft Vortices for Energy (SAVE) program.

Unresolved aspects

A number of aspects of the formation flight problem remain unresolved. Computational analysis has been almost exclusively limited to steady, inviscid computations. The limited number of detailed experiments identify viscous effects such as vortex induced separation in close vortex encounters where aerodynamic benefits are optimal. Mutual interference between vortex and wing, vortex-induced separation, and modification of the wing boundary layer can all significantly contribute to the general effects of the wake interaction problem. Furthermore, unsteady effects in trailing vortices, discussed in more detail later in Section 1.3, will invariably complicate vortex encounters.

1.2.2 Blade-Vortex interaction

The second major category is blade-vortex interaction (BVI). This topic typically refers to vortex interactions in the context of rotating machinery such as helicopter blades. Both parallel and perpendicular vortex impingements play important roles. Parallel vortices shed from a blade impose the most severe unsteady response and are

largely two-dimensional in nature. The perpendicular interactions have been found to be typically less severe, but are highly three-dimensional, complex, and provide asymmetrical, unsteady load distributions to a follower blade. Convenient to the current work, many of the experimental analyses on the perpendicular aspect of BVI have been conducted for a stationary, rather than rotating, follower blade. Therefore, these insightful studies significantly contribute to the general understanding of vortex wing interactions and are directly applicable to the current work. The most relevant of these articles are described in the following.

Patel and Hancock[55] conducted a qualitative wind tunnel study of two-dimensional blade sections at $\alpha = 0^\circ$ subjected to a trailing vortex generated upstream. Surface oil flow patterns of a close interaction revealed secondary separation imposed by the vortex as it traverses the surface as well as a small degree of lateral displacement. Smoke visualizations indicated breakdown of the otherwise stable vortex upstream of the airfoils when placed in a direct impingement. Breakdown ensued above the blades near the mid-chord when placed close to the wing surface. The flow visualizations of McAlister and Tung[56] demonstrated a streamwise vortex can burst when subject to stall above an airfoil at high angle of attack. Both of these studies demonstrate highly unsteady behaviors arising as a direct consequence of vortex-wing interaction that do not appear to have been explored in further detail.

Wittmer *et al.*[57] studied BVI in the context of parallel tandem wings and demonstrated close positioning rapidly diminishes vortex circulation and causes a rapid increase in turbulent fluctuations immediately downstream of interaction. A later study by Wittmer and Devenport[58] showed that secondary vorticity induced by vortex-surface interaction in conjunction with the follower blade wake turbulence contribute to the rapid dissipation of the incident swirling flow. More recently, Zanotti *et al.*[59] provided stereo PIV of a perpendicular vortex passing over a pitching airfoil and found alternating patterns of localized vortex-induced stall can significantly increase air load

hysteresis. Bhagwat *et al.*[60] obtained sectional load distributions and revealed a highly asymmetrical distribution of vortex-induced surface forces partly attributed to three-dimensionality imposed by the follower blade tip.

1.2.3 Vortex-fin interaction

A number of works that appeared around the turn of the century explored the influence of vortices generated by delta wings on aircraft fins and discussed sources of buffeting. Practically speaking, these studies were motivated by flow separation on leading-edge surfaces of fighter aircraft operating at high angles of attack, see Figure 1.7, and provide some of the best insight for the implications for unsteady fluid dynamics in perpendicular vortex encounters. Most of these cases involve a broken-down vortex (Section 1.3.4) upstream of a vertical fin; an emphasis related to the strong influence of vortex breakdown type[61] or position[62] on buffeting behavior. This section surveys the literature most pertinent to the current study.

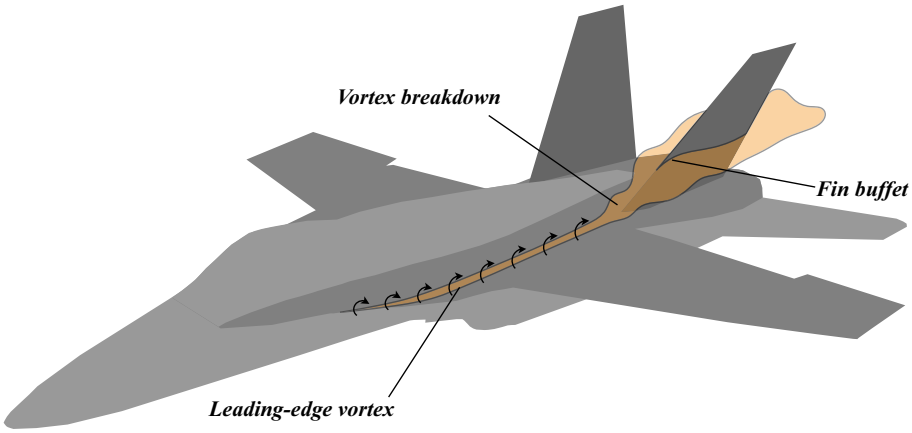

Figure 1.7: Streamwise vortex interaction with an aircraft fin

Mayori and Rockwell[1] conducted water-tunnel experiments on the impingement of a streamwise-oriented vortex that experiences breakdown upstream of a thin plate. Encounter of the incident vortex resulted in a bifurcation in which components of the swirling flow travel on either side of the plate following breakdown and produce a

chaotic flow field as they recombine in the wake. The trajectory of each component, depicted in Figure 1.8(a), was shown to diverge from the incidence location in opposite directions. This effect can be understood to be consistent with the interaction of an inviscid vortex with a solid surface[63] and shown in Figure 1.8(b). The self-induced velocity of the counter-rotating vortices results in motion of the virtual pair. Similar bifurcation and vortex-surface interaction was observed the close-formation experiment of Ref. [49] which was again consistent with the influence of image-effects of the wing surface.

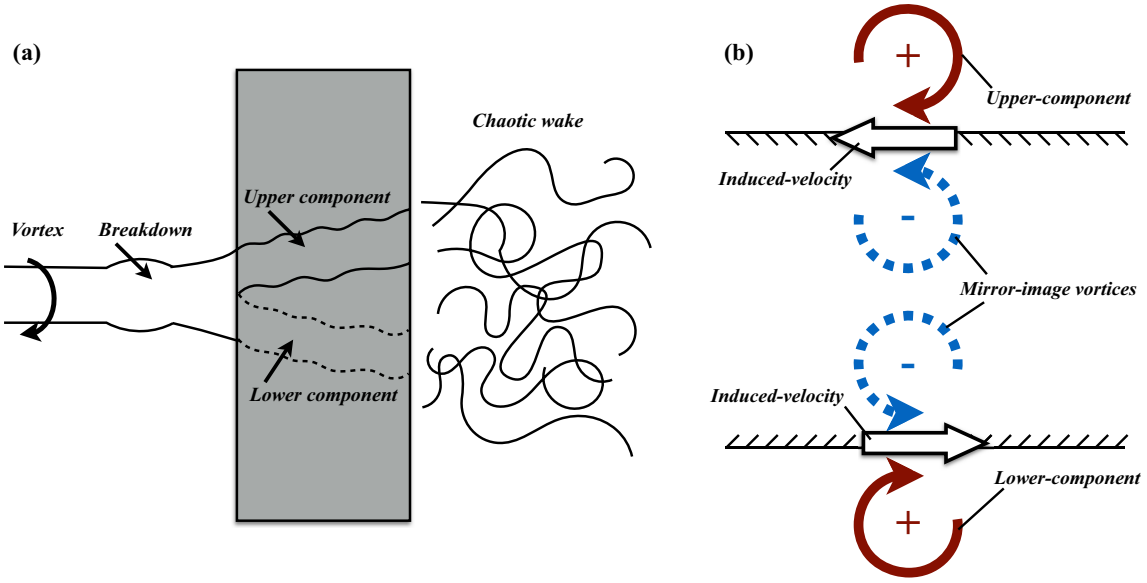

Figure 1.8: (a) Vortex-surface interaction as described by Mayori and Rockwell[1], (b) image-effects during vortex-surface interaction

Secondly, fluctuations in the surface pressure were related to the wavelength of the vortical structures over the plate. Larger scale/wavelength vorticies will tend to produce higher pressure fluctuations on the wing surface. Control of the incident vortex produced a more disorganized vortical structure upstream of the fin. The lower-amplitude pressure fluctuations resulted in a diminished correlation of the incident vortex with surface loading. Consequently, flow control was identified as a means to reduce fin buffeting. Later, additional water-tunnel experiments of Canbazoglu *et*

al.[64] showed the impingement of a streamwise vortex on a swept fin. In this case, vortex impingement resulted in the formation of a secondary counter-rotating vortex on the outboard side and stronger vorticity fluctuations along the fin leading-edge.

Following the previous woks, Wolfe *et al.*[61] investigated the direct impingement of streamwise vortices generated by an upstream delta wing using particle image velocimetry to evaluate the influence of the incident vortex on surface pressure fluctuations. As in the previous cases, the streamwise vortex was broken down upstream of the plate. Flow structure and unsteady loading were evaluated for a number of vertical, and lateral spacings of the incident vortex. The dominant frequency in pressure load fluctuations was found to be relatively insensitive to actual positioning while the amplitude of pressure fluctuations was shown to be strongly dependent on vortex breakdown position. Hence, the level of pressure fluctuations could be mitigated through flow control of the vortex breakdown or diverting the vortex to a less sensitive location.

Later, Gordnier and Visbal[2] used solutions of the unsteady three-dimensional Navier-Stokes equations to explore the sources of fin buffeting in the experiments of Ref. [61] in more detail. Three-dimensional leading-edge separation, bifurcation, and unsteady loading induced by the upstream vortices from a delta wing were revealed in this work. Spiral breakdown, Figure 1.9, of the streamwise vortex was directly related to feedback from the separated flow on the flat plate. This undulating behavior resulted in the formation of unsteady vortical features over the wing surface and consequently highly unsteady loading on the plate's forces and moments. Investigation of the mutual interaction between stall on the plate and breakdown of the incident vortices underscores the importance of detailed numerical simulations in understanding highly dynamic streamwise vortex-surface interactions.

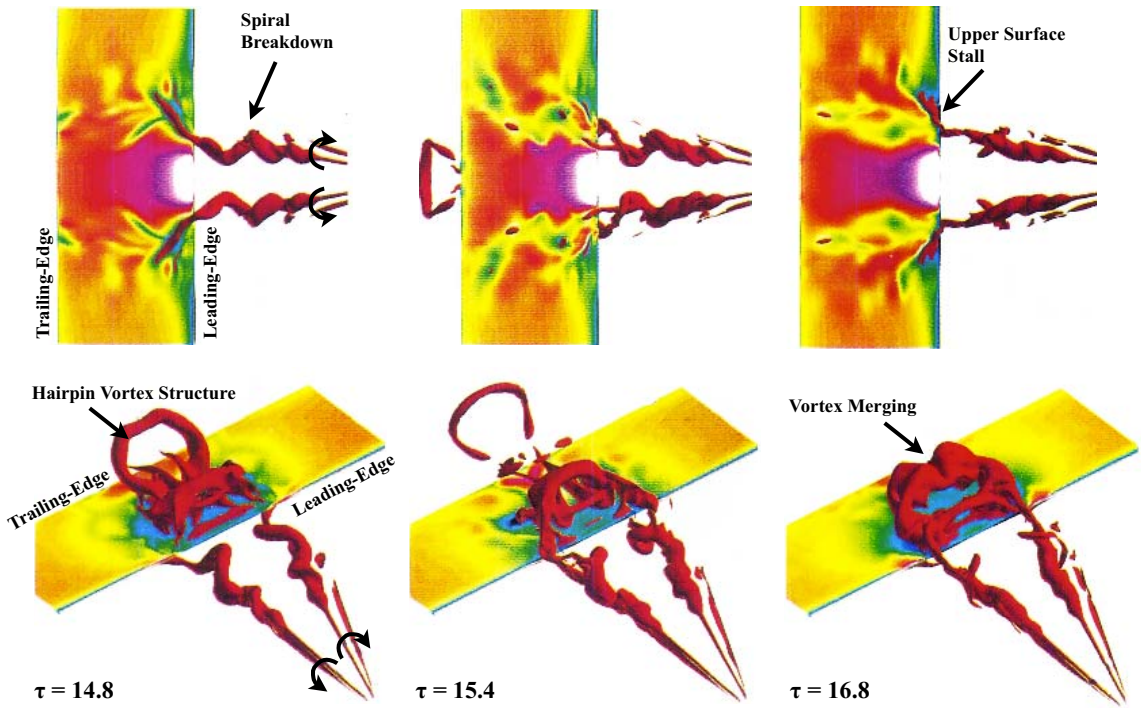

Figure 1.9: Unsteady, three-dimensional structure of vortex impingement on a plate[2]

Gursul and Xie[65] provided experimentation that suggests several other vortex-related phenomena in addition to breakdown that contribute to fin buffet. Fluctuations in breakdown location and vortex shedding can both provide unsteady loading on a vertical plate. More recently, Gursul and Xie[66] conducted a water tunnel study to evaluate the influence of forced fin oscillations on the unsteady fluid dynamics in the fin buffeting problem. Their work revealed a correlation between the fin oscillation frequency and the amplitude of vortex breakdown location upstream of the fin. Most notably, the ability for disturbances to propagate upstream decreased with increasing oscillation frequency suggesting behavior much like a low-pass filter.

Lambert and Gursul[67] measured the tip acceleration of a fin subject to a broken-down vortex. They found inboard fin positions were the most susceptible to dynamic behavior and demonstrated through PIV measurements that maximum buffet occurs when the shear layer of the breakdown region impinges on the fin. Another experiment

by Phillips *et al.*[68] investigated the interaction of a leading-edge vortex from a delta wing impinging on a flexible fin. In this case, the adverse pressure gradient associated with the fin induced a breakdown of the incident vortex. Application of a deflected jet was used to control and delay vortex breakdown to a location behind the fin subsequently diminishing buffet. This work demonstrated control of dynamic behavior in a streamwise vortex not by deflecting the vortex, but by delaying instability.

1.3 Unsteady physics

Much of the work on unsteady physics of streamwise vortices, with the exception of vortex breakdown, has been conducted in order to better understand the progression of turbulence in the otherwise persistent trailing vortices of aircraft rather than study the potential implications for vortex-surface interaction which is the goal of the present work. The following sections provide a brief survey of the most prevalent unsteady physical phenomena that can contribute to the perpendicular vortex-surface interaction problem. This section is not intended to be a thorough review of the field of study, but rather an introduction to each of the most important topics relevant to this document.

1.3.1 Crow instability

The first class of unsteady behavior to be discussed here is the long-wave or Crow instability named for the discovering researcher[69]. This instability typically occurs when the mutual strain field imposed by the counter-rotating vortex in a pair of trailing vortices resonates with a long, bending Kelvin wave and amplifies perturbations in either, but typically both, vortices. This particular phenomenon is considered a long-wave instability due to the axial wavelength being much larger than

the vortex core. The Crow instability is unique to counter-rotating vortex pairs. For instance, Jimenez[70] and Bristol *et al.*[71] both showed the Crow instability cannot arise in the case of co-rotating vortices which is more conducive for the growth of short-wave instabilities discussed next. Late stage development of the Crow instability eventually culminates in the periodic connection of the initially parallel vortices into an intermittent series of ring-like flow structures when disturbance amplitude becomes sufficiently large, portrayed in Figure 1.10(a). This behavior ultimately leads to the decomposition and dissipation of the initially persistent trailing vortex pair[72].

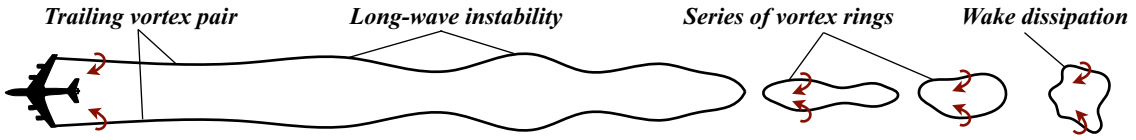

(a) Long-wave (Crow) instability

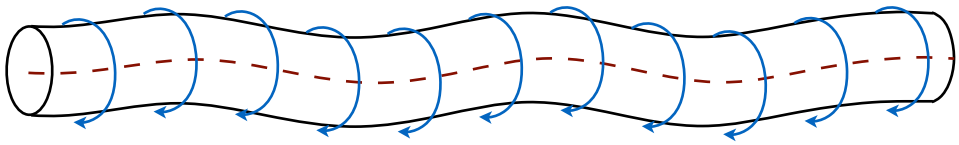

(b) Short-wave (Elliptical) instability

Figure 1.10: Cooperative instabilities between parallel streamwise vortices: (a) long-wavelength (Crow) instability and (b) short-wavelength (elliptical) instability

1.3.2 Elliptical instability

Elliptical instabilities refer to a second class of unsteady behavior in columnar vortices, as portrayed in Figure 1.10(b), and have much shorter wavelengths than the aforementioned Crow instability–typically on the order of the vortex core size. This instability derives its name from the elliptical distortion of two-dimensional streamlines in the vortex core provided by the influence of external strain fields[73]. Subsequently, short-wave instabilities arise when a Kelvin-mode or a Kelvin-mode pair of the elliptical flow field resonate with the external strain field[73]. Contrary to

the Crow instability, strain fields provided by either counter or co-rotating vortices can promote the growth of short-wave instabilities[74]. Several authors[74, 75] have shown elliptic instability for closely positioned parallel vortices is conducive to the transfer of energy between the swirling flow regions and ultimately leads to dissipation through the non-linear growth phases as vortical structures decompose and become more disorganized[72].

Earlier observations of the tendency for this unsteady behavior to accelerate the destruction of persistent trailing vortices have spurred much interest in the aerodynamic community in recent years. Enhanced dissipation of trailing vortices would improve safety for aircraft flying in close proximity or reduce the spacing between take-off and landings at airports. When several streamwise vortices exist behind an aircraft due to multiple aerodynamic or control surfaces, short-wave instabilities are also responsible for a vortex-merging phenomenon that consequently reduces the number of wake vortices[76].

Relative to the current problem, elliptical instabilities are not limited to the mutual induction of parallel swirling flow regions as many of the theoretical and experimental works described in the review by Kerswell[73] describe the growth of elliptic instability due to generic strain fields. It is not unreasonable to expect vortex-surface interaction to elicit this phenomenon through viscous shear or image-effects with an aerodynamic surface. Interaction between incident swirling flow and an adjacent follower wing tip vortex is capable of succumbing to this particular instability. Ryan *et al.*[77] have studied the elliptical instability of unequal strength axial vortices relevant to such a condition. Similarly, cooperative instability between parallel streamwise vortices will appear as a significant aspect of the unsteady flow described later in this document.

1.3.3 Hydrodynamic instability

Strain fields are not the only mechanism to promote the growth of disturbances in streamwise vortices. Isolated columnar vortices with an axial velocity component can become susceptible to short-wave instabilities independent of an external influence. The growth of short-wave perturbations has been widely studied for the q-vortex[78] which is a common model for an aircraft trailing vortex far downstream. The specifics of the q-vortex will be discussed in more detail upon its first use in Chapter 5.

Typically, the ratio of tangential to axial velocities dictates the growth of unstable modes[79]. For instance, Leibovich and Stewartson[80] conducted an asymptotic analysis on the q-vortex and derived a stability criterion solely dependent on the swirl ratio, $q = \Gamma/2\pi r_v \Delta u \approx 1.576 V_0/\Delta u$, where V_0 is the maximum tangential velocity and $\Delta u = U_\infty - u_{\min}$ is the axial velocity difference with the free stream. They found that when the swirl ratio is sufficiently large, rotation suppresses the growth rate of unstable modes at all radial positions. For $q < 1.5$, azimuthal instabilities appear in an annular concentration within the vortex core and take on a helical structure in the three-dimensional flow-field. The sign of the azimuthal wave-number, n, of these spiral instabilities depends upon the streamwise velocity profile of the vortex[81]. Wake-like axial profiles result in $-n$ wavenumber instabilities that propagate in the direction opposing the swirling flow. Reversal of the axial velocity profile to a jet-like vortex simply results in a sign change, $+n$, of the same spiral modes[82].

Other types of hydrodynamic instability of a single q-vortex have been found such as the viscous instability modes described by Khorrami[82] or Mayer and Powell[83] and the so-called center-modes of Fabre and Jacquin[84] that occur in higher Reynolds number flows. More information on the fundamental analysis of these and other unsteady behaviors can be found in the review by Ash and Khorrami[79]. While the taxonomy of hydrodynamic instability of axial vortices is a complex and diverse field, it will become apparent later that the helical-modes of instability described above

can be a robust and influential behavior in streamwise vortex-surface interactions.

1.3.4 Vortex breakdown

Vortex breakdown, also frequently called vortex bursting, is perhaps the most severe of the unsteady vortex behaviors documented in the literature. A detailed description or review of this complex and highly non-linear phenomenon is well outside the scope of this dissertation. A very brief synopsis is provided below to introduce the concept as it pertains to the current topic.

Although some debate exists in the technical community on a systematic definition of vortex breakdown, the phenomenon typically entails an abrupt change in vortex diameter followed by large-scale fluctuations downstream[85, 86]. A stricter definition proposed by Leibovich[87] requires a stagnation point followed by flow reversal contained within a small streamwise extent. Two topologies generally appear when breakdown ensues: spiral or bubble-type[88], both well-portrayed by the dye visualizations of Lim and Cui[3] in Figure 1.11. The bubble-type topology describes an abrupt axisymmetric swelling of the vortex core followed by a chaotic, often helical, flow structure downstream. Spiral-type breakdown is inherently non-axisymmetric and consists of a large amplitude helical structure immediately following of the onset of breakdown. Broadhurst[89] demonstrated spiral mode instability can evolve from the non-linear growth of helical mode instabilities.

Figure 1.11: Bubble (left) and spiral (right) breakdown[3]

This feature, either bubble or spiral-type, is known to be a generic transformation of the general flow structure and pervades in the swirling flow of many technological

applications. It has been an extensively studied topic for the unsteady flow above slender (delta) wings[88] and shown to be the cause of abrupt changes in aerodynamic forces and contribute to control difficulties[90]. It has also been known to be an influential factor in the service-life of vertical fins[65], contributes to the decay of trailing vortices[91, 92], and has been observed on revolving wings[93] to name a small set of the aerodynamic applications.

1.3.5 Vortex meandering

Vortex meandering, or wandering, describes random low-frequency motion of the trailing vortex core from its mean position. This unsteady behavior significantly contributes to measurement errors of the mean velocity profiles in experimental studies. Devenport *et al.*[94] proposed a now widely used approach to correct for meandering in experimental measurements of trailing vortices.

Despite being a well-known unsteady streamwise vortex behavior, a unified explanation of its origins still escapes aerodynamics researchers. A number of possible sources have been suggested for its origin, but none of them conclusively proven. Probably the most commonly attributed source is a high sensitivity to background fluctuations such as those inherent to wind tunnel flows[95], atmospheric turbulence [94], and wake turbulence[72]. More recently, several authors have proposed Biot-Savart induction as a potential contributor. For instance, Rokhsaz *et al.*[96] suggested self-induction as a possible cause while Gursul and Xie[97] proposed induction of small scale vortices provided by Kelvin-Helmholtz instability in the shear layer. One additional proposed origin are the viscous center mode instabilities of Fabre and Jacquin[84] briefly introduced in Section 1.3.3.

Contribution to the understanding of this complex and elusive topic is well outside the scope of this dissertation, but is noteworthy for its implications in the current work that will become apparent later. While meandering behavior is typically small

in amplitude, typically around $\sigma = 0.01c$, see for instance the measurements in Ref. [94]. However, they can grow to many times to core diameter [95] far downstream. One recent study[98] reported meandering amplitudes of to up to $\sigma = 0.085c$ at only four chords behind the wing. In all cases, meandering behavior tends to increase further downstream. External factors such as free stream or wake turbulence can exacerbate wandering amplitudes. Bailey and Tavoularis[99] reported a more than tenfold increase in wandering amplitude in the presence of free stream turbulence.

1.4 Research contributions

Although progress has been made to improve the understanding and prediction of impacts in the application of streamwise-oriented vortex interactions, a number of issues must still be addressed. In the context of formation flight, an overwhelming majority of the work consists of steady inviscid analyses for the optimization of aerodynamic loads. One set of steady RANS computations[54] has emerged in the last couple of years. Meanwhile, several experimental works[47, 55, 100, 56, 101] and flight tests[25] suggest that both viscous and unsteady effects can be very important factors.

The rich dynamics associated with trailing vortices are not well-understood in the context of tandem wings. Crow (Section 1.3.1) and elliptical (Section 1.3.2) instabilities in addition to spiral breakdown (Section 1.3.4) may significantly affect the interaction of an axial vortex with a surface and result in buffeting behavior. High dynamic loading can reduce the service life of structural components and result in early airframe failure. Streamwise vortex-surface interactions remain a fertile and important topic for discovery and understanding.

Experimental analysis to date lacks the ability to provide sufficient temporal or spatial resolution to fully describe the salient fine-scale three-dimensional features of

many complex evolving flows. For example, the unsteady Navier-Stokes simulations by Gordnier and Visbal[2] helped to reveal the complicated and interrelated physics involved between spiral breakdown and unsteady leading-edge separation for slender wing vortices impinging on a plate. High-fidelity computational analysis can play a crucial role in addressing the many unresolved aspects within the broader class of problems, but sufficiently detailed numerical simulations have been historically limited by computational cost and complexity required by the problem setup. Therefore, this dissertation seeks to expand the current knowledge of this topic by providing the necessary high-fidelity implicit large-eddy simulations capable of elucidating the detailed unsteady fluid physics.

The first aim of this work is to characterize and understand the primary phenomena that appear in perpendicular vortex-wing interactions. This study differs from the fin-buffet problem in that it explores the interactions of otherwise stable-laminar vortices with an aerodynamic surface and reveals the unsteady physics directly related to vortex-surface interaction rather than due to breakdown preceding impingement. In order to help disentangle the intertwined physics related to fluid-structure interaction, two complimentary and well defined configurations, designed to provide a more fundamental understanding of the problem, are employed. Due to the basic nature of this research, the findings of this work extend well to the general class of streamwise vortex-surface interaction and are not limited to the single application of formation flight.

Fuel-efficient trends in airframe designs tend to lighter weight structures and high aspect ratios becoming increasingly prone to aeroelastic behaviors. Unsteady fluid dynamics can be inherently coupled to the structural dynamics of compliant structures and is perhaps best portrayed by the fin-buffet problem[62, 1, 61, 2, 68, 67]. Fluctuating loads provided by any manner of unsteady fluid dynamics can excite natural frequencies of an aerodynamic structure. Bending or pitching oscillations have

to potential to provide feedback effects to the incident flow[66]. Mutual interaction between the fluid and structural dynamics has the potential to produce sustained oscillations and in the worst case lead to catastrophic failure.

Therefore, the second major goal of this dissertation is to explore the influence of aeroelasticity in streamwise-vortex encounters. Exploration of the structural response and its subsequent impact on the detailed flow structure will lead to a better understanding of the favorable/unfavorable effects of structural compliance in the presence of swirling flows. This work encompasses the first high fidelity study on aeroelasticity in perpendicular vortex interactions and reveals a number of important consequences of wing compliance. Full aeroelastic simulations are presented followed by isolation of the effects provided by both static and dynamic deformations.

The described analysis necessitates the use of highly advanced numerical tools. To this end, the extensively validated multi-physics research code *Fluid Dynamics Lab 3D Aeroelastic* (*FDL3DAE*) was chosen for the current work. This aeroelastic solver couples a high-order implicit large-eddy simulation (ILES) approach with geometrically non-linear mixed Reissner-Mindlin plate elements. Details of the solution procedure are provided in Chapter 2.

1.5 General configuration

A generic depiction of the configuration of interest in this work is provided in Figure 1.12 in order to introduce the general problem. Here, a rectangular flat plate wing with an aspect-ratio of $\mathcal{AR} = 6$ and thickness of $t/c = 0.03$ operates at a chord-based Reynolds number of $\mathrm{Re} = 30,000$ and is oriented at an angle of attack of $\alpha_F = 5^\circ$. This wing, referred to henceforth as the *follower wing*, is subjected to a streamwise vortex under different parameters in each chapter.

The streamwise-oriented vortex is generated upstream of the leading-edge with

its upwash on the inboard side of the wing and downwash on the outboard side. The lateral and vertical positioning of the vortex generator is measured relative to the wingtip mid-chord by the parameters Δy and Δz, respectively. Two different approaches are utilized to generate the vortex in this work: (1) a leader wing flying in close proximity, and (2) a q-vortex[78] imposed at the inflow boundary.

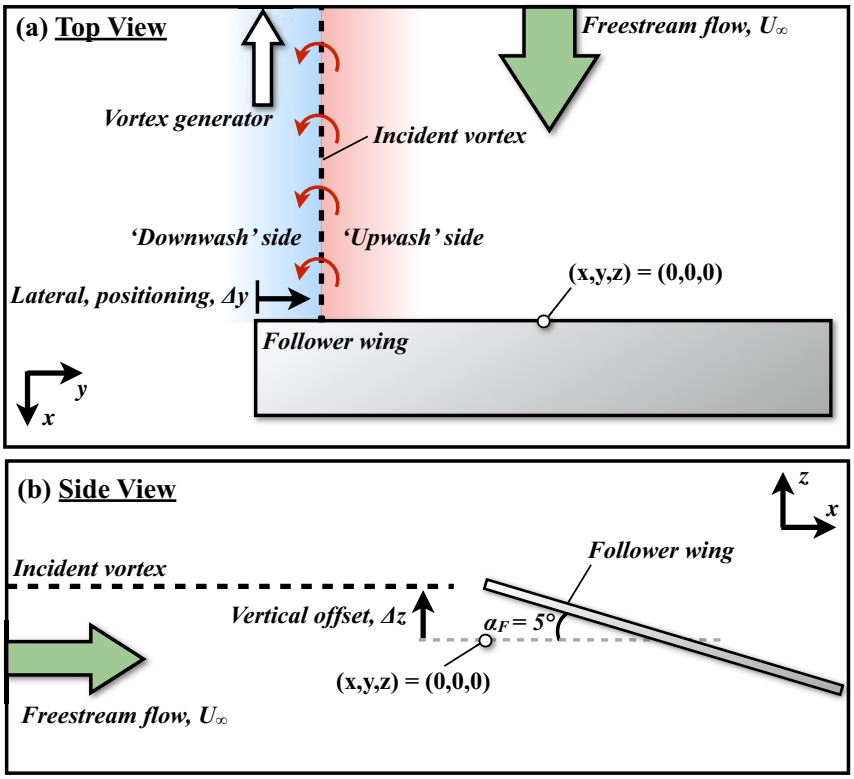

Figure 1.12: General configuration: (a) top view and (b) side view

This particular setup provides a canonical configuration that helps to reduce the overall number of parameters of a very complex problem, allows for systematic exploration of the parameter space, and is conducive to providing a better fundamental understanding of the complex physics associated with streamwise vortex-surface interactions. Several aspects of streamwise vortex-interaction are explored in this dissertation including: lateral and vertical positioning of the streamwise vortex, leader wing angle of attack, follower wing flexibility, and imposed static and dynamic deformations of the follower wing. Each portion of this work deviates from this baseline

description to some extent where the specific configuration used for each section is introduced in the corresponding chapter.

1.6 Document organization

The organization of this document follows the general path of research and discovery shown in Figure 1.13 and described in the following. This work began by exploring a follower wing subject to a physically generated vortex emanating from a leader wing flying in close-proximity. Several aspects of the problem were explored including the lateral positioning and angle of attack of the leader wing and flexibility of the follower wing. While this analysis provided significant insight to the general problem, needs for further simplification were identified in order to better isolate and characterize the unsteady physics. Next, the approach employed in a congruent work[102, 5] was adopted and the effects of flexibility were explored. Here, the physical trailing vortex from the leader wing was replaced with a q-vortex imposed at the inflow boundary in order to remove complicating factors of the tandem wing configuration. Significant time-mean bending deformations in addition to small-amplitude oscillations were observed, but the static (time-mean) component was found to provide the most significant impact on the unsteady fluid dynamics. This unexpected finding motivated further research into the effects of vertical positioning on the imposed vortex definition as a more rigorous exploration on the effects of vortex-induced bending. Finally, the effects of dynamic aeroelastic deformations were analyzed by subjecting the incident vortex to forced bending oscillations on the follower wing in order to provide understanding of the potential influence of dynamic aeroelasticity not captured in the passive aeroelastic simulations.

The remaining sections of this dissertation are organized in the following manner:

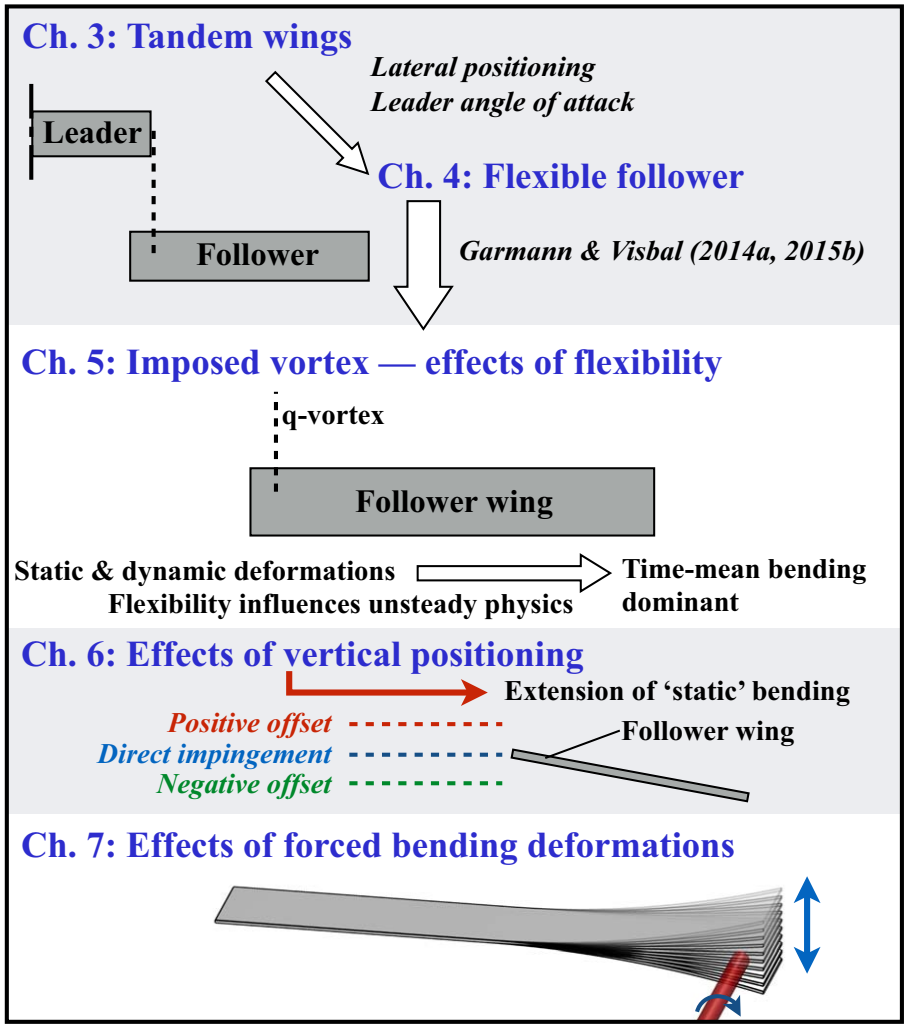

Figure 1.13: Chronological order of research conducted

Chapter 2 provides details regarding the methodology used for different portions of this work. Topics include: high-fidelity implicit large-eddy simulation (ILES), geometrically non-linear plate element, and the coupling process between the two procedures.

Chapter 3 presents simulations of rigid flat plate wings in a close formation. The effect of lateral positioning and strength of the incident vortex are evaluated in this section. This research provides unique insight into the unsteady behaviors that can arise and describes where viscous effects are important to aerodynamic loads.

Chapter 4 investigates the effect of follower wing flexibility in close formation. Time-mean vortex-induced bending can shift interaction away from the intended regime and provide a notable change to wake evolution immediately behind the follower wing.

Chapter 5 subjects the follower wing to a stronger streamwise vortex isolated from complicating factors provided by the leader wing. This approach elicits a more pronounced interaction and removes interrelated factors. This section describes the impact of wing compliance on vortex stability and unsteady loading and reveals the major influence of flexibility by isolating the effects of static from dynamic deformations.

Chapter 6 demonstrates the impact of vertical positioning on rigid wings and identifies stablizing and destabilizing operating regimes. The clear upstream influence of the wing due to adverse pressure gradients is revealed and spiraling undulations are linked to hydrodynamic instability.

Chapter 7 clarifies dynamic aeroelastic effects using forced bending oscillations to isolate the dynamic component of flexible wings. The influence on feedback response and unsteady flow structure are emphasized in this chapter.

Chapter 8 summarizes the main contributions of this dissertation and provides recommendations for future work.

Chapter 2

Methodology

This chapter provides a description and references for the methodology contained within the in-house aeroelastic solver *FDL3DAE*. The important details regarding spatial and temporal discretization are provided for both the fluid and structural components as well as their coupling procedure. An additional validation test is presented demonstrating the capability of the fully coupled procedure.

2.1 Fluid Solver

The implicit large-eddy simulation (ILES) approach used for the fluid dynamics side of *FDL3DAE* is described first. The governing equations, spatial and temporal discretization, and implicit filtering are described in the following.

2.1.1 Governing equations

The formulation begins with the three-dimensional, compressible, unsteady Navier-Stokes equations cast in strong conservation form and transferred from Cartesian coordinates (x, y, z, t) in the physical domain to the computation domain in curvilinear coordinates (ξ, η, ζ, τ)[103, 104]. The system of equations are non-dimensionalized

and written in vector form as,

$$\frac{\partial}{\partial \tau}\left(\frac{\mathbf{U}}{J}\right)+\frac{\partial \mathbf{F}_I}{\partial \xi}+\frac{\partial \mathbf{G}_I}{\partial \eta}+\frac{\partial \mathbf{H}_I}{\partial \zeta}=\frac{1}{\mathrm{Re}}\left[\frac{\partial \mathbf{F}_v}{\partial \xi}+\frac{\partial \mathbf{G}_v}{\partial \eta}+\frac{\partial \mathbf{H}_v}{\partial \zeta}\right] \tag{2.1}$$

where the vector of conservative variables is given by $\mathbf{U}=\{\rho,\rho u,\rho v,\rho w,\rho E\}^T$, $J=\partial(\xi,\eta,\zeta,\tau)/\partial(x,y,z,t)$ is the transformation Jacobian[105]. The non-dimensional time is given by $\tau=\Delta t U_\infty/c$ where U_∞ is the free stream velocity, c is the reference chord length. $\mathrm{Re}=\rho U_\infty c/\mu$ is the Reynolds number based on the chord length where ρ is the fluid density and μ is the dynamic viscosity.

The inviscid flux vectors are given by

$$\mathbf{F}_I=\frac{1}{J}\begin{bmatrix}\rho U\\ \rho uU+\xi_x p\\ \rho vU+\xi_y p\\ \rho wU+\xi_z p\\ (\rho E+p)U-\xi_t p\end{bmatrix},\mathbf{G}_I=\frac{1}{J}\begin{bmatrix}\rho V\\ \rho uV+\eta_x p\\ \rho vV+\eta_y p\\ \rho wV+\eta_z p\\ (\rho E+p)V-\eta_t p\end{bmatrix},\mathbf{H}_I=\frac{1}{J}\begin{bmatrix}\rho W\\ \rho uW+\zeta_x p\\ \rho vW+\zeta_y p\\ \rho wW+\zeta_z p\\ (\rho E+p)W-\zeta_t p\end{bmatrix} \tag{2.2}$$

where

$$\begin{aligned}U&=\xi_t+\xi_x u+\xi_y v+\xi_z w\\ V&=\eta_t+\eta_x u+\eta_y v+\eta_z w\\ W&=\zeta_t+\zeta_x u+\zeta_y v+\zeta_z w\end{aligned} \tag{2.3}$$

are the contravariant velocities and

$$E=\frac{T}{(\gamma-1)M_\infty^2}+\frac{1}{2}(u^2+v^2+w^2) \tag{2.4}$$

is the internal energy. Here the quantities u, v, and w are the Cartesian velocity components, p is pressure, and T is temperature.

The viscous flux vectors are given by

$$\mathbf{F}_v = \frac{1}{J}\begin{bmatrix} 0 \\ \xi_{x_i}\sigma_{i1} \\ \xi_{x_i}\sigma_{i2} \\ \xi_{x_i}\sigma_{i3} \\ \xi_{x_i}(u_j\sigma_{ij} - \Theta_i) \end{bmatrix}, \mathbf{G}_v = \frac{1}{J}\begin{bmatrix} 0 \\ \eta_{x_i}\sigma_{i1} \\ \eta_{x_i}\sigma_{i2} \\ \eta_{x_i}\sigma_{i3} \\ \eta_{x_i}(u_j\sigma_{ij} - \Theta_i) \end{bmatrix}, \mathbf{H}_v = \frac{1}{J}\begin{bmatrix} 0 \\ \zeta_{x_i}\sigma_{i1} \\ \zeta_{x_i}\sigma_{i2} \\ \zeta_{x_i}\sigma_{i3} \\ \zeta_{x_i}(u_j\sigma_{ij} - \Theta_i) \end{bmatrix} \tag{2.5}$$

in indicial notation where the stress tensor (σ_{ij}) and heat flux vector (Θ_i) are given by

$$\sigma_{ij} = \mu\left(\frac{\partial\xi_k}{\partial x_j}\frac{\partial u_i}{\partial\xi_k} + \frac{\partial\xi_k}{\partial x_i}\frac{\partial u_j}{\partial\xi_k} - \frac{2}{3}\delta_{ij}\frac{\partial\xi_l}{\partial x_k}\frac{\partial u_k}{\partial\xi_l}\right) \tag{2.6}$$

and

$$\Theta_i = -\left[\frac{1}{(\gamma-1)M_\infty^2}\right]\left(\frac{\mu}{Pr}\right)\frac{\partial\xi_j}{\partial x_i}\frac{\partial T}{\partial\xi_j} \tag{2.7}$$

Here M_∞ and γ are the freestream Mach number and ratio of specific heats ($\gamma = 1.4$) respectively where $M_\infty = 0.1$ for all cases in this work for an effectively incompressible flow. Additionally, Stoke's hypothesis was used for the bulk viscosity coefficient where $\lambda = -2/3\mu$. The Prandtl number, Pr, was chosen as a constant value of Pr = 0.72. Sutherland's law and the perfect gas law, $p = \rho T/\gamma M_\infty^2$, were used to close the Navier-Stokes equations. Each of the flow variables are normalized by the free stream quantities except pressure which is non-dimensionalized by $\rho_\infty U_\infty^2$ and lengths are scaled by the chord.

2.1.2 Time integration

Time-marching is accommodated using the implicit, approximately factored Beam and Warming[106] scheme. Shifting to delta form and applying Newton-like sub-

iterations, this procedure is written for Eq. 2.1 as

$$\begin{aligned}
&\left[\left(\frac{1}{J}\right)^{p+1} + \psi^i \Delta\tau \delta_\xi^{(2)} \left(\frac{\partial \mathbf{F}_I^p}{\partial \mathbf{U}} - \frac{1}{\mathrm{Re}}\frac{\partial \mathbf{F}_I^p}{\partial \mathbf{U}}\right)\right] J^{p+1}\times \\
&\left[\left(\frac{1}{J}\right)^{p+1} + \psi^i \Delta\tau \delta_\xi^{(2)} \left(\frac{\partial \mathbf{G}_I^p}{\partial \mathbf{U}} - \frac{1}{\mathrm{Re}}\frac{\partial \mathbf{G}_I^p}{\partial \mathbf{U}}\right)\right] J^{p+1}\times \\
&\left[\left(\frac{1}{J}\right)^{p+1} + \psi^i \Delta\tau \delta_\xi^{(2)} \left(\frac{\partial \mathbf{H}_I^p}{\partial \mathbf{U}} - \frac{1}{\mathrm{Re}}\frac{\partial \mathbf{H}_I^p}{\partial \mathbf{U}}\right)\right] J^{p+1}\times \qquad (2.8) \\
= -\psi^i \Delta\tau &\left[\left(\frac{1}{J}\right)^{p+1} \frac{(1+\psi)\,\mathbf{U}^p - (1+2\phi)\,\mathbf{U}^n + \phi \mathbf{U}^{n-1}}{\Delta\tau} + \mathbf{U}_I^p \left(\frac{1}{J}\right)_\tau^p + \right. \\
&\left. \delta_\xi \left(\mathbf{F}_I^p - \frac{1}{\mathrm{Re}}\mathbf{F}_v^p\right) + \delta_\eta \left(\mathbf{G}_I^p - \frac{1}{\mathrm{Re}}\mathbf{G}_v^p\right) + \delta_\zeta \left(\mathbf{H}_I^p - \frac{1}{\mathrm{Re}}\mathbf{H}_v^p\right)\right]
\end{aligned}$$

where $\partial/\partial\mathbf{U}$ are flux Jacobians, δ denotes spatial differentiation in the coordinate direction of the respective subscript, $\psi^i = 1/(1+\psi)$ and $\psi = 1/2$ gives second-order temporal accuracy. The quantity $\Delta\mathbf{U} = \mathbf{U}^{p+1} - \mathbf{U}^p$ permits the sub-iteration procedure where $\mathbf{U}^p$ represents the p^{th} approximation of $\mathbf{U}^{n+1}$. On the first sub-iteration, $p = 1$ and $\mathbf{U}^p = \mathbf{U}^n$. Equation 2.8 is iterated within a time step where $\mathbf{U}^p$ goes to $\mathbf{U}^{n+1}$ as p goes to ∞. This approach removes errors associated with factorization and linearization of Eqn. 2.1 as well as the explicit application of boundary conditions and preserves 2nd-order temporal accuracy. The sub-iteration procedure also provides a significant benefit for coupling with the structure solver as will be described later in Section 2.3.

Stability for the solution of Eq. 2.8 is enhanced using non-linear artificial dissipation terms described in Refs. [107] and [108] on the implicit side. The computational efficiency of the implicitly factored approach is further improved using the diagonalization methods of Pulliam and Chausee[109].

2.1.3 Spatial discretization

Spatial discretization of the governing equations is accomplished using the high-order compact finite differencing formulation of Lele[110] and follows the specific approach described in Refs. [111, 112]. Up to 6th-order spatial derivatives along a coordinate line in the computational domain can be obtained by solving the tridiagonal system

$$\alpha\phi'_{i-1} + \phi'_i + \alpha\phi'_{i+1} = b\frac{\phi_{i+2} - \phi_{i-2}}{4} + a\frac{\phi_{i+1} - \phi_{i-1}}{2} \tag{2.9}$$

where ϕ is any scalar quantity and ϕ_i is its spatial derivative. The constants a,b, and α are found using Taylor series expansion of Eq. 2.9 and elimination of the leading truncation error terms for a specified order of accuracy. Values of $\alpha = 1/3$, $a = 14/9$, and $b = 1/9$ give the five-point, sixth-order compact scheme used for the interior points of the computational domain.

Points near boundaries require the application of one-sided terms to retain a tridiagonal form. Spatial derivatives at the first and last points in a coordinate line are determined using

$$\phi'_1 + \alpha_1\phi'_2 = a_1\phi_1 + b_1\phi_2 + c_1\phi_3 + d_1\phi_4 + e_1\phi_5 \tag{2.10}$$

where $\alpha_1 = 3$, $a_1 = -17/2$, $b_1 = 3/2$, $c_1 = 3/2$, $d_1 = -1/6$, and $e_1 = 0$ provide a 5-point fourth-order approximation at the 1st and Nth points. Similarly, the first point off each boundary is determined from

$$\alpha_2\phi'_1 + \phi'_2 + \alpha_2\phi'_3 = a_2\phi_1 + b_2\phi_2 + c_2\phi_3 + d_2\phi_4 + e_2\phi_5 \tag{2.11}$$

where $\alpha_2 = 3/14$, $a_2 = -19/28$, $b_2 = -5/42$, $c_2 = 6/7$, $d_2 = -1/14$ and $e_2 = 1/84$ gives a 5-point, 5th-order solution for points 2 and $N - 1$.

Inviscid flux derivatives are obtained by solving for the flux values at each cor-

responding point and solving the tridiagonal system described above. Viscous fluxes are bit more involved. First, derivatives of primitive values are obtained using the approach above. Components of the viscous flux vectors are then computed using these values and flux derivatives are then obtained by a second application of the compact scheme.

2.1.4 Low-pass spatial filtering and implicit large-eddy simulation

The compact discretization described in Section 2.1.3 is a centered scheme. As such, it is not inherently dissipative and can become susceptible to numerical instability provided by the growth of high-frequency modes. In order to suppress the unrestricted growth of the spurious components of the solution, a Padé-type high-order low-pass filtering technique[111, 113] is applied in the spatial domain. This approach facilitates numerical stability without adversely degrading the accuracy of the original compact discretization by restricting the applied dissipation to high wave-number content not well-resolved by the underlying spatial discretization.

Given a generic scalar value, ϕ, the filter template for interior stencil points is given by

$$\alpha_f \hat{\phi}_{i-1} + \hat{\phi} + \alpha_f \hat{\phi}_{i+1} = \sum_{m=0}^{N} \frac{a_m}{2} \left(\phi_{i+m} + \phi_{i-m}\right) \tag{2.12}$$

where $\hat{\phi}$ are the filtered versions of the input quantity, a_m are coefficients for the specified scheme, and α_f is a free parameter. A proper choice of coefficients provides a $2N^{th}$-order formula on a 2N + 1 point stencil. Specific values for these coefficients can be found in Ref. [114]. The filter is applied to the conserved variables along each transformed coordinate direction once after each time step or sub-iteration. An 8th-order filter is used for the interior points in the present work. Near the boundaries of coordinate lines, one-sided formulations are needed due to the larger stencil of the

filter scheme. This approach, which retains the tridiagonal form, is described in Ref. [114] along with the appropriate coefficients.

An important aspect of this formulation is that the form of the Navier-Stokes equations in Eq. 2.1 is left *unfiltered* and used to solve laminar, transitional, and turbulent flow regions without change. This is accomplished using an implicit large-eddy simulation (ILES) procedure. The ILES procedure makes use of the high-order low-pass Padé-type filter, described above, in place of the sub grid scale (SGS) and heat flux terms normally used in large-eddy simulations. For transitional and turbulent flows, the high-order spatial discretization in conjunction with high-order filtering provide an effective implicit LES approach in place of traditional SGS models. This has been well demonstrated in Refs. [115], [116] and more recently in [117]. Mathew *et al.*[118] has provided reinterpretation of the ILES approach in the context of an Approximate Deconvolution Model[119]. As the grid resolution increases or Reynolds number decreases, the ILES approach is effectively direct numerical simulation (DNS).

2.2 Structural Dynamics Solver

The sections contained here describe the methodology pertaining to the structural dynamics component of *FDL3DAE*. The specific geometrically non-linear plate element formulation, finite element discretization, and time-integration techniques utilized are discussed in the following.

2.2.1 Geometrically non-linear mixed Reisner-Mindlin plate element

The structural portion of the aeroelastic simulations is handled using a nonlinear mixed Reissner-Mindlin plate element[120]. This theory differs from Kirchoff plate theory in that the fibers normal to the mid-plane remain straight, but do not neces-

sarily remain normal to the deformed mid-plane. Second, the same fibers are not permitted to extend (or contract). These conditions are known as Mindlin's hypothesis or the director inextensibility condition in the literature. These assumptions permit transverse shear deformation effects and allow the model to represent both thick and thin plates. Reissner-Mindlin formulations are attractive due to their simplicity and versatility for a large range of plate thicknesses[121].

Consider a plate with mid-plane denoted by Ω and a constant thickness of h. The description of this plate below follows the derivations presented in both Refs. [120] and [122] where the method originated. These works contain some of the finer details excluded here. Mindlin's hypothesis typically limits Reissner-Mindlin theory to small strains unless large displacements/displacement gradients are accounted for using a rotation tensor in the kinematical description. This is accommodated through

$$\mathbf{u} = \hat{\mathbf{u}} + z(\boldsymbol{R} - \boldsymbol{I})\hat{\mathbf{n}} \tag{2.13}$$

where $\mathbf{u} = \{u, v, w\}^T$ and $\hat{\mathbf{u}} = \{\hat{u}, \hat{v}, \hat{w}\}^T$ are the vectors of general and mid-plane displacements respectively in the Cartesian (x,y,z) co-ordinate system, $\boldsymbol{I}$ is the identity tensor, $\hat{\mathbf{n}}$ is a unit vector pointing in the direction normal to the mid-plane (z-direction), and $\boldsymbol{R}$ is a proper orthogonal rotation tensor defined by the Rodrigues formula given in exponential form[123] as

$$\boldsymbol{R} = \boldsymbol{I} + \boldsymbol{S}(\boldsymbol{\Lambda}) + \frac{\boldsymbol{S}(\boldsymbol{\Lambda})^2}{2} + \frac{\boldsymbol{S}(\boldsymbol{\Lambda})^3}{6} + ... \tag{2.14}$$

where $\boldsymbol{S}(\boldsymbol{\Lambda})$ is defined as

$$\boldsymbol{S}(\boldsymbol{\Lambda}) = \begin{bmatrix} 0 & 0 & \theta \\ 0 & 0 & \psi \\ -\theta & -\psi & 0 \end{bmatrix} \tag{2.15}$$

The values of ψ and θ are rotations of fibers orthogonal to the mid-plane. Truncating

Eq. 2.14 to the first three non-identity terms and substituting into Eqn. 2.13 results in the three term approximation to the displacement vector

$$\mathbf{u} = \hat{\mathbf{u}} + z\left(\boldsymbol{S}(\boldsymbol{\Lambda}) + \frac{\boldsymbol{S}(\boldsymbol{\Lambda})^2}{2} + \frac{\boldsymbol{S}(\boldsymbol{\Lambda})^3}{6}\right)\mathbf{n} \tag{2.16}$$

expressed in component form by

$$u = \hat{u} + z(\theta - \frac{1}{6}(\theta^3 + \theta\psi^2)), \tag{2.17}$$

$$v = \hat{v} + z(\psi - \frac{1}{6}(\theta^2\psi + \psi^3)), \tag{2.18}$$

$$w = \hat{w} - \frac{1}{2}z(\theta^2 + \psi^2), \tag{2.19}$$

A mixed element approach is employed for the energy functional used in the variational statement. The principal of minimum potential energy is applied for the bending and membrane energy terms. The Hellinger-Reissner variational principle[124] describes the shear energy term. The resulting functional, including viscous structural damping ($c\dot{\mathbf{u}}$), nonconservative surface traction ($\boldsymbol{\Phi}$), body forces ($\mathbf{b}$), and concentrated point loads ($\mathbf{F}$) is given as

$$\begin{aligned}\Pi(\mathbf{u},\mathbf{Q}) = \int_\Omega \big(&\tfrac{1}{2}\epsilon^T\mathbf{N} + \tfrac{1}{2}\kappa^T\mathbf{M} - \tfrac{1}{2}\mathbf{Q}^T\boldsymbol{C}_s^{-1}\mathbf{Q} + \\ &\gamma^T\mathbf{Q} - \hat{\mathbf{u}}^T\mathbf{b} - \mathbf{u}^T\boldsymbol{\Phi} - \mathbf{D}^T\mathbf{F} + \hat{\mathbf{u}}^T hc\dot{\hat{\mathbf{u}}} + \boldsymbol{\Lambda}^T\tfrac{ch^3}{12}\dot{\boldsymbol{\Lambda}}\big)\,\mathrm{d}\Omega\end{aligned} \tag{2.20}$$

where the vector $\boldsymbol{\Lambda} = \{\theta, \psi, 0\}^T$, and $\mathbf{D}$ are the displacements. Bending, membrane and shear stress resultant vectors are represented by

$$\mathbf{M} = \begin{bmatrix} \int_{-h/2}^{h/2}\sigma_{xx}z\,dz \\ \int_{-h/2}^{h/2}\sigma_{yy}z\,dz \\ \int_{-h/2}^{h/2}\sigma_{xy}z\,dz \end{bmatrix}, \quad \mathbf{N} = \begin{bmatrix} \int_{-h/2}^{h/2}\sigma_{xx}\,dz \\ \int_{-h/2}^{h/2}\sigma_{yy}\,dz \\ \int_{-h/2}^{h/2}\sigma_{xy}\,dz \end{bmatrix}, \quad \mathbf{Q} = \begin{bmatrix} \int_{-h/2}^{h/2}\sigma_{xz}\,dz \\ \int_{-h/2}^{h/2}\sigma_{yz}\,dz \end{bmatrix} \tag{2.21}$$

respectively. The components from $\boldsymbol{\sigma}$ pertain to the second Piola-Kerchoff stress tensor. The vectors ϵ, κ, and γ correspond, respectively, to the bending, membrane, and shear strains and are determined using the full Green-Lagrange strain tensor. Only linear elastic and isotropic materials are used in the current work. Therefore, the stress resultants are linearly related to the strain vectors by

$$\mathbf{M} = \frac{h^3}{12}\boldsymbol{E}\kappa, \quad \mathbf{N} = h\boldsymbol{E}\epsilon, \quad \mathbf{Q} = \boldsymbol{C}_s\gamma \tag{2.22}$$

and the matrices $\boldsymbol{E}$ and $\boldsymbol{C}_s$ are given by

$$\boldsymbol{E} = \frac{E}{1-\nu}\begin{bmatrix} 1 & \nu & 0 \\ \nu & 1 & 0 \\ 0 & 0 & \frac{1}{2}(1-\nu) \end{bmatrix}, \quad \boldsymbol{C}_s = khG\begin{bmatrix} 1 & 0 \\ 0 & 1 \end{bmatrix} \tag{2.23}$$

Here, E is the Young's modulus, ν is Poisson's ratio, and G is the shear modulus. The value for k is set at 5/6 for isotropic plates. The mixed functional in Eq. 2.20 results in both displacement and force terms as field variables which provide extra degrees of freedom to be discretized in the finite element formulation.

Applying Hamilton's principle to Eq. 2.20 results in

$$\begin{aligned} &\int_{t_0}^{t_1}\left[\int_\Omega\left(\rho_s h\delta\mathbf{u}_m^T\ddot{\mathbf{u}}_m + \rho_s h^3/12\delta\boldsymbol{\Lambda}^T\ddot{\boldsymbol{\Lambda}} + \delta\epsilon^T\mathbf{N} + \delta\kappa^T\mathbf{M} - \delta\mathbf{Q}^T\boldsymbol{C}_s^{-1}\mathbf{Q} + \delta\mathbf{Q}^T\gamma^T + \delta\gamma^T\mathbf{Q}\right)\mathrm{d}\Omega\right]\mathrm{d}t = \\ &\int_{t_0}^{t_1}\left[\int_\Omega\left(h\delta\mathbf{u}_m^T\mathbf{b} + \delta\mathbf{u}_m^T\Phi + z\delta\boldsymbol{\Lambda}^T\Phi - \delta\mathbf{u}_m^T hc\dot{\mathbf{u}}_m - \delta\boldsymbol{\Lambda}^T\tfrac{ch^3}{12}\dot{\boldsymbol{\Lambda}}\right)\mathrm{d}\Omega + \delta\mathbf{D}^T\mathbf{F}\right]\mathrm{d}t \end{aligned} \tag{2.24}$$

where ρ_s is the density of the structure. This variational statement is the end goal of this section and will be used to provide finite element discretization next.

2.2.2 Finite element discretization

The variational statement in Eq. 2.24 now must be discretized for application in a finite element model. Here, a mixed approach is applied where the degrees of

freedom provided by the shear stress resultants are interpolated in a manner different from the displacement and rotations. Given $\mathbf{d}_{\hat{\mathbf{u}}}$, $\mathbf{d}_{\mathbf{\Lambda}}$, and $\mathbf{q}$ are the degree of freedom vectors for displacement, rotation, and shear, respectively of the discretized system, the interpolation scheme for each can be written as

$$\hat{\mathbf{u}} = \boldsymbol{N}_{\hat{\mathbf{u}}}\mathbf{d}_{\hat{\mathbf{u}}}, \quad \mathbf{\Lambda} = \boldsymbol{N}_{\mathbf{\Lambda}}\mathbf{d}_{\mathbf{\Lambda}}, \quad \mathbf{Q} = \boldsymbol{N}_s\mathbf{q} \tag{2.25}$$

where $\boldsymbol{N}_{\hat{\mathbf{u}}}$, $\boldsymbol{N}_{\mathbf{\Lambda}}$, and $\boldsymbol{N}_s$ are the shape function matrices. The strain are related to displacements through

$$\epsilon = \overline{\boldsymbol{B}}_m\mathbf{d}, \quad \delta\epsilon = \boldsymbol{B}_m\delta\mathbf{d}, \tag{2.26a}$$

$$\kappa = \overline{\boldsymbol{B}}_b\mathbf{d}, \quad \delta\kappa = \boldsymbol{B}_b\delta\mathbf{d}, \tag{2.26b}$$

$$\gamma = \overline{\boldsymbol{B}}_s\mathbf{d}, \quad \delta\gamma = \boldsymbol{B}_s\delta\mathbf{d}, \tag{2.26c}$$

where the new degree of freedom vector is defined as $\mathbf{d} = \{\mathbf{d}_{\hat{\mathbf{u}}}, \mathbf{d}_{\mathbf{\Lambda}}\}^T$. The corresponding shape function matrix is

$$\boldsymbol{H} = \begin{bmatrix} \boldsymbol{N}_{\hat{\mathbf{u}}} & \mathbf{0} \\ \mathbf{0} & \boldsymbol{N}_s \end{bmatrix} \tag{2.27}$$

Substituting the above relations into Eq. 2.24 and assuming $\delta\mathbf{d}$ and $\delta\mathbf{q}$ are arbitrary provides the residual equations of motion

$$\begin{aligned}\mathbf{R}_1 = &\underbrace{\int_{\hat{\Omega}} \boldsymbol{H}^T \boldsymbol{G}_1 \boldsymbol{H} \mathrm{d}\hat{\Omega}}_{\text{Mass matrix}} \ddot{\mathbf{d}} + \underbrace{\int_{\hat{\Omega}} \boldsymbol{H}^T \boldsymbol{G}_2 \boldsymbol{H} \mathrm{d}\hat{\Omega}}_{\text{Damping matrix}} \dot{\mathbf{d}} \\ &+ \underbrace{\int_{\hat{\Omega}} \boldsymbol{B}_m^T \boldsymbol{N} \mathrm{d}\Omega_e + \int_{\hat{\Omega}} \boldsymbol{B}_b^T \boldsymbol{M} \mathrm{d}\hat{\Omega} + \int_{\hat{\Omega}} \boldsymbol{B}_s^T \boldsymbol{Q} \mathrm{d}\hat{\Omega}}_{\text{Internal loads}} \\ &\underbrace{- \int_{\Omega_e} \boldsymbol{H}^T \boldsymbol{G}_3 \mathbf{b} \mathrm{d}\Omega_e - \int_{\hat{\Omega}} \boldsymbol{H}^T \boldsymbol{G}_4 \boldsymbol{\Phi}_2 \mathrm{d}\hat{\Omega} - \sum_{i=1}^{n} \mathbf{f}_i}_{\text{External loads}} = \mathbf{0}\end{aligned} \tag{2.28}$$

$$\mathbf{R}_2 = \underbrace{- \int_{\hat{\Omega}} \boldsymbol{N}_s^T \boldsymbol{C}_s^{-1} \boldsymbol{N}_s \mathrm{d}\hat{\Omega} \mathbf{q} + \int_{\hat{\Omega}} \boldsymbol{N}_s^T \overline{\boldsymbol{B}}_s \mathrm{d}\hat{\Omega} \mathbf{d}}_{\text{Internal loads}} = \mathbf{0} \tag{2.29}$$

$\boldsymbol{\Phi}_2$ is an auxiliary traction vector defined by $\boldsymbol{\Phi}_2 = \{\boldsymbol{\Phi}, \Phi_x, \Phi_y\}^T$. The arrays $\mathbf{f}_i$ are the externally applied point loads located at element nodes. The various $\boldsymbol{G}$ matrices are defined by

$$\begin{aligned} \boldsymbol{G}_1 &= \begin{bmatrix} \rho_s h \boldsymbol{I}_3 & \mathbf{0} \\ \mathbf{0} & \frac{\rho_s h^3}{12} \boldsymbol{I}_2 \end{bmatrix} \quad \boldsymbol{G}_2 = \begin{bmatrix} hc \boldsymbol{I}_3 & \mathbf{0} \\ \mathbf{0} & \frac{ch^3}{12} \boldsymbol{I}_2 \end{bmatrix} \\ \boldsymbol{G}_3 &= \begin{bmatrix} h \boldsymbol{I}_3 & \mathbf{0} \\ \mathbf{0} & \mathbf{0} \end{bmatrix} \quad \boldsymbol{G}_4 = \begin{bmatrix} \boldsymbol{I}_3 & \mathbf{0} \\ \mathbf{0} & C_1 \boldsymbol{I}_2 \end{bmatrix} \end{aligned} \tag{2.30}$$

The value of C_1 in $\boldsymbol{G}_4$ is replaced with either $+h/2$ or $-h/2$ depending on whether the specific traction load is acting on the top or bottom surface of the plate. $\boldsymbol{I}_2$ and $\boldsymbol{I}_3$ are 2×2 and 3×3 identity matrices respectively.

The element described is a quadrilateral element and therefore has four nodes. Conformal mapping is used to transfer between the real domain (x, y) and the reference domain (ξ, η). The coordinate transformation is accomplished using bi-linear shape functions through

$$\mathbf{X} = \sum_{i=1}^{4} N_i \mathbf{x}_i \tag{2.31}$$

where $\mathbf{X} = \{x, y\}$ and $\mathbf{x}_i = \{x_i, y_i\}$. The N_i bilinear shape functions are defined by

$$N_i = \frac{1}{4}(1 + \xi_i\xi)(1 + \eta_i\eta) \tag{2.32}$$

The element formulation in *FDL3DAE* allows for polynomial refinement (p-refinement) of the finite element interpolations. As such, higher-order polynomial interpolation is available based on the hierarchical set of shape functions described by Szabó and Babŭska [125]. The higher order polynomials were not applied in this work and description of them is therefore left in Ref. [120].

The mixed element formulation must also handle the shear stress resultants introduced to the energy functional by the application of the Hellinger-Reissner principle. These additional degrees of freedom are independent from the displacements and rotations. Products of the normalized Legendre polynomials are used to interpolate the degrees of freedom produced by the extra term. Here $\boldsymbol{N}_s$ is further specified as

$$\boldsymbol{N}_s = \begin{bmatrix} \boldsymbol{B} & \mathbf{0} \\ \mathbf{0} & \boldsymbol{B} \end{bmatrix} \tag{2.33}$$

and $\boldsymbol{B}$ contains products of the normalized Legendre polynomials, $l_n(\xi) = \sqrt{n + 1/2}L_n(\xi)$, where $\boldsymbol{B} = \{l_0(\xi)l_0(\xi), l_1(\xi)l_0(\eta), l_0(\xi)l_1(\eta), l_1(\xi)l_1(\eta)\}$.

The structural element used in this dissertation has been well tested for numerous canonical test cases in Refs. [120] and [122] and shown to perform exceptionally well compared to the well-tested to the geometrically non-linear ANSYS SHELL181 element. The methodology described above is quite suitable to model the large induced deformations provided by streamwise vortex interactions.

2.2.3 Time integration

The time-integration scheme for the finite element model is now introduced. Because of the geometric non-linearity introduced by Eq. 2.17, solution of the residual equations of motion provided by Eqs. 2.28 and 2.29 will require an iterative procedure. The formulation provided in this section follows loosely that described in the recent non-linear FEA book by Borst[126]. The equations of motion can be generalized to

$$\mathbf{R}^{t+\Delta t} = \mathbf{r}^{t+\Delta t} + \boldsymbol{M}\ddot{\mathbf{a}}^{t+\Delta t} + \boldsymbol{C}\dot{\mathbf{a}}^{t+\Delta t} = \mathbf{0} \tag{2.34}$$

where $\mathbf{a} = \{\mathbf{d}_{\hat{\mathbf{u}}}, \mathbf{d}_{\boldsymbol{\Lambda}}, \mathbf{q}\}^T$ is a vector of all degrees of freedom, $\mathbf{r}^{t+\Delta t} = \mathbf{r}_{\text{ext}}^{t+\Delta t} - \mathbf{r}_{\text{int}}^{t}$ is the static out-of-balance force vector and $\mathbf{R}$ is the dynamic residual force vector.

The internal and external load vectors are more specifically defined as

$$\mathbf{r}_{\text{int}} = \begin{bmatrix} \underbrace{\int_{\hat{\Omega}} \boldsymbol{B}_m^T \boldsymbol{N} \mathrm{d}\hat{\Omega}}_{\text{Membrane}} + \underbrace{\int_{\hat{\Omega}} \boldsymbol{B}_b^T \boldsymbol{M} \mathrm{d}\hat{\Omega}}_{\text{Bending}} + \underbrace{\int_{\hat{\Omega}} \boldsymbol{B}_s^T \boldsymbol{Q} \mathrm{d}\hat{\Omega}}_{\text{Shear}} \\ -\int_{\hat{\Omega}} \boldsymbol{N}_s^T \boldsymbol{C}_s^{-1} \boldsymbol{N}_s \mathrm{d}\hat{\Omega}\mathbf{q} + \int_{\hat{\Omega}} \boldsymbol{N}_s^T \overline{\boldsymbol{B}}_s \mathrm{d}\hat{\Omega}\mathbf{d} \end{bmatrix} \tag{2.35}$$

$$\mathbf{r}_{\text{ext}} = \begin{bmatrix} \underbrace{\int_{\Omega_e} \boldsymbol{H}^T \boldsymbol{G}_3 \mathbf{b} \mathrm{d}\Omega_e}_{\text{Body loads}} - \underbrace{\int_{\hat{\Omega}} \boldsymbol{H}^T \boldsymbol{G}_4 \boldsymbol{\Phi}_2 \mathrm{d}\hat{\Omega}}_{\text{Traction loads}} - \underbrace{\sum_{i=1}^{n} \mathbf{f}_i}_{\text{Point loads}} \\ \mathbf{0} \end{bmatrix} \tag{2.36}$$

where the appropriate terms have been extracted from Eqs. 2.28 and 2.29. Similarly, the mass and damping matrices are extracted from the residual equations of motion and given as

$$\boldsymbol{M} = \begin{bmatrix} \int_{\hat{\Omega}} \boldsymbol{H}^T \boldsymbol{G}_1 \boldsymbol{H} \mathrm{d}\hat{\Omega} & \mathbf{0} \\ \mathbf{0} & \mathbf{0} \end{bmatrix} \tag{2.37}$$

$$\boldsymbol{C} = \begin{bmatrix} \int_{\hat{\Omega}} \boldsymbol{H}^T \boldsymbol{G}_2 \boldsymbol{H} \mathrm{d}\hat{\Omega} & \mathbf{0} \\ \mathbf{0} & \mathbf{0} \end{bmatrix} \tag{2.38}$$

Temporal integration is accommodated through the discretization of time derivative terms $\dot{\mathbf{a}}$ and $\ddot{\mathbf{a}}$. Many different techniques can be applied to these terms such as the Newmark schemes or Hilber-Hughes-Taylor (HHT) method [127]. Here, the Newmark average-acceleration technique is applied which provides an implicit, unconditionally stable, 2nd-order time integration scheme. The formal order of accuracy of the time-marching scheme is the same is that used for the fluid dynamics solutions as described in Section 2.1.2. This approach requires $\dot{\mathbf{a}}^{t+\Delta t}$ and $\mathbf{a}^{t+\Delta t}$ to be written as

$$\dot{\mathbf{a}}^{t+\Delta t} = \dot{\mathbf{a}}^{t} + \frac{\Delta t}{2}\left(\ddot{\mathbf{a}}^{t} + \ddot{\mathbf{a}}^{t+\Delta t}\right) \tag{2.39}$$

$$\mathbf{a}^{t+\Delta t} = \mathbf{a}^{t} + \frac{\Delta t}{2}\left(\dot{\mathbf{a}}^{t} + \dot{\mathbf{a}}^{t+\Delta t}\right) \tag{2.40}$$

Solving for $\ddot{\mathbf{a}}^{t+\Delta t}$ and $\dot{\mathbf{a}}^{t+\Delta t}$ in the above equations and substituting into Eq. 2.34 reduces $\mathbf{R}^{t+\Delta t}$ to a function of only $\mathbf{r}_{\text{int}}^{t+\Delta t}$ and $\mathbf{a}^{t+\Delta t}$ as unknowns. Because $\mathbf{r}_{\text{int}}^{t+\Delta t}$ is a function of $\mathbf{a}^{t+\Delta t}$, $\mathbf{R}^{t+\Delta t}$ is nonlinear. The residual equations of motion can be linearized through a truncated Taylor series expansion of the internal force vector,

$$\mathbf{r}_{\text{int}}^{t+\Delta t} = \mathbf{r}_{\text{int}}^{t} + \left.\frac{\partial \mathbf{r}_{\text{int}}}{\partial \mathbf{a}}\right|_{n}\left(\mathbf{a}^{t+\Delta t} - \mathbf{a}^{t}\right) = \mathbf{r}_{\text{int}} + \boldsymbol{K}_{0}^{t}\Delta\mathbf{a} \tag{2.41}$$

where $\boldsymbol{K}_{0}^{t}$ is a static tangent stiffness matrix evaluated at time level t and $\Delta\mathbf{a}$ is the displacement increment.

Solving Eqs. 2.39 and 2.40 for $\ddot{\mathbf{a}}^{t+\Delta t}$ and $\dot{\mathbf{a}}^{t+\Delta t}$, respectively gives

$$\ddot{\mathbf{a}}^{t+\Delta t} = \frac{4}{\Delta t^{2}}\Delta\mathbf{a} - \frac{2}{\Delta t}\dot{\mathbf{a}}^{t} - \ddot{\mathbf{a}}^{t} \tag{2.42}$$

$$\dot{\mathbf{a}}^{t+\Delta t} = \frac{2}{\Delta t}\Delta\mathbf{a} - \dot{\mathbf{a}}^{t} \tag{2.43}$$

Substituting these along with Eq. 2.41 into Eq. 2.34 reduces the system of equations

to

$$\boldsymbol{K}_{\text{eff}}^{t}\Delta\mathbf{a} = \Delta\mathbf{r}_{\text{eff}} \tag{2.44}$$

where $\boldsymbol{K}_{\text{eff}}^{t} = \boldsymbol{K}_{0}^{t} + \frac{4}{\Delta t^2}\boldsymbol{M} + \frac{2}{\Delta t}\boldsymbol{C}$ and

$$\Delta\mathbf{r}_{\text{eff}} = \mathbf{r}_{\text{ext}}^{t+\Delta t} - \mathbf{r}_{\text{int}}^{t} + \boldsymbol{M}\left(\frac{4}{\Delta t^2}\dot{\mathbf{a}}^{t} + \ddot{\mathbf{a}}^{t}\right) + \dot{\mathbf{a}}^{t} \tag{2.45}$$

Once Eq. 2.44 is solved for $\Delta\mathbf{a}$, $\mathbf{a}^{t+\Delta t} = \mathbf{a}^{t} + \Delta\mathbf{a}$ can be updated followed by $\dot{\mathbf{a}}^{t+\Delta t}$ and $\ddot{\mathbf{a}}^{t+\Delta t}$ through Eqs. 2.39 and 2.40. In general, this process would lead to a non-zero residual $\mathbf{R}^{t+\Delta t}$ due to the linearization applied in Eq. 2.41. This is alleviated through a predictor-corrector algorithm. The above steps encompass the 'predictor' portion of the solution procedure. The Newton-Raphson corrector step is described next.

Consider a truncated Taylor series expansion applied to $\mathbf{r}^{t+\Delta t}$:

$$\mathbf{r}_{i+1}^{t+\Delta t} = \mathbf{r}_{i}^{t+\Delta t} + \frac{\partial\mathbf{r}}{\partial\mathbf{a}}\delta\mathbf{a}^{t+\Delta t} = \mathbf{r}_{i}^{t+\Delta t} + \boldsymbol{K}_{0}^{t+\Delta t}\partial\mathbf{a}^{t+\Delta t} \tag{2.46}$$

where i is the index of iteration. Next, from Eq. 2.39

$$\delta\dot{\mathbf{a}}^{t+\Delta t} = \frac{2}{\Delta t}\delta\mathbf{a}^{t+\Delta t} \tag{2.47}$$

and then from Eq. 2.40

$$\delta\ddot{\mathbf{a}}^{t+\Delta t} = \frac{4}{\Delta t^2}\delta\mathbf{a}^{t+\Delta t} \tag{2.48}$$

Substituting the last three equations into Eq. 2.34 yields

$$\mathbf{r}_{i+1}^{t+\Delta t} = \mathbf{r}_{i}^{t+\Delta t} + \boldsymbol{K}_{\text{eff}}^{t+\Delta t}\delta\mathbf{a}^{t+\Delta t} \tag{2.49}$$

where the form of $\boldsymbol{K}_{\text{eff}}^{t+\Delta t}$ is the same as $\boldsymbol{K}_{\text{eff}}^{t}$ described above. The 'correct' solution can be approached by assuming $\mathbf{r}_{i+1}^{t+\Delta t} = \mathbf{0}$ when $\mathbf{r}_{i}^{t+\Delta t} \neq \mathbf{0}$. This results in a linear system of equations that can be easily solved in an iterative fashion until sufficient

convergence:

$$-\boldsymbol{K}_{\text{eff}}^{t+\Delta t}\delta \mathrm{a}^{t+\Delta t} = \mathbf{r}_i^{t+\Delta t} \tag{2.50}$$

This process requires the solution of two different linear systems of equations in Eq. 2.44 and Eq. 2.50 which are accomplished using the open-source parallel sparse multi frontal solver MUMPS.

2.3 Aerodynamic and structural coupling

A key part of any aeroelastic computation is an accurate coupling between the fluid and structural components of the model. Aerodynamic forces are passed from the fluid mesh to the structural model while displacements are returned from the structural solver and imposed on the fluid grid. Because the structural and fluid meshes may not necessarily coincide, interpolation between the two is necessary. In the present work, interpolation is accomplished using the finite element shape functions providing a conservative approach.

Loose temporal coupling between the aerodynamic and structural models can adversely affect solution integrity[128]. In order to eliminate this time lag, the two physics models are implicitly coupled through the sub-iteration procedure described in Section 2.1.2. Surface forces and structural displacements are interchanged at each sub-iteration where the grid is adjusted to the new deformations. This process completely synchronizes both models in time and preserves second order temporal accuracy for both. Furthermore, factorization and linearization errors are eliminated by the global sub-iteration strategy.

The aerodynamic mesh must be capable of deforming with the structure. A simple algebraic method presented in Ref.[129] is used to deform the aerodynamic mesh in accordance with the structural deformation. Grid velocities are determined using

second order temporal differencing of the position vector

$$\frac{\partial \mathbf{x}^{n+1}}{\partial t} = \frac{3\mathbf{x}^{n+1} - 4\mathbf{x}^{n} + \mathbf{x}^{n-1}}{2\Delta t} \tag{2.51}$$

where $\mathbf{x} = \{x, y, z\}^T$.

The coupled solution procedure has been shown to compare well with experimental data for flexible delta wings[122] and membrane airfoils[130] and quite suitable for a range of practical problems. To further support confidence in the methodology chosen for this work, one additional validation test case is presented in the next section.

2.3.1 Verification: vortex-induced oscillations of a flexible structure

The topology for this simulation consists of a square bluff body and a rectangular beam in its wake as shown in Fig. 2.1(a) where the thin rectangular section serves as a highly flexible structure. This geometry is subjected to freestream flow at a 0° angle of attack. Vortices shed from the body induce periodic deformations of the flexible structure as demonstrated in Fig. 2.1(c). Fluid-structure interactions of vortex induced shedding in the wake of a bluff body have been previously presented by Wall and Ramm[131] in which nine-node plane-stress elements were coupled with an incompressible Navier-Stokes solver.

An overset grid is applied for the fluid portion of the present computation and is comprised of a patchwork of six grid regions as shown in Fig. 2.1(b) where a 5-point coincident overlap is supplied between grid blocks. No-slip conditions are imposed at the solid surfaces where velocities are determined by the grid motion and freestream conditions are applied at the farfield located 100 chords away from the body. The structural grid consists of sixty geometrically non-linear mixed Reisner-Mindlin plate elements along the length of the flexible structure. The structural nodes located at

the structure base are constrained in all degrees of freedom to model a cantilever beam. Physical dimensions and material/fluid properties are presented in Fig. 2.1(a) and Table 2.1 respectively. The physical dimensions are non-dimensionalized for the fluid solver using the length of the flexible structure, $L_{\text{ref}} = 0.04$ (m), resulting in a Reynolds number of $Re_L = 1330$ or $Re_D = 332$ based on the bluff body diameter.

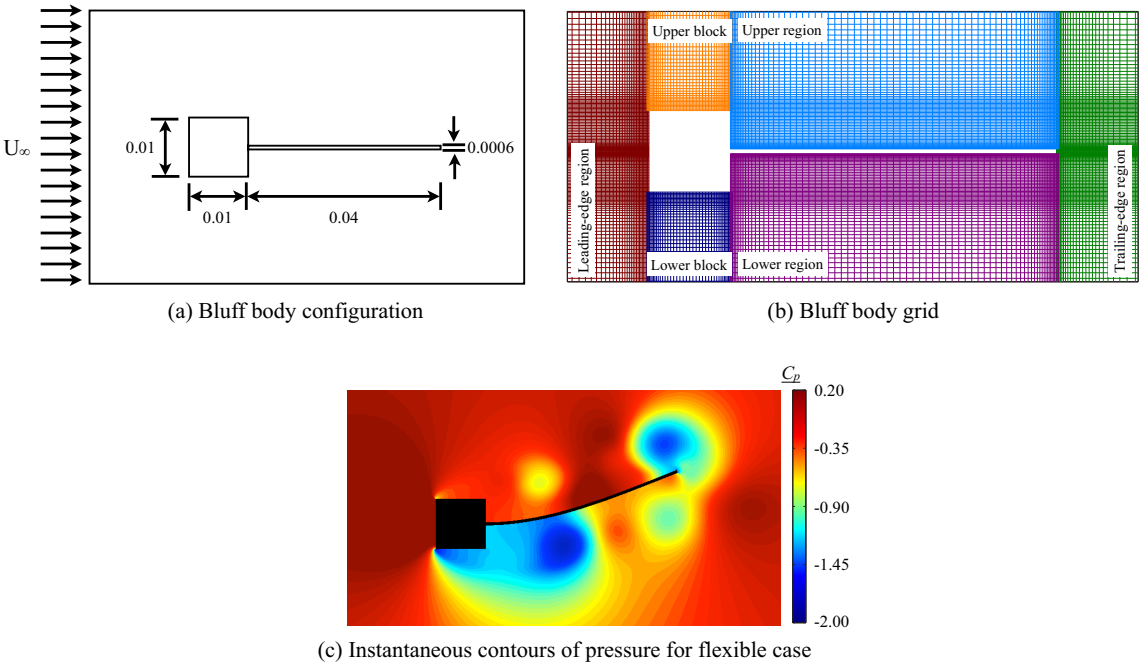

(a) Bluff body configuration

(b) Bluff body grid

(c) Instantaneous contours of pressure for flexible case

Figure 2.1: Test case for vortex-induced oscillations of a flexible structure in the wake of a bluff body. Frame (a) shows the configuration where dimensions are given in meters, (b) demonstrates the overset grid topology used and (c) portrays a contour plot of the instantaneous pressure coefficient near maximum displacement.

Table 2.1: Dimensional fluid and structure properties for the bluff body test case

Structure properties		Fluid properties	
Young's modulus, E	0.25 (MPa)	Freestream velocity, U_∞	0.513 (m/s)
Material density, ρ_s	100 (kg/m^3)	Fluid density, ρ_f	1.18 (kg/m^3)
Poisson's ratio, ν	0.35	Viscosity, μ	1.82×10^{-5} (Pa $\cdot$ s)

Fluid-structure interaction simulations are initiated from a previously computed solution using a rigid structure and allowed to evolve for a dimensional time of $t = 5$

(s) using a non-dimensional time step of $\Delta t U_\infty / L_{\text{ref}} = 5 \times 10^{-4}$. Deformations for the center and tip of the structure are shown in Fig. 2.2(a) for the full computational time. Here, a periodic state appears as early as two seconds. Deformations of the structure tip from two cycles are compared with those presented in Ref. [131] in Fig. 2.2 after deformations reach a periodic state. Both cases show favorable comparison of deformations.

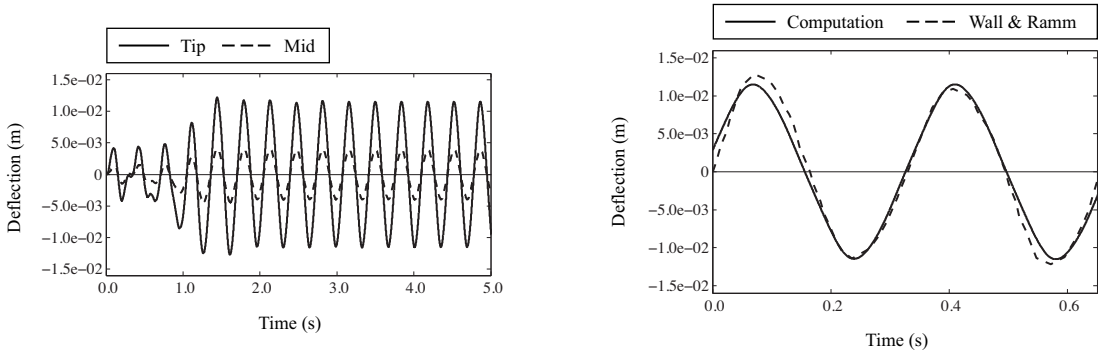

(a) Structural tip and mid span deformation

(b) Comparison of tip deformations

Figure 2.2: Deformations of the beam are shown for (a) the first five seconds of the computational solution and (b) comparison between tip deflections with reported values.

Chapter 3

Vortex interaction between rigid wings in close proximity

The current chapter analyzes the streamwise vortex interaction in the context of a formation-like configuration. In this case, the impinging flow is physically generated upstream by a leader wing. The emphasis of this section is to explore and characterize the viscous and unsteady mechanisms that may occur in such a configuration as well as their impact on aerodynamic forces. To this end, the setup utilizes simple rectangular geometries in order to reduce the number of parameters of an otherwise complex problem. Several lateral positions and angles of attack of the leader wing are evaluated in order to modify vortex position and strength elucidating their impact on the resulting flow fields.

As previously described in Chapter 1, wake-interaction studies have been almost exclusively limited to inviscid analysis while the exploration of unsteady physics in the context of vortex-fin interaction has focused solely on the response of an aerodynamic surface to breakdown unrelated to impingement. The present configuration subjects an aerodynamic surface to a physical streamwise vortex that is otherwise stable absent interaction with the follower wing.

The work presented in this chapter is important to the scope of this dissertation for several reasons. Several unsteady behaviors are identified and characterized. Each of the features discussed appear to arise as a direct consequence of vortex/surface interaction. Further investigation is warranted to clarify their origin and influence on unsteady loading. The impact of viscous interaction is elucidated and its importance clarified. To date, unsteady viscous effects have been largely neglected in the context of formation flight. These findings provide critical insight and direction to following studies regarding streamwise-oriented vortex interactions. The following sections describe the problem setup and some of the results from this work. Two parameters are explored in this chapter including the lateral wing spacing and leader-wing angle of attack.

3.1 Problem setup

Figure 3.1 depicts the problem configuration in which the streamwise-oriented vortex interaction is provided by the trailing vortex of a leader wing placed upstream of a follower wing. This setup permits a significant level of control for the current problem. The positioning of the incident vortex can be modified by changing the location of the leader wing while the size and strength can be adjusted by varying the leader wing angle of attack.

Both wings are identical and consist of a rectangular cross-section and planform with squared-off corners, aspect-ratio $\mathcal{R} = b/c$ of 6, uniform thickness of $t/c = 0.03$ and operate at a Reynolds number of $\mathrm{Re} = 30,000$. Angle of attack for both the leader and follower wings are described by α_L and α_F respectively where $\alpha_F = 5^\circ$ for all cases in this dissertation. This particular choice of Reynolds number and angle of attack were chosen in order to study streamwise vortex interaction with a transitional/turbulent separated flow. Both $\alpha_L = 5^\circ$ and 8° leader wing angles of

attack are explored in this chapter.

The trailing vortex position is controlled using the spacing parameters of Δx and Δy in Figure 3.1(a) and Δz in Figure 3.1(b) which describe the longitudinal, lateral, and vertical spacing between the two wings, respectively. All cases explored in this section use $\Delta x/c = 5$ and $\Delta z/c = 0$ while the spacing parameter of Δy varies from $-0.15c$ to $0.30c$ where a positive value corresponds with a spanwise overlap of the two wingtips.

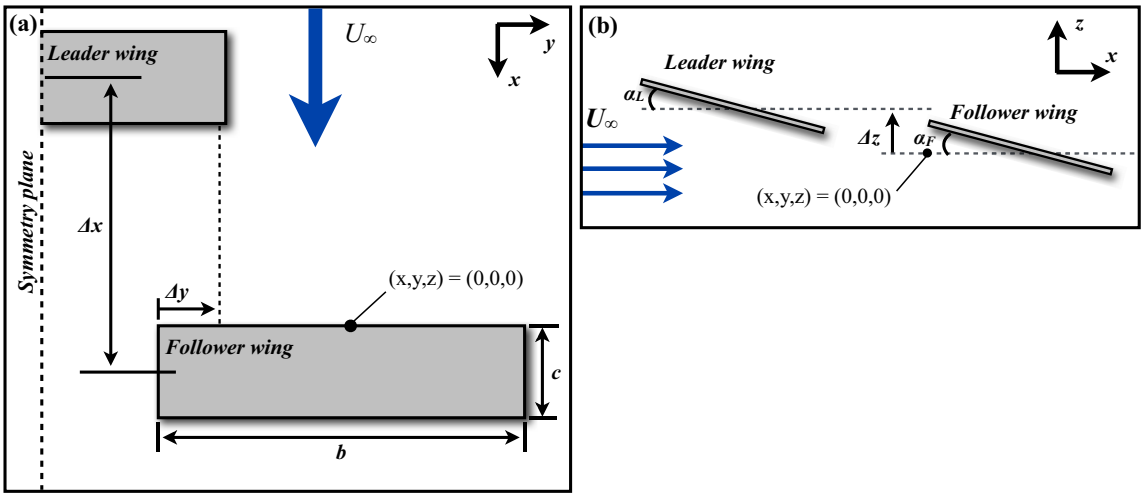

Figure 3.1: Configuration for problem setup; (a) shows a top view and (b) portrays a side view.

This configuration represents one example of the more generic problem of a streamwise vortex impinging upon an aerodynamic surface. The trailing vortices for both $\alpha_L = 5°$ and $8°$ leader wings do not breakdown absent interaction with the follower wing. Rather, the otherwise stable, free vortex is subject to instabilities or breakdown imposed as a direct consequence of interaction with the follower wing.

3.2 Numerical considerations

Due to the presence of multiple wing bodies, a nested grid configuration efficiently discretizes the computational domain. This topology, which is demonstrated in Figure

3.2, consists of 19 total grids in order to properly model the detailed fluid physics near each body and preserve the trailing vortex emanating from the leader wing. The first set of blocks consists of a series of nearfield grids which wrap around each wing (red) and are designed to resolve the transitional and turbulent nearfield flow structure. These near-wing grid systems are composed of leading-edge, trailing-edge, upper, lower and two tip grid regions. The described multiple grid configuration is applied in order to accommodate high-order stencils at the squared-off corners of the flat plate wing and includes a four-point coincident overlap between adjacent grids eliminating the need for high-order interpolation within this set. The leader wing group differs from the follower wing system only in the fact that half the grid points in the spanwise direction are replaced by a symmetry plane.

A second set of blocks serves to connect the regions between the nearfield grids. This group, shown in Figure 3.2, consists of two intermediate meshes (yellow) and a vortex mesh (gray). The intermediate grids are constructed using the distributions from each of the nearfield systems and are coarsened to roughly 2/3 the number of points in each coordinate direction. The vortex mesh maintains the fine spacing of the nearfield groups in order to preserve the trailing vortex as it travels between the two bodies. Communication between these grids and the nearfield systems is non-coincident and therefore Chimera overset[132] methodology with high-order interpolation[133] is employed. Finally, the nearfield and intermediate blocks are wrapped in a coarsened farfield group (blue) that rapidly stretches to the outer boundaries located at 20-100 chord lengths from the wing surfaces. Grid point clustering is maintained in the farfield blocks in order to minimize volume ratios in the overlap regions. The final mesh utilized in the present simulations consisted of over 85 million grid points and was decomposed into a total of 944 sub-blocks for parallel processing. Details of mesh dimensions are provided in Section 3.3.

Boundary conditions for the described grid system are applied in the following

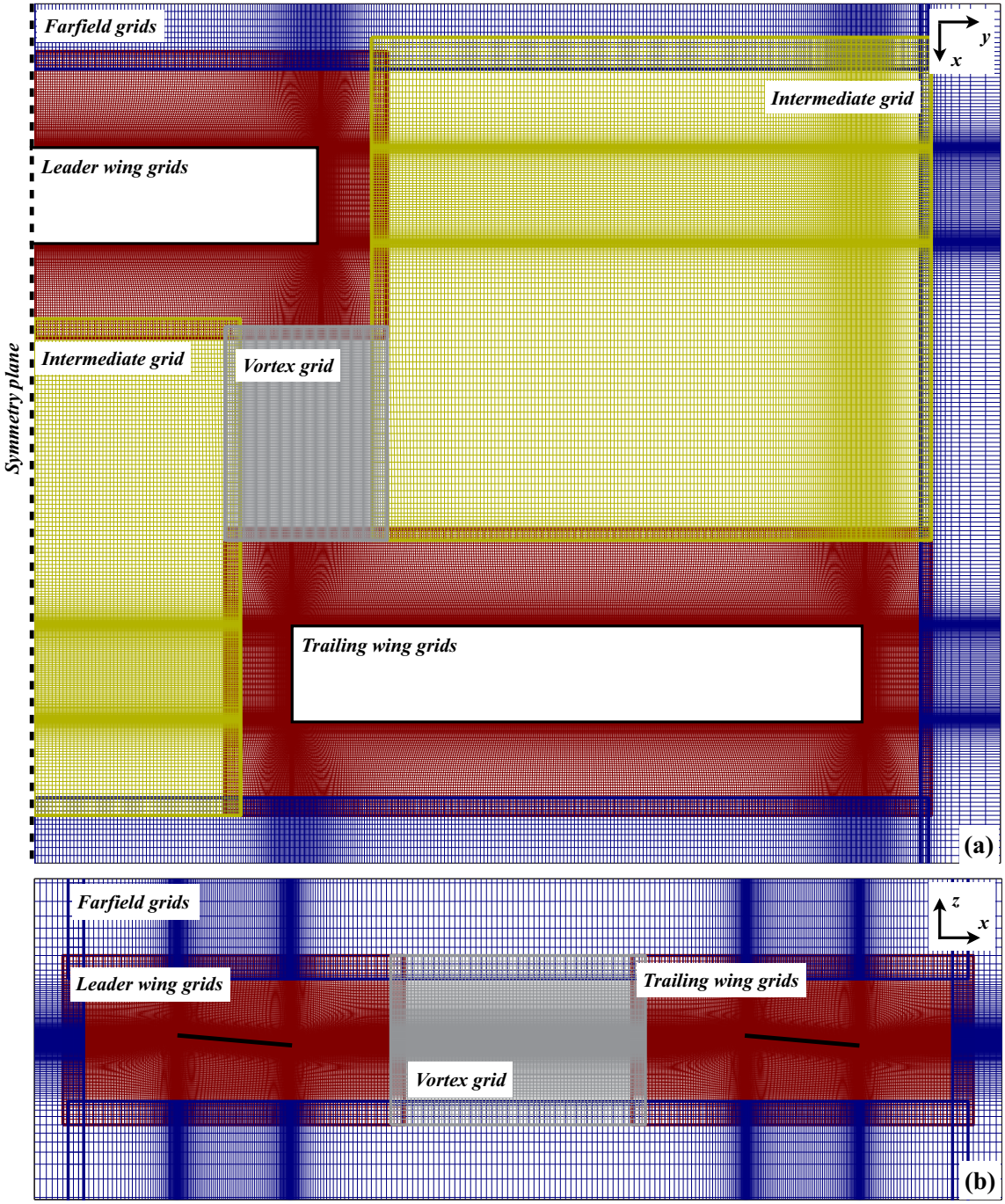

Figure 3.2: Overset multi-wing grid system used; (a) shows a top-view of the full grid system and (b) portrays a sideview.

manner. The wing surfaces employ a no slip condition where surface velocities are imposed at the corresponding boundary points. In addition, third-order adiabatic ($\partial T/\partial n = 0$) and zero normal pressure gradient ($\partial P/\partial n = 0$) conditions are enforced. Freestream conditions are imposed at the inlet, pressure, and suction-side farfield boundaries. This condition is applied in a manner similar to the approach provided in Ref. [134]. The high-order, low-pass filter is used in conjunction with rapidly stretching the mesh outside of the region of interest. This serves as a buffer for spurious reflections. Energy not supported as the mesh expands is reflected in the form of high-frequency modes which are eliminated by the highly discriminating filter. Simple extrapolation of all variables is employed on the outflow and side farfield boundaries.

Each of the following computations were initially run for $\tau = 25$ non-dimensional times allowing for the elimination of startup transients and the propagation of the trailing vortex past the follower wing. The simulations were then run for an additional $\tau = 10$ allowing for the collection of time-mean and statistical data. Each of the simulations presented utilizes a non dimensional time step of $\Delta\tau = 0.0001$ in order to provide sufficient temporal resolution for the fine-scale flow structure.

3.3 Effect of grid resolution

To evaluate the influence of grid resolution on the solutions obtained, computations were performed on several grids for a spanwise wingtip overlap of $\Delta y/c = 0.30$. Meshes were constructed from the baseline topology described in the previous section including two coarsened grids and one refined. Relevant dimensions of each system are provided in Table 3.1 where $\delta z_s/c$ is the surface normal spacing, $\delta x_{s,max}/c$ is maximum streamwise surface spacing, and $\delta y_{s,max}/c$ is the maximum spanwise surface spacing. Table 3.2 provides the time-mean drag, lift, and quarter-chord pitching moment co-

Table 3.1: Grid refinement details.

		Nominal spacing		
Grid	Num. points	$\delta z_s/c$	$\delta x_{s,max}/c$	$\delta y_{s,max}/c$
Coarser	$28,969,019$	1.59×10^{-4}	1.59×10^{-2}	3.18×10^{-2}
Coarse	$57,056,825$	1.26×10^{-4}	1.26×10^{-2}	2.52×10^{-2}
Medium	$85,178,439$	1.10×10^{-4}	1.10×10^{-2}	2.20×10^{-2}
Fine	$113,916,695$	1.00×10^{-4}	1.00×10^{-2}	2.00×10^{-2}

Table 3.2: Leader wing time-mean loads.

	Time-mean loads		
Grid	C_D	C_L	C_{M_y}
Coarser	0.0812	0.497	0.087
Coarse	0.0787	0.458	0.107
Medium	0.0779	0.446	0.111
Fine	0.0777	0.442	0.112

efficients ($\overline{C}_D$, $\overline{C}_L$, $\overline{C}_{M_y}$respectively) for the leader wing which change by less than 1% between the two finest meshes. Convergence of these integrated quantities with increasing resolution provides reasonable confidence that the present computations are grid independent.

The effect of grid resolution on the trailing vortex is illustrated in Figures 3.3(a) and (b) which plot streamwise and tangential velocity profiles across the vortex core respectively. As with the integrated time-mean loads, an excellent collapse of the time-averaged velocity profiles is observed for the two finest grids. This demonstrates the trailing vortex is well-resolved as it develops from the leader wing and preserved as it propagates towards the follower wing. The time-mean flow structure of the streamwise vortex encounter on the follower wing for the four grids is shown in Figure 3.4 using an iso-surface of Q-criterion[135] colored by streamwise vorticity. Q-criterion is defined by the second invariant of the velocity gradient tensor where a positive value indicates that rotation dominates strain and shear. Minimal differences in the general flow structure occur with grid refinement and the same basic behavior is captured at the vortex encounter for all four cases. The bulk portion of the incident vortex travels

across the suction surface and small time-mean structures emitted from the wingtip leading-edge (inset) are well preserved. Due to the minimal differences between the two finest meshes for all quantities investigated, the *medium* resolution grid was chosen for all subsequent computations.

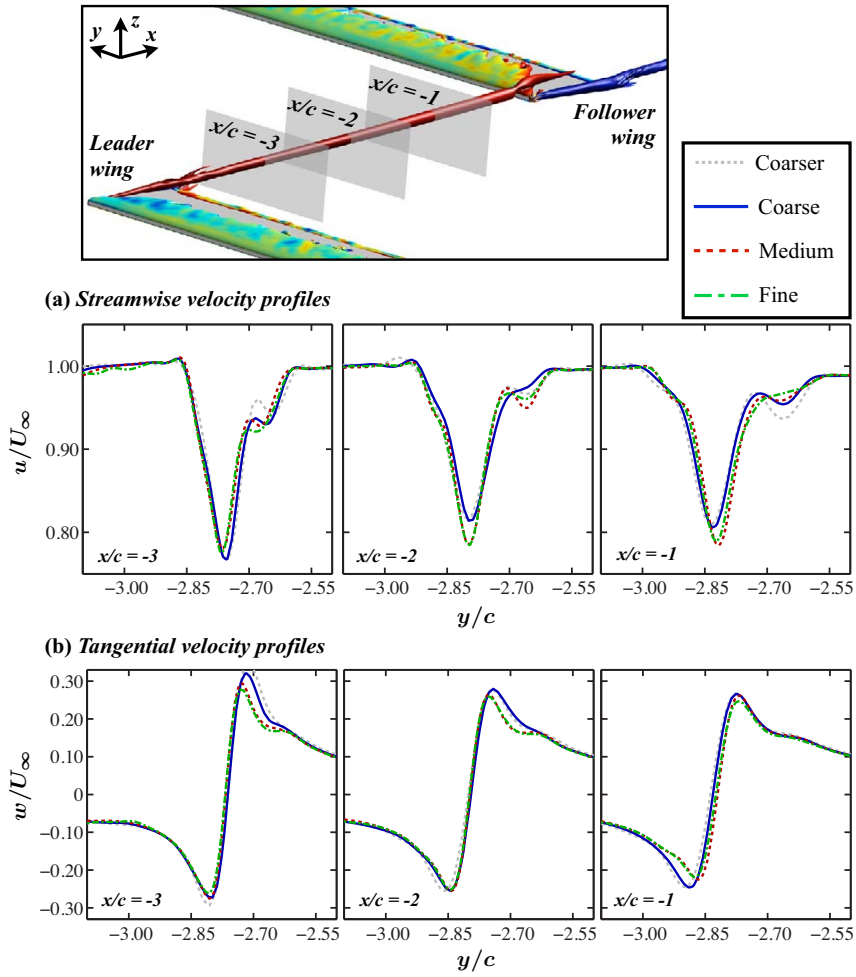

Figure 3.3: Effects of grid resolution; (a) time-mean streamwise velocity and (b) time-mean streamwise velocity across the vortex core at several streamwise locations.

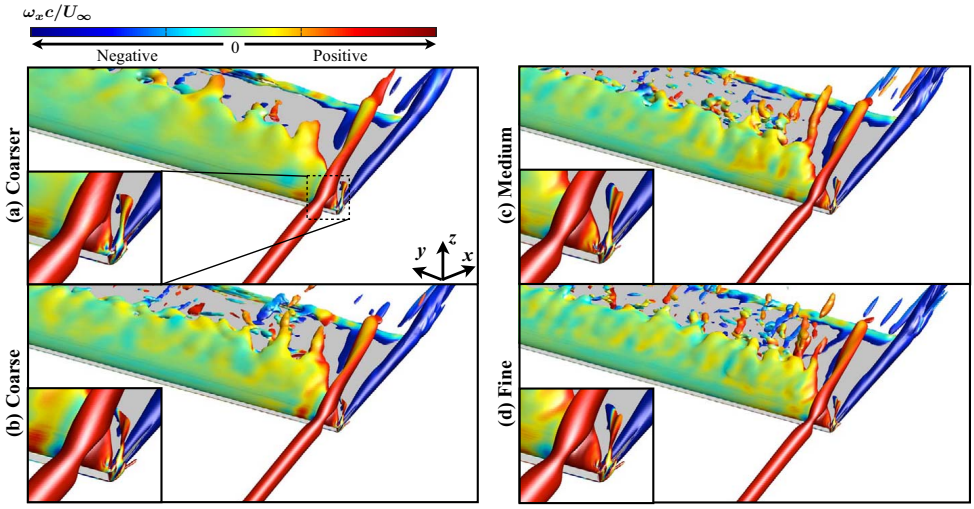

Figure 3.4: Effects of grid resolution on the flow structure of a vortex encounter using time-mean Q-criterion iso-surfaces for $\Delta y/c = 0.30$ ($Q = 2$).

3.4 Effect of lateral spacing

The goal of this section is to survey several lateral positions of a trailing vortex incident on a finite-aspect-ratio wing and develop an understanding of the flow structure and loading that results from the vortex encounter. This exploration will produce a better understanding of the flow structure and potential sources of unsteadiness. Several cases are compared to a single wing with values for the lateral spacing ranging from $\Delta y/c = 0.30$ to -0.15 and shown in Figure 3.5.

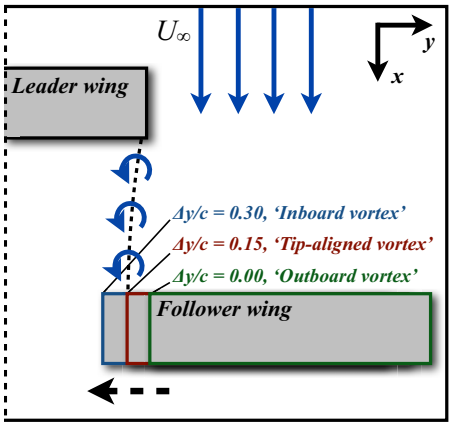

Figure 3.5: Lateral positions between leader and follower wings.

Because the trailing vortex tends to shift inboard of the wingtip during the rollup process, see for instance Ramaprian and Zheng[136], its position when it encounters the follower wing does not necessarily coincide directly with the lateral spacing. In order to better describe the vortex positioning relative to the follower wing, the location of maximum vorticity in the axial vortex was measured one chord upstream from the follower wing leading-edge and recorded in Table 3.3. Here, it should be noted that the vortex position is outboard for $\Delta y/c = -0.15$ and 0.00, incident close to the wingtip for $\Delta y/c = 0.15$, and inboard for $\Delta y/c = 0.30$ as portrayed in Figure 3.5. In the cases of the incident vortex traveling outboard of the follower wing's tip, as occurs for $\Delta y/c = -0.15$ and 0, the inherent behavior is qualitatively similar although more pronounced for $\Delta y/c = 0$. Therefore, the 'outboard' regime will be represented by only the $\Delta y/c = 0$ case for brevity. While the parameter $\Delta y/c$ refers to the relative lateral positioning between the leader and follower wingtips, more descriptive names for each case are used interchangeably throughout this article. These are based on the actual lateral position of the incident vortex when it reaches the follower wing, shown in Figure 3.5 and described by *inboard*, *tip-aligned*, and *outboard*, for the $\Delta y/c = 0.30$, 0.15, and 0 cases respectively.

Table 3.3: Incident vortex positioning at $x/c = -1.0$ upstream of follower wing leading-edge.

Vortex position	$\Delta y/c = -0.15$	$\Delta y/c = 0.00$	$\Delta y/c = 0.15$	$\Delta y/c = 0.30$
$\Delta y_v/c$	-0.273	-0.114	0.025	0.185
$\Delta z_v/c$	0.033	0.045	0.048	0.042

3.4.1 Time-mean flow structure

A general view of the flow structure involved in the interaction of the incident vortex on a follower wing is portrayed by an iso-surface of time-mean Q-criterion[135] depicted in Figure 3.6. Q-criterion is defined by the second invariant of the velocity

gradient tensor where a positive value indicates that rotation dominates strain and shear. The flow structure of a single wing is provided for reference in Figure 3.6(a). When the incident vortex is placed outboard, as in $\Delta y/c = 0$, mutual induction of the closely positioned follower tip and incident vortices results in an upward and inboard deflection of both features as shown in Figure 3.6(b). A small lateral shift to a tip-aligned position of $\Delta y/c = 0.15$ produces a different interaction between the incident and tip vortices. Figure 3.6(c) shows that the time-mean incident vortex wraps around the tip vortex as it passes over the wing and both are deflected downward in the wake of the follower wing. A final lateral shift in the vortex position to $\Delta y/c = 0.30$ results in yet another flow regime shown in 3.6(d). Here, the incoming vortex, now positioned inboard, travels primarily over the suction surface and then inboard while quickly weakening as it propagates toward the trailing-edge.

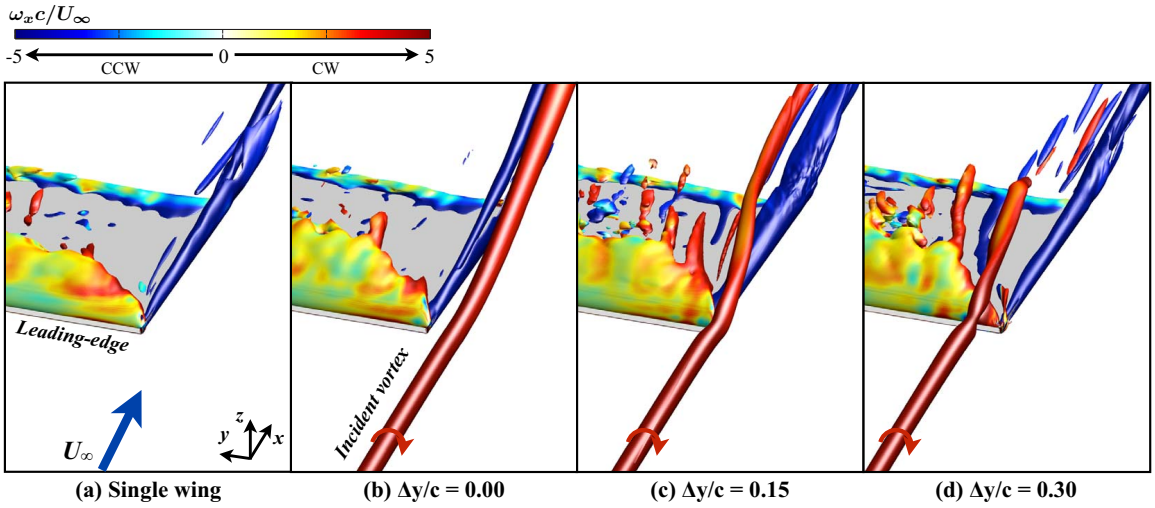

Figure 3.6: Time-mean iso-surface of Q-criterion colored by streamwise vorticity ($Q = 2$).

Cross-sections of streamwise vorticity are extracted at several streamwise positions along the chord and behind the follower wing in Figure 3.7 to more clearly elucidate the interaction between the incident vortex and the follower wing. Dark arrows convey the sense of rotation for streamwise vortices while lighter arrows demonstrate the trajectory of vortex pairs. For the outboard position, $\Delta y/c = 0$, the streamwise vortex

interaction is best described by simple vortex-dipole effects. This concept is portrayed in Figure 3.7(b). Here, the incident vortex, denoted as (1) at $x/c = 0.05$, travels outboard of the follower wingtip. The self-induced velocity between the incident axial structure and newly formed, oppositely-signed follower wing tip vortex, labeled as (3), results in a motion of the pair that is both upward and inboard. The tip vortex of the follower wing has become larger and lifted away from the wing surface compared to that of the single wing as it develops from $x/c = 0.50$ to 1.0. This results from an increased effective angle of attack due to the incident vortex upwash and self-induced velocity of the vortex-dipole which enhances the tip-vortex feeding-sheet. By one chord length behind the wing ($x/c = 2$) the position of the vortex pair is significantly upward and inward relative to its single-wing counterpart in Figure 3.7(a). This repositioning of wake features modifies the evolution of the wake behind the follower wing and can be expected to alter interactions with additional aerodynamic surfaces placed downstream. A similar upward and inward trajectory of wake features has also been observed experimentally in the PIV measurements of Inasawa *et al.*[49]

Moving further inboard, $\Delta y/c = 0.15$, the axial vortex, marked by (1) in Figure 3.7(c), impinges very close to the follower wingtip and the resulting vortex interaction becomes more complex. Here, a juxtaposition leads to the vortices wrapping about each other with the incoming vortex initially moving upward, $x/c = 0.05 - 0.25$, inboard, $x/c = 0.50 - 0.75$, and then downward toward the upper surface, $x/c = 0.75 - 1$. The vortex pair and downward motion persists behind the wing as shown for $x/c = 1.25 - 2$. This behavior exhibits another significant change in the wake features with only a small variation in lateral positioning between the leader and follower wings. Meanwhile, the follower wingtip vortex, annotated as (3) at $x/c = 0.5$, is clearly influenced by this lateral position compared to the other cases. The close positioning of the two features pushes the tip vortex inboard and closer to the wing such that it hugs the upper surface inboard of the wingtip. Consequently, this vortical

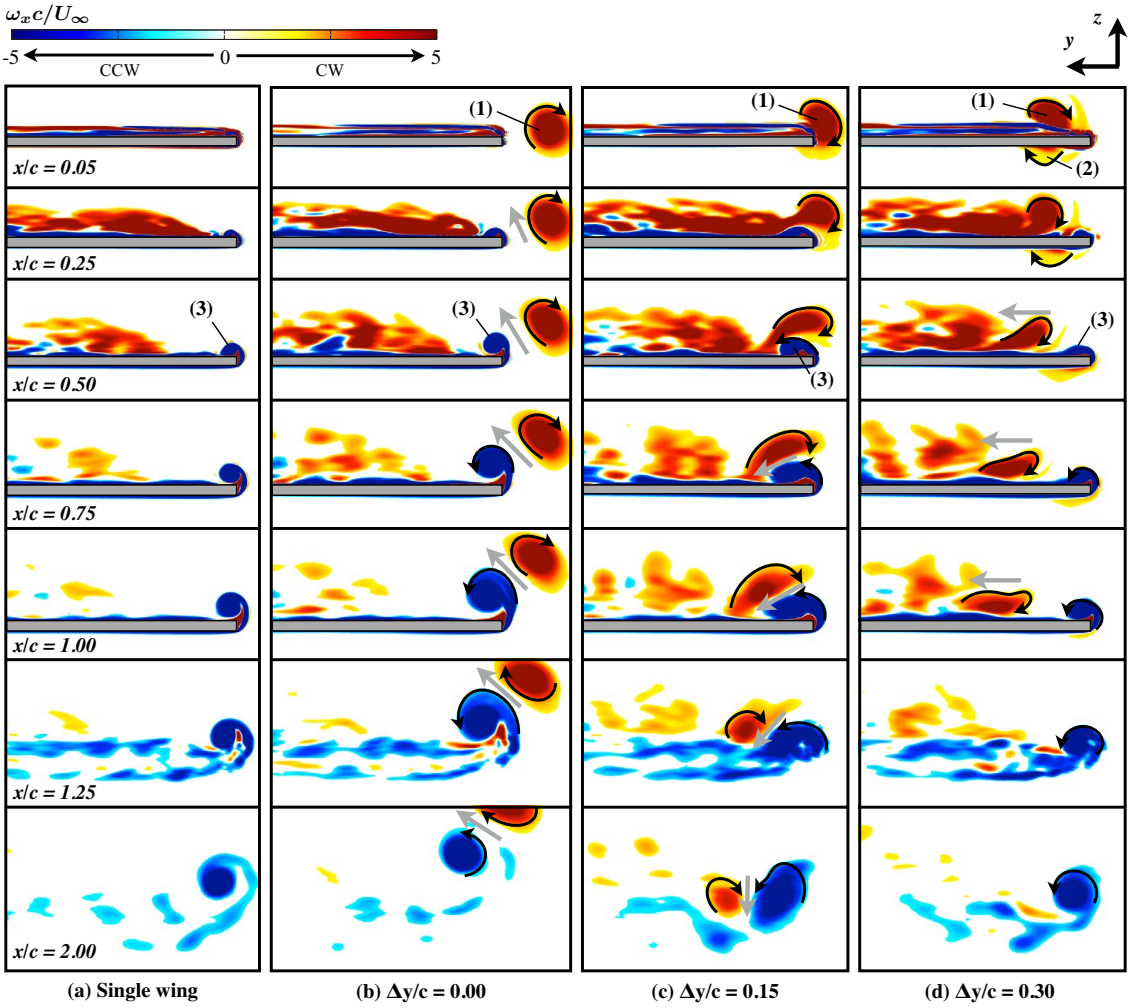

Figure 3.7: Slices of time-mean streamwise vorticity contours at selected streamwise positions for (a) single wing, (b) $\Delta y/c = 0$, (c) $\Delta y/c = 0.15$, and (d) $\Delta y/c = 0.30$.

feature can be expected to have a stronger imprint on the wing surface. As the tip vortex leaves the wing it takes on a more diffused and elliptical cross-section compared to that of the isolated wing as shown for $x/c = 2$.

The largest wingtip overlap $\Delta y/c = 0.30$ results in an axial vortex-impingement that is inboard of the follower wingtip, again annotated as (1) in Figure 3.7(d). Most of the incident trailing vortex passes over the suction surface and then travels inboard as it moves downstream, $x/c = 0.25$ to 1. This trend is reminiscent of the self-induced motion of an inviscid vortex with its mirror-image at a solid surface[63]. This effect is consistent with observations from the fin-buffet experiment of Mayori and Rockwell[1] and formation flight experiment of Inasawa *et al.*[49]. While the incoming vortex primarily travels over the suction side, bifurcation of the axial structure is evident in the time-mean flow. For example, $x/c = 0.05$ shows a small portion of streamwise vorticity, marked by (2), on the lower surface which quickly moves toward the wingtip, $x/c = 0.50 - 0.75$. This outboard motion of the lower component results from the interaction of a vortex with its mirror-image at a solid surface and reinforced by the spanwise flow over the wingtip on the pressure side. Similar bifurcation and vortex-surface interaction has been shown experimentally in the case of a streamwise vortex incident on a fin in Ref. [1] and for wings in close-formation flight in Ref. [49]. Immediately behind the wing $x/c = 1.25 - 2$ the incident vortex is no longer discernible due to a rapid dissipation as it travels over the wing. While the tip vortex appears similar in nature to that of the single wing in Figure 3.7(a) it has been weakened by the presence of a streamwise vortex encounter.

Figure 3.8 provides the minimum pressure coefficient in the follower wing tip vortex core at several streamwise positions and demonstrates the change in the strength of the tip vortex for each lateral position of the incident vortex. The outboard, $\Delta y/c = 0$, vortex position clearly enhances the tip vortex strength resulting in a minimum pressure nearly five times lower than its single wing counterpart at the

mid-chord. This strong low pressure region quickly attenuates downstream but remains the strongest tip vortex at all streamwise positions. A marked enhancement in pressure minimum is primarily due to a locally increased effective angle of attack provided by the incident vortex upwash. For example, $\overline{c}_{p,min} = -0.6$ at the mid chord of the leader-wing at $\alpha_L = 5°$ angle of attack but quickly decreases to a comparable $\overline{c}_{p,min} = -2.0$ when the leader-wing angle of attack is increased to $\alpha_L = 8°$. The tip aligned ($\Delta y/c = 0.15$) incident vortex initially strengthens the tip vortex but this enhancement diminishes as the incident vortex travels inboard and downstream. The inboard, $\Delta y/c = 0.30$ impingement results in a weaker tip vortex compared to the single wing at all streamwise positions. Because of the inboard position of the incident vortex, the wingtip is placed in a region of downwash which results in a diminished tip vortex strength.

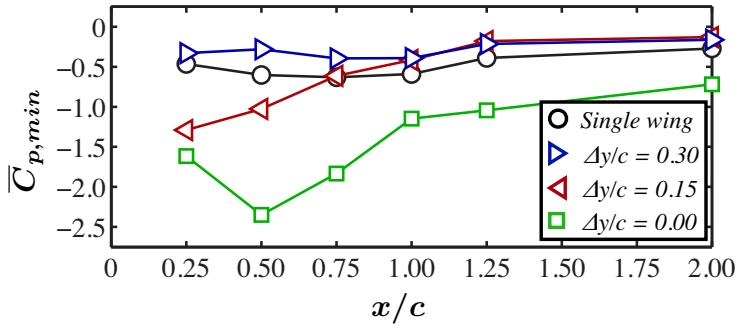

Figure 3.8: Minimum time-mean pressure coefficient in the follower wing tip vortex core.

Analysis of the time-mean surface topology lends additional insight into the impact of incident vortex location on the general flow structure. Contours of pressure coefficient and limiting surface streamlines are shown for a quarter-span of the suction-surface near the vortex encounter in Figure 3.9(a) and provides a relative comparison of the flow structure and surface loads to those of an isolated wing. In general, the flow field for the single wing is characterized by a separation bubble beginning at the leading-edge and primary flow attachment near the mid-chord. This is more clearly

depicted in Figure 3.10 where the primary attachment line for the single wing is approximated by tracing the inversion of streamwise friction coefficient, $\overline{C}_{f,x}$, on the upper surface.

Subjecting the follower wing to a trailing vortex elicits several changes to the surface flow topology. The primary attachment line moves further downstream for all vortex impingements characteristic of a larger separation region due to a local increase in effective angle of attack. This is again more clearly portrayed in Figure 3.10 for half the wing span where the vortex encounter cases are represented by only the $\Delta y/c = 0.15$ case due to qualitatively similar behavior. Flow separation eventually returns to the single wing behavior on the opposite midspan (not shown) as the influence of vortex-induced upwash diminishes.

The flow topology and surface pressure are more clearly differentiated near the wingtip in Figure 3.9(a). Compared to the isolated wing, the outboard incident vortex ($\Delta y/c = 0$) demonstrates a decrease in surface pressure beneath the strengthened tip vortex. Moving the vortex encounter to the wingtip ($\Delta y/c = 0.15$) results in a wider band of tip-region suction compared to both the single wing and $\Delta y/c = 0$ cases. A secondary-separation line, marked by (1) and traced by a dashed line, has moved inboard and is more prominent compared to the previous cases as a consequence of the tip vortex being pushed toward the surface as shown in Figure 3.7(c). An inboard, $\Delta y/c = 0.30$ vortex results in a weaker suction region along the wingtip corresponding with the diminished tip vortex. Also notable is the formation of a stable focus near the leading-edge corner. This swirling pattern, denoted by (2), coincides with a strengthened suction region compared to the other cases shown. This variation in surface pressure topology due to vortex positioning directly translates to the aerodynamic loading as will be made apparent in Section 3.4.3.

Figure 3.9(b) shows contours of streamwise vorticity on a portion of the wing near the vortex encounter on the suction-side surface and serves to portray the imprint of

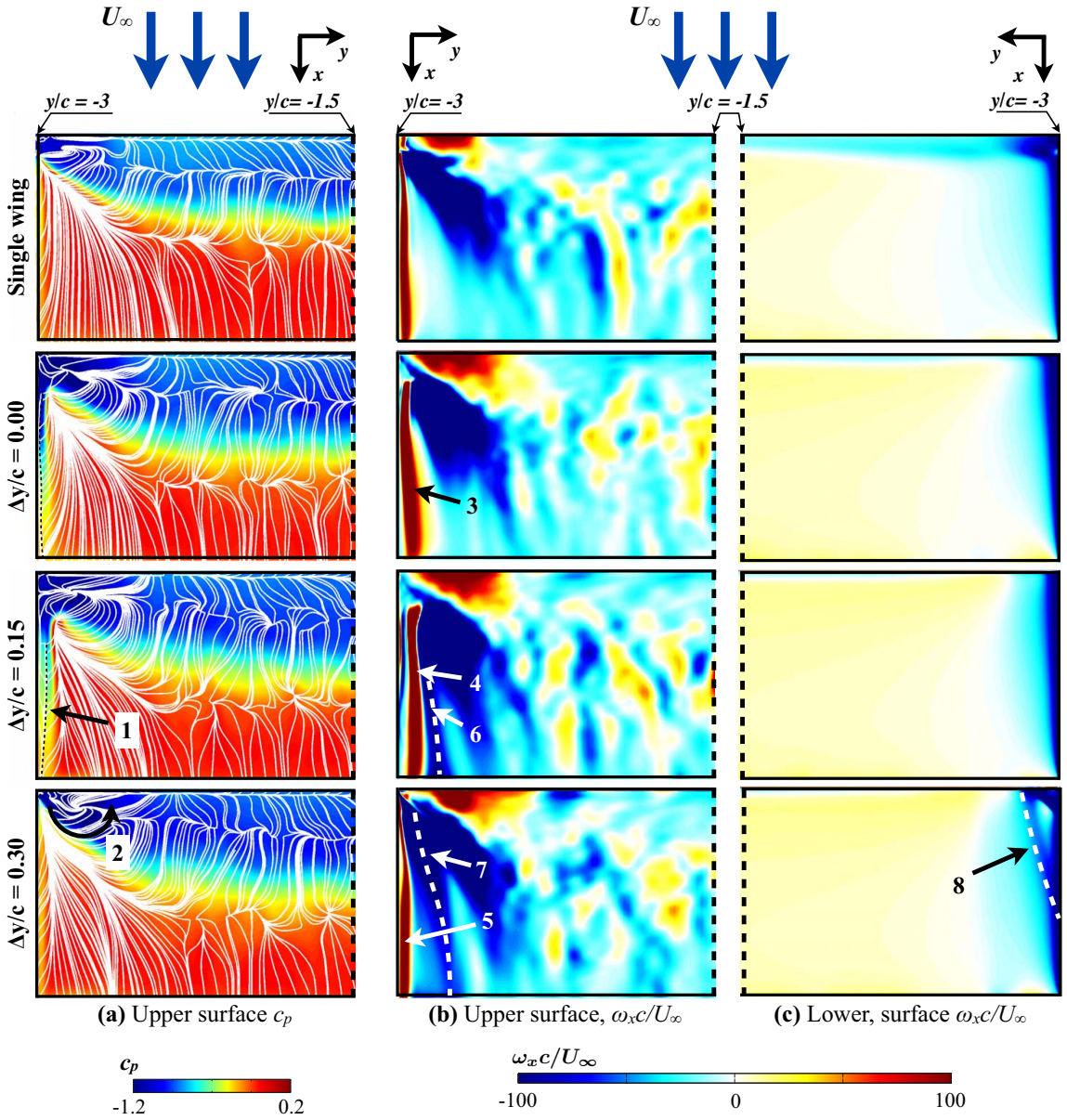

Figure 3.9: Time-mean surface contours of (a) suction-side pressure coefficient and surface restricted streamlines (b) suction-side streamwise-vorticity, and (c) pressure-side streamwise vorticity near vortex encounter.

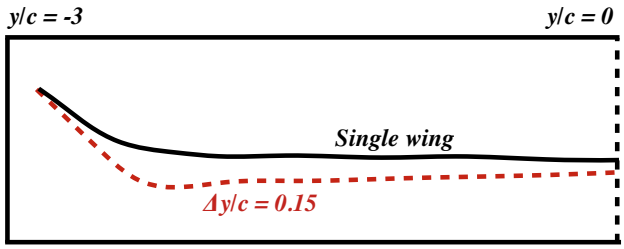

Figure 3.10: Time-mean reattachment line for the single wing and tip-aligned cases.

the tip vortex on the wing. For the single wing, a band of oppositely-signed (positive) wall-induced vorticity appears beneath the tip vortex which increases in the presence of an outboard streamwise vortex in $\Delta y/c = 0.00$, denoted by (3). This band shifts inboard and becomes more concentrated, denoted as (4), when the tip vortex is driven against the surface for $\Delta y/c = 0.15$, in Figure 3.7(c). Label (5) points to a narrow band and then sudden expansion of wall-induced vorticity indicative of the delayed tip vortex formation for the inboard, $\Delta y/c = 0.30$ vortex encounter.

The imprint of the incident vortex is also apparent in the contours of surface vorticity. This is shown for the suction surface in Figure 3.9(b) where a trace of negative wall-induced vorticity is shown for $\Delta y/c = 0.15$ beginning near the mid-chord by annotation (6) demonstrates the imprint of the incident vortex as it wraps around the tip and tends toward the wing surface. In the $\Delta y/c = 0.30$ case, a wider band of negative wall-induced vorticity, traced by a dashed white line and noted as (7), follows the upper component of the incident vortex and more clearly demonstrates its inboard trajectory. A second imprint of the incident vortex is apparent on the lower surface in Figure 3.9(c) where the imprint of a much weaker lower surface component of the bifurcated vortex for the inboard case is clearly portrayed on the pressure side contour and marked as (8). This narrow band of negative vorticity travels outboard and into the tip vortex feeding sheet as it propagates downstream.

3.4.2 Unsteady flow structure

This section explores the instantaneous flow structure in order to better understand the unsteady fluid dynamics that may lead to buffeting loads. Figure 3.11 depicts several snapshots of instantaneous Q-criterion iso-surfaces for each case with the single wing provided in Figure 3.11(a). Figure 3.11(b) shows a top view of the instantaneous flow structure for the outboard vortex encounter, $\Delta y/c = 0.0$. Helical substructures are observed to form in the tip vortex feeding sheet similar to those

observed in the leading-edge vortex of delta wings[137]. In the wake, both the follower and leader wing trailing vortices exhibit an undulating behavior as they propagate downstream. While the leader wing vortex instability appears to be the more pronounced of the two, the wavelength of both features is on the order of the separation between the two vortices indicative of a long wavelength mutual inductive instability.

Figure 3.11(c) shows a top view of an instantaneous Q-criterion iso-surface for the tip-aligned vortex ($\Delta y/c = 0.15$). The incident vortex becomes quite unstable near the mid-chord as it moves inboard due its interaction with the tip vortex. Figure 3.11(d) shows a higher value of Q-criterion to more clearly elucidate instantaneous tip vortex flow structure at the same instant of time. The wing orientation has been changed for improved visualization of the tip vortex which takes the form of an undulating spiral. This behavior does not indicate breakdown of the tip vortex, but is rather a product of the unsteady interaction between the two streamwise vortices. The larger appearance of the time-mean tip-vortex flow structure shown in Figures 3.6(c) and 3.7(c) is a consequence of this unsteady vortex interaction.

The instantaneous flow structure for the inboard ($\Delta y/c = 0.30$) case is shown in Figure 3.11(e). Observation of the incident vortex shows that it initially maintains its coherence as it traverses the first half of the upper surface. Near the mid-chord, the incident vortex begins to lose stability and connects with vortical structures in the separated flow region located on the inboard side of the vortex. Ultimately, the streamwise vortex becomes amalgamated with the turbulent flow field and reoriented in the spanwise direction as it approaches the trailing-edge. By the time the axial vortex reaches the trailing-edge, it is weakened to the extent it is no longer recognizable, consistent with the attenuation of streamwise vorticity observed in the time-mean flow in Figure 3.7. Another unsteady feature unique to this case is the ring-like substructures shown to form in the suppressed tip-vortex feeding sheet. Fourier analysis of the rolling moment coefficient, provided in the Section 3.4.3, reveals this unsteady

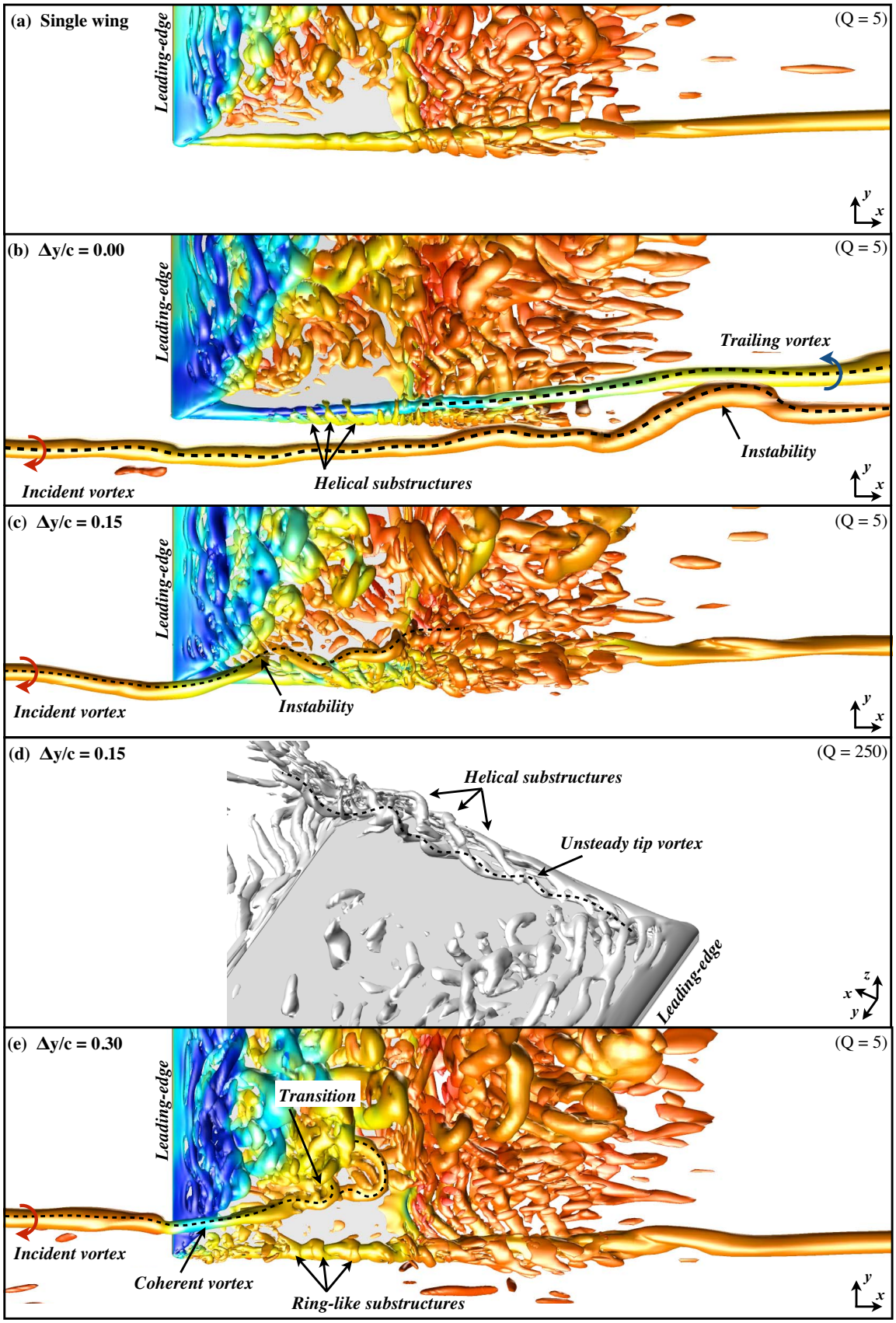

Figure 3.11: Instantaneous iso-surface of Q-criterion for several lateral positions.

feature is a source of buffeting loads that can impact the lifecycle of an aerodynamic surface.

Contours of suction-side pressure fluctuations are provided in Figure 3.12 for each lateral position and the isolated wing. The tip-aligned ($\Delta y/c = 0.15$) case results in the most distinct pressure fluctuations where a band of pronounced $\overline{p'p'}$ appears immediately beneath the tip vortex. Mutual induction between the incident and tip vortices, Figure 3.7(c), drives the tip vortex close to the wing surface, while strong interaction between the two features provides a highly chaotic flow, Figure 3.11(d), thereby translating to strong pressure fluctuations on the wing surface. Being located on the most outboard portion of the wing, this unsteady behavior can be expected to influence fluctuations in the rolling moment.

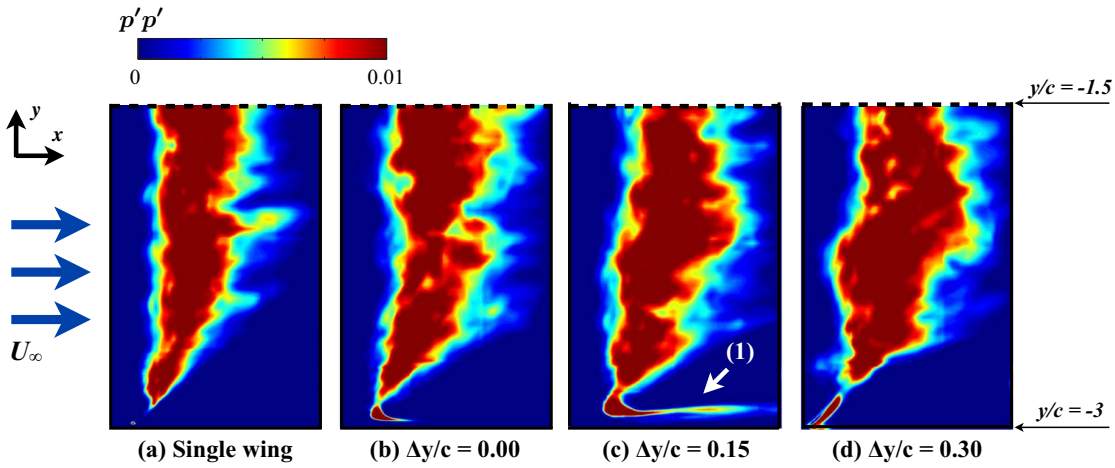

Figure 3.12: Surface contours of suction-side pressure fluctuations for a portion of the wing near the vortex encounter.

3.4.3 Aerodynamic loads

This section evaluates the connection between the physical mechanisms previously described with aerodynamic loads. The time-mean aerodynamic forces for the follower wing are shown in Table 3.4 and compared to those of single wing for reference. In general, the time-mean drag coefficient, $\overline{C}_D$ increases for the follower wing while

remaining relatively unchanged with lateral spacing. The presence of the incident vortex results in a significantly enhanced lift coefficient which is highest for the most inboard vortex position studied. Lift-to-drag ratios increase as the incident vortex moves inboard approaching an 8.7% enhancement compared to that of a single wing.

Table 3.4: Time-mean aerodynamic loads.

	$\overline{C}_D$		$\overline{C}_L$		$\overline{L/D}$		$\overline{C}_{M_x}$	$C_{M_{x,\mathrm{RMS}}}$
	Value	% diff.	Value	% diff.	Value	% diff.		$(\times 10^{-3})$
Single wing	0.077	-	0.433	-	5.65	-	0.002	9.8
$\Delta y/c = -0.15$	0.082	+6.7%	0.495	+14.3%	6.05	+7.1%	-0.062	8.7
$\Delta y/c = 0.00$	0.082	+7.2%	0.500	+15.4%	6.08	+7.7%	-0.072	10.3
$\Delta y/c = 0.15$	0.082	+7.4%	0.505	+16.6%	6.13	+8.5%	-0.077	8.9
$\Delta y/c = 0.30$	0.083	+7.6%	0.507	+17.0%	6.14	+8.7%	-0.067	11.0

A negative induced rolling moment, $\overline{C}_{M_x}$, appears for each of the vortex encounter cases with a maximum at $\Delta y/c = 0.15$. Variation in the rolling moment coefficient between lateral position is fairly significant where a 15% difference occurs when moving from the $\Delta y/c = 0.30$ and 0.15 cases. Such sensitivity in $\overline{C}_{M_x}$ to a small change in lateral spacing implies that uncertainty or variation in the vortex position could be a dominant factor in unsteady loading. This effect can be expected to amplify in the presence of a stronger vortex. In comparison, the root-mean-square of C_{M_x} fluctuations, provided in Table 3.4, shows that the level of unsteady loading on the follower wing is both small and comparable to that of a single wing for each lateral position of the streamwise vortex.

While the instabilities associated with the different streamwise vortex interactions do not appear to translate into a severe change in the amplitude of unsteady loads for this particular configuration, observation of the time-mean forces does suggest a significant variation could arise with a change in vortex positioning. For instance, the references on vortex meandering discussed in Section 1.3.5 demonstrate the capability of unsteady phenomena from a fixed wing trailing vortex to sweep across the charac-

teristic flow regimes and spanwise load distributions presented in the present chapter. Motion of either aerodynamic surface due to maneuvering, atmospheric turbulence, or aeroelasticity can further contribute to shifts in lateral or vertical positioning of the incident vortex.

Fourier analysis of the rolling moment coefficient is provided in Figure 3.13 which demonstrates how unsteady loading is distributed in frequency space. While $\Delta y/c = 0.15$ exhibits the most significant surface pressure fluctuations, Figure 3.12, no well defined frequencies can be linked to the band of pressure fluctuations. The inboard vortex position, $\Delta y/c = 0.30$, does convey a clearly defined peak at a non-dimensional frequency of $\mathrm{St}_c = fc/U_\infty = 5.4$. This value corresponds with the unsteady behavior of the ring-like substructures shown in Figure 3.11(d) which were determined to have a frequency of roughly $5 \leq \mathrm{St}_c \leq 6$. Though small in amplitude, this high frequency component could impact the fatigue-life of aerodynamic structures.

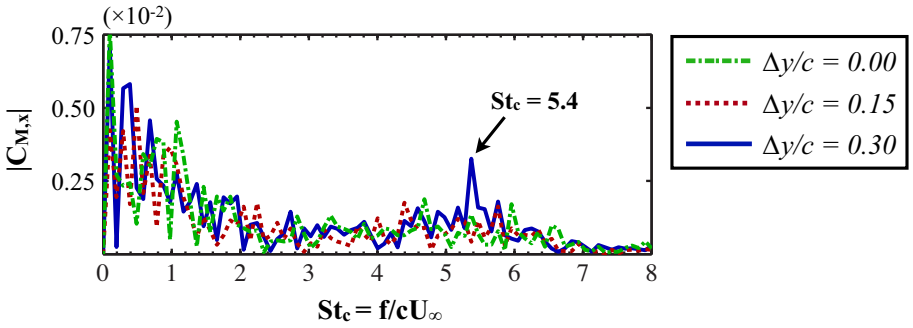

Figure 3.13: Fourier analysis of rolling moment coefficient.

Figure 3.14 shows several representations of the time-mean distribution of lift coefficient per unit length plotted along the wing span and helps to differentiate the aerodynamic loading for each lateral position. Figure 3.14(a) demonstrates that each case results in a significant lift enhancement distributed over a large portion of the wing span compared that of the isolated wing. The bulk of lift enhancement can be largely attributed to the increased effective angle of attack induced by the incident vortex upwash, an inviscid effect. Assuming a linear lift-curve slope valid for pre-

stall angles of attack, and $C_L = 0$ at $\alpha = 0°$ for the symmetrical flat plate, the inviscid lift contribution due to upwash can be removed at each spanwise position by linearly scaling lift by the local effective angle of attack: $C'_{l,\text{rescaled}}(y) = \alpha_0/\alpha_{\text{eff}} C'_l(y)$ where α_0 is the baseline angle of attack for the follower wing of 5°. The increase in α_{eff} was obtained by computing the difference in time-mean velocity profiles from the isolated wing along the wingspan one chord-length upstream for each case. The rescaled sectional lift coefficient per unit length is plotted in Figure 3.14(b) where all four follower lift profiles collapse to that of the isolated case over most of the span. Only within one chord length of the vortex-encounter wingtip does the distribution depart from that of the isolated wing due to the stronger vortex-surface interaction near the vortex-side wingtip. It is in this region that the loads are most strongly impacted by viscous effects and have the greatest influence on the variation in rolling moment demonstrated in Table 3.4.

Focusing on the vortex-encounter in the wingtip region, Figure 3.14(c), the lift distributions for each case are more clearly differentiated in the viscously dominated region. The lift spike near the wing tip, associated with low pressure beneath the tip vortex (see Figure 3.9(a)), exhibits a marked difference between the various lateral spacings. The inboard, $\Delta y/c = 0.30$, position results in a diminished spike in the local lift coefficient consistent with a weakened tip vortex in the presence of downwash. For $\Delta y/c = -0.15$ and 0.00 the outboard position of the incident vortex strengthens the tip vortex and generates a locally enhanced lift beneath the tip vortex. In the case of $\Delta y/c = 0.15$ the tip vortex was shown in Figure 3.7(c) to be pushed against the wing surface as a consequence of the self-induced velocities of the incident and forming streamwise vortices. In this case, not only is the local lift distribution enhanced in the tip region, it covers a larger surface area. Becsause the roll moment is most sensitive to changes in lift on the most outboard regions of the wing, it is not surprising this case coincides with the maximum $\overline{C}_{M,x}$.

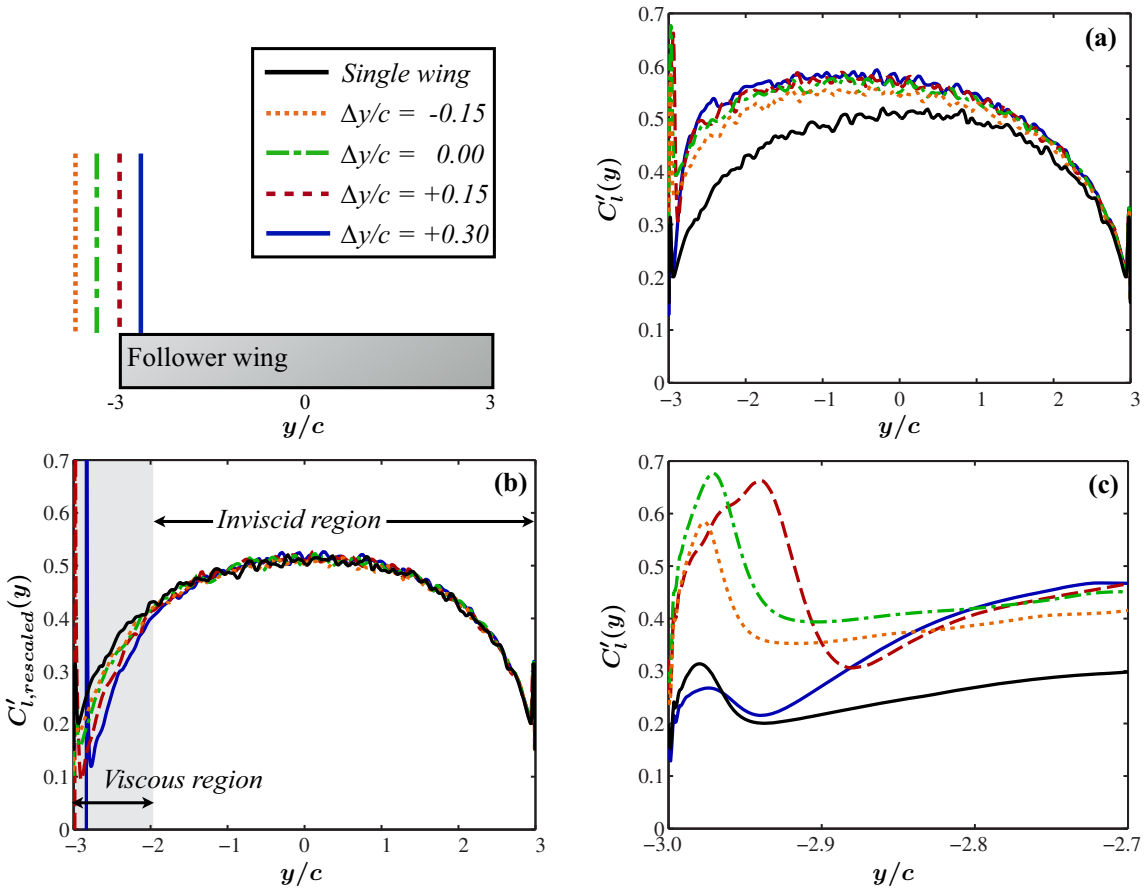

Figure 3.14: Time-mean lift coefficient per unit length plotted (a) along the wing span, (b) scaled by the local effective angle of attack, and (c) near the incident vortex encounter.

3.5 Comparison with experiment

PIV measurements from a water tunnel experiment were recently provided by McKenna *et al.*[4]. This study investigated a streamwise vortex generated by a leader wing placed upstream of a rectangular flat plate follower wing with uniform thickness $t/c = 0.03$ at a low angle of attack, similar to the computational work described above. It should be noted that the experiment and computation differ in the choice of several parameters which are provided in Table 3.5.

The primary differences between the two cases lie in the choice of the leader wing and chord-based Reynolds number. The lower Reynolds number of the water tunnel

experiment can be expected to provide a less transitional flow structure and more viscously dominated flow whereas the higher Reynolds number of the computational work was intended to explore the vortex interaction with unsteady, transitional, and separated flow as described in Section 3.1. Delisi[138] has reported measurements of trailing vortices behind full aircraft and scale models and demonstrated consistent behavior over a large change in Reynolds number. As will become apparent in the following discussion, remarkably similar behavior can be expected for a range of operating conditions.

Table 3.5: Parameters for computation and experiment

	Computation	Experiment
Re	30,000	8,000
$\Delta x/c$	5	4
Leader profile	Flat plate	NACA0012
α_L	5°	16°
Follower profile	Flat plate	Flat plate
α_F	5°	4°
$\Gamma_v/U_\infty c$	0.105	0.394
$q = \Gamma_v/2\pi r_v \Delta u$	1.99	2.04
$\Delta u/U_\infty$	0.21	0.27
r_v/c	0.04	0.114

The higher angle of attack and smooth planform of the leader wing in the experiment generates a larger and stronger incident vortex, as measured by the core size, r_v, and circulation Γ_v respectively. Other properties of the impinging vortex, such as the vortex swirl (q), and velocity deficit (Δu) differ only by a small amount. This section is not intended to serve as a direct, detailed comparison between computation and experiment due to the challenge of matching the many parameters involved in a tandem wing configuration. Rather, a qualitative comparison of the mean flow between similar cases is provided in this section and is useful to verify the physical behavior of the computations in the preceding sections.

Figure 3.15 provides contours of streamwise vorticity ($\omega_x c/U_\infty$) for a vortex placed

outboard of the follower wingtip. In addition to Both computation and experiment exhibit an upward and inboard motion due to mutual induction between the counter-rotating incident and tip vortices, labeled by (1) at $x/c = 0.5$. Tip vortices in both cases are significantly enhanced due to the increased effective angle of attack provided by the incident vortex upwash. Self-induced motion of the vortex dipole continues in the wake, denoted by (2) at $x/c = 1.25$, where both features have moved significantly upward and inboard immediately behind the wing.

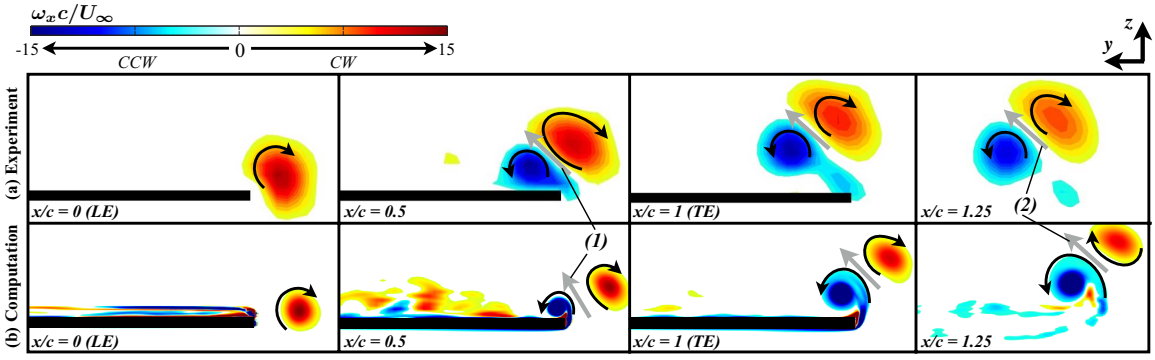

Figure 3.15: Contours of time-mean streamwise vorticity at selected streamwise positions for (a) experiment [4] and (b) computation for an outboard positioned vortex.

Next, a comparison for the tip-aligned encounter is provided in Figure 3.16. Mutual induction between incident and tip vortices, shown by annotation (1), directs the pair of counter-rotating vortices inboard at $x/c = 0.5$ where the tip vortex is pushed very close to the wing surface. Mutual induction between the counter-rotating vortices causes the incident vortex to wrap around the wingtip as it moves downstream. Ultimately, the vortex dipole remains in the wake with a downward trajectory marked by (2).

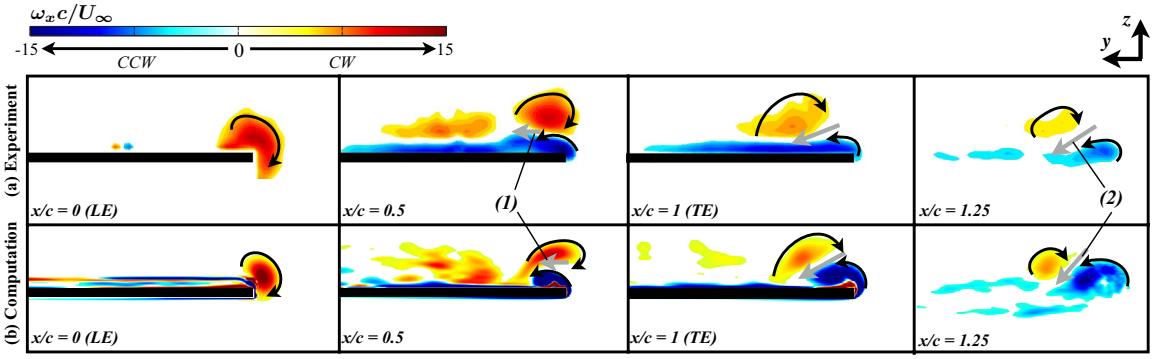

Figure 3.16: Contours of time-mean streamwise vorticity at selected streamwise positions for (a) experiment [4] and (b) computation for a tip-aligned vortex.

Finally, Figure 3.17, provides a comparison for an inboard encounter. In both cases, the incident vortex traverses inboard as it passes over the wing, labelled by (1) at $x/c = 0.5$. The incident vortex continues to move inboard and quickly attenuate as it approaches the trailing-edge in both cases, marked by (2) at $x/c = 1$. Downstream, the tip vortex is clearly weakened compared to the previous lateral positions, denoted by (3) at $x/c = 1.25$. One feature not captured in the experiment due to the shadow region on the pressure-side is a small region of positive vorticity indicative of a bifurcated incident vortex, label by (4) at $x/c = 0$.

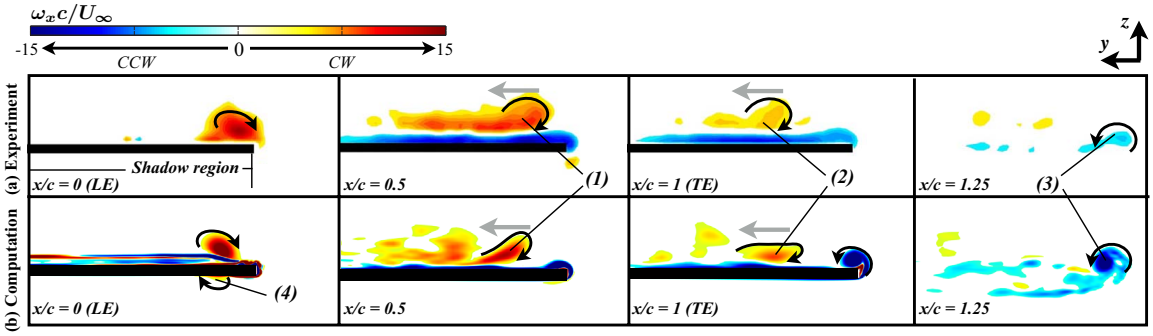

Figure 3.17: Contours of time-mean streamwise vorticity at selected streamwise positions for (a) experiment [4] and (b) computation for an inboard vortex.

The above qualitative comparison between the computations of this chapter and a similar experiment corroborate each of the most important features observed in the time-mean flow and discussed in greater detail in the following section. Good agree-

ment between the two cases provides further confidence in the detailed analysis of the numerical simulations provided in this document. Additionally, consistent behavior despite some parametric differences suggests the physics explored in this dissertation are robust and can be expected to persist through a range of operating conditions. Therefore, the discussions supplied in this dissertation provide a fundamental groundwork for the understanding of streamwise-oriented vortex-surface interactions.

3.6 Effect of leader wing angle of attack

This section investigates the effect of raising the leader wing angle of attack to $\alpha_L = 8°$, thereby increasing both the size and strength of the incident trailing vortex on the flow structure and aerodynamic loading. The follower wing remains at $\alpha_L = 5°$ and the lateral wingtip overlap is chosen as $\Delta y/c = 0.30$. The inboard position was chosen for this case in order to explore the influence of a stronger vortex directly impinging on a follower wing. As in the previous section, the actual location of the incident vortex one chord-length upstream of the follower wing is recorded in Table 3.6. An increased interaction between the leader wing trailing vortex pair moves the incident vortex downward providing for a more head-on collision with the follower wing. It will become apparent in the following discussion that this vertical position has some effect on the incident vortex behavior. A more systematic evaluation on the effects of vertical positioning is provided in Chapter 6. In the lateral direction, the larger incident vortex has shifted slightly toward the follower wingtip. Time-mean streamwise and tangential velocity profiles are shown in Figures 3.18(a) and (b) respectively which demonstrate the size and strength of the new incident vortex compared to the previous $\alpha_L = 5°$ case.

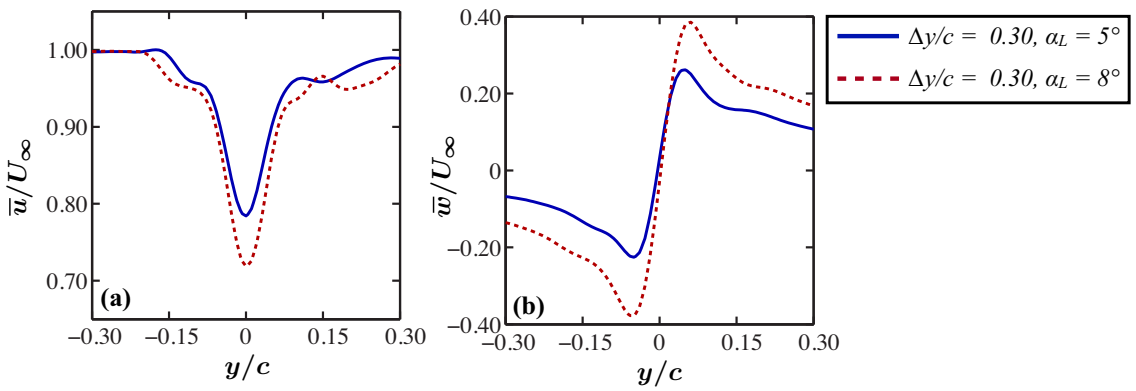

Figure 3.18: Time-mean (a) streamwise and (b) tangential velocity profiles across the vortex core measured one chord length upstream of the follower wing.

Table 3.6: Effective position of the incident vortex at $x/c = -1.0$.

Vortex positioning	$\alpha_L = 5°$	$\alpha_L = 8°$
$\Delta y_v/c$	0.185	0.145
$\Delta z_v/c$	0.042	0.020

3.6.1 Time-mean flow structure

Time-mean streamwise vorticity contours are provided in Figure 3.19 for the isolated wing, $\alpha_L = 5°$, and $8°$ cases and demonstrate changes in the flow structure that result from the modified incident vortex. Because of the greater strength and lower effective vertical offset, the impinging vortex results in a more even bifurcation between the upper and lower surfaces, for $x/c = 0.05$ in Figure 3.19(c). The upper surface component, labeled as (1), tends inboard as it travels downstream, $x/c = 0.05 - 0.25$. By $x/c = 0.50$, the incident vortex is nearly indistinguishable losing its identity much sooner than the $\alpha_L = 5°$ case. Meanwhile, the lower surface component of the bifurcated vortex, marked by (2), tends outboard as it propagates downstream, $x/c = 0.05 - 0.50$, and then (3) wraps around the tip vortex, $x/c = 0.50$. The impact of the stronger lower surface component of the incident vortex results in a more disorganized formation of the tip vortex, shown for $x/c = 1.00$ and denoted

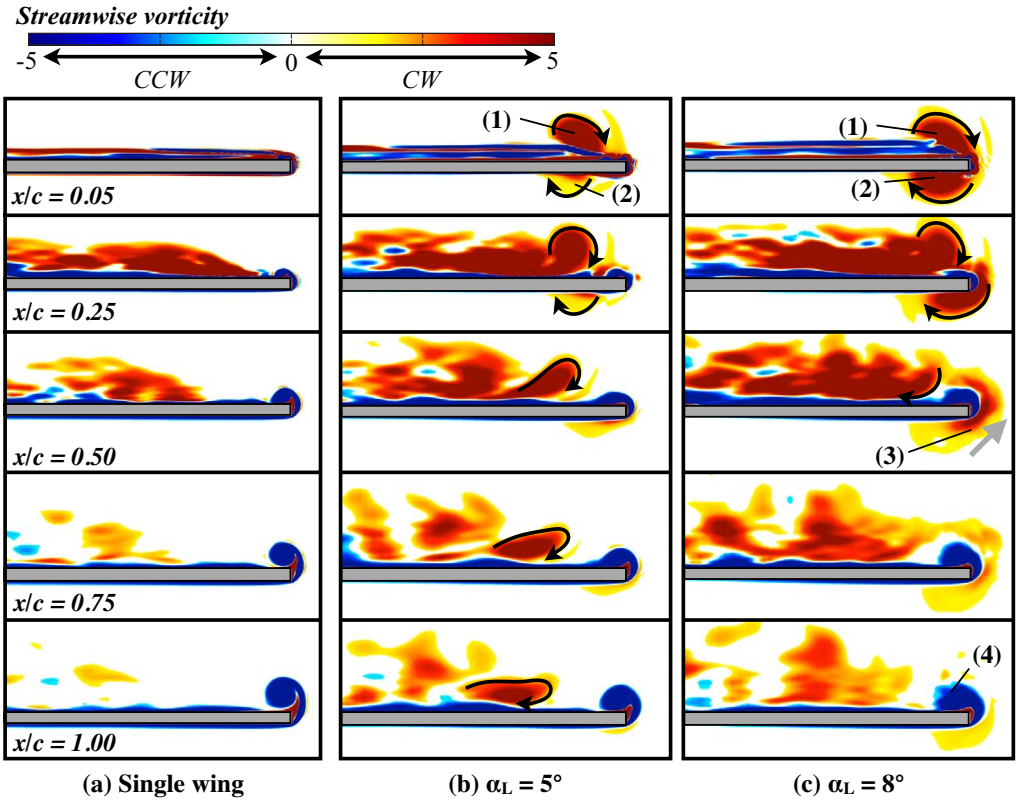

Figure 3.19: Cross-sections of time-mean streamwise vorticity for (a) single wing, (b) $\alpha_L = 5°$, and (c) $\alpha_L = 8°$.

by (4).

The surface flow topology is shown in Figure 3.20 where time-mean limiting surface streamlines overlay contours of time-mean surface pressure coefficient on the suction-side. Two factors are apparent when the leader wing changes from $\alpha_L = 5°$ to 8°. First, the separation bubble, indicated by a larger region of suction, has clearly advanced further downstream as can be expected for an increased local effective angle of attack. Second, enhanced separation results in a more prominent swirl pattern about a stable focus near the leading-edge compared to the $\alpha_L = 5°$ case, indicated by a black arrow.

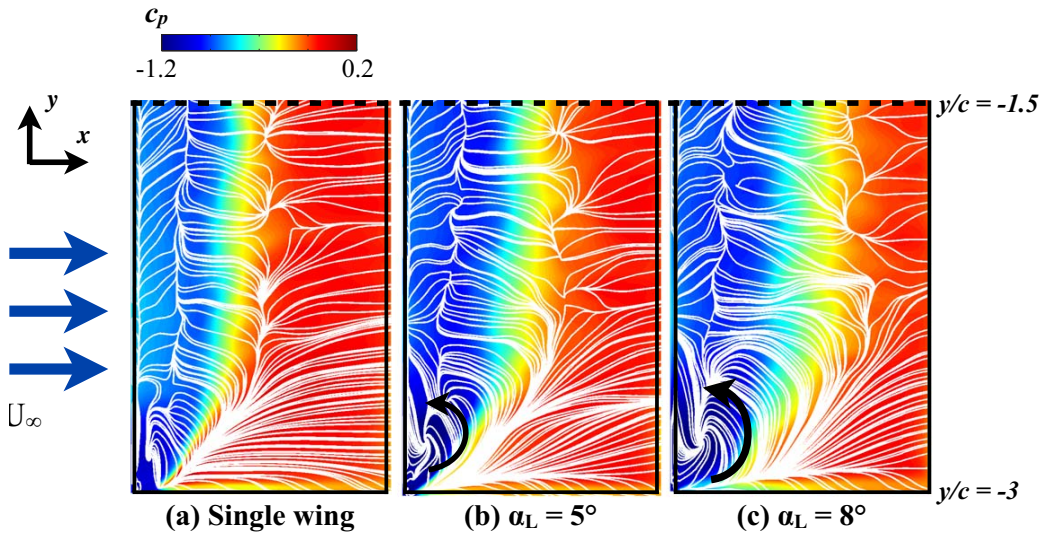

Figure 3.20: Contours of time-mean upper-surface pressure coefficient and surface restricted streamlines for (a) single wing, (b) $\alpha_L = 5°$, and (c) $\alpha_L = 8°$.

3.6.2 Unsteady flow structure

Figure 3.21 shows top and bottom views of an iso-surface of instantaneous Q-criterion and provides a qualitative overview of the instantaneous flow structure. First, looking at the lower surface in Figure 3.21(a), the lower component of the vortex is visibly apparent and tends outboard over the wingtip as shown in the time-mean flow. Moving to the upper surface in Figure 3.21(b), the pressure-side component can be seen to periodically loop about the tip vortex as it is shed into the wake contributing to the disorganized appearance of the tip vortex noted in Figure 3.19(c). In the instantaneous flow, the upper-surface component of the incident vortex maintains its coherence for a short distance as it travels over the leading-edge. Compared to the $\alpha_L = 5°$ case in Fig. 3.11(d), the upper surface component decays more rapidly. Two factors could contribute to this effect: a weaker suction-side component due to the more even bifurcation and stronger influence of the enhanced separation region on the inboard side.

Although not well portrayed in the current chapter, an important unsteady feature is visible in Figure 3.21(b). An indentation in the Q-criterion iso-surface is visible

immediately in front of the wing and indicates the response of the vortex to stagnation upon impingement with the leading-edge. This culminates in a spiraling undulation very close to the wing. At the instance of time shown, the incident vortex is pinching off of the upper-surface component (Figure 3.21(b)) and begins contributing to the pressure-side component (Figure 3.21(a)). This alternating pattern is the mechanism that permits the time-mean bifurcation shown in Figure 3.19(c) and is very similar to the spiraling instability shown more clearly for an impinging q-vortex by Garmann and Visbal[5]. It is intriguing to note that rather than divert to either side of the wing, the vortex develops an instability mode. This particular behavior will be much more thoroughly characterized later in Chapter 6.

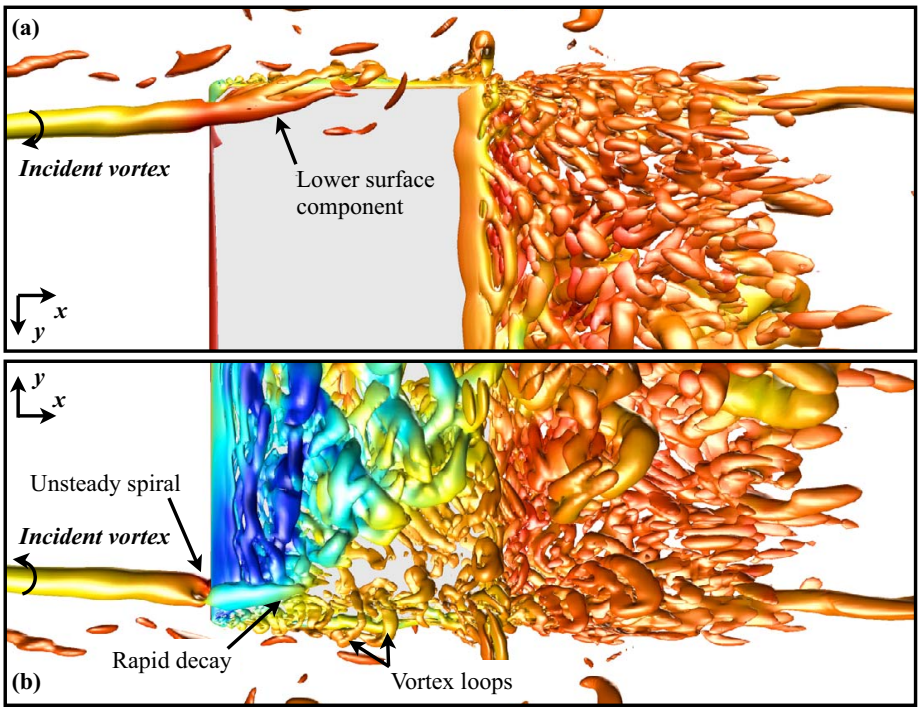

Figure 3.21: Instantaneous iso-surface of Q-criterion ($Q = 5$) for (a) bottom view and (b) top view for $\alpha = 8°, \Delta y/c = 0.30$.

3.6.3 Aerodynamic loads

The time-mean aerodynamic loads for this vortex-interaction are compared to a single wing and the $\alpha_L = 5°$ cases in Table 3.7 while the distribution of lift coefficient

per unit length are provided in Figure 3.22(a). As can be expected, the stronger upwash results in a higher lift coefficient and significantly improved lift-to-drag ratio. Figure 3.22(b) shows the distribution of lift along the wingspan for $\alpha_L = 8°$ collapses to that of the isolated wing over most of the span when rescaled by the local effective angle of attack. A second effect of the stronger axial vortex is a rolling moment that has nearly doubled the previous value. Although the magnitude of the rolling moment has increased for this interaction, the root-mean-square $C_{M_{x,\mathrm{RMS}}}$, of the time-history is still comparable to those observed for a single wing. As in the previous computations, fluctuations in the incident vortex core are more likely to dominate unsteady loading – in this case uncertainty in the vortex strength which could arise from aeroelastic pitching behavior in the vortex generator.

Table 3.7: Time-mean aerodynamic loads for $\Delta y/c = 0.30$.

	C_D		C_L		L/D		C_{M_x}	$C_{M_{x,\mathrm{RMS}}}$
	Value	% diff.	Value	% diff.	Value	% diff.		$(\times 10^{-3})$
Single wing	0.077	-	0.433	-	5.65	-	0.002	9.8
$\alpha_L = 5°$	0.083	+7.6%	0.507	+17.0%	6.14	+8.7%	-0.067	11.0
$\alpha_L = 8°$	0.085	+11.0%	0.548	+26.5%	6.44	+14.0%	-0.116	13.0

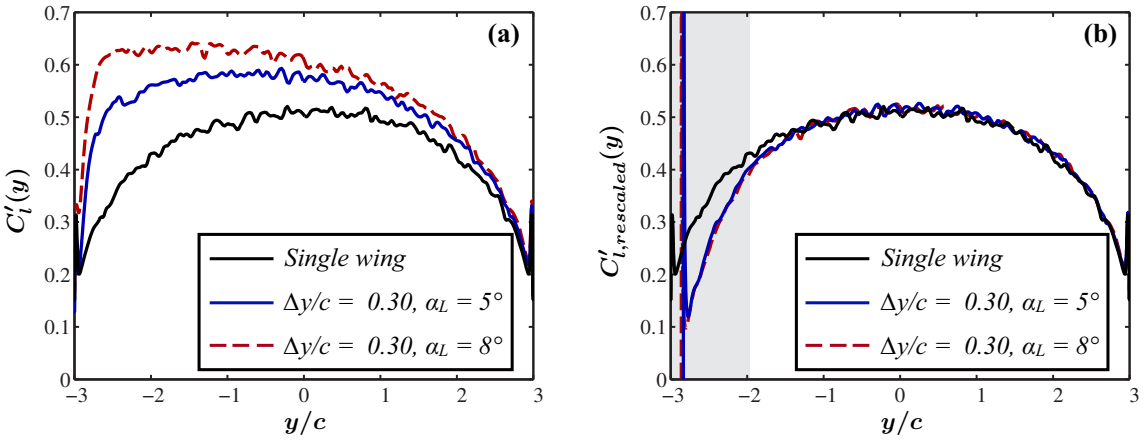

Figure 3.22: Time-mean lift per unit length (a) along the wingspan and (b) scaled by the local effective angle of attack.

3.7 Summary

This chapter examined the flow physics during interaction of finite-aspect-ratio wings operating in close proximity in order to develop a better fundamental understanding of streamwise-oriented vortex surface interactions. Two wings were placed with a streamwise separation of $\Delta x/c = 5$, follower-wing angle of attack of $\alpha_F = 5°$ and Reynolds number of $\mathrm{Re} = 30,000$. The streamwise vortex in this case was provided by a tip vortex emanating from the leader wing.

Investigation of the time-mean flow field revealed three distinct flow regimes occur within a relatively small range of lateral positions for the impinging vortex. Mutual induction between the incident and tip vortices was found to be influential in determining the trajectory of the incident vortex and evolution of the wake behind the follower wing. For example, when the incident vortex was positioned outboard, the self-induced velocity of the vortex dipole provided an upward trajectory of the vortex pair in the wake of the follower-wing. Conversely, mutual induction for a tip-aligned incident vortex redirected the pair of streamwise vortices downward in the follower-wing's wake. An inboard vortex experienced bifurcation in the time-mean flow with a dominant portion of vorticity passing over the suction-side. The upper-surface component of the vortex tended inboard due to interaction with its mirror-image in the wing surface and experienced rapid attenuation. This marked variation in flow structure with lateral position would have ramifications for surface loads and interaction with subsequent aerodynamic surfaces downstream.

Analysis of the instantaneous flow characterized several unsteady phenomena. The outboard positioned vortex, being adjacent to the counter-rotating follower wing tip vortex, demonstrated undulations reminiscent of long-wavelength mutual inductive instabilities common to trailing vortex pairs. This particular unsteady feature would have implications for wake dissipation or in the case of interaction with a third wing or aerodynamic surface. In the tip-aligned case, strong interaction between

the incident and tip vortices elicited highly unsteady behavior close to the wingtip. This marked flow disturbance enhanced surface pressure fluctuations beneath the tip vortex and provided a clear impact to the unsteady loads. The inboard positioned vortex demonstrated rapid dissipation of the impinging vortex on the suction side due to an accelerated transition to turbulence. The rapid decomposition of the vortical structure is likely due to a combination of interaction with transitional flow in the separated region and the susceptibility of streamwise vortices to suction-side adverse pressure gradients. A similar behavior is more clearly demonstrated in Chapter 6.

The higher leader wing angle of attack case provided a stronger vortex that more directly impinges with the follower-wing's leading-edge. This specific encounter supplied a more vibrant depiction of unsteady behaviors for an inboard positioned vortex. Namely, the direct impingement results in a spiraling instability upstream of the wing that permits the bifurcation observed in the time-mean flow. The behavior of this helical instability will be more thoroughly addressed later in Chapters 5 and 6.

Evaluation of aerodynamic forces revealed significant lift enhancement compared to a single wing distributed over most of the span and an induced rolling moment for every case. Much of this improved lift can be attributed to an inviscid increase in effective angle of attack due to the incident vortex upwash. Nonetheless, viscous effects were shown to be important in the vicinity of the vortex encounter. Here, interaction between the incident and tip vortices significantly altered the load distribution and influenced the time-mean rolling moment coefficient. While the fluctuations in the instantaneous loads were not very different from that of a single wing for the static cases presented, much larger variations in rolling moment and buffeting loads would be encountered if the vortex were to move through the various flow regimes that occur with changes to lateral positioning. Lateral change in vortex position is feasible in the applications of vortex meandering, long wavelength instabilities, atmospheric turbulence, or uncertainty in the vortex generator position due to maneuvering or

aeroelastic effects. These findings motivate future studies on transient streamwise vortex encounters.

Chapter 4

Vortex interaction with a flexible wing in close-proximity

While Chapter 3 identified a number of unsteady and time-mean phenomena associated with vortex/surface interaction on a rigid wing, this chapter serves as a first step into understanding of the aeroelastic implications for streamwise vortex interacting with a flexible wing. The impact of the presence of a streamwise vortex in close-formation on wing dynamics, deformations, flow structure, and aerodynamic loading is explored. The work depicted in this chapter is important for several reasons:

1. To the best of the author's knowledge, this work provides the first three-dimensional unsteady, viscous, aeroelastic computations of flexible wings operating in tandem.

2. Both static and dynamic aspects of aeroelasticity are shown to influence the flow structure and aerodynamic loading.

3. Demonstrates how flexibility in light-weight, large aspect ratio wings might have implications in structural longevity.

4. Analysis provides motivation for a more systematic and detailed study of aeroelastic effects.

4.1 Problem setup

The tandem wing configuration utilized in this chapter is identical to that described in Section 3.1. The choice of geometric parameters is narrowed in this case to the single leader wing angle of attack of $\alpha_L = 5°$, longitudinal spacing of $\Delta x/c = 5$, lateral position of $\Delta y/c = 0.30$, and vertical offset of $\Delta z/c = 0$ shown in Figure 4.1. The previous choice of Reynolds number of $\mathrm{Re} = 30,000$ and follower wing angle of attack of $\alpha_F = 5°$ are continued in this section. As before, the leader and follower wings are chosen as rectangular flat plate wings, with an aspect-ratio of $\mathcal{R} = 6$, and uniform thickness of $t/c = 0.03$.

Rather than vary the properties of the incident vortex or its position, the parametric exploration in this chapter sheds light on the impact of structural rigidity. In addition to the rigid follower, two flexible structures were used for comparison with Young's moduli of $E = 69$ GPa and 34.5 GPa for the *moderately flexible* and *highly flexible* plates respectively. A reference chord length of $c = 0.1$ m, plate thickness of $t_s = 0.01c$, material density of $\rho_s = 2700$ kg/m^3, and and Poisson's ratio of $\nu = 0.30$ were chosen for both plates. As a point of reference, the moderately flexible wing is representative of a thin aluminum plate. The dynamic pressure was set as $1/2\rho_f U_\infty^2 = 58.5$ which corresponds to water tunnel conditions. This set of parameters was chosen in order to induce clearer buffeting loads, supply a structural time scale tractable for LES computations, and provide an experimentally reproducible configuration.

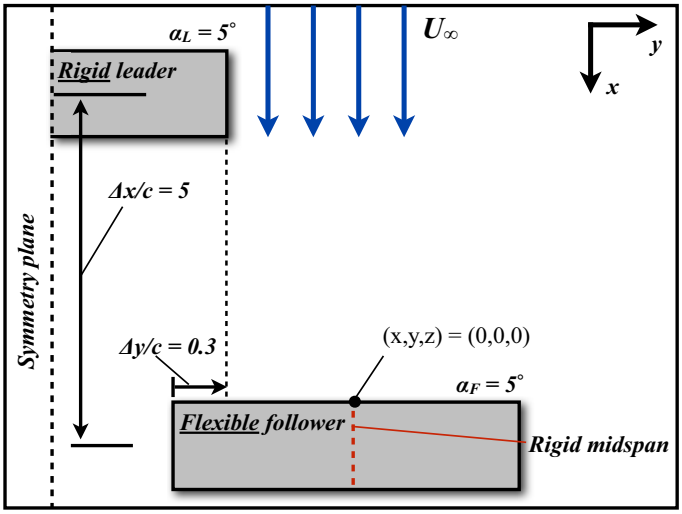

Figure 4.1: Problem setup with a flexible follower wing.

Table 4.1: Structure properties

	Rigid	Moderately Flexible	Highly Flexible
t_s/c	N/A	0.01	0.01
ρ_s (kg/m^3)	N/A	2700	2700
E (GPa)	∞	69	34.5
ν	N/A	0.30	0.30

Figure 4.2 provides additional notation useful for the following discussion. Namely, the wingtip closest to the vortex impingement, located at $y/c = -3$, is referred to as the *vortex encounter-side* and denoted by the subscript v while the wingtip furthest from the vortex encounter, located at $y/c = 3$, is described as the *outboard-side* and denoted by the subscript o. Wing twist, θ, is measured at both of these locations where a positive value is consistent with a positive measure of angle of attack.

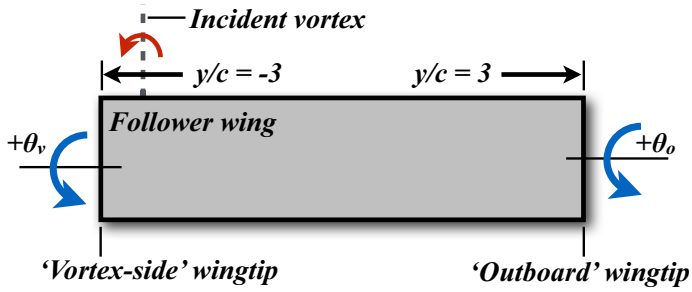

Figure 4.2: Additional notation for the flexible follower wing configuration.

4.2 Numerical considerations

The fluid-dynamics portion of the simulations are conducted using a spatial discretization and boundary conditions identical to those described in Section 3.2. In addition to the fluid-dynamics mesh, coupled aeroelastic solutions require a structural component. A two-dimensional finite element mesh, shown in Figure 4.3, is placed in the mid-plane of the wing structure as demonstrated in Figure 4.4 where all elements are uniformly spaced. Details regarding structural element resolution and the specific mesh chosen for all following computations are provided in Section 4.3. Forces and deformations are interchanged between fluid and structure meshes as described in Section 2.3. Boundary conditions on the finite element mesh consist of constraining all degrees of freedom on element nodes along the wing midspan. All remaining finite element nodes are unconstrained. This approach models fixed-free wings mounted to an aircraft body in steady flight.

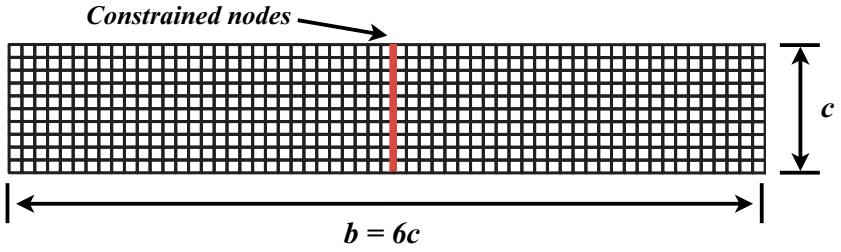

Figure 4.3: Structural element grid.

Figure 4.4(b) shows the fluid dynamics mesh has been rotated about the follower wing mid-chord by α_F. This coordinate rotation of the fluid dynamics mesh aligns the wing with the reference coordinate system (x_s, y_s, z_s) of the structural solver. Nominal modifications to the fluid dynamics solution procedure are required for this adjustment. Namely, the new approach requires an angle of attack to be prescribed at the far field rather than simply orienting the wing relative to the inflow boundary as was done in Chapter 3. In practice, the two approaches are seamless. The following

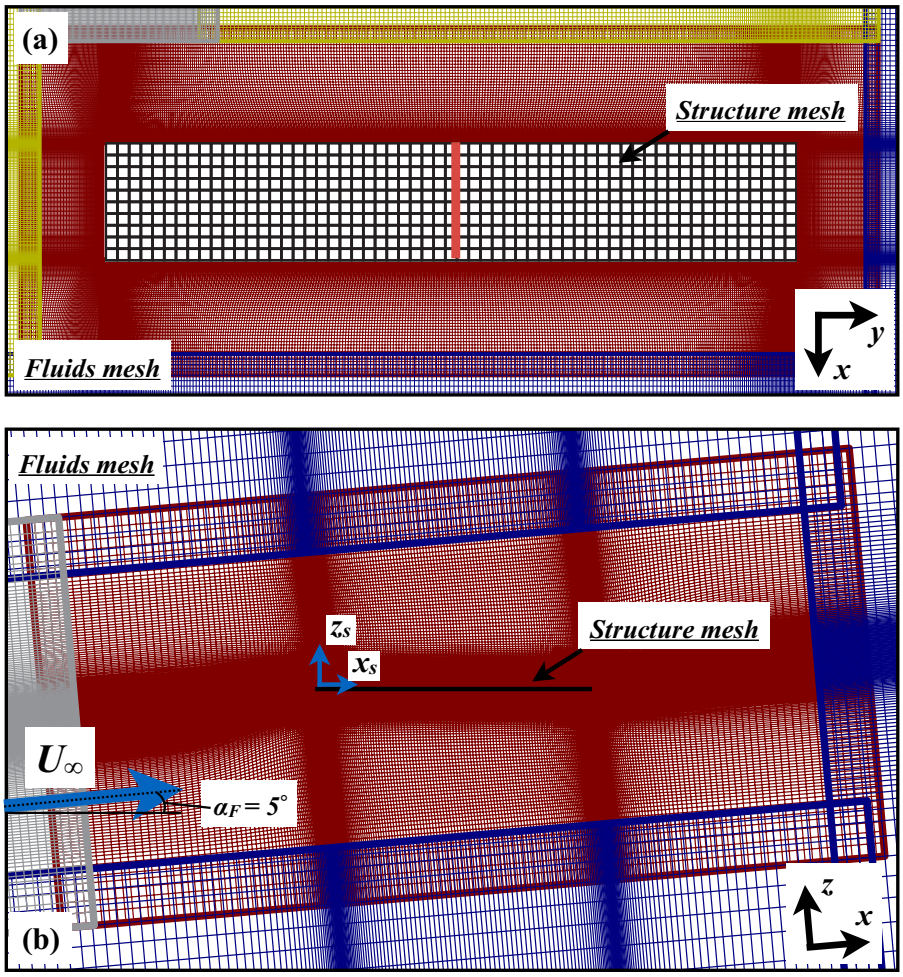

Figure 4.4: Coupled fluid/structure grids; (a) top view and (b) side view.

discussion will continue describing the problem in terms of the original coordinates of the fluid mesh (x, y, z) for consistency and clarity.

Each of the fluid-structure interaction cases are initialized from the previously completed rigid solution provided in Chapter 3. Aeroelastic solutions are allowed to run an additional $\tau = 10$ in order for the fluid and structure behaviors to return to a time-asymptotic state. The collection of statistical data was then conducted over a final run of $\tau = 10$.

4.3 Effect of grid resolution

The suitability of grid resolution for the fluid dynamics solutions was demonstrated in Section 3.3. The preceding evaluation of computational accuracy holds for the simulations in the present chapter. Therefore, a full grid resolution study for the fluid dynamics mesh is not repeated in the current section. Rather, the following discussion examines the resolution of the structural model independently.

Evaluation of the suitability for the finite element mesh is two-fold. First, static deformations are compared between the three structural mesh sizes provided in Table 4.2. Each discretization is subjected to forces extracted from the time-mean loads provided by the rigid solution for an inboard vortex position ($\Delta y/c = 0.30$). This is accomplished by interpolating the surface forces to the structural model in the same manner as the full aeroelastic computations. Deformations are then obtained by running an independent static solution with the prescribed loading using the parameters for the *highly flexible* wing. The representative loading and resulting deformations are shown in Figure 4.5. This approach provides for a comparison for the effects of resolution on deformations representative of the time-mean deflections experienced in the full aeroelastic simulations.

Table 4.2: Structural mesh dimensions.

Grid	Dimensions	Grid size
Coarse	10×60	600
Mid	14×86	1204
Fine	20×120	2400

Vertical deflections for the statically loaded wings are recorded for both the inboard and outboard wingtips at the mid-chord nodes in Table 4.3. Here, d_z describes the mid-plane deflections normal to the free stream direction (z-direction) rather than normal to the wing surface (z_s-direction), as in: $d_z = \hat{w}\cos(-\alpha_F) + \hat{u}\sin(-\alpha_F)$. The mid-chord deflection on the outboard wingtip, $d_{z,o}$, represents the deflection at the

point on the wing furthest from the impinging vortex while the inboard wingtip deflection, $d_{z,v}$, represents the vertical deflection on the wingtip closest to the incident vortex. Both wingtips exhibit converging deflections where differences between subsequent refinement is on the order of 0.01% on both sides. As should be expected, deflections converge in an increasing manner with successive refinement, as observed in Table 4.3. That is, coarser discretizations are effectively more constrained and therefore stiffer than more refined grids[127].

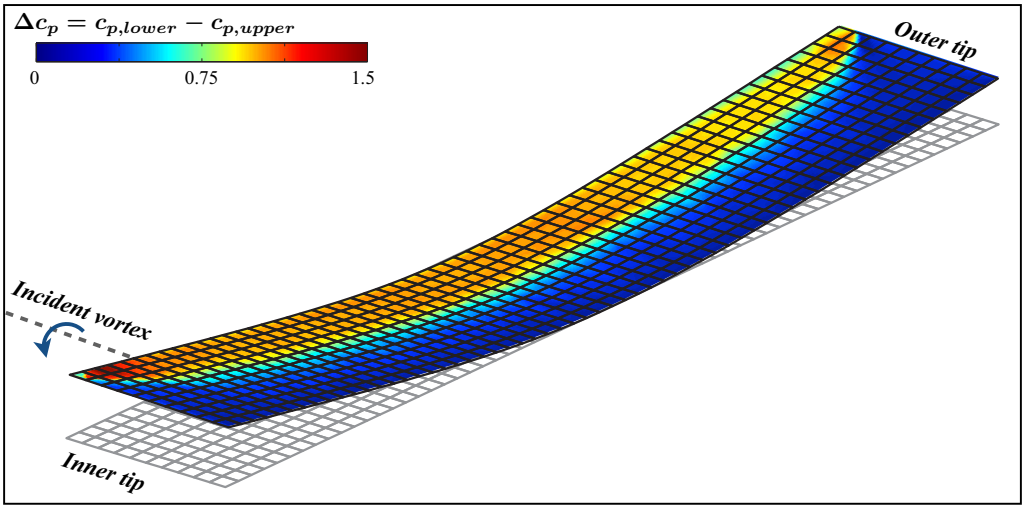

Figure 4.5: Surface pressure difference contours on the deformed *coarse* structural mesh. Deformations are exaggerated for improved visualization.

The grid work, W_{grid}, is used as a second parameter to provide a more discriminating comparison of the three element meshes. This quantity is defined here as the summation of the nodal deflections, $\hat{\mathbf{u}}_m$, dotted with the nodal loads, $\mathbf{R}$

$$W_{\text{grid}} = \sum_{i=1}^{N_s} (\hat{\mathbf{u}}_m \cdot \mathbf{R})_i$$

where N_s is the total number of nodes for each structural mesh. This summation provides an integrated value for evaluation of the entire structural model. As before, refinement between successive grids differs on the order of 0.01%. Therefore, the *coarse* structural mesh is suitable to accurately model static or time-mean wing de-

flections in full aeroelastic computations. Coarser grids were not considered in order to provide a sufficiently smooth deformation of the flat plate wing.

Table 4.3: Wing tip deflections and grid work for statically loaded plates

Grid	$d_{z,o}/c$	$d_{z,v}/c$	W_{grid} (N · m)
Coarse	7.784×10^{-2}	9.791×10^{-2}	5.870×10^{-3}
Mid	7.787×10^{-2}	9.793×10^{-2}	5.872×10^{-3}
Fine	7.789×10^{-2}	9.794×10^{-2}	5.873×10^{-3}

The second portion of the analysis evaluates the structural mesh dynamics by subjecting the plate to an initial vertical acceleration as shown in Figure 4.6(a). This stand-alone dynamic solution was conducted using the same time step as used in the aeroelastic analysis in order to elicit and compare the first bending and twisting modes of deformation. The frequency spectra of bending and twisting deformations at the wingtip, shown in Figure 4.6(b) and (c) respectively, demonstrate that identical frequencies are predicted by all three levels or resolution. Therefore, the *coarse* structure grid was deemed sufficient to also model the dynamic component of the aeroelastic simulations. It should be noted that frequencies depicted for this isolated case are not likely to be representative of those experienced in a coupled fluid-structure interaction in which the wing experiences viscous damping due external loading.

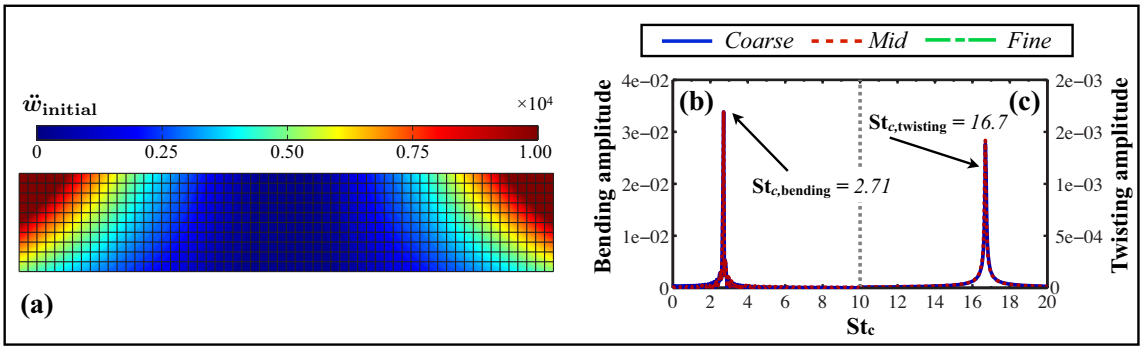

Figure 4.6: (a) Initial acceleration, $\ddot{w}_{\text{initial}}$, for dynamic analysis and Fourier analysis of (b) bending and (c) twisting deformations at the wingtip mid-chord

4.4 Effect of flexibility

4.4.1 Compliant wing deformations

This section introduces the results obtained from the coupled fluid-structure interaction simulations by describing the static and dynamic response of the flexible plate. Time-mean vertical deflection and twist at both wingtips are recorded in Table 4.4. The vortex-side wingtip exhibits a larger time-mean deflection, $\overline{d}_{z,v}$, than the outboard wingtip, $\overline{d}_{z,o}$. Similarly, the time mean wingtip twist, $\overline{\theta}$, is higher on the vortex-side of the wing. This positive twisting rotation amounts to a slight increase in the effective angle of attack. A bias in deformations on the vortex-encounter side of the wing is consistent with the asymmetric lift distribution shown for rigid wings in Section 3.4.3.

The nature of spanwise bending for both the compliant wings can be well-described as primarily a static-aeroelastic effect. This would implicate an effective change in vertical positioning of the streamwise vortex with respect to the wing surface which will be discussed in more detail in the next section. Wing twisting is much more dynamic although the response is small in amplitude. Fourier analysis of the wingtip twists, depicted in Figure 4.7, shows a dominant frequency of $\mathrm{St}_c = 4.8$ for both the inboard and outboard sides of the moderately flexible wing. Interestingly, this oscillation is weaker on the vortex encounter-side. The primary unsteady phenomenon responsible for this behavior is revealed through analysis of the instantaneous flow in Section 4.4.3 and provides a magnified effect on pitching moment oscillations in Section 4.4.4. The highly flexible wing elicits a dominant twisting frequency higher in amplitude, but at a much lower frequency of $\mathrm{St}_c = 0.5$. Although this specific component of the wing dynamics appears at both wingtips, it is much more pronounced on the vortex-encounter side.

Table 4.4: Time-mean flexible wingtip midchord deflections and twist

Wing structure	$\overline{d}_{z,v}/c$	$\overline{d}_{z,o}/c$	$\overline{\theta}_v$	$\overline{\theta}_o$
Moderately flexible	0.050	0.039	0.17°	0.15°
Highly flexible	0.103	0.082	0.33°	0.29°

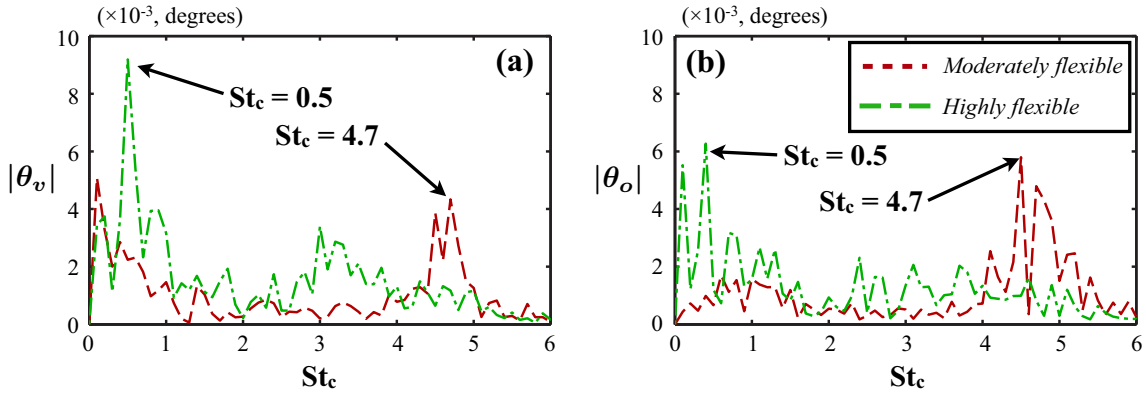

Figure 4.7: Fourier analysis of twisting deformations at the (a) vortex-side and (b) outboard wingtips

4.4.2 Time-mean flow structure

This section describes the impact of flexibility on the time-mean flow structure. Looking now at the time-mean flow field, the effect of aeroelastic deformations becomes more clear. A general overview of the flow topology using an iso-surface of time-averaged Q-criterion is provided in Figure 4.8. Compared to the rigid $\Delta y/c = 0.30$ case provided in Figure 4.8(a) for reference, the upper-surface component of the incident vortex for the moderately flexible wing, shown in Figure 4.8(b), rapidly attenuates. This behavior is much like that of the stronger vortex provided by the $\alpha_L = 8°$ leader-wing. The upper-surface component disappears altogether for the highly flexible wing in Figure 4.8(c) where the incident vortex passes mostly along the pressure-side and then wraps about the wingtip as it approaches the trailing-edge.

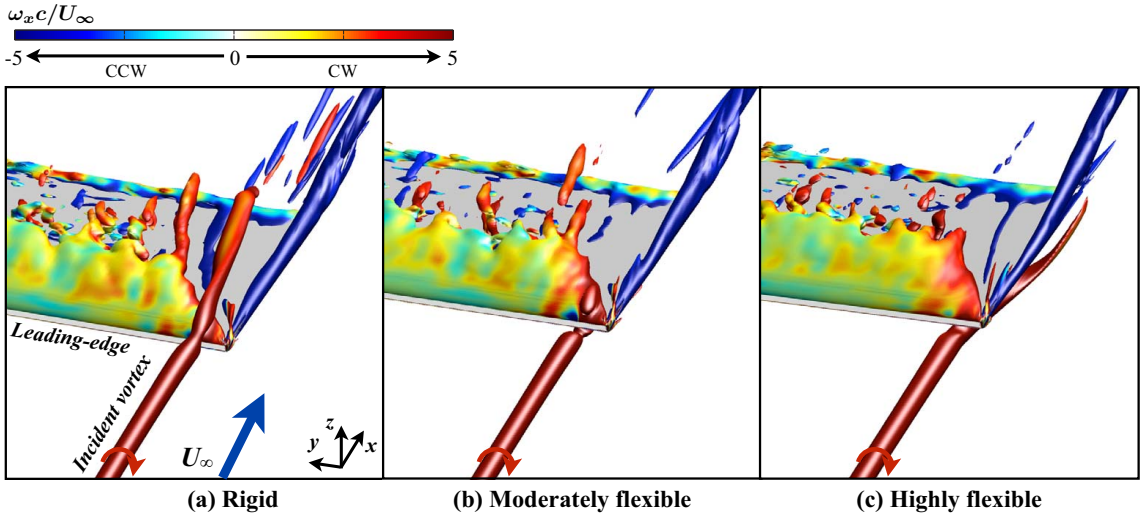

Figure 4.8: Iso-surface of time-mean Q-criterion ($Q = 2$) colored by streamwise vorticity shows the time-mean flow structure for rigid and flexible wings.

The dominant modification to the time-averaged flow field for the flexible wings can be primarily attributed to the static aeroelastic spanwise bending. This is more clearly depicted by cross-sections of time-averaged streamwise vorticity at several streamwise locations in Figure 4.9. Compared to the rigid case in Figure 4.9(a), the $\overline{d}_{z,v}/c = 0.05$ time-mean deflection of the moderately flexible wing's vortex-side tip repositions the surface in such a manner that the incident vortex, labeled as (1), is in a more direct collision with the leading-edge. The bifurcation of this direct impingement is reminiscent to that of the $\alpha_L = 8°$ leader-wing case previously shown in Figure 3.19. As in the rigid cases, the upper surface portion travels inboard while the lower surface component moves toward and then over the wingtip, $x/c = 0.50$, wrapping around the tip vortex, marked by (2), and then quickly dissipates. The suction-side component attenuates rapidly in a manner similar to the $\alpha_L = 8°$ rigid case in Section 3.6.

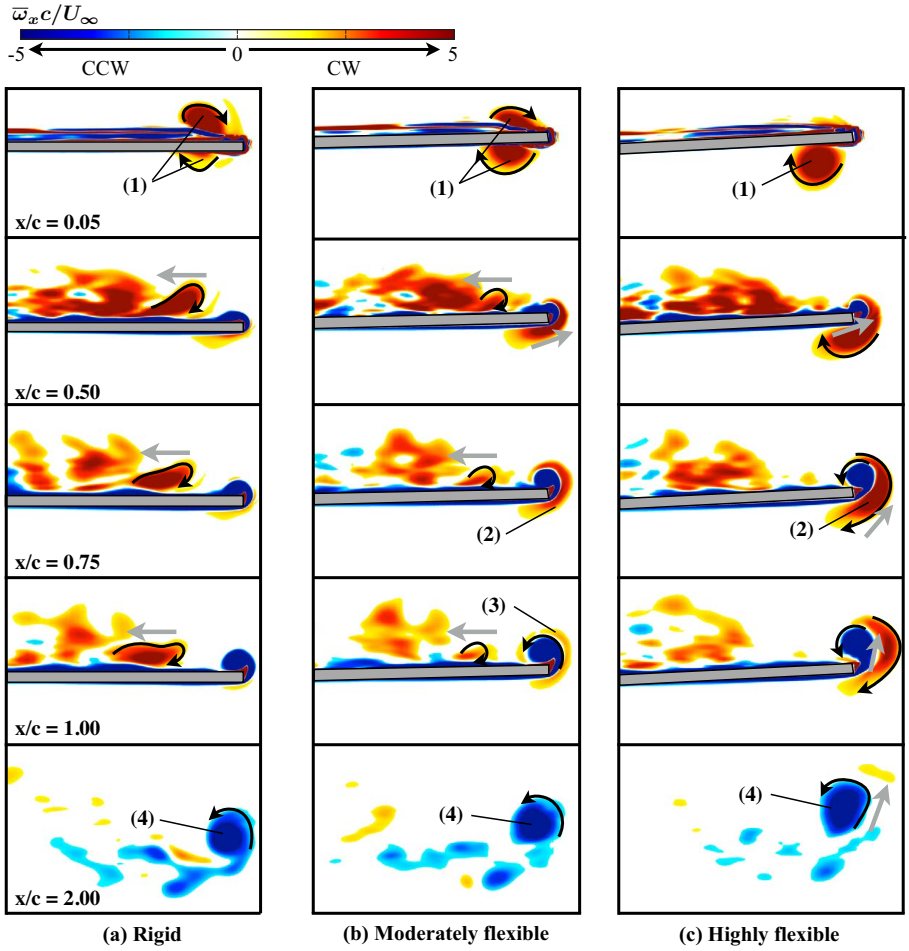

Figure 4.9: Contours of time-mean streamwise vorticity at several streamwise locations for the rigid and flexible wings.

The larger deflection of the highly flexible wingtip, ($\overline{d}_{z,v}/c = 0.103$), repositions the aerodynamic surface with respect to the incident vortex, as shown in Figure 4.9(c), in such a manner that it produces an entirely new regime in which the incident vortex, labeled by (1), appears to travel exclusively along the pressure surface. The stronger vorticity of the single coherent structure produces a greater influence on the tip vortex development, noted as (2). Consequently, the tip vortex is directed outboard, $x/c = 0.75$, and upward, $x/c = 1.00$ away from the wing. A change in vertical positioning provided by static aeroelastic deformation results in yet another form in the follower wing's wake evolution, annotated by (4), which moves the follower wing tip vortex upward and outboard compared to that of the single wing and rigid

wing cases. This is in contrast to the downward induction of the $\Delta y/c = 0.15$ case and upward/inboard wake induction of the $\Delta y/c = 0$ and $\Delta y/c = -0.15$ cases investigated previously in Chapter 3.

Contours of time-mean streamwise vorticity on the suction-side surface near vortex impingement in Figure 4.10 provide further insight into the general flow structure associated with each case. Regions of negative vorticity, traced by dashed white lines, indicate the imprint of the suction-side vortex component in each case. Compared to the rigid wing, the imprint on the moderately flexible wing is much weaker and disappears before reaching the trailing-edge. A trace of negative vorticity on the highly flexible wing indicates the presence of a very weak upper-surface component to the incident vortex not clearly portrayed in the time-mean iso-surface of Q-criterion in Figure 4.8(c) or streamwise vorticity in Figure 3.19(c). On the lower surface of the wing, shown in Figure 4.11, the pressure-side component of the incident vortex can be seen to rapidly increase in strength with increasing flexibility.

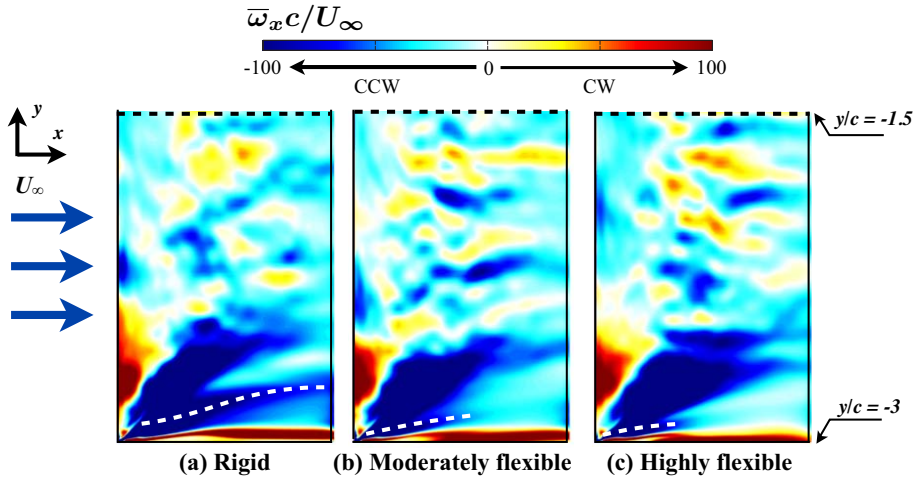

Figure 4.10: Contours of time-mean streamwise vorticity on the suction-side surface near vortex impingement for rigid and flexible wings.

As the lower-surface component of the incident vortex increases in strength with flexibility, so too does its impact on the pressure-side. This influence is demonstrated using time-averaged pressure coefficient contours and limiting surface streamlines for

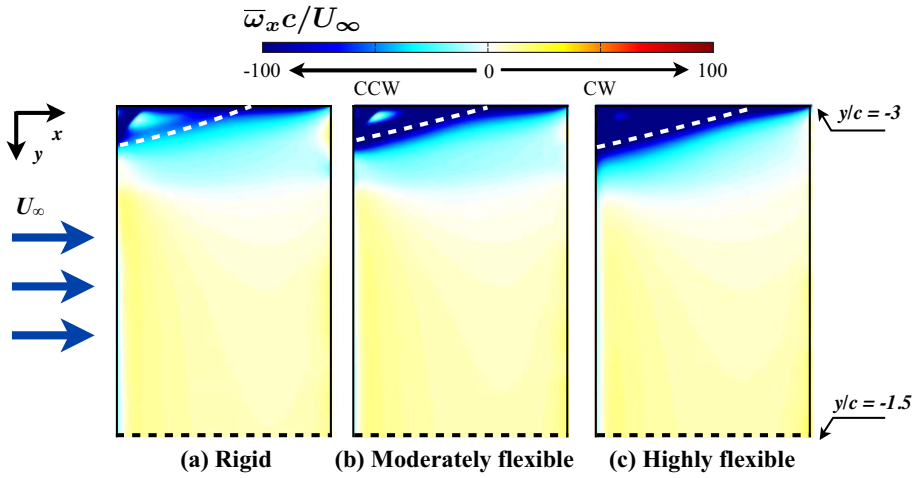

Figure 4.11: Contours of time-mean streamwise vorticity on the pressure-side surface near vortex impingement for rigid and flexible wings.

the lower-surface in Figure 4.12. An increase in the lower-surface vortex strength with flexibility corresponds with a growing low pressure region near the wing tip. Suction due to the vortex passing along the pressure-side of the wing would tend to reduce the lift-enhancement but also diminish the negative induced roll moment provided by vortex impingment. The limiting surface streamlines also exhibit a more outboard trajectory as the lower surface component strengthens with increasing flexibility, consistent with the self-induced velocity of a vortex with its mirror image in the wing surface.

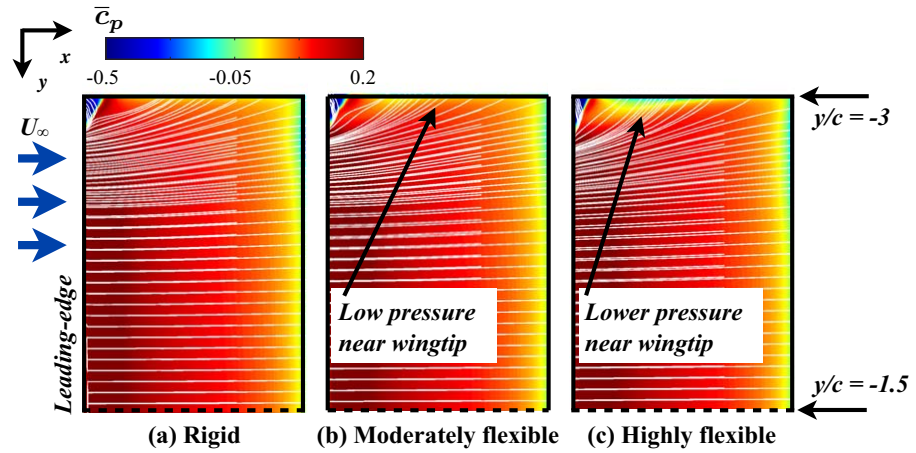

Figure 4.12: Time-mean pressure coefficient contours and limiting surface streamlines on the pressure-side surface near vortex impingement for rigid and flexible wings.

Figure 4.13 shows a side view of a cross-section of time-mean streamwise pressure-gradient intersecting the incident vortex as it approaches the follower wing. Figure 4.13(a) shows an adverse pressure gradient at the leading-edge of the wing associated with flow stagnation against the aerodynamic surface and a favorable pressure gradient above the wing associated with acceleration over the leading-edge. The predominant suction-side component of the rigid case would tend to benefit from the favorable pressure gradient as it initially travels over the leading-edge.

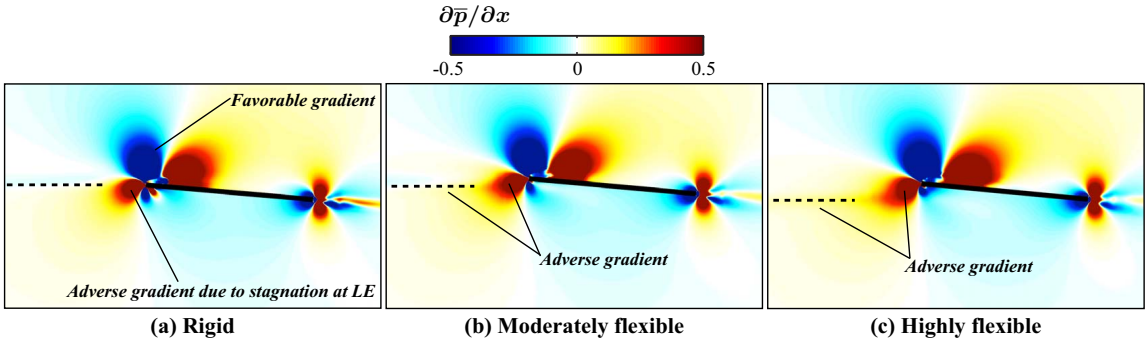

Figure 4.13: Contours of time-mean streamwise pressure gradient at $y/c = -2.85$ for (a) rigid, (b) moderately flexible, and (c) highly flexible wings.

The small vertical offset provided by time-mean bending of the moderately flexible wing shifts the vertical position of the vortex downward relative to the leading-edge. This places the vortex more in line with the adverse gradient provided by flow stagnation with the leading-edge. The adverse gradient provides a small degree of influence upstream of the wing where positive $\partial\overline{p}/\partial x$ appears to encroach further upstream as shown in Figure 4.13(b). The same effect is shown more clearly for the highly flexible wing in Figure 4.13(c) where the larger time-mean bending shifts the vortex further beneath the wing. The adverse gradient permeates even further upstream in the trailing vortex in this case indicating the highly flexible wing provides a stronger upstream influence. It is interesting to note that the upstream influence is greatest for this case even though the core flow of the incident vortex does not directly impinge against the leading-edge as it did for the moderately flexible wing.

The pressure regimes experienced by the incident vortex are notable due to their significance on the breakdown of axial vortices in wind tunnel experiments, see for instance the seminal work by Sarpkaya[139]. Although no specific adverse effect is identified for the present configuration, this particular trend, if sustained under harsher conditions such as a higher angle of attack or a less stable incident vortex, could induce more severe unsteady phenomena, such as vortex bursting. The favorable pressure gradient above the wing, as seen in Figure 4.13(a), may provide for a beneficial placement in terms of the stability of the incident vortex while a negative vertical offset might be avoided in the context of formation flight. Static aeroelastic deformations of high aspect ratio wings could shift the impinging flow into an unintended regime thereby generating undesirable fluctuations in the incident flow. This is directly shown to be the case in Chapter 5. The ramifications of pressure gradients provided by vortex positioning are a primary topic of Chapter 6 and shown to generate a highly unsteady feedback response in an isolated incident vortex.

4.4.3 Unsteady flow structure

Although deformations are predominantly of a static nature, several unsteady behaviors influence the general flow field. This section provides more detail of the instantaneous flow behavior in conjunction with the aeroelastic response. A snapshot of the instantaneous Q-criterion iso-surfaces is provided in Figure 4.14 where iso-surfaces are colored by the pressure coefficient. Looking at the top view of the moderately flexible wing, shown in Figure 4.14(a), the upper-surface component of the split incident vortex is visible. It benefits from the favorable pressure gradient above the leading-edge, shown in Figure 4.13(b), before rapidly attenuating as it enters the adverse pressure gradient just downstream of the leading-edge. Meanwhile, the lower-surface component, visible in Figure 4.14(b), tends outboard, consistent with image-effects with the surface and wraps around the wingtip.

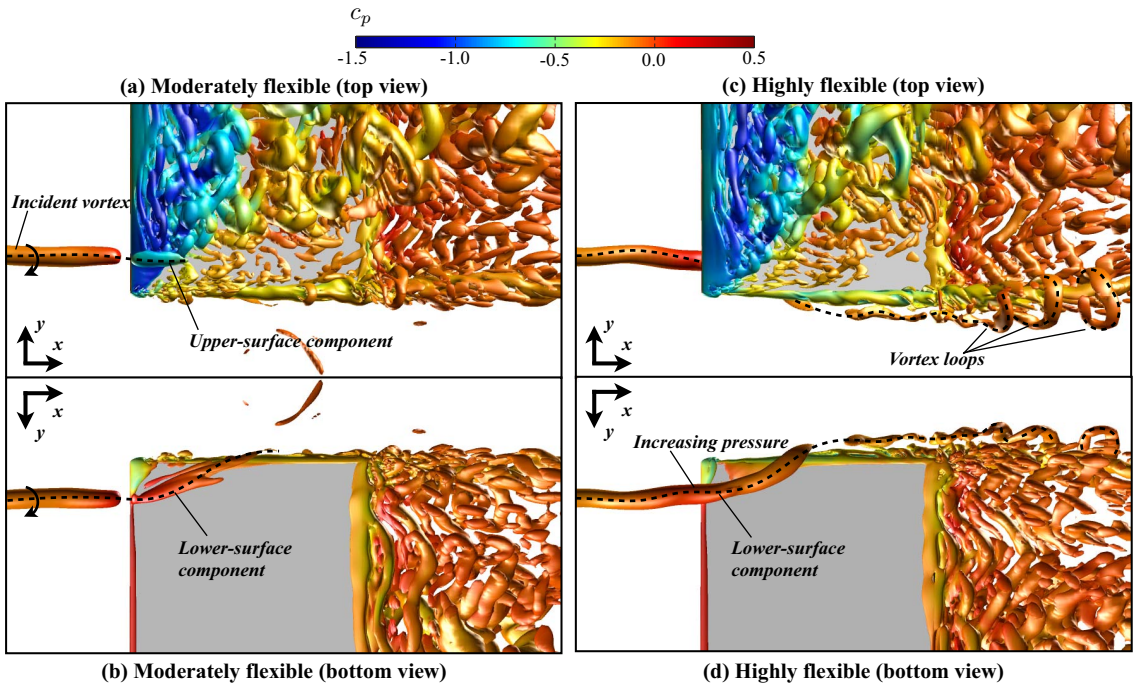

Figure 4.14: Instantaneous iso-surface of Q-criterion ($Q = 5$) for (a) top and (b) bottom views of the moderately flexible wing shown on the left-hand side while (c) top and (d) bottom views of the highly flexible wing are shown on the right-hand side. Iso-surfaces are colored by pressure coefficient.

As stated previously, the highly flexible wing provides a larger bending deformation which places the incident vortex primarily beneath the wing, shown in Figure 4.14(d). The vortex then travels outboard and around the wingtip as it advances downstream quickly decomposing into smaller-scale structures in the process. The result of these transitional features is more clearly portrayed in the top-side view of the highly flexible wing in Figure 4.14(c) where they are shown to periodically wrap about the follower-wing tip vortex enveloping it in a sequence of vortex loops downstream of the trailing-edge.

Now, taking a closer look at the moderately flexible wing, dynamic aeroelastic effects become more apparent. Figure 4.15(a) shows the instantaneous surface pressure coefficient on the lower surface. A ripple pattern in c_p, marked by (1), appears on the outboard tip side of the wing and is unique to the moderately flexible case. A span-

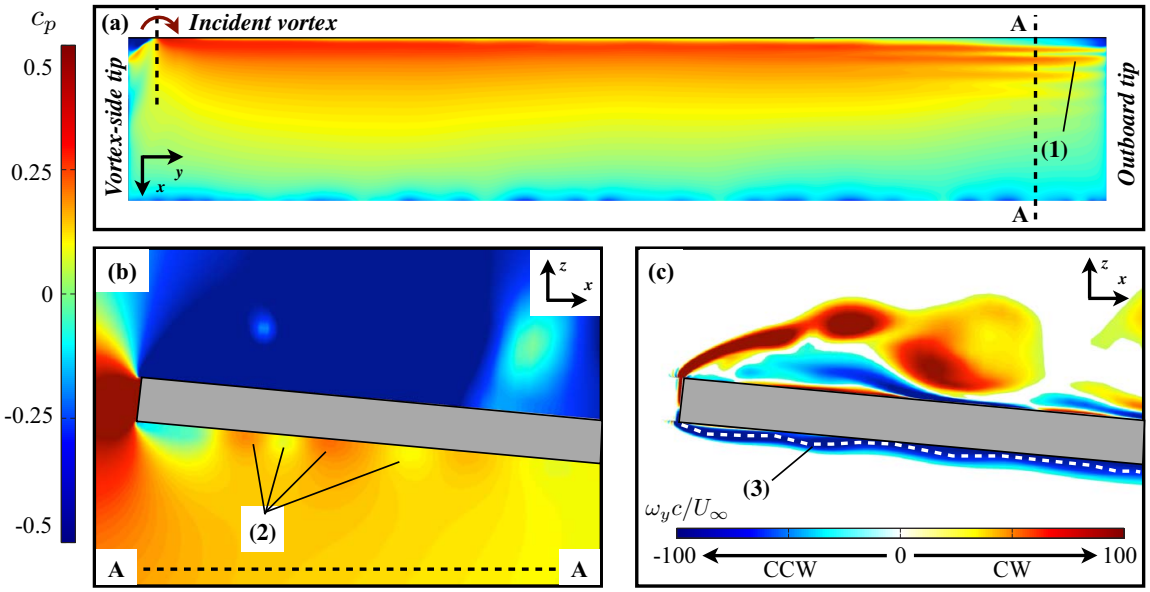

Figure 4.15: Contours of instantaneous pressure coefficient for the moderately flexible wing on the (a) lower surface and (b) cross-section marked by A-A. Frame (c) shows contours of instantaneous spanwise vorticity across the cross-section marked by A-A for the moderately flexible wing

wise slice of c_p is provided in Figure 4.15(b) taken at the cross-section marked by A-A in Figure 4.15(a). Here, the ripple pattern, again labeled by (2), takes on the form of alternating packets of positive and negative c_p. A similar spanwise slice is provided for instantaneous spanwise vorticity, $\omega_y c/U_\infty$, in Figure 4.15(c) where instability in the pressure-side shear layer, marked by (3), coincides with the pressure fluctuations. The coupling between this instability and twisting mode deformations results in fluctuating pressure near the leading-edge and an amplified twisting behavior, shown in Figure 4.7, producing limit-cycle-oscillations. Interestingly, this instability is not observed on the vortex encounter side of the wing where the higher effective angle of attack appears to stabilize the lower surface shear layer and suppress pitching oscillations.

Figure 4.16 shows the mean-squared suction-side surface pressure fluctuations for the single, rigid, and both flexible wings and provides for a comparison of the amplitude of unsteady loads on the wing surface. The distribution of $\overline{p'p'}$ takes on the

same general form for all three vortex-encounter cases in that elevated surface pressure fluctuations appear further downstream than the single wing and are distributed over a larger surface area. This behavior is consistent with enhanced vortex-induced separation for the rigid and flexible wings as the highest pressure fluctuations typically occur near the line of reattachment. One difference is readily apparent for the highly flexible case in that the level of $\overline{p'p'}$ is much lower than all other cases. This decrease in surface pressure fluctuations, located on the most outboard portion of the highly flexible plate, culminates in a large decrease of rolling moment fluctuations as will become apparent in Section 4.4.4.

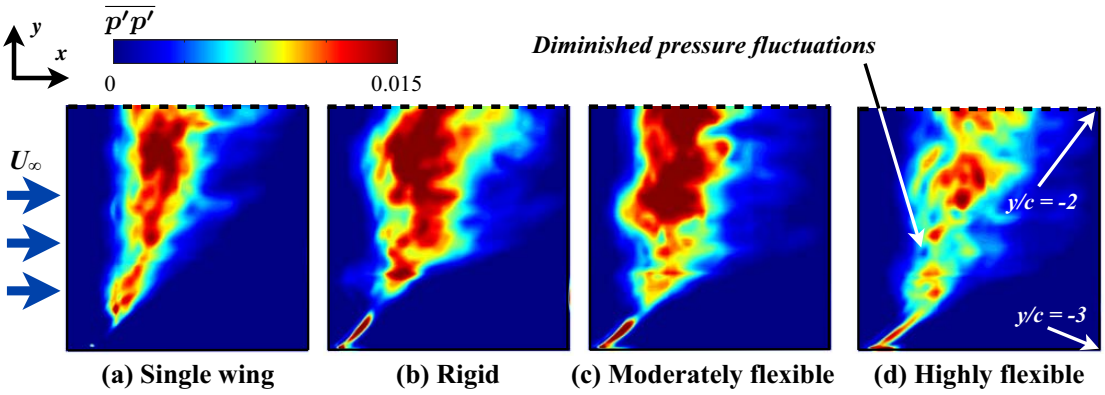

Figure 4.16: Contours of pressure fluctuations on a portion of the upper surface

4.4.4 Aerodynamic loads

The time-mean aerodynamic loads for the flexible wings are provided in Table 4.5 alongside the single-wing and rigid cases for comparison. Both flexible plates experience a small decline in $\overline{L/D}$. This drop can be largely attributed to several effects. First, an increase in the effective angle of attack due to the time-mean wing twist can be expected to increase both lift and drag. Second, the upward deflection of the wingtips reorients the normal forces on the suction surface slightly inboard producing a small side force component and attenuation of lift. Third, the vertical

Table 4.5: Time-mean aerodynamic loads for rigid and flexible wings.

	C_D		C_L		L/D		C_{M_x}	$C_{M_{x,\mathrm{RMS}}}$
	Value	% diff.	Value	% diff.	Value	% diff.		($\times 10^{-3}$)
Single wing	0.077	-	0.43	-	5.64	-	0.002	9.82
Rigid	0.083	+7.6%	0.51	+17.0%	6.14	+8.7%	-0.067	10.10
Moderately flexible	0.083	+8.1%	0.50	+15.7%	6.05	+7.1%	-0.074	8.51
Highly flexible	0.085	+10.4%	0.51	+18.6%	6.07	+7.4%	-0.070	5.62

offset of the incident vortex provided by the time-mean spanwise bending can be expected to have some influence on the wing behavior.

The time-averaged rolling moment coefficient, $\overline{C}_{M_x}$, is shown for both the moderately and highly flexible wings and compared to the rigid computation. A small increase in effective angle of attack provided by wing twisting, which is higher on the vortex encounter side of both cases, contributes a greater imbalance in spanwise loading thereby further reducing $\overline{C}_{M_x}$ for both of the compliant wings compared to the rigid case. This behavior contributes to a 10% increase in the magnitude of the rolling moment coefficient for the moderately flexible wing. While the difference in wingtip twisting is greater for the highly flexible wing, the rolling moment coefficient experiences a smaller, 5% increase in magnitude compared to the rigid case. Two factors are identified that contribute to the less severe rolling moment of the highly flexible plate. First, the larger spanwise camber on the vortex encounter-side of the wing provides a more significant loss of the lift component than experienced by the moderately flexible wing. Second, suction provided by the vortex as it passes beneath the wing close to the tip, shown in Figure 4.12(c), partially counteracts the negative induced $\overline{C}_{M,x}$. This effect is more clearly demonstrated using a stronger vortex later in Chapter 6 where negative vertical positioning ($\Delta z/c = -0.25$) of an isolated streamwise vortex is shown to drive $\overline{C}_{M,x}$ much closer that of an isolated wing.

Instantaneous lift, roll, and pitching moment coefficients along with corresponding Fourier analysis is provided in Figure 4.17. Beginning with the C_L time-history in

Figure 4.17(a), both flexible cases appear to reduce fluctuations in the instantaneous lift coefficient compared to the rigid wing. This effect is more clearly elucidated in the Fourier analysis of C_L, Figure 4.17(b), where the moderately flexible wing exhibits a single clearly defined peak near $\mathrm{St}_c = 0.5$ and the highly flexible wing portrays no dominant frequencies.

A more significant decrease in fluctuations occurs for the rolling moment coefficient. The time history of C_{M_x}, provided in Figure 4.17(c), demonstrates that higher frequency content has been largely removed from the moderate and highly flexible wings and the frequency spectra of $C_{M,x}$ in Figure 4.17(e) shows the highly flexible wing produces much lower amplitudes. The highly flexible structure exhibits root-mean-square of the rolling moment, $C_{M_{x,\mathrm{RMS}}}$, in Table 4.5 that is roughly half that of the rigid case. This behavior directly corresponds with the diminished suction-side pressure fluctuations observed in Figure 4.16(c). The particular cause of this attenuated response is not clear in the present computations, but may be related to small pitching oscillations shown in Figure 4.7. The ability of the flexible wings to reduce fluctuations in the rolling moment coefficients during a vortex encounter would have implications in prolonging the fatigue life cycle of aerodynamic surfaces.

The time-history of the pitching moment, C_{M_y}, is particularly interesting where strong, persistent, higher frequency oscillations in the rolling moment portray a dominant trend for the moderately flexible wing. While the Fourier analysis for the rigid and highly flexible cases are comparable, a strongly dominant frequency appears at $\mathrm{St}_c = 4.8$ for the moderately flexible wing directly matching the clearly defined oscillations in wing twisting, shown in Figure 4.7. This effect is a consequence of the coupling between instability in the lower surface shear-layer with the twisting mode reminiscent of limit-cycle-oscillations on the outer wingtip previously shown in Figure 4.15. The disappearance of this phenomena at the higher flexibility can be attributed to several factors. A higher flexibility leads toward a decoupling of the structure with

shear-layer instabilities. Strain hardening provided by large deformations can also attribute to the shift in structural behavior.

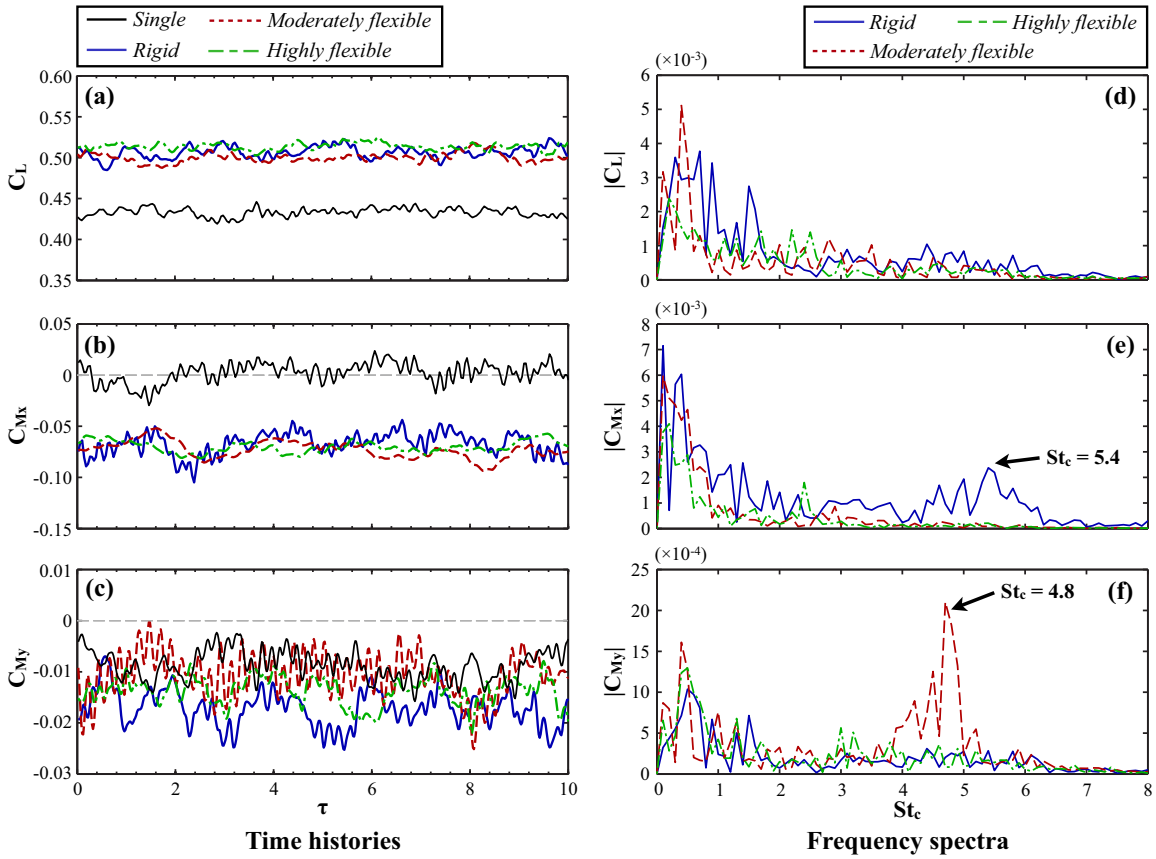

Figure 4.17: Force measurements for rigid and flexible wings: instantaneous (a) lift, (b) roll, and (c) pitching moments shown on the left and Fourier analysis of (d) lift, (e) roll, and (f) pitching moments is shown on the right.

4.5 Summary

High-fidelity implicit LES computations coupled with a geometrically non-linear plate element were employed in the current chapter in order to investigate the static and dynamic aeroelastic response of a flexible wing placed in close proximity to a rigid leader wing. The flexible follower was positioned such that the trailing vortex from the leader wing impinges upon the leading-edge inboard of the wingtip for the undeformed, rigid wing. Primary attention was given to modifications of the flow

structure and unsteady response due to aeroelastic deformations.

Spanwise bending deformations were observed to be predominately static in nature and served to provide an effective vertical offset of the incident vortex relative to the leading-edge. These essentially static deformations provided a more direct impingement of the incident vortex on the moderately flexible wing and caused it to pass beneath the surface of the highly flexible plate. This effective negative vertical offset promoted an upward and outboard trajectory of the follower wing tip vortex generating a new mode of wake-evolution in addition to those described in Chapter 3. Vortex-induced static bending deformations have the potential to shift vortex interaction away from the intended regime by imposing a vertical offset thereby generating a characteristic change in the overall flow structure.

Sustained twisting oscillations were observed for both the moderate and highly flexible plates, but small in amplitude. These small amplitude oscillations where shown to clearly influence the unsteady flow structure and aerodynamic loads as revealed by the appearance of several unique modifications to the instantaneous flow. Twisting mode vibrations of the moderately flexible wing coupled with instability in the lower-surface shear layer to generate pronounced oscillations in the pitching moment. This sustained behavior would be expected to contribute to a degradation of the wing's structural life-cycle. Upwash on the vortex encounter-side of the wing helped to locally suppress this dynamic effect. While the highly flexible wing portrayed larger oscillations in wing twist, suction-side surface pressure fluctuations were markedly diminished. Contrary to the response of the moderately flexible wing, the highly flexible plate would be expected to prolong the fatigue-life of the plate structure. This behavior may be a consequence of passive flow control due to the small-amplitude twisting oscillations and suggests the possibility of favorable aeroelastic tailoring.

Analysis of the time-mean aerodynamic loads showed a small decrease in $\overline{L/D}$

and an increase in $\overline{C}_{M,x}$ for both flexible cases compared to the rigid wing. This behavior is consistent with an increased effective angle of attack provided by twisting deformations and loss of lift to side-force provided by spanwise camber. The decrease in magnitude of the rolling moment between the moderately and highly flexible wings can be partially attributed to an increase in lower-surface suction provided by the stronger pressure-side component of the incident vortex. This observation suggests a negative vertical offset could help to partially counteract the vortex-induced rolling moment.

A couple of trends noted in the present chapter motivate further investigation. First, the incident vortex is subjected to a fairly strong adverse pressure gradient when passing beneath the wing for the highly flexible case. Adverse pressure gradients are known to be a critical factor for breakdown of axial vortices. While no specific instability can be attributed to this feature in the present cases, this observation serves as a cautionary note for the potential of a negative vertical offset to induce unsteady phenomena and buffeting loads. A vertical shift in position may unintentionally encountered by static aeroelastic deformation or relative motion between the two aircraft. Second, the favorable unsteady load characteristics of the highly flexible wing, allegedly provided by passive flow control due to small amplitude twisting oscillations, merits further investigation. This would be ideally approached through a more direct analysis, perhaps using forced pitching oscillations of a single wing.

Chapter 5

Isolated streamwise vortex interactions with rigid and flexible wings

Each of the preceding chapters explored the interaction of streamwise vortices in the context of wings operating in close proximity. The configuration and parameters investigated in Chapters 3 and 4 were conducive to the exploration and analysis of the fluid dynamics and aeroelastic response of a follower wing to a physically generated streamwise vortex provided by an identical leader wing. While a significant level of insight on the characteristic time-mean and unsteady behaviors were obtained from the preceding configuration, the need for further simplification is described in the following points:

1.) The roll-up process of the leader-wing trailing vortex is difficult to predict. This provides uncertainty in the effective lateral or vertical positioning of the incident vortex with respect to the follower wing, demonstrated in Figure 5.1. Although the efforts of the previous chapters were successful in subjecting the follower wing to the intended range of vortex positions, uncertainty in the actual vortex trajectory

provided some difficulty in systematically exploring the parameter space. A more precise method of positioning the incident vortex relative to the follower wing would reduce the complexity of the problem in general and permit more rigorous exploration of the parameter space.

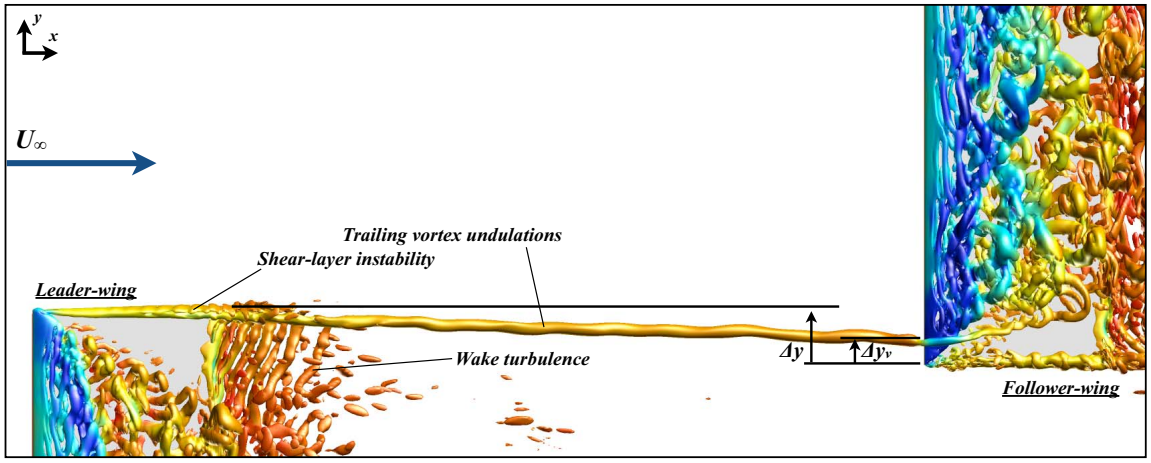

Figure 5.1: Top view of instantaneous Q-criterion ($Q = 5$) for both leader and follower-wings. Several aspects of this configuration complicate understanding of streamwise vortices: 1.) The trajectory of the leader-wing trailing vortex produces difficulty in accurately placing the incident vortex, 2.) Some instability in the trailing vortex is propagated from leader-wing, 3.) The influence of shear-layer instabilities and wake turbulence.

2.) A fundamental understanding of the unsteady behaviors provided by streamwise vortex/surface interaction is complicated by the influence of the leader-wing. For example, a small degree of fluctuation appears in the leader-wing trailing vortex, shown in Figure 5.1. The swirl strength, $q = \Gamma/2\pi r_v \Delta u$, was measured to be near $q \approx 2$ a short distance upstream of the follower wing and which would tend to fall within the stable regime for axial vortices with swirling flow[80]. Therefore, this behavior does not appear to be related to feedback response from the follower wing, but its origin is unclear in the present computations due to the presence of several influential factors unrelated to vortex/surface interaction. These include wake turbulence shed from the main body of the leader-wing and shear-layer instabilities that form in the leader-wing feeding sheet, both identified in Figure 5.1. The strain field provided

by the counter-rotating trailing vortex from the opposite wingtip can also promote mutual inductive (Kelvin-mode or Crow) instability unrelated to vortex-surface interaction.

3.) Chapter 4 suggested the impact of dynamic aeroelastic deformations can be important, but oscillation amplitudes are too small for the influence to be made saliently clear. A stronger vortex may promote more vibrant dynamics and provide a clearer depiction of the unsteady fluid dynamics.

4.) Providing sufficient resolution for ILES computations of tandem wings is taxing on computational resources and prohibits the number of parameters that can be explored.

In order to more clearly isolate the unsteady behaviors directly related to vortex-surface interaction, an approach similar to that first used by Garmann and Visbal[102] is adopted in the current chapter and used through the remainder of this dissertation. Here, the leader-wing is replaced by a q-vortex[78] imposed at the inflow boundary. The goal of this chapter is to explore and understand unsteady interactions that may arise when an initially stable, laminar streamwise vortex interacts with both rigid and flexible wings. The canonical configuration employed and its merits are described in more detail in Section 5.1 and then compared with the tandem wing configuration in Section 5.4. The interaction due to compliant wings is described in Section 5.6 followed by an isolation of the influence of static aeroelastic response in Section 5.7.

5.1 Problem setup

The configuration provided in this chapter employs the interaction of a streamwise-oriented vortex with a finite-aspect-ratio flat plate wing. The wing has an aspect-ratio of $\mathcal{AR} = 6$ and thickness of $t/c = 0.03$ and operates at a chord-based Reynolds number of $\mathrm{Re} = 30,000$ and angle of attack of $\alpha = 5^\circ$. The streamwise vortex

is imposed upstream of the wing at the inflow boundary located 9.5 chord lengths upstream of the leading-edge. Its position is described by the initial lateral and vertical offsets of Δy and Δz demonstrated in Figure 5.2, where $\Delta y = (y_{\text{vortex}} - y_{\text{tip}})$ and $\Delta z = (z_{\text{vortex}} - z_{\text{midchord}})$. These parameters define the positioning of the vortex relative to the wingtip and mid-chord, respectively, at the inflow boundary. Each case evaluated in this chapter places the vortex inboard of the wingtip with an initial lateral offset of $\Delta y/c = 0.25$ and a vertical offset of $\Delta z/c = 0$.

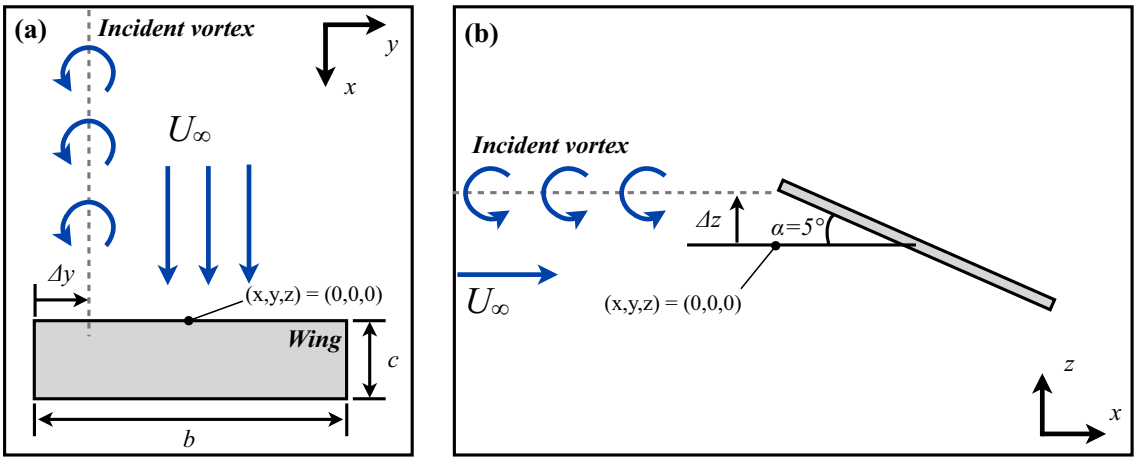

Figure 5.2: Configuration for streamwise-oriented vortex impingement; (a) top view, (b) side view.

The leader-wing trailing vortex is generated by imposing a q-vortex [78] upstream as shown in Figure 5.2. This vortex is described analytically in cylindrical coordinates by defining the radial, circumferential, and axial velocities as

$$u_r(r) = 0 \tag{5.1}$$

$$u_\theta(r) = \frac{q_0 \Delta u_0}{r/r_v}\left(1 - e^{-(r/r_v)^2}\right) \tag{5.2}$$

$$u_x(r) = 1 - \Delta u_0 e^{-(r/r_v)^2} \tag{5.3}$$

respectively where r_v is a measure of the vortex radius, Δu_0 is the initial maximum

velocity deficit, and q_0 is the initial swirl ratio defined by

$$q_0 = \Gamma_0 / 2\pi r_v \Delta u_0 \approx 1.567 V_0 / \Delta u_0 \tag{5.4}$$

where V_0 is the maximum tangential velocity. The tangential and axial velocity profiles of the q-vortex are shown in Figure 5.3 where the physical definitions of Δu_0, r_v, and V_0 are annotated for clarity.

For the cases explored in this chapter, the initial swirl strength is chosen to be $q_0 = 2$, with a radius of $r_v = 0.1c$, and axial velocity deficit of $\Delta u_0 = 0.4 U_\infty$ resulting in a maximum circumferential velocity of $V_0 \approx 0.5 U_\infty$. A similar application of this vortex was successfully employed by Garmann and Visbal[102] to evaluate several lateral positions at a lower Reynolds number and angle of attack. The specific values for the vortex parameters place the swirling flow within the stable regime predicted by Leibovich and Stewartson[80] where $q \geq \sqrt{2}$ prevents the amplification of short-wave perturbations. It should be noted this criterion is a sufficient, but not necessary condition, for instability. Other forms of unsteady behavior can occur for $q > \sqrt{2}$, such as those described in Section 1.3, have the potential to arise in streamwise vortices. However, other instabilities are unlikely to appear in the present configuration and are not encountered in practice. For instance, the viscous center modes of Fabre and Jacquin[84] are more likely to appear at higher Reynolds numbers and cooperative instabilities (see Sections 1.3.1 and 1.3.2) are prevented by removing the strain field imposed by the counter-rotating trailing vortex from the leader wing. Therefore, the present configuration permits evaluation of instabilities that may arise as a direct consequence of interaction between a stable, free vortex with an aerodynamic surface rather than the natural growth of unstable modes preceding impingement.

Figure 5.3 shows tangential and axial velocity profiles measured behind the isolated flat plate wing and compared to a fitted q-vortex with the same diameter and

swirl properties. Comparison between the single wing trailing vortex and the fitted q-vortex shows that the imposed definition provides a very good approximation to the trailing vortex of the present low Reynolds number flat plate wing. One important difference should be noted here: a second velocity deficit appears on the outboard side, $r/c \approx 0.25$, of the physical vortex. This feature is a remnant of the feeding sheet for the trailing vortex that has not completely rolled up at this streamwise location. The specific choice of q_0, r_v, and Δu_0 given above provides a much higher circulation, $\Gamma_v/U_\infty c = 0.503$, and larger core size, but a comparable swirl ratio to the single wing trailing vortex.

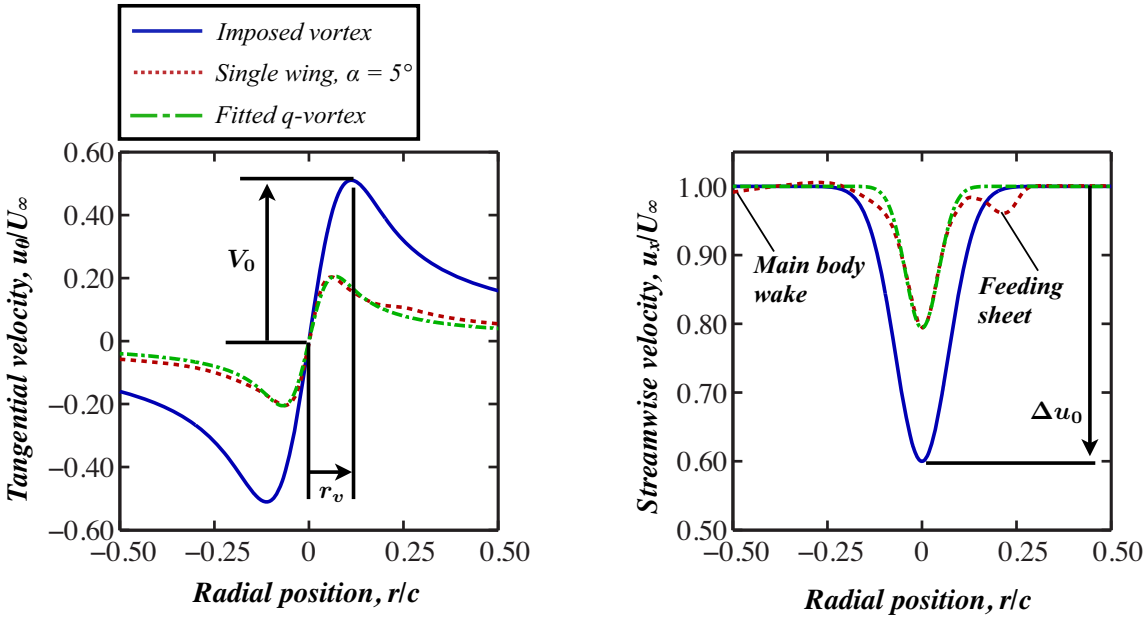

Figure 5.3: Comparison of (a) tangential and (b) axial velocity profiles for the flat plate trailing vortex and imposed q-vortex.

The configuration described above provides for a canonical streamwise vortex surface interaction. This well-defined configuration further simplifies an otherwise very complex problem and helps to better elucidate the underlying physics. The use of a flat-plate wing further decreases complexity by removing geometry effects, such as wing curvature, and promotes flow separation that may occur on smooth profiles at higher Reynolds numbers. The use of a well-defined vortex permits understanding of

instabilities that may arise in the context of theoretical fluid dynamics. Application of the q-vortex intentionally removes several complicating factors encountered for the tandem wing configuration investigated in Chapters 3 and 4 allowing for a more fundamental analysis of streamwise vortex interactions.

5.2 Numerical considerations

This setup utilizes a similar nested grid as that employed in Chapter 3 with some modifications necessary for the new approach. A portrayal of the final mesh topology is demonstrated in Figure 5.4 and consists of a hierarchy of 16 total grids in order to properly model the detailed fluid physics. The first set of blocks, designed to resolve the transitional flow structure near the wing body, consists of a series of fine-scale grids which wrap around the wing surface depicted by the red colored region in Figure 5.4. The near-wing grid system is composed of leading-edge, trailing-edge, upper, lower and two tip grid regions. As in the previous chapters, this particular multiple grid configuration is applied in order to accommodate high-order stencils at the squared-off corners of the flat plate wing and includes a four-point coincident overlap between adjacent meshes eliminating the need for high-order interpolation within this set.

An additional refined grid block serves to preserve the incident vortex as it propagates from the inflow boundary, shown in Figure 5.4 in gray. This new region is constructed using the same point distribution as the near field group. Finally, each of these blocks is wrapped in a far field system which is coarsened to roughly 2/3 the number of points as that of the near field and vortex meshes and rapidly stretched to the far field boundary. Communication between the far field and near field groups is non-coincident and therefore Chimera overset [132] methodology with high-order interpolation [133] is employed. Grid point clustering is maintained in the far field

blocks in order to minimize volume ratios in the overlap regions. The final grid used throughout Chapters 5-7, consists of 60 million grid points and is further decomposed into 688 sub-blocks for parallel processing.

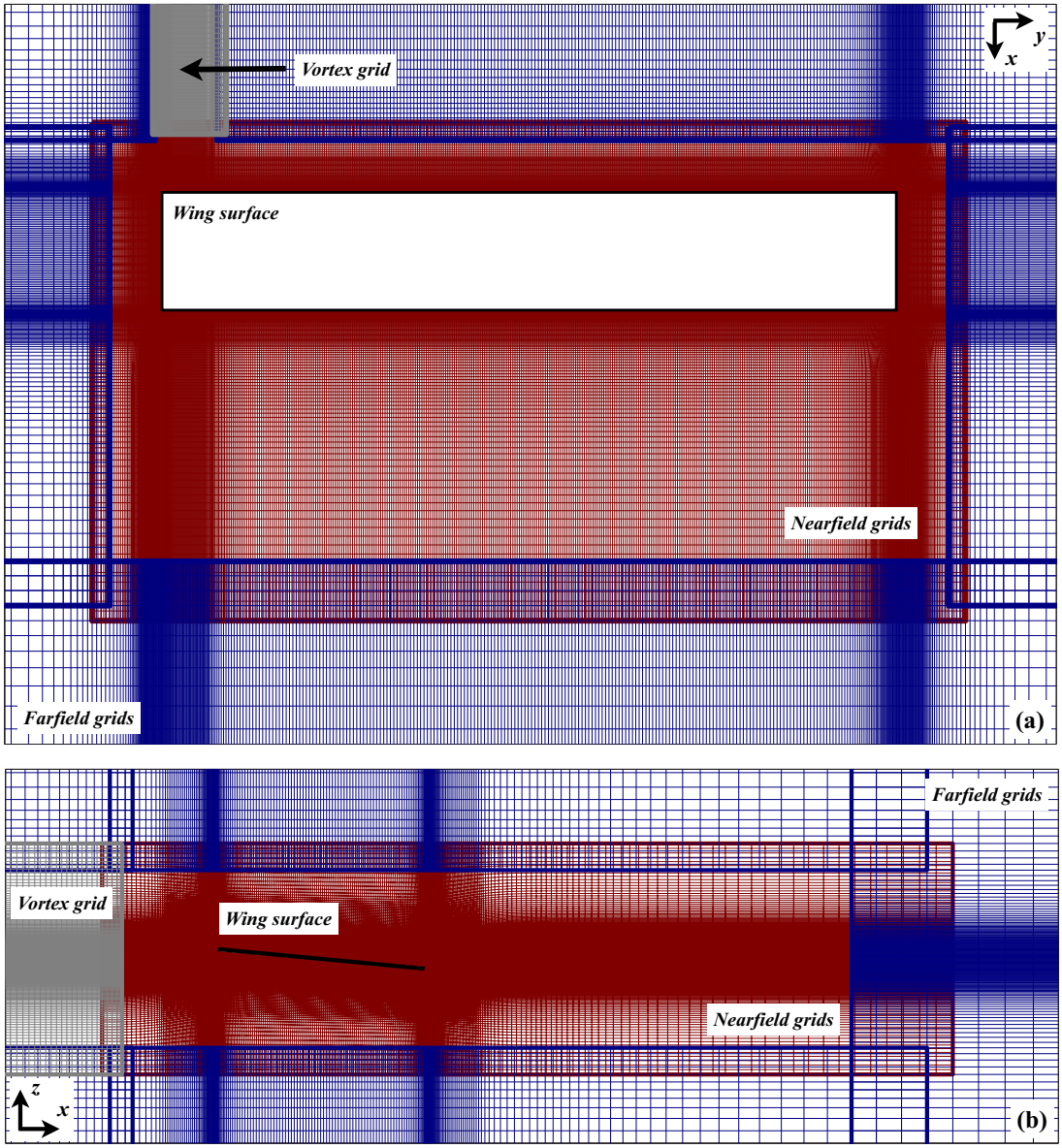

Figure 5.4: Overset multi-wing grid system used; (a) shows a top-view and (b) portrays a sideview.

Boundary conditions for the described configuration are applied in a similar fashion as the previous chapters, with some modifications. The solid boundaries at the wing surfaces employ a no-slip condition where surface velocities due to wing motion

are imposed at the corresponding surface points. In addition, third-order adiabatic ($\partial T/\partial n = 0$) and zero normal pressure gradient ($\partial P/\partial n = 0$) conditions are applied. Boundary treatments at the far fields differ from the previous cases only at the inflow boundary where the free stream velocity and incoming vortex are prescribed with first-order extrapolation of pressure. All other far field boundaries, located 50 to 100 chord lengths away from the wing, employ first-order extrapolation of the primitive variables with the exception of pressure which is set to the free stream value. It should be noted that properties of the high-order filter and rapid mesh stretching are again exploited in the manner described by Visbal and Gaitonde [134].

A two-dimensional finite element mesh, described previously in Section 4.2 and shown in Figure 4.3, is again placed in the mid-plane of the wing body within the fluid dynamics mesh. As before, forces and deformations are interchanged between fluid and structure grids in the manner described in Section 2.3. Boundary conditions on the finite element mesh consist of constraining all degrees of freedom on element nodes along the wing midspan while all remaining finite element nodes are unconstrained.

The rigid cases presented in the current and following chapters were initially run for $\tau = 30$ non-dimensional times allowing for the elimination of startup transients and the propagation of the vortex past the wing. The rigid computation was then run for an additional $\tau = 10$ allowing for the collection of time-mean and statistical quantities. Each of the aeroelastic computations were then initialized from the previously completed rigid cases and run for an additional $\tau = 20$ permitting solutions to return to a time-asymptotic state and allowing sufficient time to collect statistical data. A nondimensional time step of $\Delta\tau = 0.0001$ is used in order to provide sufficient temporal resolution for the fine-scale flow structure.

5.3 Effect of grid resolution

The effect of grid resolution was evaluated for the case of an initial $\Delta y/c = 0.25$ lateral offset and $\Delta z/c = 0$ vertical offset relative to a rigid wing. Three levels of resolution for the mesh system described in the previous section were constructed and presented here for comparison. Table 5.1 lists global dimensions and scale factors for each grid along with maximum streamwise $\delta x_{s,max}/c$, spanwise $\delta y_{s,max}/c$, and surface normal $\delta z_s/c$ spacing for each mesh on the wing surface.

Grid	Num. points	Scale factor	$\delta x_{s,max}/c$	$\delta y_{s,max}/c$	$\delta z_s/c$
Coarse	$17,649,961$	0.29	1.56×10^{-2}	3.05×10^{-2}	2.28×10^{-4}
Mid	$59,671,456$	1.00	1.03×10^{-2}	2.02×10^{-2}	1.51×10^{-4}
Fine	$139,080,415$	2.33	0.78×10^{-2}	1.50×10^{-2}	1.14×10^{-4}

Table 5.1: Grid refinement details

Table 5.2 provides a comparison of the time-mean aerodynamic loads for each grid where, C_L, C_D, $C_{M,y(c/4)}$, and $C_{M,x}$ describe the lift, drag, quarter-chord pitching moment, and rolling moment respectively. Observation of the time-averaged lift, drag, and moment coefficients demonstrates significantly decreasing changes in all forces as resolution increases. Collapse of these integrated quantities between the two finer grids provides confidence in the resolution of the present computations.

	$\overline{C}_D$	$\overline{C}_L$	$\overline{C}_{M,y(c/4)}$	$\overline{C}_{M,x}$
Coarse	0.094	0.659	-0.076	-0.118
Mid	0.090	0.630	-0.039	-0.136
Fine	0.089	0.622	-0.035	-0.137

Table 5.2: Time-averaged forces

Figures 5.5(a) and (b) portray streamwise and vertical velocity profiles respectively across the vortex core measured two chord lengths ($x/c = -2$) upstream of the leading-edge. All levels of resolution produce indistinguishable results demonstrating the vortex mesh for all of the current grid systems are suitable to preserve

the streamwise vortex as it approaches the wing. The instantaneous flow structure of the vortex encounter for each mesh is shown in Figure 5.6(a) using an iso-surface of Q-criterion. Here, the *mid* and *fine* grids portray the same qualitative behavior in the incident vortex upstream of the leading-edge while the *coarse* mesh reveals a slightly different structure in the incident vortex helical instability which has also shifted further upstream. While the *fine* grid resolves smaller-scale structures, the same qualitative behavior is observed for both the *mid* and *fine* grids over the entire wing. The time-mean flow, depicted in Figure 5.6(b), is qualitatively similar for all three cases. Observation of all quantities of interest in the current study shows little change between the two higher resolution meshes and demonstrates suitability of the *mid*-level grid which is used in all following computations.

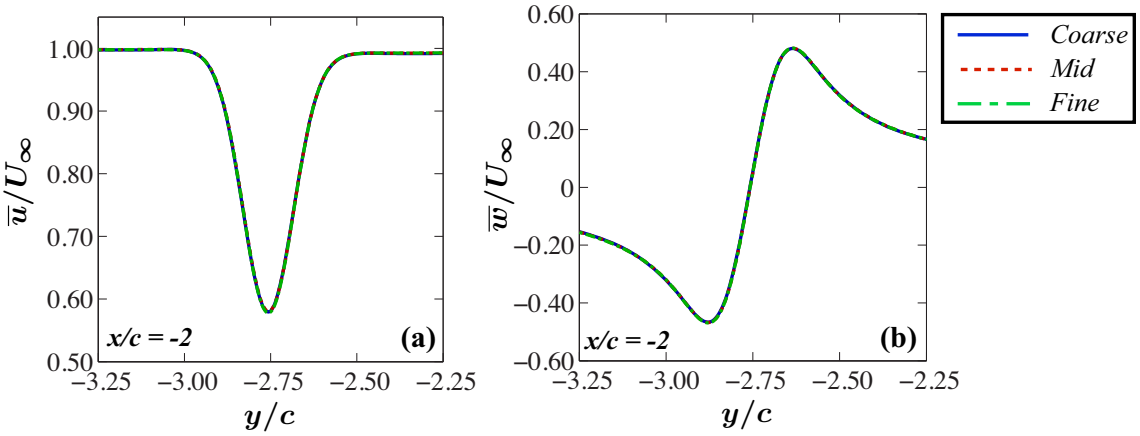

Figure 5.5: Effect of grid resolution on time-mean (a) streamwise and (b) tangential velocity across the vortex core measured two chord lengths upstream of the wing.

The effect of grid resolution on the structural model is partially repeated for the new configuration using the same approach as described in Section 4.3. As before, static deformations of the wing are evaluated using the time-mean surface loads from the rigid wing computation. Three structural meshes with uniformly spaced elements were investigated in this section and dimensions for each are shown in Table 5.3. Nodal vertical deflections are recorded for both the vortex-side and outboard wingtips

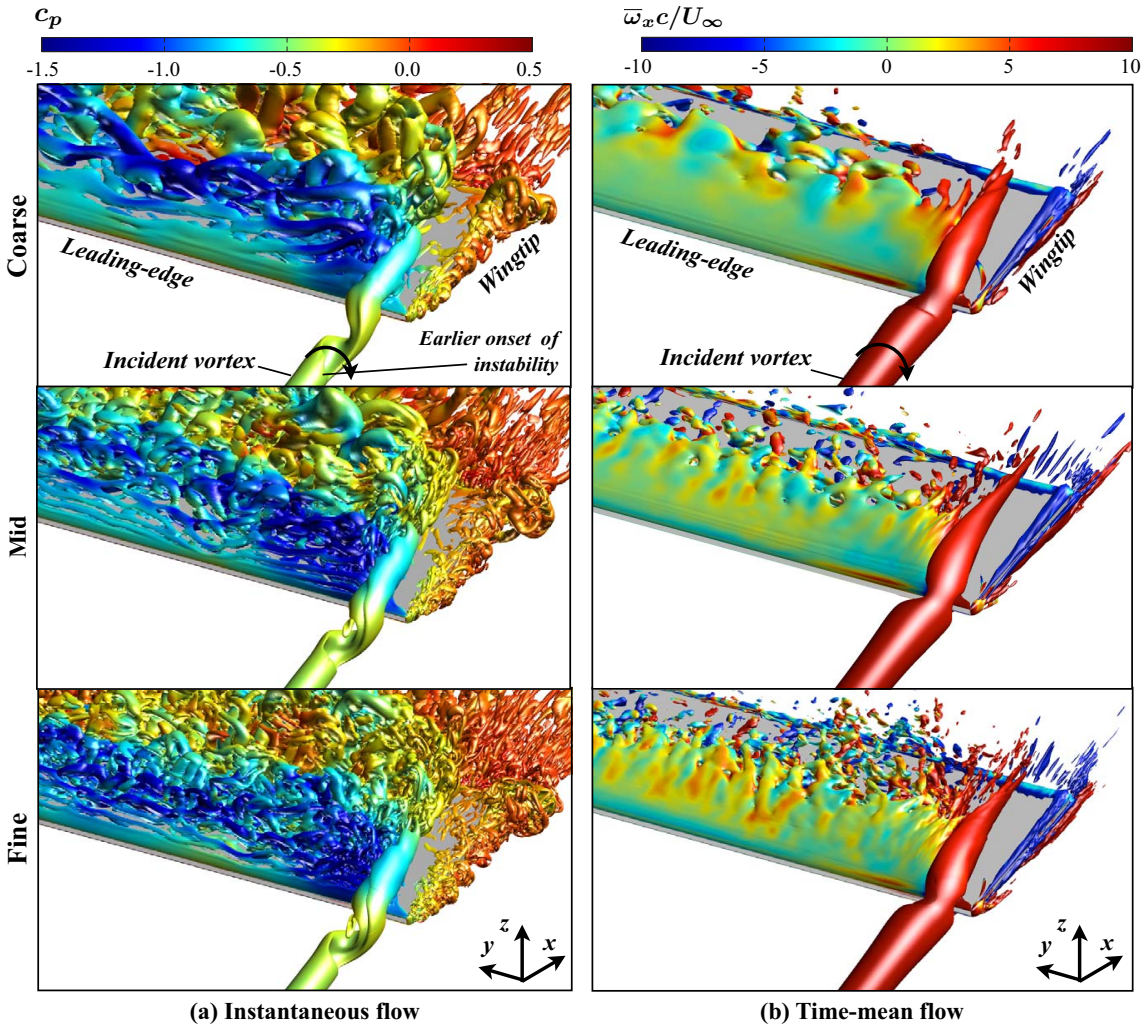

Figure 5.6: Effect of grid resolution on (a) the instantaneous flow using an iso-surface of Q-criterion ($Q = 15$) and (b) the time-mean flow using an iso-surface of Q-criterion ($Q = 5$).

taken at the midchord in Table 5.4 using the properties for the moderately flexible wing. The corresponding wingtip mid chord deflections provided in Table 5.4 differ on the order of 0.01%. Grid work, W_{grid}, is computed for the three grids as a more discriminating evaluation of wing deformations. As stated previously, this calculation provides an integrated value for evaluation of deformations on the entire structural model and shows changes on the order of 0.01% with successive refinement.

Table 5.3: Structural mesh dimensions

Grid	Dimensions	Grid size
Coarse	10×60	600
Mid	14×86	1204
Fine	20×120	2400

Table 5.4: Wing tip deflections and grid work

Grid	$d_{z,o}/c$	$d_{z,v}/c$	$W_{\text{grid}}(\text{N} \cdot \text{m})$
Coarse	4.661×10^{-2}	6.630×10^{-2}	4.781×10^{-3}
Mid	4.661×10^{-2}	6.631×10^{-2}	4.782×10^{-3}
Fine	4.662×10^{-2}	6.632×10^{-2}	4.783×10^{-3}

5.4 Comparison of isolated vortex and tandem wings

This section describes the main differences and similarities in the instantaneous and time-mean flow structure between the streamwise vortex interactions involved in the tandem wing and imposed vortex cases. Figure 5.7 shows a top view of the time-mean Q-criterion for the $\alpha_L = 5°$ and $\alpha_L = 8°$ tandem wing cases from Chapter 3 and the current, imposed vortex case. As the incident vortex increases in strength from $\alpha = 5°$ to $\alpha = 8°$, the general flow structure becomes more similar to the imposed vortex case. While the upper-surface component of the incident vortex for the $\alpha_L = 5°$ case attenuates as it approaches the trailing-edge, both of the stronger $\alpha_L = 8°$ and imposed vortex cases demonstrate a more rapid attenuation due a direct impingement with the leading-edge and more even bifurcation of the incident vortex following impingement. The $\alpha_L = 8°$ case portrays a much earlier destruction of the coherent vortex due to its relatively weaker strength compared to the imposed vortex case. Just upstream of the leading-edge, both the $\alpha_L = 8°$ and imposed vortex cases portray an indentation in the time-mean Q-criterion indicative of similar unstable behavior shown more clearly in the instantaneous flow.

A snapshot of instantaneous Q-criterion for all three cases is provided in Figure

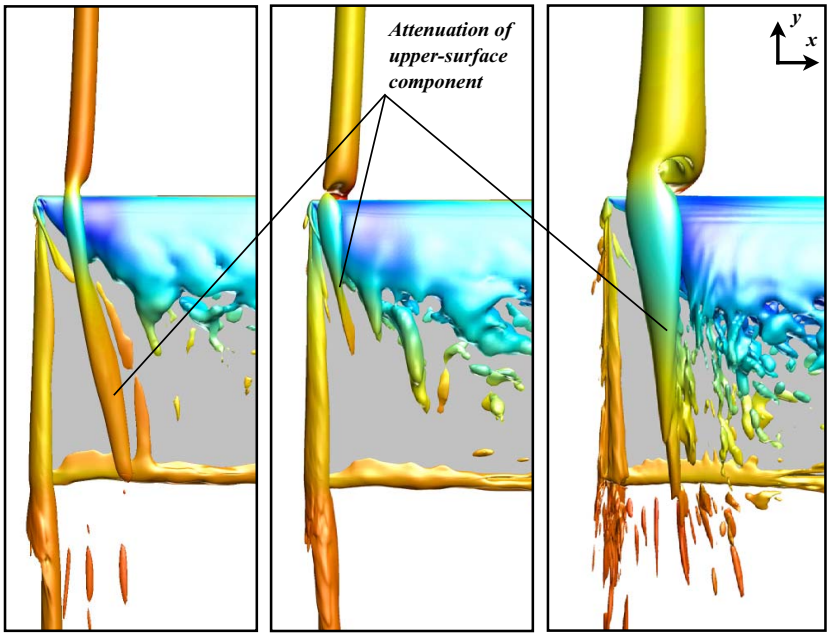

Figure 5.7: Comparison of time-mean flow for tandem wing and imposed vortex cases using an iso-surface of Q-criterion ($Q = 5$).

5.7. Each interaction shows that attenuation of the upper surface component is influenced by interaction with transitional flow structure provided by the separation region inboard of vortex impingement. In the $\alpha_L = 5°$ case, the incident vortex periodically connects with vortical structures on its inboard side as described previously in Section 3.4. Both the $\alpha_L = 8°$ and imposed vortex cases degenerate into smaller-scale structures comparatively earlier. This factor may be influenced by both a weaker upper surface component due to a more even bifurcation and a stronger separation imposed by enhanced upwash from the stronger vortices. Upon impingement with the leading-edge, the incident vortex of the $\alpha_L = 8°$ and imposed vortex cases develops a spiraling instability much more pronounced in the imposed vortex case.

Time-mean surface pressure coefficient contours and surface restricted streamlines are plotted in Figure 5.9 and compare the surface flow topology for the single wing, tandem wing, and imposed vortex cases. Consistent with previous observations, increasing effective angle of attack provided by upwash from the incident vortex pro-

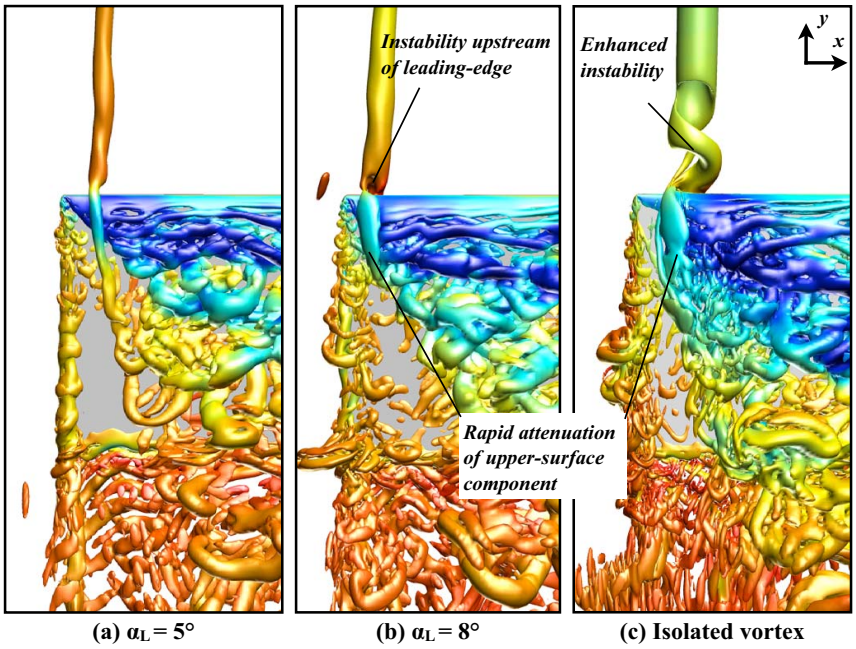

Figure 5.8: Comparison of instantaneous flow for tandem wing and imposed vortex cases using an iso-surface of Q-criterion ($Q = 15$).

duces a larger separation region as the vortex becomes stronger from Figures 5.9(b) to (d). This is indicated by both the growing region of suction and approximated line of reattachment in the surface restricted streamlines. A time-mean recirculation region just inboard of the vortex encounter is consistent between all three cases as indicated by a stable focus and enhanced suction. This swirling flow region grows with vortex strength and its influence on surface pressure is significant enough in the imposed vortex case in Figure 5.9(d) to influence the time-mean loading. This is demonstrated in Figure 5.10 where a large spike in the time-mean lift coefficient per unit length coincides with the strong suction in the swirling flow region. A similar local enhancement in lift is shown to persist for all inboard positions of the incident vortex in the work by Garmann and Visbal[5].

In general, the tandem wing cases tend to the behavior of the imposed vortex as the incident vortex increases in size and strength. This observation conveys the relevance of using the q-vortex model in the present section for analysis of streamwise

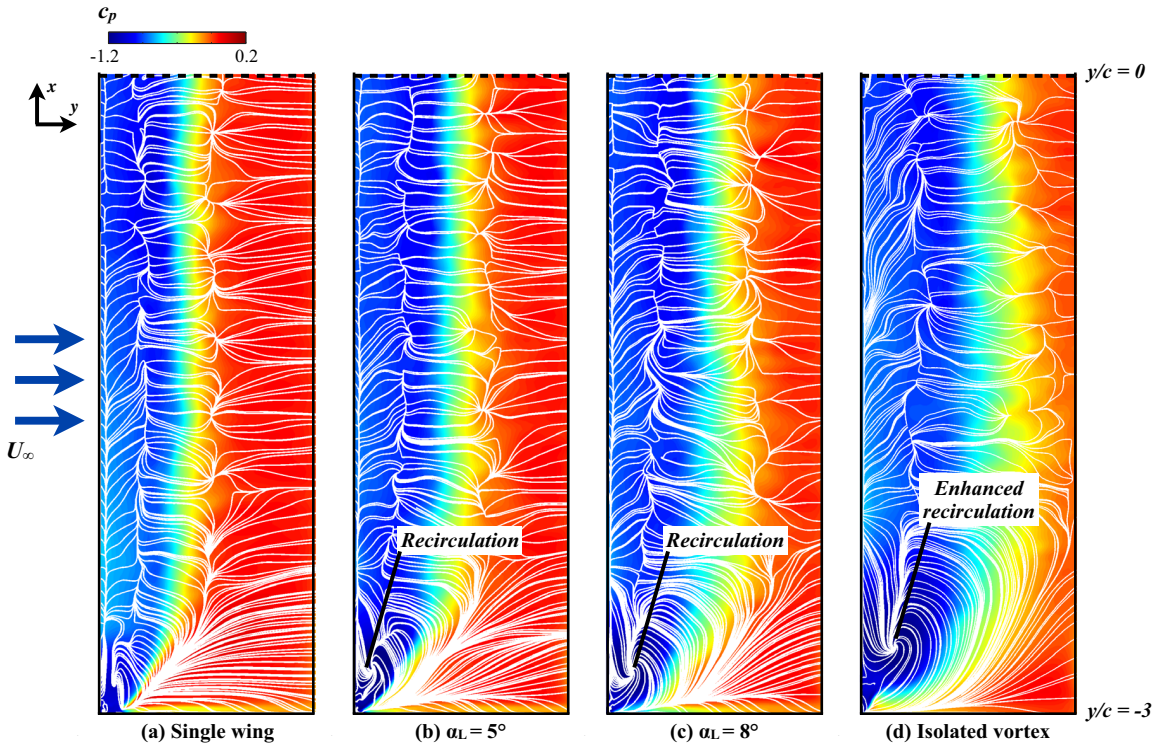

Figure 5.9: Comparison of time-mean surface pressure and limiting surface streamlines for the isolated wing, tandem wing and imposed vortex cases.

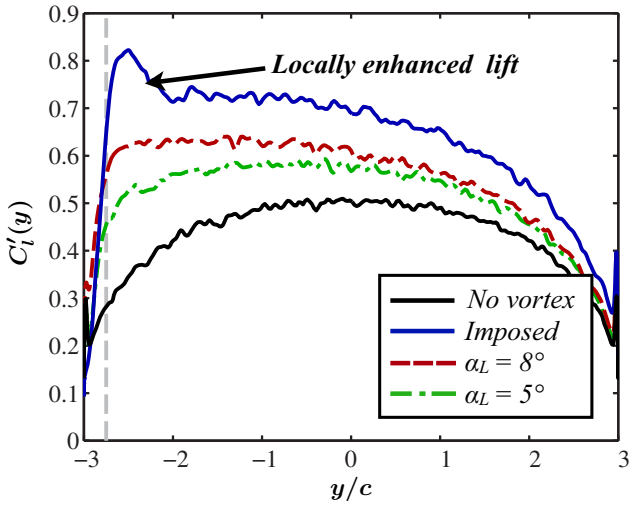

Figure 5.10: Distribution of lift coefficient per unit length along the wingspan for the isolated wing, tandem wing, and imposed vortex cases.

vortex interactions with low Reynolds number wings. Two important, and intentional, distinctions are apparent between the tandem wing and imposed vortex approaches. First, fluctuations in the tandem wing vortex upstream of the follower likely provided by wake turbulence or shear layer instabilities of the generator wing, have been successfully removed in the imposed vortex case. Therefore, the upstream response in the single, stable, laminar vortex is solely a consequence of vortex-surface interaction which can be more rigorously studied here. Second, a more pronounced response is elicited in the imposed vortex case allowing for clearer depiction and characterization of unsteady behavior.

5.5 Comparison with previous work

Figure 5.11 shows similar views of the instantaneous flow for the previous application of the q-vortex by Garmann and Visbal[5] in Figures 5.11(a) and (b) and the current case in Figures 5.11(c) and (d). Both cases use an identical wing, initial positioning of $\Delta y/c = 0.25$ and $\Delta z/c = 0$, and the same vortex properties, but the wing in Ref. [5] operates at a lower $\mathrm{Re} = 20,000$ and $\alpha = 4°$. Instability upstream of the leading-edge is common to both cases where Ref. [5] shows spiraling undulations emanating from interaction with the leading-edge. The higher angle of attack and Reynolds number of the present case subjects the vortex to a more severe interaction that successfully elicits a more pronounced unsteady response. This engenders an abrupt change in flow structure and expansion of the vortex core in the time-mean flow, but is not vortex breakdown in the strict sense defined by Leibovich [87], that is, there is no stagnation or flow reversal.

The helical instability in the present work appears to provide larger amplitude fluctuations, but is confined closer to the leading-edge. The primary frequency in both in cases is close to $\mathrm{St}_c \approx 1.0$ and, as will become apparent in Chapter 6, independent

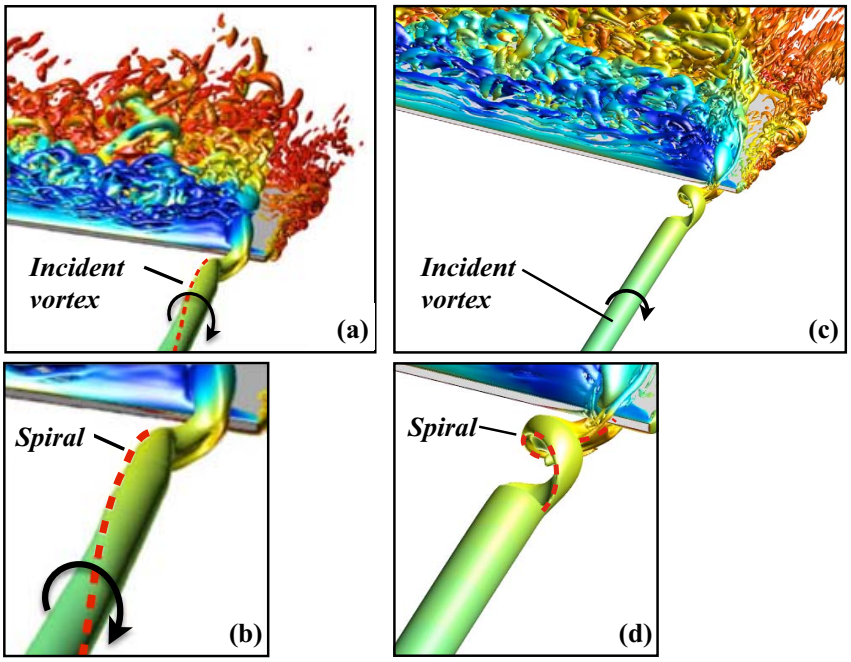

Figure 5.11: Comparison of instantaneous flow between Garmann and Visbal[5] and the current work using a snapshot of instantaneous Q-criterion ($Q = 15$). Frames (a) and (b) show the Re $= 20,000$, $\alpha = 4°$ case while (c) and (d) show the current Re $= 30,000$ and $\alpha = 5°$ case.

of the specific interaction, and in Chapter 7 resilient to wing oscillations. These observations suggest the time-scales of the vortex instability are a characteristic of the vortex itself rather than its specific interaction with the wing. Further exploration on the effects of Re and α are outside the scope of this dissertation but are excellent topics for future work.

5.6 Effect of flexibility

The goal of this section is to subject flexible wings to a stronger interaction supplied by the imposed vortex. This enhanced interaction provides a clearer aeroelastic response of the wing structure and feedback effects on the incident vortex. Two compliant wings are evaluated where the *moderately flexible* structure has an elastic modulus of $E = 69$ (MPa) and the *highly flexible* wing is $E = 34.5$ (MPa). The

density, poisson's ratio, characteristic length, and thickness of both plate models are chosen to be $\rho_s = 2700$ (kg/m^3), $\nu = 0.30$, $c = 0.1$ (m), and $t/c = 0.01$ respectively. For reference, the moderately flexible wing is comparable to a thin aluminum plate. The dynamic pressure is set as $1/2\rho_f U_\infty^2 = 58.5$ which corresponds with water tunnel conditions. These are the same parameters used for the flexible structures in Chapter 4. As before, this particular choice of parameters is both tractable for LES computations and reproducible in experimental studies.

5.6.1 Compliant wing deformations

The wing deformations are explored in this section in order to provide insight into the influence of a streamwise-oriented vortex on the static and dynamic components of the elastic structures. Table 5.5 lists the time-mean wingtip vertical deflections, $\overline{d}_z$ and twisting $\overline{\theta}$. Both the moderate and highly flexible wings exhibit time-mean tip deflections that are significantly larger on the vortex encounter-side due to an asymmetric spanwise distribution of lift, shown for the rigid wing in Figure 5.10. This effectively translates into a vertical offset of the surface placing the incident vortex axis beneath the leading-edge in both cases, depicted in Figure 5.12. Time-mean wingtip twisting behavior is also shown in Table 5.5 which shows the time-averaged twisting deformations are larger for the highly flexible wing, as can be expected. However, there is little change in $\overline{\theta}$ between the vortex encounter and outboard-sides of the wing for either flexible structure.

Table 5.5: Time-mean wingtip deformations.

	$\overline{d}_{z,v}/c$	$\overline{d}_{z,o}/c$	$\overline{\theta}_v$	$\overline{\theta}_o$
Moderately flexible	0.067	0.047	0.17°	0.16°
Highly flexible	0.133	0.099	0.32°	0.31°

A time-history of vertical displacements at the wingtip midchords is depicted in Figure 5.13(a) over the last $\tau = 10$ of simulation time. For both the moderate and

highly flexible cases, the vortex encounter-side tip exhibits a pronounced dynamic response compared to the essentially static displacements of the outboard tip of both flexible structures. Fourier analysis of the spanwise bending deformations, shown in Figure 5.14(a) clarifies the dominant frequency components for each plate. A single clearly defined non-dimensional frequency of $\mathrm{St}_c = fc/U_\infty = 0.46$ appears for the highly flexible wing whereas the moderately flexible plate exhibits two additional frequency components of $\mathrm{St}_c = 0.91$ and 0.23. These are essentially a harmonic and sub-harmonic respectively of the single dominant frequency of the highly flexible structure. In both cases, the dominant frequency of bending oscillations is $\mathrm{St}_c = 0.46$ and roughly a sub-harmonic of the primary frequency of vortex instability, measured to be $\mathrm{St}_c = 0.9$ (see Chapter 6).

A time-history of twisting deformations at both wingtips is provided in Figure 5.13(b) in which the flexible and highly flexible wings demonstrate small amplitude high-frequency components and larger-amplitude low-frequency components of twisting on the vortex encounter-side. The larger-amplitude frequencies of the twisting deformations, obtained from the FFT of θ in Figure 5.14(b), directly correspond to those observed for the bending deformations at $\mathrm{St}_c = 0.46$. This indicates the dynamic response is largely driven by unsteadiness in the flow field rather than excitation of structural modes.

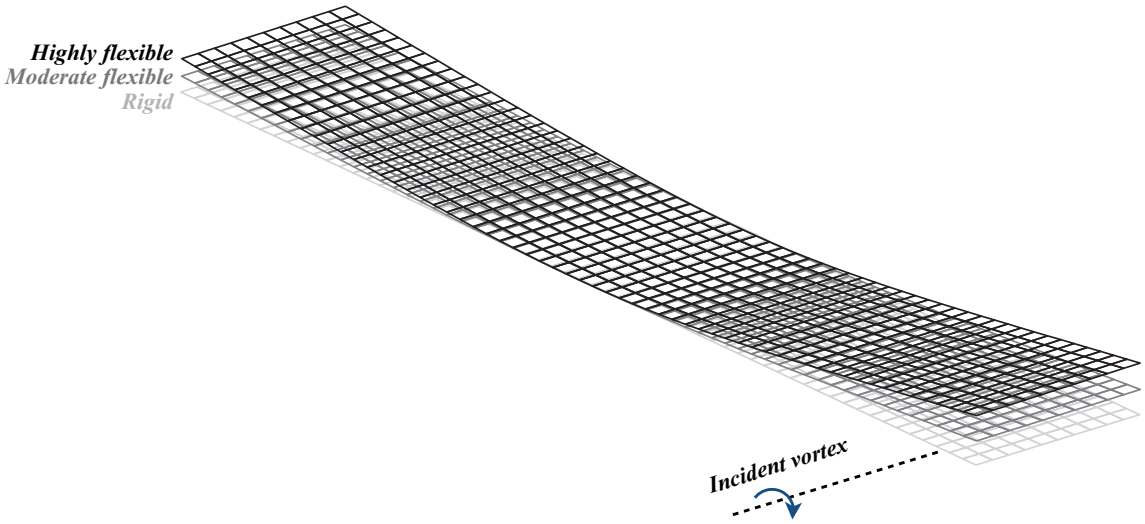

Figure 5.12: Time-mean deformations for the moderate and highly flexible wings result in an effective vertical offset of the vortex relative to the leading-edge. Deformations are amplified for visual purposes.

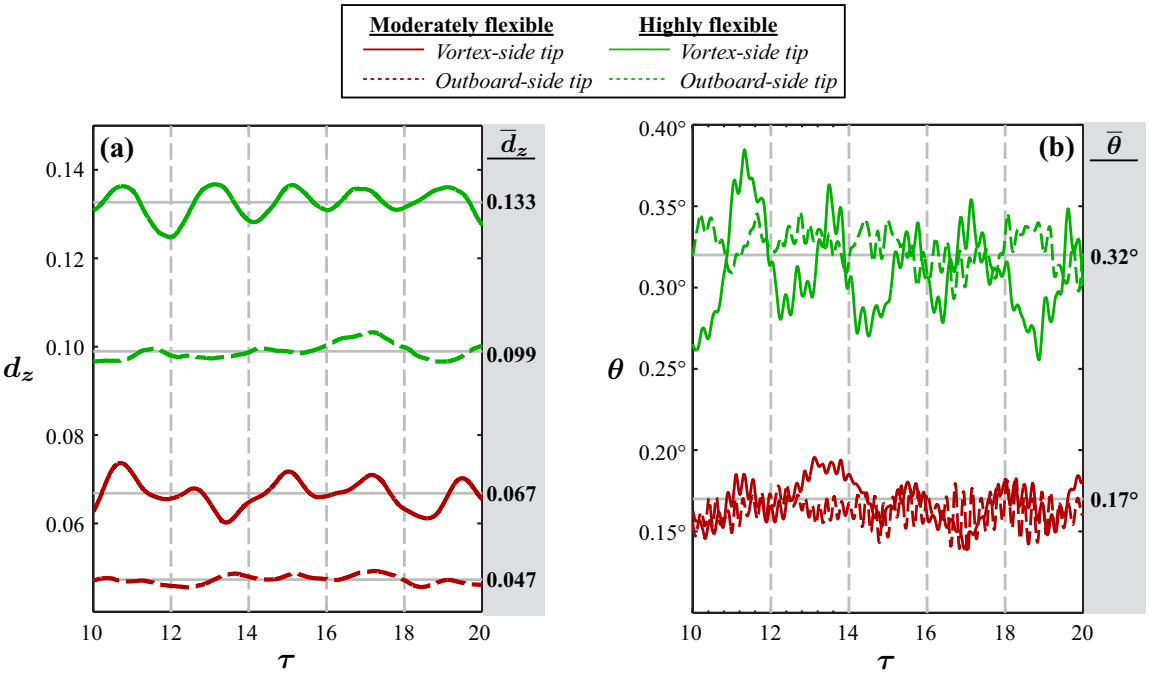

Figure 5.13: Time-history of (a) wingtip vertical deflections and (b) wingtip twisting. Time-mean values are provided to the right of each figure.

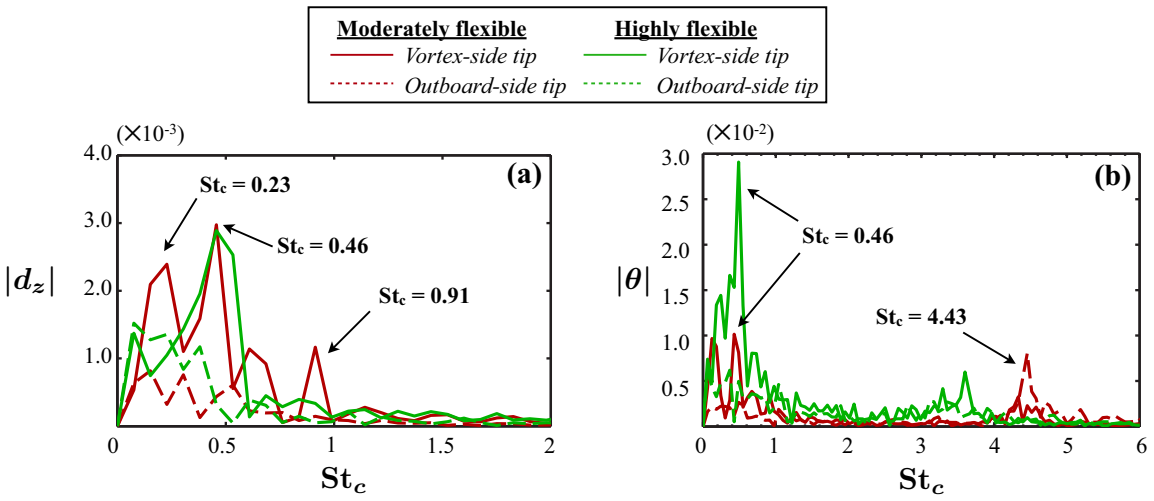

Figure 5.14: Fourier analysis of (a) wingtip vertical deflection and (b) wingtip twisting deformations.

An additional clearly defined peak is found in the wing twist frequency spectrum at a higher frequency of $\mathrm{St}_c = 4.43$. This higher frequency component is found only on the outboard wingtip of the moderate flexible plate and is consistent with the behavior of the moderately flexible wing in Chapter 5. As in the previous chapter, these oscillations appear to be a coupling between shear-layer instabilities on the lower outboard surface and twisting-mode deformations of the plate, rather than a consequence of vortex-surface interaction. Upwash from the incident vortex was shown in Chapter 5 to partially stabilize the shear-layer reducing the amplitude of this frequency component on the vortex encounter-side. Here, the stronger upwash provided by the imposed vortex completely removes this frequency content from the vortex-side of the wing. Increasing stiffness that accompanies large deformations provided by the vortex-induced bending can also contribute to the removal of this phenomenon on the vortex-side of the wing.

5.6.2 Time-mean flow structure

The time-mean flow structure about the rigid, moderate, and highly flexible plates is depicted in Figure 5.15 where Figure 5.15(a) shows a top view of an iso-surface of Q-criterion while Figure 5.15(b) shows a bottom-view. The rigid wing portrays a slight expansion of the time-mean incident vortex as it approaches the leading-edge, and then bifurcation between the upper and lower surfaces of the plate. A more significant expansion of the incident vortex diameter is observed for both the moderate and highly flexible plates. Similar bifurcation to that observed for the rigid plate is found on the flexible structures, but partitioning of the incident vortex is increasingly biased towards the lower surface with increasing flexibility. This is a consequence of the effective vertical offset provided by the time-mean bending on the vortex-side of the wing.

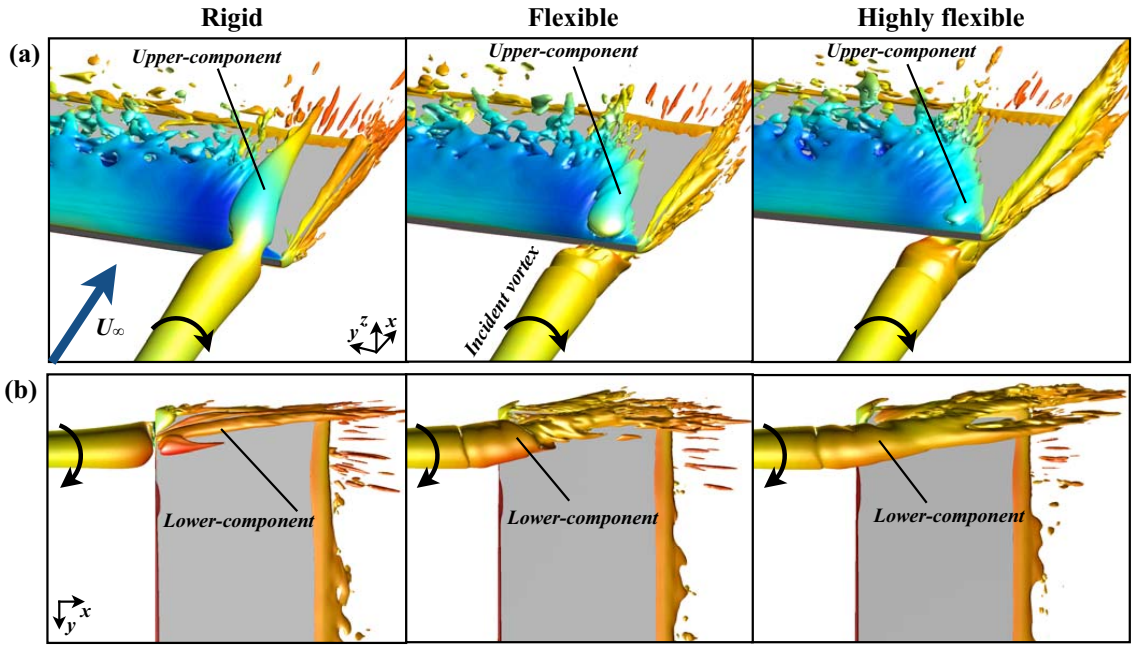

Figure 5.15: Iso-surfaces of time-mean Q-criterion for rigid and flexible wings (Q = 5) where (a) shows a top view and (b) portrays a bottom view

5.6.3 Unsteady flow structure

A snapshot of the instantaneous flow structure is provided in Figures 5.16(a)-(c) for the rigid, moderate, and highly flexible plates respectively. As previously mentioned, the incident vortex develops an unsteady helical pattern preceding impingement with the leading-edge of the rigid wing. This spiraling flow structure alternates between the top and bottom surfaces intermittently contributing to vortical components on either side of the plate and is responsible for the expansion of the time-mean vortex diameter upstream of all three wings in Figure 5.15. This phenomenon is similar to the pinch-off and reconnect process well-described in the preceding work by Garmann and Visbal [5]. Instability in the incident vortex appears to be exacerbated by both flexible plates where the unsteady helix is shown to become much more pronounced in Figures 5.16(b) and (c). This enhanced instability provides a secondary spiral, traced by a dashed red line, in addition the the primary helix, traced by a dashed blue line, indicative of higher modes of instability in the more perturbed vortex of the aeroelastic cases.

A bottom view of the instantaneous flow structure is shown in Figures 5.16(d)-(f) for the rigid, moderate, and highly flexible plates respectively, and more clearly demonstrates the effect of elasticity on the unsteady flow structure. Here, the time-mean bending deformation, $\overline{d}_{z,v}/c = 0.07c$, on the vortex-side of the moderately flexible plate allows a more significant portion of the unsteady vortex to pass along the lower-surface. A vertical shift of the moderately flexible wing in conjunction with enhanced instability provides larger amplitude fluctuations in the pressure-side flow field which engenders some degree of buffeting response of the compliant structure, shown in Figure 5.13. This trend is shown to persist for the highly flexible wing in Figure 5.16(f) where the larger $\overline{d}_{z,v}/c = 0.133$ time-mean bending deflection provides an additional bias of the highly unsteady flow to the pressure-side of the wing, further contributing to the dynamic response in Figure 5.13.

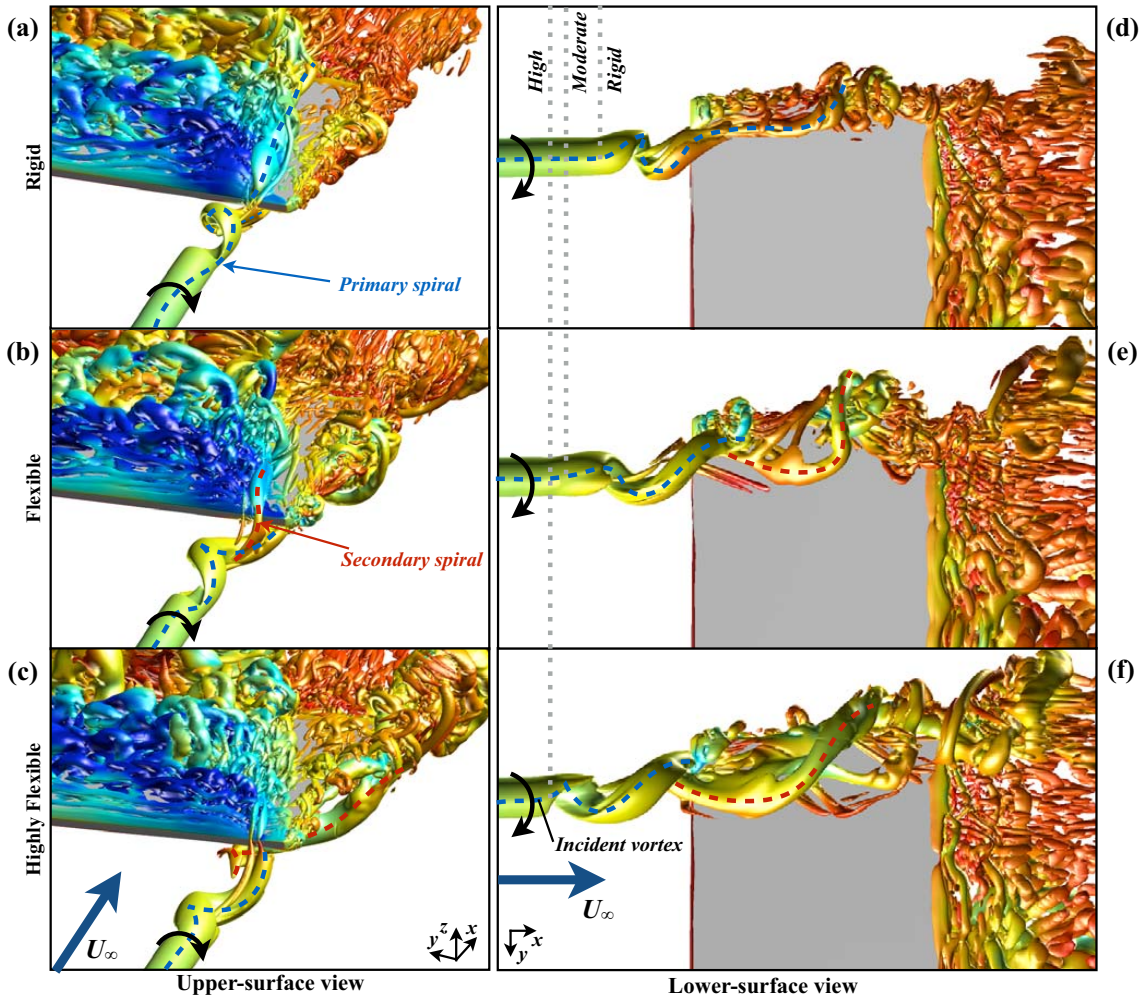

Figure 5.16: Iso-surfaces of instantaneous Q-criterion for rigid and flexible wings (Q = 15). Dotted lines roughly locate the beginning of instability.

The influence of vortex instability on the wing is best differentiated for each case by looking at contours of instantaneous pressure coefficient, c_p, on the lower surface of the wing in Figure 5.17. The imprint of the unsteady spiral is shown for the rigid wing in Figure 5.17(a) which portrays intermittent packets of low-pressure along the surface coincident with when the spiral crosses the pressure-side. A similar helical imprint is shown for the moderately flexible wing in Figure 5.17(b) where regions of suction are much stronger than the rigid case. These higher amplitude fluctuations in surface pressure will be shown later to produce significantly larger fluctuations in the aerodynamic loads. The imprint of the unsteady vortex is strongest for the highly

flexible wing in Figure 5.17(c) which conveys the lowest pressures of the three cases. Although suction is stronger for this wing, it is also more consistent providing lower amplitude fluctuations in surface pressure than the moderately flexible case.

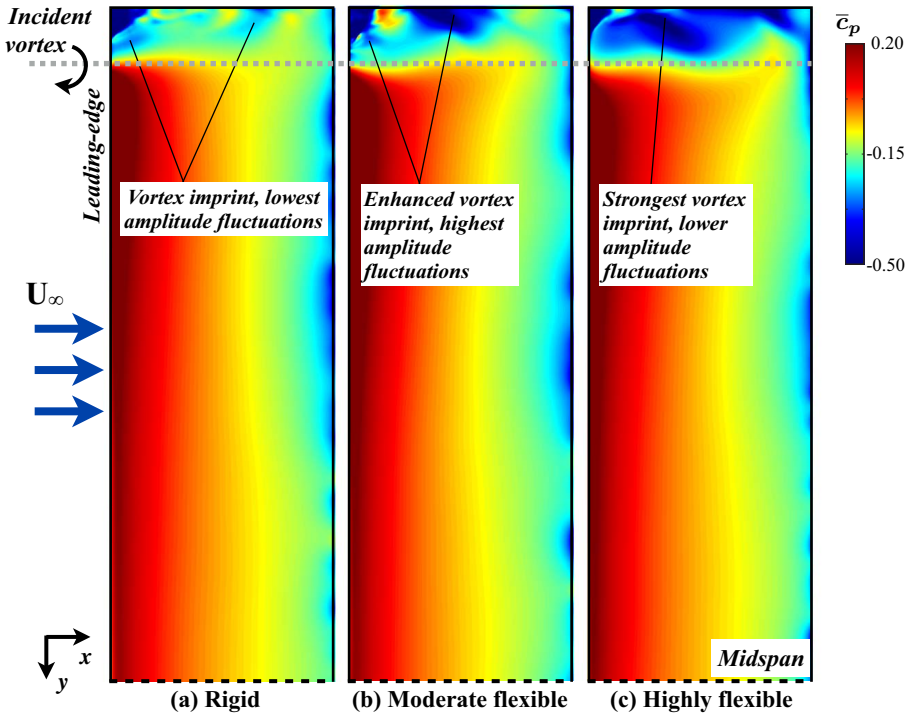

Figure 5.17: Contours of instantaneous pressure coefficient, c_p, on the lower-surface for the (a) rigid, (b), moderate, and (c) highly flexible wings.

Figure 5.18 shows cross-sections of turbulent kinetic energy, k, contours intersecting the incident vortex in the xy-plane at $z = 0.04$ and portrays the maximum upstream extent of velocity fluctuations for each wing. The kinetic energy fluctuations for the rigid wing in Figure 5.18(a) portray a small region of k upstream of the leading-edge coinciding with the onset of unsteady behavior. This elevated region of k protrudes further upstream of the leading-edge for both of the flexible cases. A comparison of iso-lines of turbulent kinetic energy upstream of the three plates shows the highly flexible wing provides the largest upstream extent of instability, slightly further than the moderate flexible case, consistent with the unsteady flow structure in Figure 5.16. Although the onset of unsteady behavior is slightly delayed for the

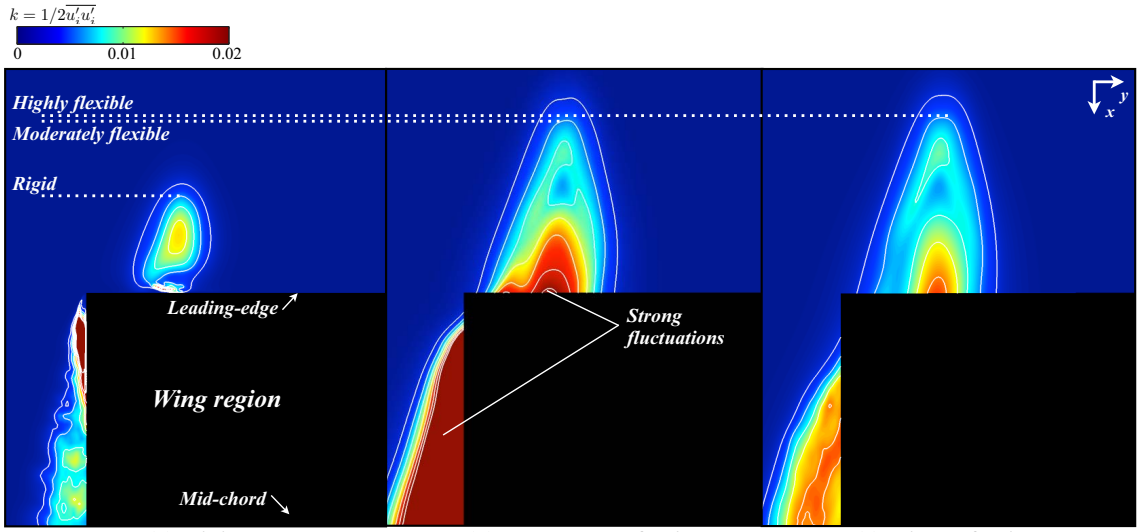

Figure 5.18: Top-down view of turbulent kinetic energy, k, contours at $z/c = 0.04$.

moderately flexible wing, the growth rate appears to be much higher due to the significantly elevated regions of kinetic energy fluctuations in Figure 5.18(b) and consistent with the amplitude of surface pressure fluctuations in Figure 5.17(b).

Clearly, the present analysis captures a significant influence of flexibility on the unsteady fluid dynamics in a streamwise-oriented vortex encounter. Two aspects of the aeroelastic response can contribute to its influence on the incident vortex. First, the time-mean spanwise bending deflection of the vortex-side wingtip effectively repositions the incident vortex relative to the wing surface, shown in Figure 5.12. This static-aeroelastic effect could result in a very different vortex-surface interaction. Second, the small-amplitude low-frequency oscillations of the dynamic response have the potential to provide feedback effects on the incident vortex. For instance, Gursul and Xie[66] demonstrated the breakdown of a leading-edge vortex over a delta wing can be particularly sensitive to lower-frequency oscillations of a fin. Uncertainty as to which of these two aspects dominates in the present flow motivates the separation of static and dynamic responses in Section 5.7 in order to isolate the main effects.

5.6.4 Aerodynamic loads

The time-mean aerodynamic loads for the rigid, flexible, and highly flexible cases are provided in Table 5.6 and compared to an identical wing without an incident vortex. An enhanced lift and lift-to-drag ratio compared to the isolated wing is apparent in all three cases. However, the benefit decreases somewhat with increasing flexibility. This effect can be explained by two factors. First, while a small increase in the effective angle of attack provided by time-mean wing twist increases lift and drag, lifting force is partially counteracted by spanwise bending. The spanwise camber provided by bending deflections partially orients the normal forces in the spanwise direction which amounts to a loss in lift to side-force. Consequently, $\overline{L/D}$ is diminished.

Table 5.6: Time-mean aerodynamic loads for rigid and flexible wings

	$\overline{C}_D$		$\overline{C}_L$		$\overline{L/D}$		$\overline{C}_{M_x}$	$\overline{C}_{M_{x,\mathrm{RMS}}}$
	Value	% diff.	Value	% diff.	Value	% diff.	Value	($\times 10^{-3}$)
No vortex	0.077	-	0.43	-	5.65	-	0.002	9.8
Rigid	0.091	+17.8%	0.63	+45.7%	6.96	+23.7%	-0.136	12.9
Moderate	0.092	+19.6%	0.64	+47.2%	6.92	+23.1%	-0.140	22.3
High	0.094	+22.6%	0.65	+50.3%	6.89	+22.6%	-0.125	12.1

Second, moving the vortex away from the surface has an influence on the aerodynamic benefits. See, for instance, Figure 5.19(a) which plots the time mean distribution of lift coefficient per unit length along the wingspan. The effective vertical offset provided by spanwise bending removes the locally enhanced lift provided by suction on the upper-surface of the rigid wing just inboard of the vortex encounter. Further inboard of the vortex, the lift distribution of the flexible wings is higher due to a larger effective angle of attack provided by wing twist which also increases drag. Placement of the vortex beneath the wing, as in the highly flexible case, produces a low pressure-region near the wingtip on the lower surface, shown in Figure 5.17, that further counteracts the lift.

Observation of the time-mean rolling moment coefficient, $\overline{C}_{M_x}$, demonstrates the

tendency for the asymmetrical lift distribution to produce a negative vortex-induced rolling moment which is highest for the moderately flexible wing and lowest for the highly flexible plate. The strong low pressure region on the lower surface of the highly flexible wing, located near the wingtip and shown in Figure 5.17(c), partially counteracts the negative vortex-induced rolling moment providing a less severe $\overline{C}_{M_x}$.

Fourier analysis of the rolling moment in Figure 5.19(b) provides some insight into the unsteady loading provided by vortex-surface interaction. The moderately flexible wing exhibits the highest amplitude components with clearly defined peaks at frequencies of $\mathrm{St}_c = 0.23$, 0.46, 0.91. The two lower frequencies are sub-harmonics of the primary vortex instability while the higher frequency coincides with the unstable mode of the incident vortex. The highly flexible wing exhibits a single, clearly defined peak at $\mathrm{St}_c = 0.46$ although much lower in amplitude than the same frequency component for the moderately flexible case. Clearly, the moderately flexible wing engenders the most unstable response of the three cases as was suggested by turbulent kinetic energy fluctuations in Figure 5.18 and instantaneous lower-surface pressure contours in Figure 5.17. Evidence of enhanced unsteady loading is further supported by the root-mean-square of the rolling moment coefficient, $C_{M_{x,\mathrm{RMS}}}$, for the moderately flexible case which is nearly double that of the rigid wing. The frequency content for both flexible wings directly aligns with that of the bending deformations in Figure 5.14(a) demonstrating the tendency for vortex-induced unsteady loads to drive dynamic response of the flexible structures.

Similar conclusions can be drawn from the Fourier analysis of the quarter-chord pitching moment shown in Figure 5.19(c). Here, the moderate flexible wing provides clearly defined peaks at the same frequencies of the bending deformations with an additional component at $\mathrm{St}_c = 4.4$. This higher frequency component is due to the same phenomenon described in Section 4.4.4. The highly flexible wing produces a single peak at $\mathrm{St}_c = 0.46$ with an amplitude comparable to the same component of

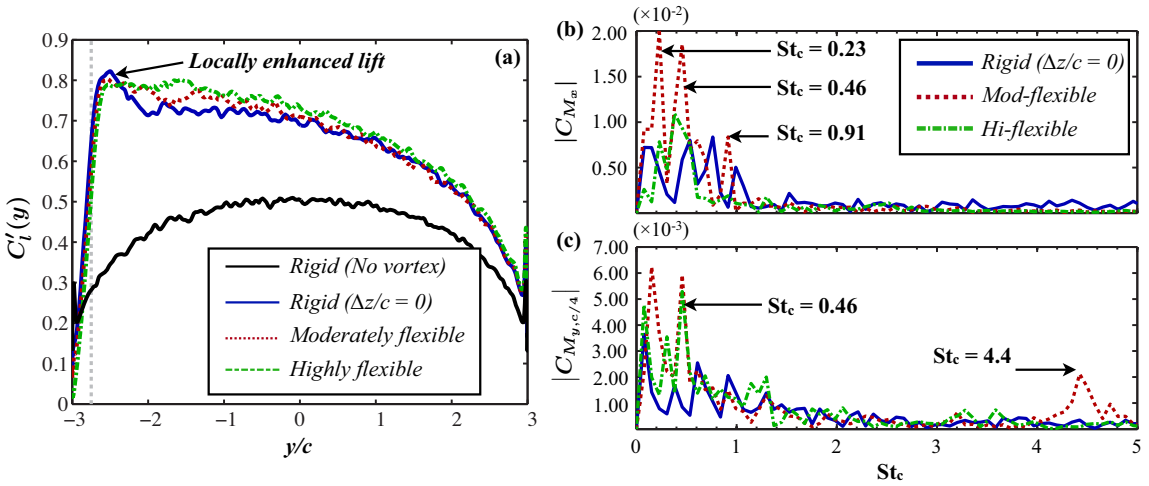

Figure 5.19: (a) Time-mean lift coefficient per unit span and Fourier analysis of (b) rolling moment, and (c) quarter-chord pitching moment coefficients for rigid and flexible wings

the moderately flexible plate. Similar amplitudes of this pitching behavior result in much larger twisting deformations for the highly flexible structure in Figure 5.14(b).

5.7 Isolation of static aeroelastic effects

Section 5.6 demonstrated wing flexibility can significantly influence vortex-surface interaction by enhancing instability upstream of the leading-edge consequently magnifying buffeting loads. Both static and dynamic components of the aeroelastic response were significant providing some uncertainty as to which is responsible for the main effects. This section decouples the static and dynamic components of the aeroelastic solutions by isolating the static deformations. This is done by deforming the rigid wing grid to match the time-mean deformations of the flexible wing cases, shown in Figure 5.20. Removal of the vortex-induced oscillations allows for a clearer explanation of the main influence provided by the static component. Computations for the rigid, bent-wing simulations were conducted in the same manner described for the undeformed rigid wing in Section 5.2.

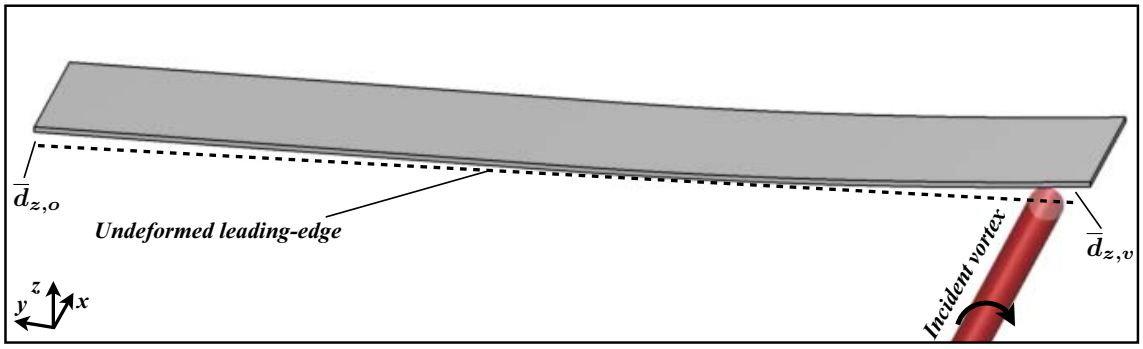

Figure 5.20: Statically deformed wing reproduces the time-mean bending deformation of the aeroelastic cases.

The impact of static deformation is perhaps most clearly portrayed using a pressure-side view of an iso-surface of instantaneous Q-criterion in Figure 5.21. Here, the full aeroelastic simulation of the moderately flexible wing and its statically deformed counterpart are compared in Figures 5.21(a) and (b) respectively, where the main vortical components for both cases are traced with dashed lines for clarity. It is readily apparent that the solutions obtained at comparable instances of time produce a nearly identical unsteady flow structure. This observation continues for the comparison of aeroelastic and statically deformed versions of the highly flexible wing in Figures 5.21(c) and (d). Again, a nearly identical topology appears for the two cases demonstrating the main contribution to the unsteady flow structure is the time-mean wing deformations. In further support of this conclusion, observation of the time-mean spanwise distribution of lift per unit length in Figures 5.22(a) and (b) for the moderate and highly flexible wings, respectively, demonstrates the average aerodynamic loading for the aeroelastic and static versions of each wing are nearly identical.

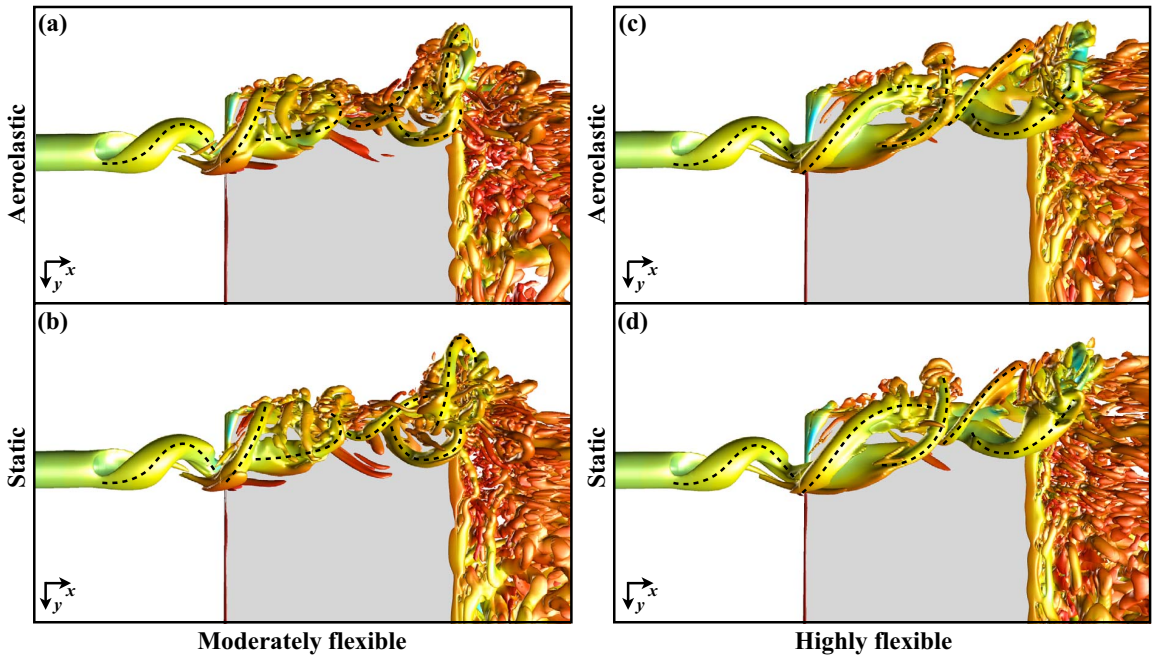

Figure 5.21: Bottom-side view of flow structure using an iso-surface of Q-criterion ($Q = 15$). Full aeroelastic and statically bent counterparts of the moderately flexible wing are shown in (a) and (b) while the same comparison is made for the highly flexible wing in (c) and (d).

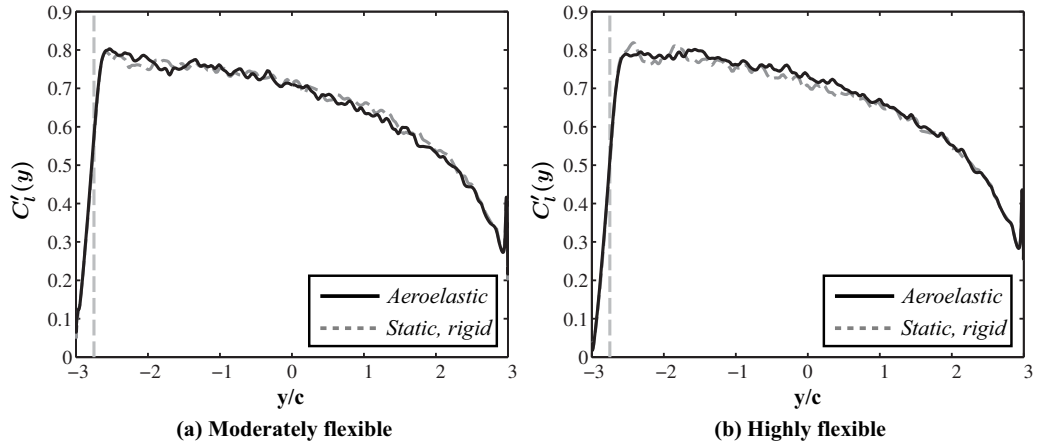

Figure 5.22: Time-mean lift coefficient per unit length along the wing span for (a) aeroelastic and static moderately flexible wings and (b) aeroelastic and static highly flexible wings.

A slice of turbulent kinetic energy contours intersecting the incident vortex in the xy-plane at $z/c = 0.04$ is shown in Figure 5.23 and provides a more discriminating comparison of the unsteady behavior for both versions of the flexible wings. The

full aeroelastic and statically bent simulations of the moderately flexible wing are compared in Figures 5.23(a) and (b) where the two cases show a nearly identical onset of unstable behavior. Some difference is found close to the leading-edge where a stronger region of k appears for the statically bent version of the moderate flexible wing immediately upstream of the leading-edge. This would suggest the dynamic component of the solution provides some degree of feedback to the incident vortex but secondary to the static component.

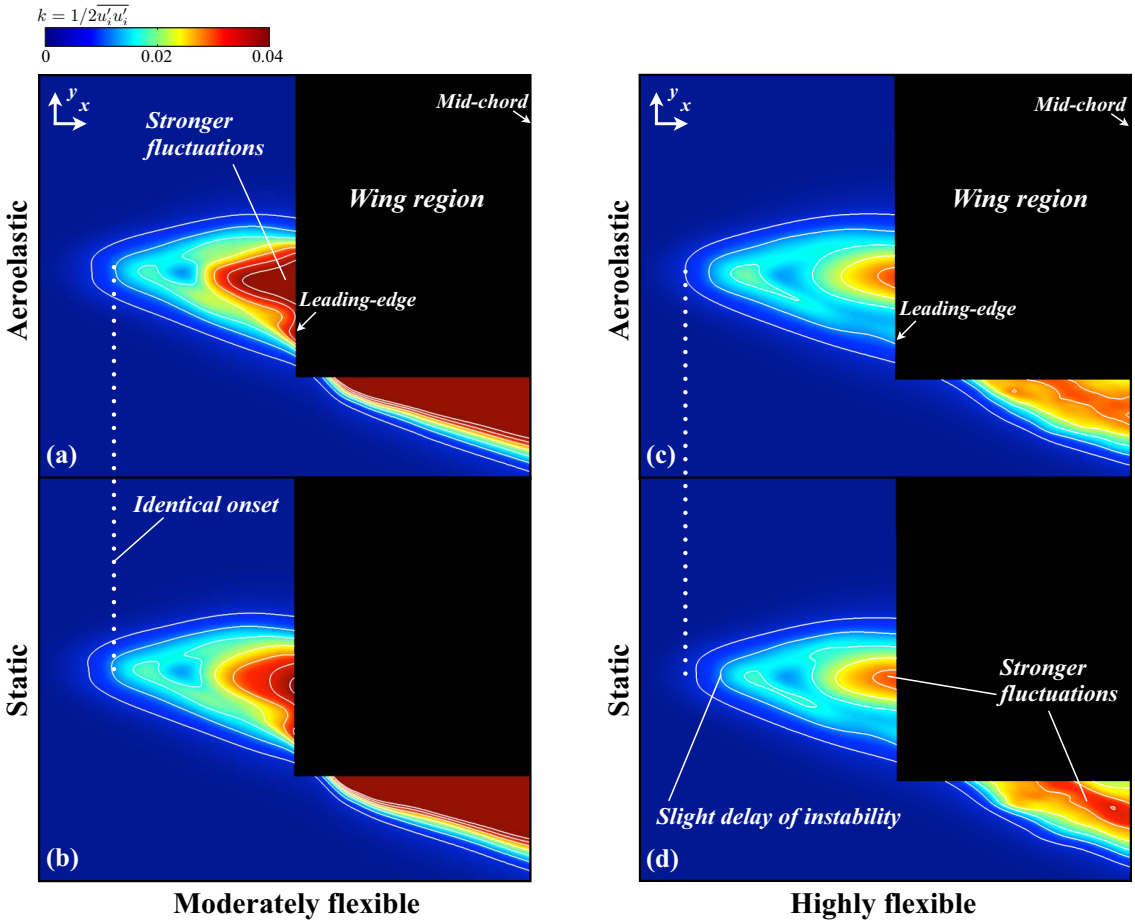

Figure 5.23: Top-down view of turbulent kinetic energy, k, contours at $z/c = 0.04$: (a) The moderately flexible wing is compared to (b) its statically deformed counterpart and the (c) highly flexible wing is compared with (d) its statically deformed counterpart.

In a similar manner, the highly flexible wing is compared to its statically bent counterpart in Figures 5.23(c) and (d) where the form of turbulent kinetic contours

are again nearly identical between the two cases. The static version differs from the aeroelastic counterpart in two ways. A minor delay in the onset of instability appears for the statically bent wing and a slight elevation in turbulent kinetic energy appears just upstream of the leading-edge and outboard of the wingtip. These observations also suggests some influence from the dynamic component, but again secondary to the time-mean deformation.

5.8 Summary

Aeroelastic computations using a high-fidelity implicit LES fluid solver coupled with geometrically non-linear Reisner-Mindlin plate elements were conducted to evaluate the influence of a streamwise-oriented vortex impinging upon both rigid and flexible wings. Each case consisted of an $AR = 6$ flat plate wing operating at a Reynolds number of $\mathrm{Re} = 30,000$ and a $\alpha = 5^\circ$ angle of attack. The vortex generator in this case was replaced by a q-vortex imposed at the inflow boundary and was aligned to provide a direct impingement with the leading-edge of the rigid wing. This approach removes complicating factors provided by a vortex generator where any unsteady response in the present configuration can be solely attributed to vortex-surface interaction.

Comparison with the tandem wing cases of Chapter 3 showed the main effects of vortex interaction tended towards that of the imposed vortex case as the leader-wing trailing vortex increased in size and strength. Namely, the spiraling instability beginning to emerge upstream of the leading-edge in the $\alpha_L = 8^\circ$ tandem wing case is much more apparent in the imposed vortex simulation. This unsteady helix spirals in a sense opposite the rotation of the swirling flow and alternates between the upper and lower surfaces of the wing thereby permitting a time-mean bifurcation of the vortical flow. The higher angle of attack and Reynolds number in the present chapter

invokes a more severe instability than that found in the previous work by Garmann and Visbal[102] providing further amplification of unsteady loads.

Three levels of flexibility were considered for evaluation including *rigid*, *moderately flexible*, and *highly flexible* wings, all pinned at the midspan. Both flexible wings exhibited a significant time-mean bending deflection on the vortex-side provided by vortex-induced asymmetric distribution of lift along the wingspan. This deformation effectively provides a small static vertical offset of the wing surface with respect the axis of the incident vortex. Small-amplitude dynamic bending and twisting deformations were found to be imposed by fluctuations in surface pressure provided by the unsteady flow structure. Frequency content of the vortex-induced oscillations were found to be distributed at harmonics and sub-harmonics of the primary instability of the incident vortex. The dominant component of the dynamic response was concentrated at roughly half the frequency of the vortex instability.

In general, flexibility was found to exacerbate the unsteady behavior of the incident vortex culminating in an earlier onset of instability and conducive to the growth of short-wave perturbations. This effect directly influenced the buffeting response of the flexible wing structures. Such unsteady loading can reduce the fatigue-life of airframes potentially leading to catastrophic failure or impose difficulty for aerodynamic control.

Uncertainty as to whether the dynamic or static component of the aeroelastic response provided the greatest influence on vortex instability motivated the isolation of static deformations. To this end, the rigid wing was deformed to match the time-mean deflections the both flexible plates providing only the static component of the aeroelastic response. Observation of time mean-loading and the instantaneous flow structure revealed nearly identical solutions between the full aeroelastic and statically deformed counterparts. Comparison of the turbulent kinetic energy within the incident vortex revealed a minor influence of the dynamic component of aeroelasticity in both wings. This analysis demonstrates the primary contribution to the shift in

unsteady response is provided by the effective static vertical offset elicited by vortex-induced loading. Feedback effects of the dynamic component appear to contribute but are secondary to the effect of static displacement.

Clearly, vertical positioning of the incident vortex provides important ramifications to the unsteady fluid dynamics in vortex-surface interactions. This identifies the need to more rigorously explore the broad implications of vertical positioning. Efforts to better understand and characterize vortex-surface interaction at different impingement locations are detailed in Chapter 6.

Chapter 6

Effect of vertical positioning

While the influence of relative lateral positioning was explored in Chapter 3 for tandem wings, as well as for an imposed vortex by Garmann and Visbal[5], the broad implications of relative *vertical* positioning for streamwise vortices are generally not well known. Previously, Chapter 4 modeled the impact of a trailing vortex on flexible wings and showed time-mean vortex-induced bending can effectively reposition the incident vortex and produce a different flow topology from the intended interaction. Chapter 5 followed this analysis with a stronger vortex/surface interaction and demonstrated the effective vertical shift provided by time-mean bending directly results in a large-scale growth in the unsteady flow structure. These observations suggest the relative vertical positioning of the vortex has important consequences for the flow behavior in streamwise vortex impingements and further motivate a more rigorous analysis of this specific parameter. The aim of the current chapter is to shed light on the ramifications of vertical positioning on the unsteady interactions of a streamwise-oriented vortex with a finite aspect-ratio flat plate wing. As will become apparent later, shifts in vertical offset subject the incident vortex to a spectrum of flow conditions, strongly dependent upon pressure gradients, that determine its unsteady behavior.

6.1 Flow structure

This section describes the impact of several vertical positions of the incident vortex on both the time-mean and unsteady flow structure about a finite aspect-ratio, *rigid*, flat plate wing. The same configuration as described in Section 5.1 is continued where the current problem encompasses the same mesh requirements. Therefore, grid independence is demonstrated in Section 5.3 and not repeated here. Several vertical positions of $-0.25 \leq \Delta z/c \leq 0.1$ are chosen at a single lateral position of $\Delta y/c = 0.25$, as shown in Figure 6.1. While a total of six vertical positions ($\Delta z/c = -0.25$, -0.10, -0.05, 0.00, 0.05, and 0.10) were explored for the present analysis, the discussion primarily focuses on the three cases of $\Delta z/c = -0.10$, 0.00, and 0.10 which represent most clearly the primary variations in flow structure. An identical wing without the incident vortex is included in the discussion as a point of reference. Each of these cases are descriptively referred to as *negative offset*, *direct impingement*, *positive offset*, and *no vortex* respectively throughout this article. Some discussion is provided for a larger offset of $\Delta z/c = -0.25$ which provides a weaker interaction, but promotes favorable aerodynamics.

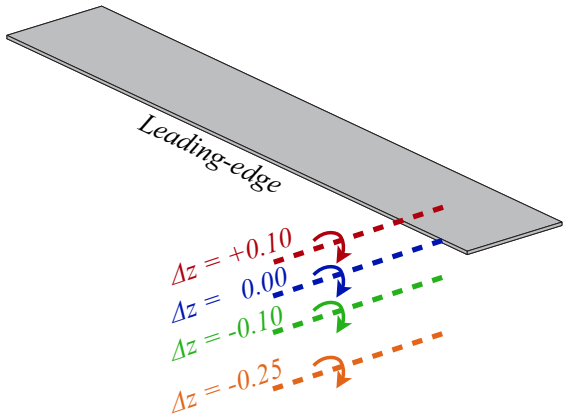

Figure 6.1: Initial vertical positioning, Δz, of the incident vortex relative to the wing.

The parameter Δz, as defined in Section 5.1, describes the initial vertical position

of the incident vortex at the inflow boundary, but does not necessarily convey the actual position of the vortex when it reaches the wing. The vortex was found to deflect upward as it approaches the wing due to flow accelerating over the leading-edge. In order to better define the vortex position, the actual vertical offset at $x/c = -0.5$ is provided as Δz_v in Table 6.1. An initial vertical offset of $\Delta z/c = 0$ results in a direct impingement with the leading-edge, higher Δz place the vortex above the wing, and lower Δz place it beneath the wing.

Table 6.1: Initial, Δz, and actual, Δz_v, vertical offsets measured at $x/c = -0.5$

	Vertical offset					
$\Delta z/c$	-0.25	-0.10	-0.05	0.00	0.05	0.10
$\Delta z_v/c$	-0.22	-0.06	-0.02	0.04	0.09	0.13

6.1.1 Time-mean flow structure

The time-mean three-dimensional flow structure related to the vortex interaction is well-portrayed using contours of time-mean streamwise vorticity at several chordwise planes in Figure 6.2. Beginning with the direct-impingment ($\Delta z/c = 0$) case provided in Figure 6.2(c), the time-mean incident vortex is shown to develop a region of diminished streamwise vorticity along its axis upstream of the wing, $x/c = -0.25$. This annular concentration of streamwise vorticity is due to the motion of an unstable laminar vortex and will become more apparent in Section 6.1.2. As the vortex impinges upon the leading-edge, $x/c = 0.01$, it bifurcates in a time-mean sense into upper and lower-surface components shown in Figure 6.2(c). The pressure-side component tends outboard as it propagates downstream consistent with mutual induction between the incident vortex and its mirror-image in the wing surface [63]. The suction-side component moves slightly inboard as it advances toward the trailing-edge. This time-mean bifurcation results from the incident vortex alternating between the upper and lower surfaces in the instantaneous flow. This unsteady process was previously

described in Chapter 5.

For the $\Delta z/c = -0.10$ offset, Figure 6.2(b), the streamwise vorticity contours reveal a similar 'hollow' core but further upstream ($x/c = -0.5$) than the $\Delta z/c = 0$ case. As the vortex approaches the leading-edge, the distribution of streamwise vorticity develops a more complex topology where a weaker inner-ring of streamwise vorticity, denoted in Figure 6.2(b) at $x/c = -0.25$, is visible. Beneath the wing, the predominant lower-surface component of the incident vortex develops a rather disorganized flow structure, $x/c = 0.01 - 1.0$, resulting from a fairly chaotic instantaneous flow field. As in the the previous case, the lower-surface component of the swirling flow tends outboard as it propagates downstream.

Placing the vortex above the wing ($\Delta z/c = +0.1$) in Figure 6.2(d) fails to elicit any remarkable change in the vorticity contours in the incident vortex as it approaches and then passes over the leading-edge. Above the wing, the time-mean flow reveals an eruption of secondary vorticity at $x/c = 0.25$ unique to the positive vertical offset cases and a more coherent upper-surface component than its counterpart in the $\Delta z/c = 0$ case.

Contours of time-mean streamwise velocity are shown for a spanwise plane intersecting the incident vortex core in Figure 6.3(a) and demonstrate several characteristic changes to axial velocity profiles in each vortex-wing interaction. The direct impingement case ($\Delta z/c = 0$) produces a large streamwise velocity deficit as the vortex approaches the leading-edge. This diminished flow speed becomes much more severe when the vortex is placed beneath the wing in the $\Delta z/c = -0.1$ case. When the vortex is above the wing, $\Delta z/c = +0.1$, the axial velocity accelerates with flow over the leading-edge alleviating the velocity deficit near the leading-edge.

Figure 6.3(b) shows contours of the time-mean pressure gradient, $\partial\overline{p}/\partial x$, on a spanwise plane intersecting the vortex core. For the $\Delta z/c = 0$ case, the incident vortex is subjected to an adverse streamwise pressure gradient associated with stagnation of

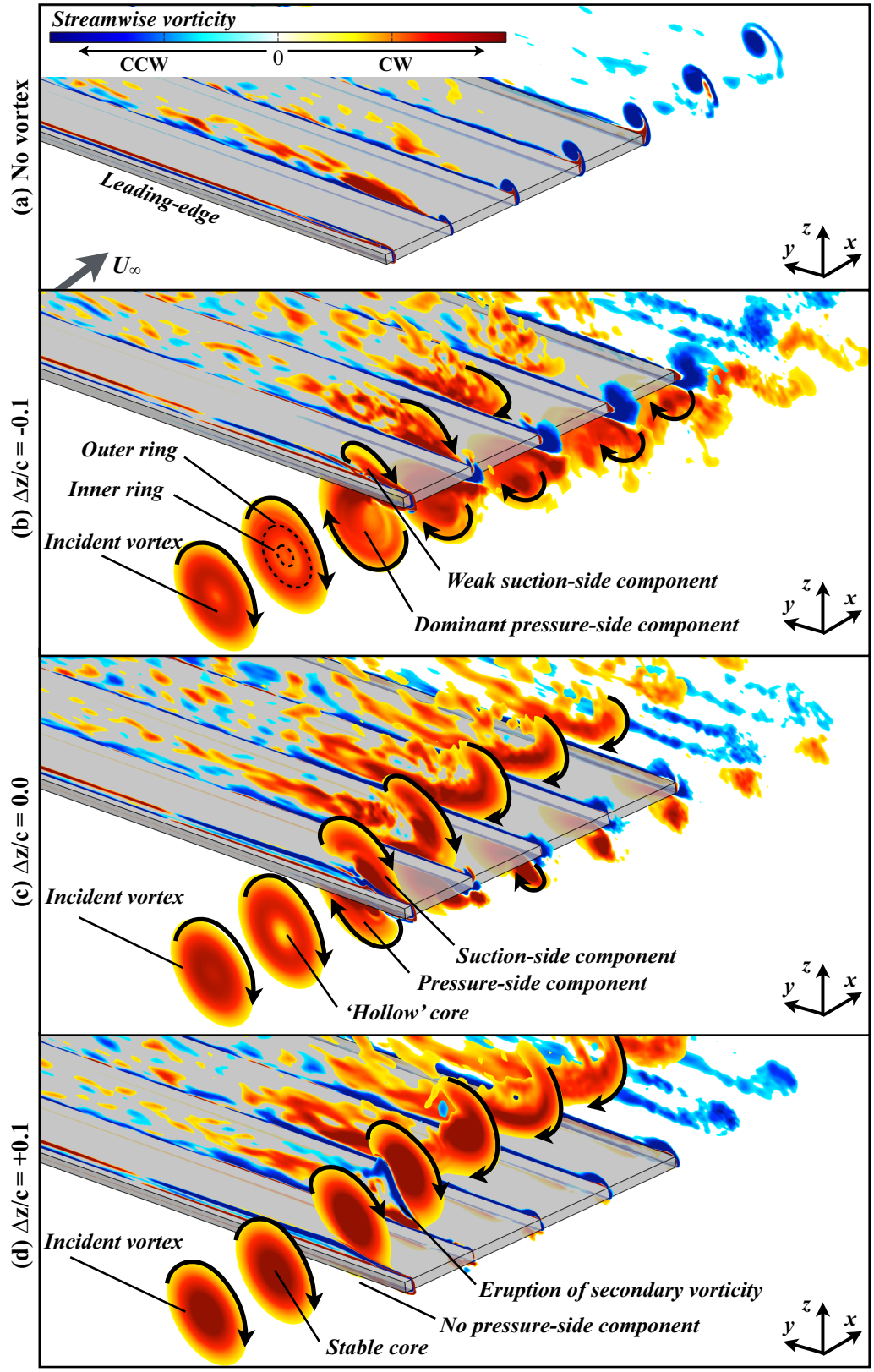

Figure 6.2: Slices of time-average streamwise vorticity at several chord-wise positions ($x/c = -0.5, -0.25, 0.01, 0.25, 0.50, 0.75, 1.00, 1.25, 1.50$). The wing is semi-transparent to provide visualization of pressure-side flow structure.

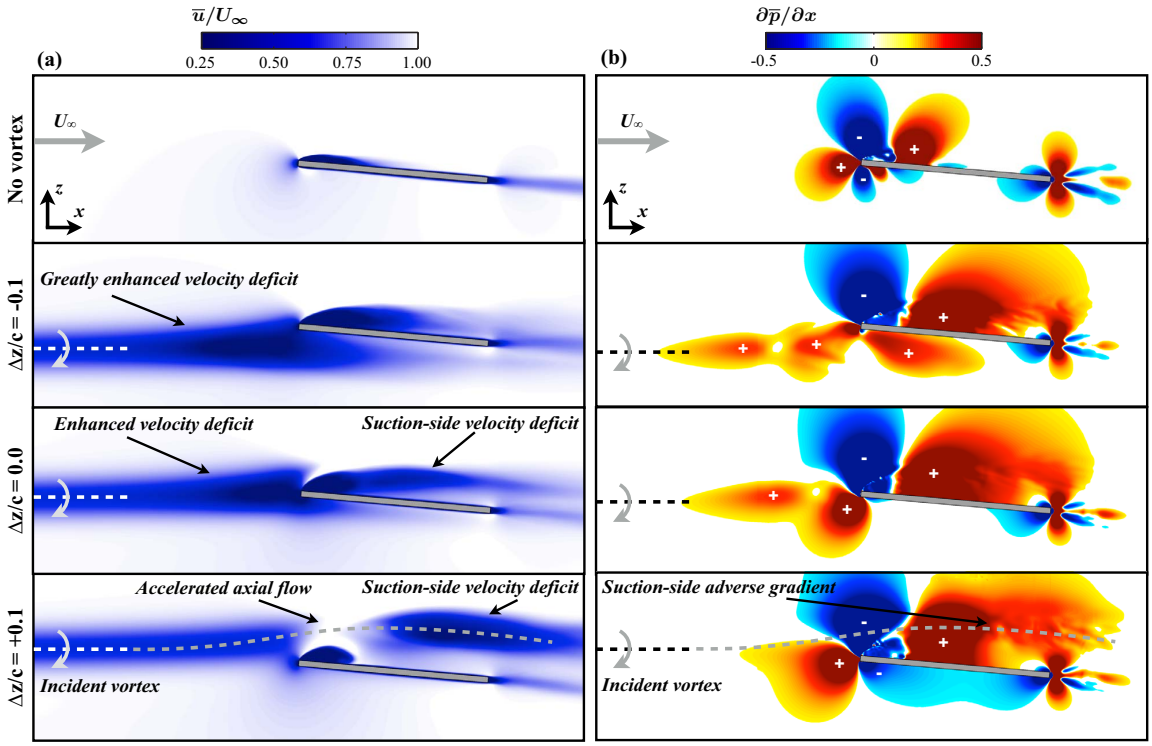

Figure 6.3: Contours of time-mean (a) streamwise velocity at $y/c = -2.75$ and (b) streamwise pressure gradient at $y/c = -2.75$ where '+' and '-' denote adverse and favorable pressure-gradient regions respectively.

flow against the leading-edge. The influence of the vortex-surface interaction is felt upstream of the leading-edge and manifests in the form of increasing pressure which would tend to decelerate the streamwise flow. For the $\Delta z/c = -0.1$ case, the pressure gradient induced by stagnation at the leading-edge is diminished compared to the $\Delta z/c = 0$ case, but results in an adverse gradient beneath the lower surface contrary to favorable $\partial\overline{p}/\partial x$ found on the pressure-side of the no vortex and $\Delta z/c = +0.1$ cases. In contrast, the $\Delta z/c = +0.1$ case shows the streamwise vortex permeating into a favorable $\partial\overline{p}/\partial x$ above the wing responsible for accelerating the core velocity of the incident vortex. Above the wing, the $\Delta z/c = +0.1$ case vortex is subjected to a large adverse $\partial\overline{p}/\partial x$ in the separated flow region near the mid chord. This results in a significantly diminished axial velocity in the vortex core shown in Figure 6.3(a) beyond the mid chord. These pressure gradient regimes characterize the effect of vertical position on the vortex-wing interaction and play a critical role in the unsteady behavior of the incident vortex addressed in more detail later.

Time-averaged surface pressure coefficient and surface-restricted streamlines are shown in Figure 6.4 for the upper surface and help to describe the near-surface flow topologies for each case. The suction-side surface pressure and streamline patterns appear to be qualitatively similar for all vertical offsets and several characteristics describe the changes in the upper surface flow topology from the isolated wing. A dashed white line is superimposed on the streamline topologies of Figure 6.4 and used to denote the approximate location of the reattachment line. Compared to the no vortex case, the reattachment line has moved downstream for each of the vertical positions. This enhanced flow separation is a consequence of an increased effective angle of attack provided by the incident vortex upwash. Although not uniform along the span, growth in the separation bubble is reminiscent of the flow topology observed for isolated wings at several higher angles of attack simulated by Visbal and Garmann[140]. A swirling streamline pattern appears just inboard of the incident

vortex and coincides with a region of enhanced suction. A larger negative vertical offset of $\Delta z/c = -0.25$ is provided in Figure 6.4(b) and exhibits the same suction-side characteristics as the closer vertical positions. Flow separation is reduced for the $\Delta z/c = -0.25$ case compared to the closer vortex positions, indicated by the approximate line of reattachment, due to a weaker upwash provided by the larger offset of the incident vortex.

A more significant differentiation between vertical positions appears in the time-mean pressure-side surface-restricted streamlines and $\overline{c}_p$ contours in Figure 6.5. The imprint of the pressure-side incident vortex component is visible for the $\Delta z/c = 0$ case as a band of decreased pressure near the wingtip and traced by a dashed white line. This locally increased suction strengthens in the presence of the more dominant lower-surface component of the $\Delta z/c = -0.1$ case. Both of these vertical offsets exhibit a streamline pattern that tends more outboard than that for the isolated wing and, as previously discussed, is consistent with the self-induced velocity between a vortex and its mirror-image in the wing surface. The band of suction disappears for $\Delta z/c = +0.1$ which lacks a pressure-side vortex component. A small low-pressure region appears for the $\Delta z/c = +0.1$ case near the leading-edge wingtip due to flow separation induced by vortex downwash.

One additional case is introduced here with a larger negative vertical offset of $\Delta z/c = -0.25$ which promotes a significant change in the lower-surface surface pressures. This case elicits a streamline pattern that tends outboard, again consistent with mirror-image effects of the wing surface, and most notably, a relatively strong suction region near the wingtip which is shown later to help counteract the negative vortex-induced rolling moment in Section 6.1.4.

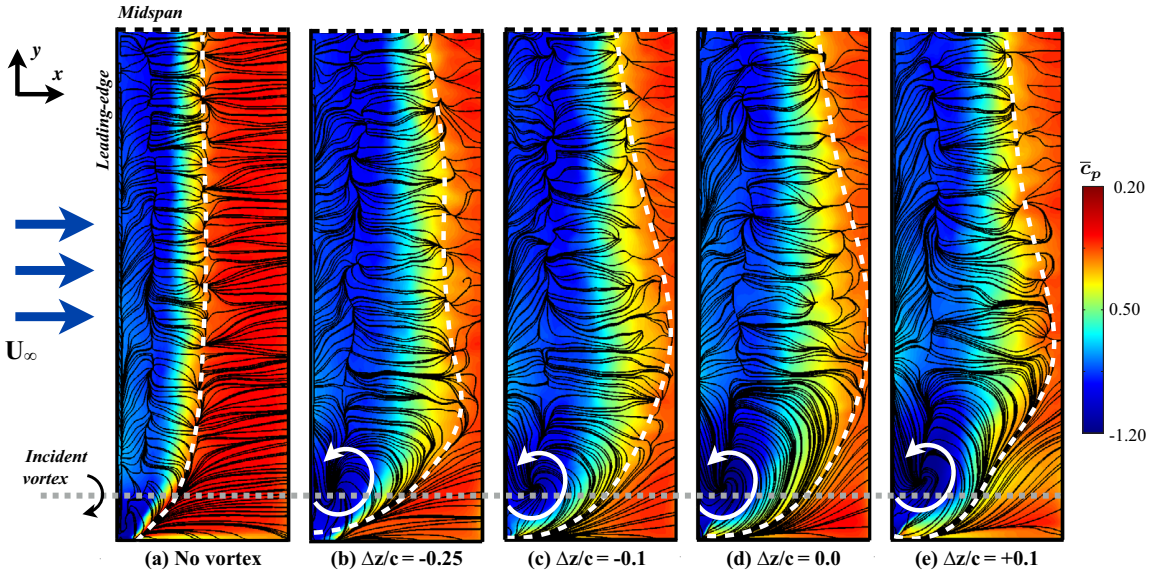

Figure 6.4: Contours of time-mean suction-side C_p and surface restricted streamlines. A white dashed line marks an approximation for the line of reattachment.

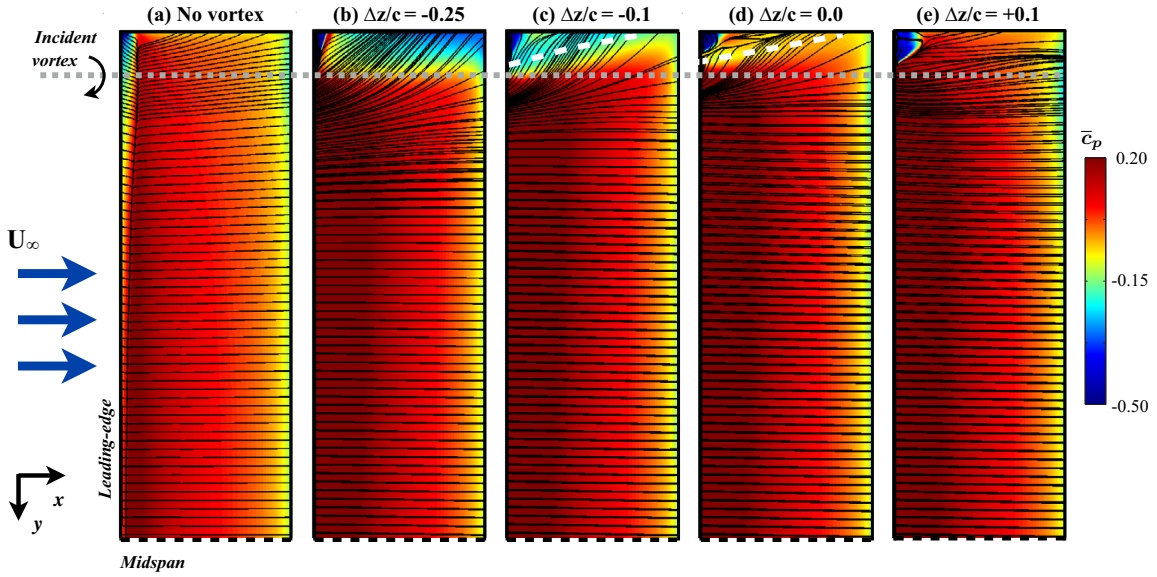

Figure 6.5: Contours of time-mean pressure-side C_p and surface restricted streamlines.

6.1.2 Unsteady flow structure

The instantaneous flow structure more clearly demonstrates the main effects of vertical positioning. Snapshots from the instantaneous flow are provided here for four

vertical positions and an isolated wing in Figure 6.6. Starting with a top-view of the direct-impingement case ($\Delta z/c = 0$) in Figure 6.6(g), the most notable feature is a helical instability that develops just upstream of the leading-edge which spirals in a sense opposite the rotation of the incident vortex. The form of vortex instability in the present case is responsible for the annular concentration of time-mean streamwise vorticity upstream of the wing in Figure 6.2. Additionally, it allows the unsteady helix to alternate between the upper and lower sides of the wing contributing to both the suction (Figure 6.6(g)) and pressure-side (Figure 6.6(h)) vortical components that appear in the time-mean flow (Figure 6.2(c)).

Figures 6.6(e) and (f) show the instantaneous flow for the $\Delta z/c = -0.10$ case. This negative vertical offset causes the unsteady helix to advance further upstream and become more pronounced than the direct impingement case consistent with the effect of time-mean deflection of the flexible wing cases evaluated in Chapter 5. The suction-side component of the incident vortex, shown in Figure 6.6(e), has diminished due to the vertical shift in position which allows the vortex to pass primarily along the lower surface. Figure 6.6(f) depicts the flow structure of the incident vortex as it passes beneath the wing. At this point the vortex maintains a spiraling motion, but has become very chaotic as it interacts with the lower surface exhibiting large amplitude fluctuations in the local flow field. While a direct impingement elicits an unsteady behavior upstream, a small vertical shift in the position generates a highly unsteady flow on the pressure-side.

Conversely, placing the incident vortex with a small positive vertical offset elicits a markedly different behavior. Figures 6.6(i) and (j) show top and bottom views, respectively, of the instantaneous flow structure for the $\Delta z/c = +0.10$ case. Most notably, this vertical position completely removes the vortex instability upstream of the wing. The incident vortex, which now passes over the suction-side, remains a stable, coherent structure until roughly the mid-chord where it begins to exhibit a

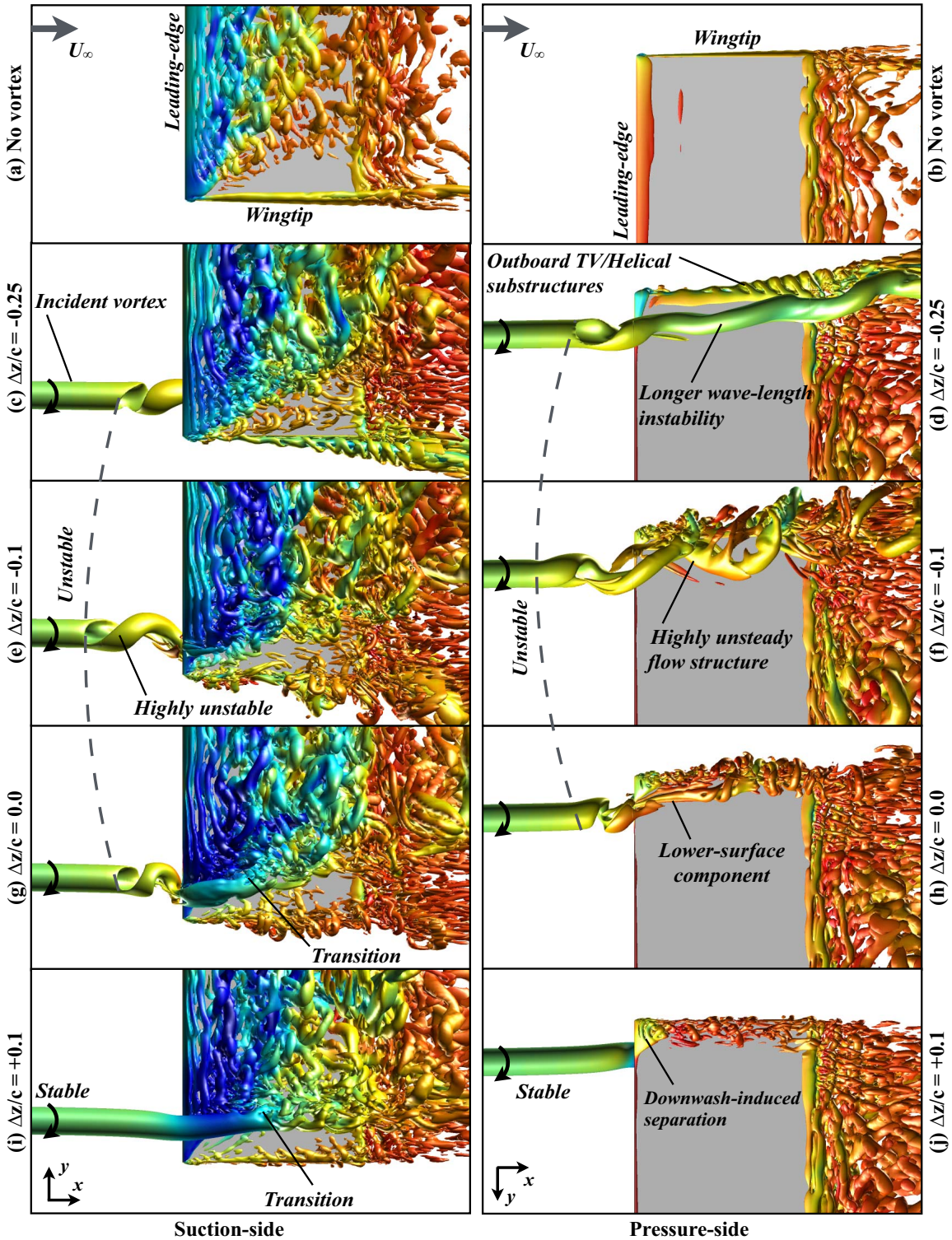

Figure 6.6: An iso-surface of instantaneous Q-criterion ($Q = 15$) for (left) top and (right) bottom views of the isolated wing and several vertical positions. A dashed line roughly locates the onset of instability.

transitional flow structure. Flow instabilities first appear on the inboard side of the vortex due to the influence of the closely positioned unsteady separated shear layer. Further downstream, the vortex develops a clear helical pattern on the outboard side visible in the side-view of instantaneous Q-criterion shown in Figure 6.7. This behavior indicates higher modal instability likely induced by higher frequency perturbations emanating from transitional flow in the inboard side of the vortex.

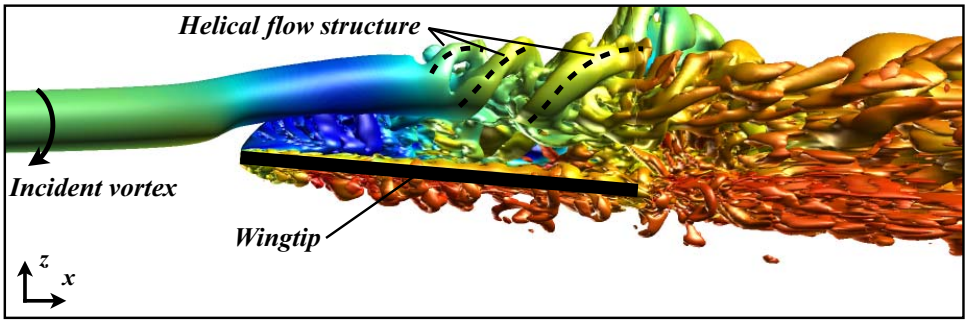

Figure 6.7: An iso-surface of instantaneous Q-criterion ($Q = 15$) for a side view of the $\Delta z/c = +0.10$ case.

One final offset of $\Delta z/c = -0.25$ is presented in figures 6.6(c) and (d) to provide a case that represents a weaker vortex-surface interaction. The flow structure for this position is best represented in the lower-side view of Figure 6.6(d) where a similar helical instability forms upstream of the wing leading-edge. However, due to the weaker interaction, this instability appears further downstream compared to the $\Delta z/c = -0.10$ case and results in a less pronounced, longer wavelength undulation that tends outboard as it propagates downstream. The large offset of the vortex places the wing in line with the outboard-oriented tangential flow on the top side of the vortex. This effect permits the formation of a tip vortex which is driven outboard of the wingtip by the tangential flow of the incident vortex, shown in Figure 6.6(d), and enveloped by helical substructures formed in the tip vortex feeding sheet.

Contours of the mean-squared pressure fluctuations, $\overline{p'p'}$, on the lower-surface are provided in Figure 6.8. The most significant pressure-side fluctuations appear near the

wingtip for the $\Delta z/c = -0.1$ case, traced by a dashed line. The highly unsteady flow structure provided by the negative vertical offset, shown in Figure 6.6(d), generates a significant level of pressure fluctuations on the wing. The direct impingement, $\Delta z/c = 0$, elicits a similar, but weaker imprint of $\overline{p'p'}$ near the wingtip. The large negative offset, $\Delta z/c = -0.25$, results in minimal pressure fluctuations on the lower surface despite exhibiting a stronger influence on the time-mean lower-surface pressure in Figure 6.5(b).

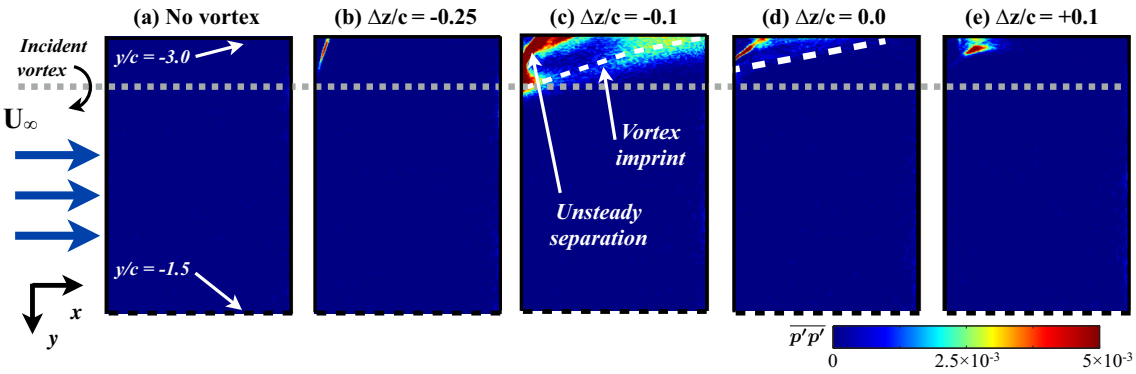

Figure 6.8: Contours of pressure-side mean-squared surface pressure fluctuations.

Another concentration of surface pressure fluctuations appears near the leading-edge and wingtip corner, annotated in Figure 6.8(c) for the $\Delta z/c = -0.1$ case, is indicative of the influence of unsteady separation provided by the spiraling instability on the downwash-side of the incident vortex. The influence of this effect on unsteady loading could be more severe for a more inboard position, given a larger region of pressure-side separation, at the same negative Δz and would be an interesting topic for further analysis.

Velocity fluctuations were collected at two locations upstream of the leading-edge for each case and used to compute the average turbulent kinetic energy spectra within a $0.1/c \times 0.1/c$ sample window centered about the incident vortex shown in Figure 6.9(a). Figure 6.9(b) portrays the energy spectra for several vertical offsets at $x/c = -0.45$ and provides a quantitative comparison of the flow instabilities. Well-defined

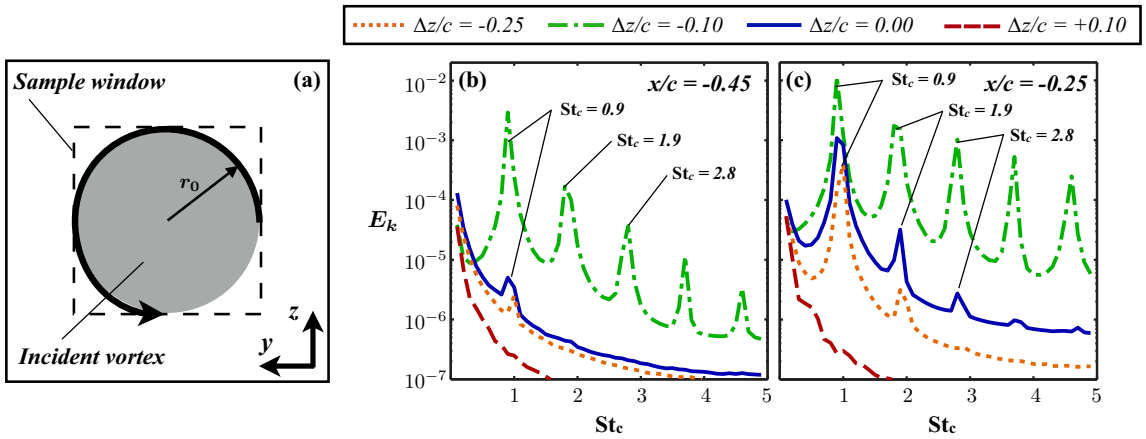

Figure 6.9: Turbulent kinetic energy spectra averaged over the sample window shown in (a) at (b) $x/c = -0.45$ and (c) $x/c = -0.25$ upstream of the wing.

frequencies are clearly depicted for the $\Delta z/c = -0.1$ case which exhibited the most pronounced helical instability in Figure 6.6. The dominant non-dimensional frequency $\mathrm{St}_c = fc/U_\infty$ of $\mathrm{St}_c = 0.9$ corresponds with the period of the large spiral in the incident vortex upstream of the wing. Several additional clearly-defined frequencies are also found at harmonics of the dominant peak for this case indicating higher modes of instability not well portrayed in Figure 6.6. The same frequencies appear for the $\Delta z/c = 0$ and -0.25 cases at a location closer to the leading-edge in Figure 6.9(c), but at much lower amplitudes than the more unstable $\Delta z/c = -0.1$ case. As expected, no frequency content stands out for the stable $\Delta z/c = +0.1$ case at either streamwise location. While the level of instability in the incident vortex is strongly affected by vertical position, the consistent timescales of the instability indicate its form evolves according to the properties of the incident vortex rather than the specific interaction.

6.1.3 Analysis of turbulence statistics

Figure 6.10 shows slices of the turbulent kinetic energy (TKE) contours at several streamwise positions for three vertical offsets and the isolated wing. Here, TKE is

defined as $k = 1/2\overline{u_i' u_i'}$ where u_i' are the fluctuating components of velocity in each coordinate direction and $i \equiv (1, 2, 3)$ refers to the x, y, and z-coordinates respectively. A transparent iso-surface of time-mean Q-criterion is superimposed to provide reference between regions of high k and the location of dominant vortical structures. Turbulent kinetic energy is a measure of the level of fluctuations from the time-mean flow in transitional and turbulent regions and also reveals instabilities in laminar flow. Both the $\Delta z/c = -0.1$ and 0 cases portray elevated turbulent kinetic energy within the incident vortex in front of the wing demonstrating an unsteady response to the upstream influence provided by the aerodynamic surface. Fluctuations appear earlier for the $\Delta z/c = -0.1$ case which experiences a more pronounced upstream response. Turbulent kinetic energy is notably absent upstream of the wing for the $\Delta z/c = +0.1$ case demonstrating flow instability in the incident vortex is mitigated for this vertical position.

Above the wing, all three vortex interaction cases demonstrate an elevated region of turbulent kinetic energy in the separated region inboard of the vortex encounter compared to the isolated wing. This behavior is consistent with enhanced separation due to an increased effective angle of attack provided by the upwash side of the incident vortex. While the suction-side contours of k are qualitatively similar for the $\Delta z/c = -0.1$ and 0 cases, the positive offset ($\Delta z/c = +0.1$) elicits several notable differences. Near the leading-edge, $x/c = 0.25$, high levels of turbulent kinetic energy appear within the shear layer of the separated flow. Further downstream, the incident streamwise vortex begins to show signs of instability. This appears first at $x/c = 0.5$ as a protrusion of turbulent kinetic energy into the vortex from the separated region. Here, the stable, laminar vortex has become receptive to disturbances provided by its juxtaposition with the separated flow region on its inboard side. Toward the trailing-edge, $x/c = 0.75$, kinetic energy fluctuations envelope the streamwise vortex indicating flow instability has permeated the entirety of the swirling flow region in

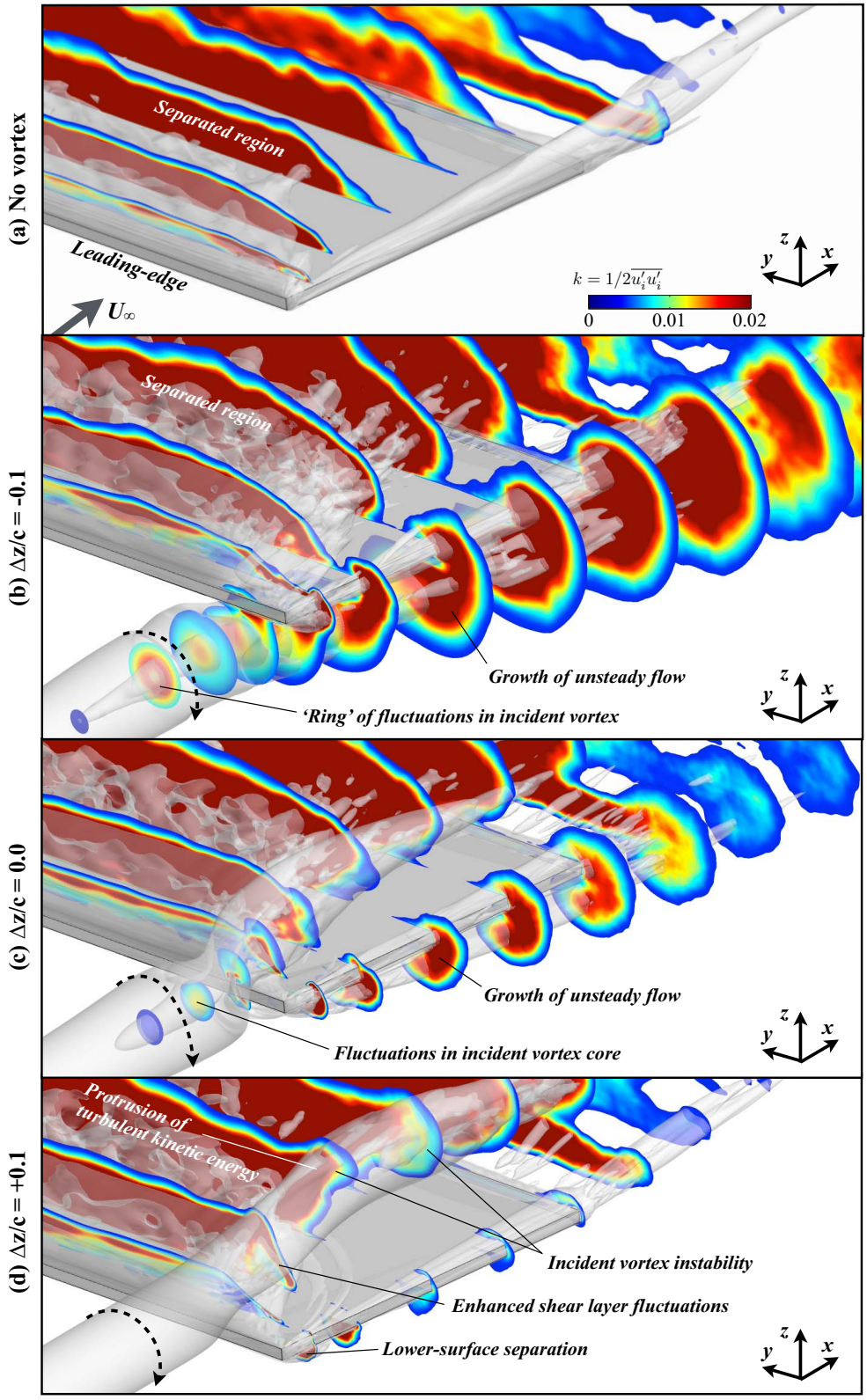

Figure 6.10: Slices of turbulent kinetic energy (k) at several chord-wise positions ($x/c = -0.50, -0.25, -0.10, 0.01, 0.10, 0.25, 0.50, 0.75, 1.00, 1.25, 1.50, 1.75$) and transparent iso-surface of time-mean Q-criterion ($Q = 5$). The wing is semi-transparent.

the form of a helical pattern visible in Figure 6.7.

A notable differentiation in turbulent kinetic energy contours appears in the pressure-side flow structure. The lower component of the direct-impingement ($\Delta z/c = 0$) vortex shows growing levels of turbulent kinetic energy beneath the wing as a consequence of its close interaction with the pressure-side surface. The negative vertical offset ($\Delta z/c = -0.1$) elicits a similar behavior, but is significantly more pronounced consistent with the highly unsteady flow field for this case. The $\Delta z/c = +0.1$ case generates comparatively little turbulent kinetic energy beneath wing with only a small region near the wingtip due to downwash-induced flow separation on the outboard side of the incident vortex.

Figure 6.11 provides contours of the so-called turbulent kinetic energy production ($\mathcal{P} = -\overline{u_i' u_k'}\,(\partial \overline{u}_i/\partial x_k)$) at several streamwise slices for the isolated wing and several vertical offsets. This quantity represents the rate of transfer of energy from the mean flow to fluctuating components and provides insight into the growth of unsteady flow behavior. Upstream of the wing, both the negative offset ($\Delta z/c = -0.1$) and direct impingement ($\Delta z/c = 0$) vortices exhibit a ring of $\mathcal{P}$ about the vortex axis. This well-organized annular concentration of turbulence production is consistent with the growth rate of helical mode instabilities for a q-vortex [141] which are maximum at a particular radial position within the vortex core.

For the positive vertical offset case ($\Delta z/c = +0.1$), no turbulence production appears upstream of the wing consistent with a stable incident vortex. Above the wing at $x/c = 0.5$, $\mathcal{P}$ contours provide insight into the transitional nature of the incident vortex as it passes over the suction surface. Here, an annular concentration of turbulence production appears in the outboard side of the incident vortex indicating the growth of helical modes, visible in Figure 6.7, and reminiscent of those observed upstream for the lower vertical positions. The unstable behavior of the incident vortex as it passes over the upper surface appears to be influenced first by interaction

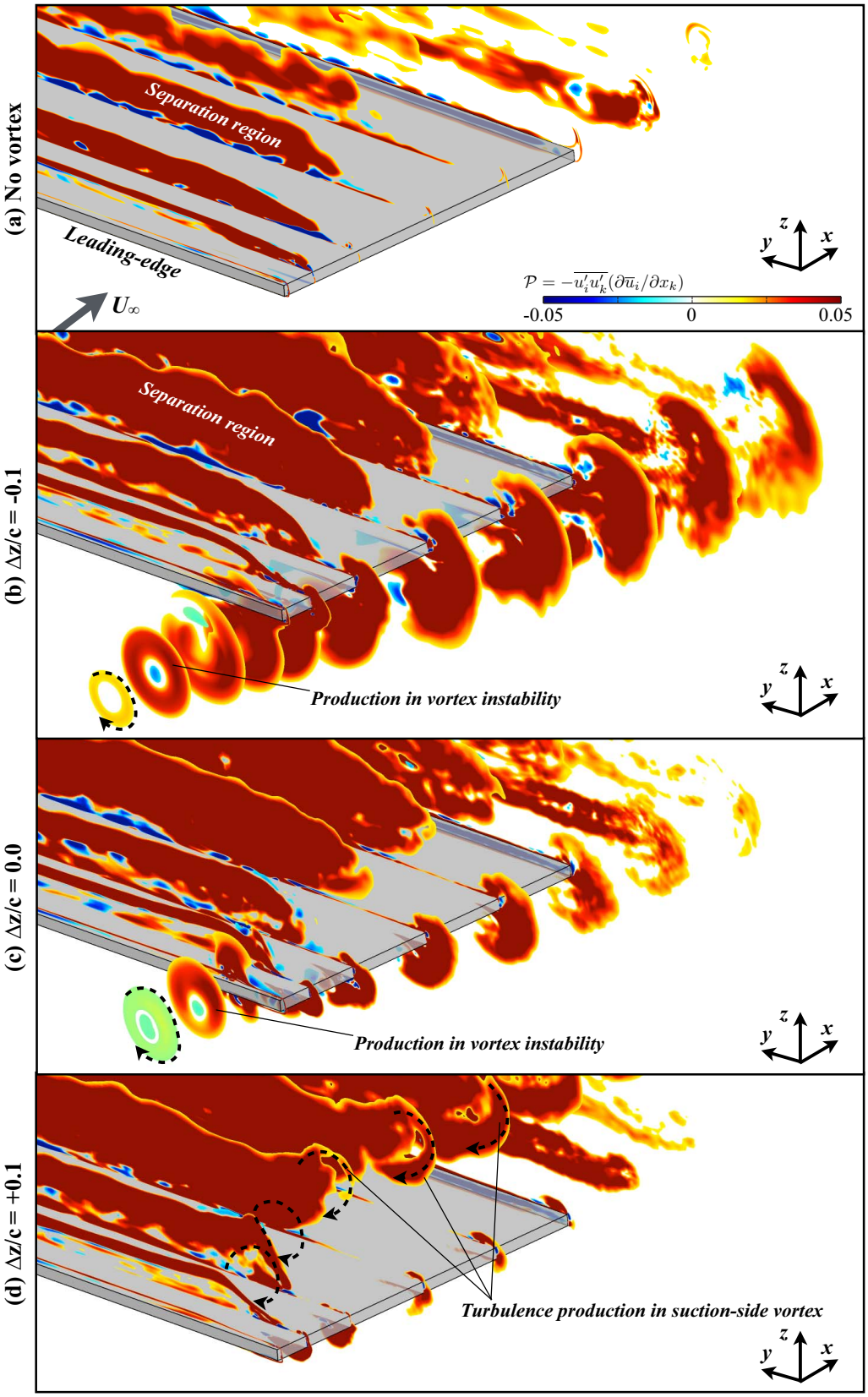

Figure 6.11: Slices of turbulence production ($\mathcal{P}$) at several chord-wise positions ($x/c = -0.40, -0.25, -0.10, 0.01, 0.10, 0.25, 0.50, 0.75, 1.00, 1.25, 1.50$). The wing is semi-transparent.

with fluctuations in the separated region followed by the natural growth of instability modes from short-wave perturbations emanating from the inboard transitional flow.

Finally, a measure of turbulence viscosity is portrayed in Figure 6.12 at several streamwise slices upstream of the leading-edge. This quantity is defined here as

$$\nu_t = -\left(\frac{\overline{u_i' u_j'} S_{ij}}{2 S_{kl} S_{kl}}\right) \tag{6.1}$$

where $S_{ij} = \frac{1}{2}\left(\frac{\partial \overline{u}_i}{\partial x_j} + \frac{\partial \overline{u}_j}{\partial x_i}\right)$. This definition provides an approximation to a linear eddy viscosity operator through a least-squares fit to the Reynolds stresses[142]. Essentially, these plots provide a good indication of what an eddy viscosity model would need to look like to provide the correct turbulence production, $\mathcal{P}$, in a turbulence model. It is currently unclear if this is the best approach for modeling guidelines in this case, but the following discussion provides a starting point on describing the complexities of evaluating the unsteady behaviors in lower-fidelity models.

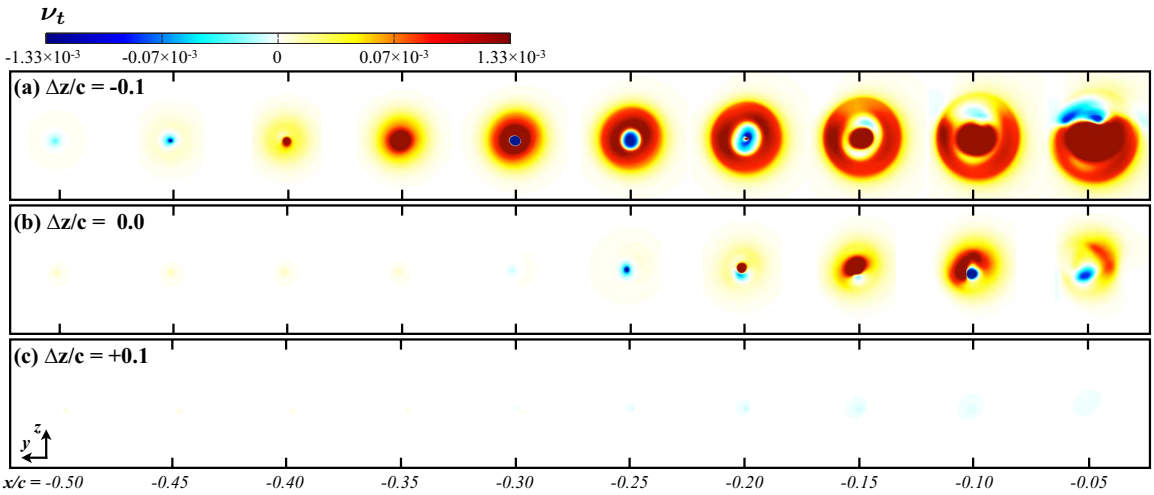

Figure 6.12: Slices of turbulence viscosity, ν_τ for (a) $\Delta z/c = -0.1$, (b) $\Delta z/c = 0$, and (c) $\Delta z/c = +0.1$.

Figure 6.12(a) shows ν_t for the $\Delta z/c = -0.1$ case. The plots begin with a small region of negative ν_t at $x/c = -0.5$ at the center of the vortex. This concentration of ν_t appears to switch sign approximately every $\Delta x/c = 0.1$ before a final region of

positive ν_t, beginning at $x/c = -0.2$, quickly grows and envelopes most of the vortex just before the leading-edge, $x/c = -0.05$. Outside of the central region, a ring of positive ν_t follows well the trends of $\mathcal{P}$ shown in Figure 6.11(b).

The same data is shown for the $\Delta z/c = 0$ case in Figure 6.12(b). Here, ν_t appears at $x/c = -0.5$ as a very weak region of positive ν_t. Little changes until $x/c = -0.3$ where this small concentration switches sign and becomes more intense by $x/c = -0.25$. Around $x/c = -0.2$, cohabiting regions of positive and negative ν_t exist at the center of the vortex where the growth of positive ν_t finally begins to dominate as the vortex approaches the leading-edge. The ν_t plots for the $\Delta z/c = +0.1$ case, shown in Figure 6.12(c), exhibit very little information of interest as can be expected for the stable incident vortex. A very faint region of negative ν_t appears at $x/c = -0.2$ but is most likely due to slight variations over time in the otherwise stable, laminar vortex.

6.1.4 Aerodynamic loads

Figures 6.13(a-d) provide a comparison of the time-mean lift, drag, lift-to-drag ratio, and rolling moment coefficient, respectively, for all vertical positions and the isolated wing. Each of these quantities demonstrate little change with vertical placement of the vortex for the range of positions considered. In contrast, Garmann and Visbal[5] showed the time-mean loads, the rolling moment in particular, were more significantly affected by the lateral placement of the incident vortex.

While time-mean loads appear to be less sensitive to vertical placement of the incident vortex, vertical offset has more significant implications for the unsteady loading as demonstrated by the root-mean-square rolling moment fluctuations $C_{M_{x,\mathrm{RMS}}}$ portrayed in Figure 6.13(e). $C_{M_{x,\mathrm{RMS}}}$ is largest for the $\Delta z/c = -0.1$ case consistent with enhancement of lower-surface pressure fluctuations, Figure 6.8(c), provided by the most unstable incident vortex. Increasing the vertical position to a direct im-

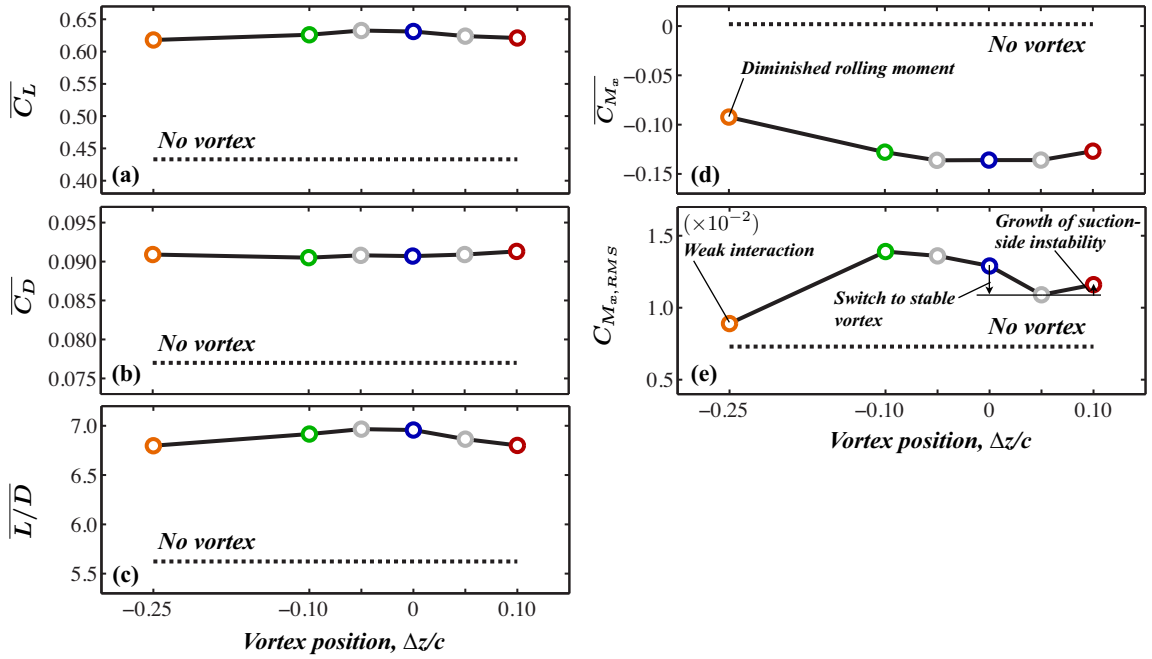

Figure 6.13: Time-mean (a) lift, (b) drag, (c) lift-to-drag ratio, (d) rolling-moment coefficient and (e) root-mean-square fluctuations of rolling-moment for several vertical positions

pingement, $\Delta z/c = 0$, reduces rolling moment fluctuations as the instability begins to attenuate. A decrease in $C_{M_{x,\mathrm{RMS}}}$ appears between the direct-impingment case, $\Delta z/c = 0$, and the small positive offset, $\Delta z/c = +0.05$, cases where the upstream vortex instability disappears. $C_{M_{x,\mathrm{RMS}}}$ increases between the $\Delta z/c = +0.05$ and $+0.1$ cases but remains below values for vortex positions that experience upstream instability. The increase in $C_{M_{x,\mathrm{RMS}}}$ between the two positive vertical offset cases ($\Delta z/c = +0.05$ and $+0.1$) is likely a consequence of a growing suction-side vortex instability visible in Figure 6.7.

The lowest rolling moment fluctuations occur for the $\Delta z/c = -0.25$ case which have dropped to values close to the isolated wing. The weaker interaction removes much of the detrimental unsteady loading ($C_{M_{x,\mathrm{RMS}}}$) and trim penalty provided by a negative induced rolling moment ($\overline{C}_{M_x}$), but retains much of the $\overline{L/D}$ benefit. In the context of formation flight, a large negative vertical offset might be attractive due to its unsteady load characteristics and reduced trim penalties. Furthermore,

the adverse consequences of vortex-induced spanwise bending, described in Chapter 5, would be mitigated as the wing would only deform away from the most unstable regimes.

6.2 Discussion on vortex stability

The preceding sections of this chapter dissected the unsteady flow structure for a small range of vertical offsets and demonstrated the implications of vertical positioning on the incident vortex behavior. This section connects the physical mechanisms of the vortex-surface interaction to the instability properties of streamwise-oriented vortices. Leibovich and Stewartson[80] derived a stability criterion for the q-vortex based solely on the swirl parameter, q, which is a ratio of the tangential to streamwise velocities. Their criteria describes a sufficient condition of $q < \sqrt{2}$ for the q-vortex that permits growth of disturbances within the vortex core. The initial value of the swirl ($q_0 = 2$) used in this work was chosen to be well within the stable regime. Nonetheless, vortex-wing interactions develop unsteady behavior reminiscent of helical instabilities for a q-vortex.

Figure 6.14(a) plots the swirl parameter, q, of the incident vortex upstream of the leading-edge which varies from its initial stable value in the streamwise direction due to the upstream influence provided by the wing. The direct-impingement, $\Delta z/c = 0$, and all negative offset cases ($\Delta z/c = -0.05$ to -0.25) result in a swirl parameter that diminishes as the vortex approaches the wing falling well below the stability threshold. This behavior indicates the vortex becomes susceptible to disturbances before reaching the wing. A helical instability develops just downstream from where the swirl falls below the stability threshold in each of these vertical positions. The swirl for the $\Delta z/c = -0.1$ case crosses the stability threshold further upstream than that for the $\Delta z/c = 0$ case consistent with the earlier onset of unstable behavior shown

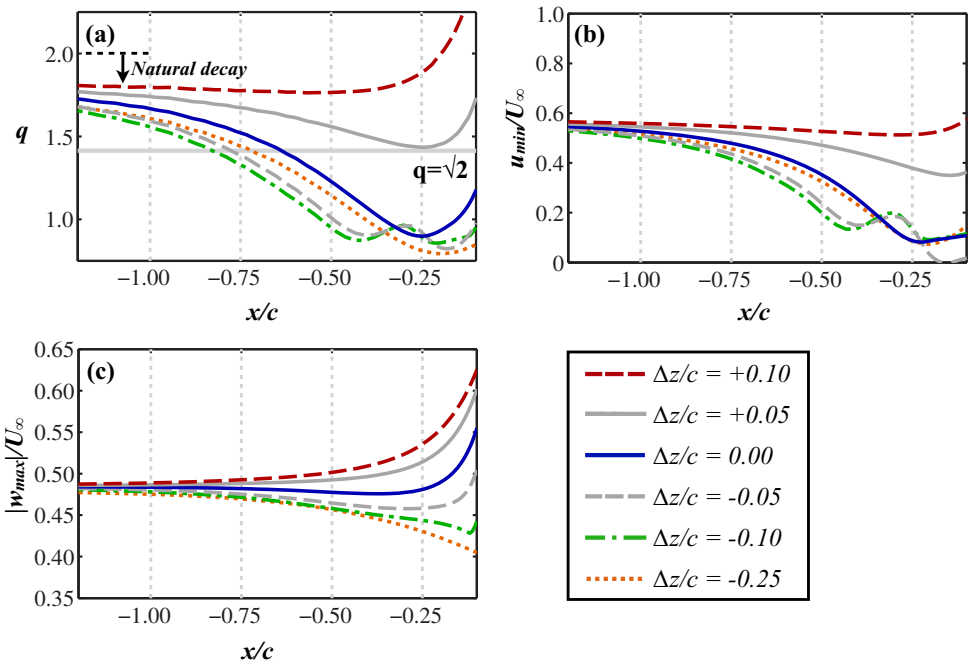

Figure 6.14: Time-mean (a) swirl parameter, (b) minimum streamwise velocity, and (c) maximum tangential velocity versus the streamwise direction upstream of the leading-edge for several Δz.

in Figure 6.6. The swirl parameter for the two positive offset cases, $\Delta z/c = +0.05$ and $+0.1$, show the incident vortex remains within the stable regime upstream of the wing consistent with the lack of unsteady behavior for both cases. While the stability criterion of Ref. [80] is not exclusively necessary for instability, the onset or lack of instability appears to be well-predicted by the linear stability properties for helical mode instability of the incident vortex in the present cases.

The swirl parameter shown in Figure 6.14(a) depends on the time-mean minimum axial velocity, u_{min}, and maximum tangential velocity, w_{max}, at each streamwise position which are plotted in Figures 6.14(b) and (c) respectively. While $q = 1.567 w_{max}/(U_\infty - u_{min})$ is linearly proportional to both values, the streamwise variation of u_{min} within the vortex clearly dominates the trends portrayed in Figure 6.14(a) for the swirl parameter. Previously, Figure 6.3 showed the response of axial velocity to the pressure gradients provided by interaction with the wing at different vertical positions which can be tied to vortex stability here. The negative vertical off-

set experiences a stronger adverse pressure gradient resulting in a quicker swirl decay due an enhanced velocity deficit that allows instabilities to initiate further upstream. The positive vertical offset aligns the vortex with a favorable pressure gradient that accelerates axial flow and preserves swirl upstream of the leading-edge.

The connection between the onset of unstable behavior and the swirl parameter is further supported by observing the instantaneous flow for a small positive initial offset of $\Delta z/c = +0.05$ in Figure 6.15. Here an indentation in the instantaneous Q-criterion is indicative of a tendency toward unstable behavior that never manifests. Rather, the vortex diverts over the leading-edge. The swirl parameter for $\Delta z/c = +0.05$ in Figure 6.14(a) drops to just above the stability threshold upstream of the leading-edge indicating the vortex nearly enters an unstable regime consistent with the instantaneous flow.

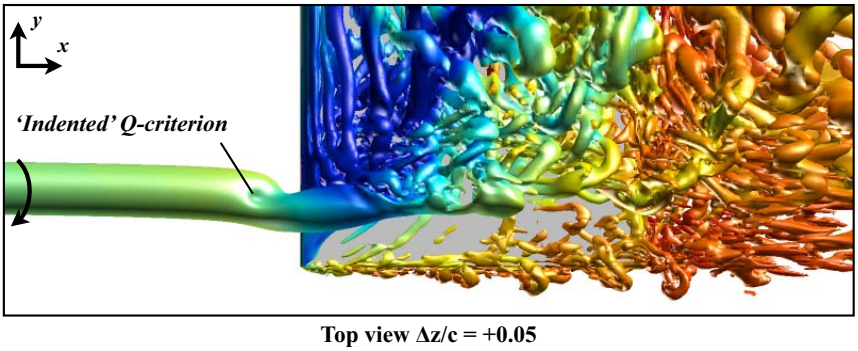

Figure 6.15: Top view of instantaneous Q-criterion iso-surfaces ($Q = 15$) for the $\Delta z/c = +0.05$. An indentation in Q-criterion suggests the beginning of instability.

A positive vertical offset is not sufficient to guarantee a stable vortex-wing interaction. For example, the flow visualizations of McAlister and Tung[56] portray breakdown of a trailing vortex over a stalled two-dimensional airfoil. This observation indicates angle of attack is also likely to play a significant role. For instance, a stronger separation/stall-induced adverse pressure gradient on the suction-side could promote instability and breakdown. This concept appears to influence the incident vortex behavior on the suction-side of the $\Delta z/c = +0.1$ case past the mid chord.

Figure 6.3(b) shows a region of adverse $\partial\overline{p}/\partial x$, strongest near the mid chord, associated with flow separation above the wing. In response, an enhanced velocity deficit is produced in the vortex core downstream of the mid chord and portrayed in Figure 6.3(a). This appears to drive the vortex into an unstable regime above the wing near the mid chord permitting the growth of unstable helical modes visible in Figure 6.7.

As a final note to this section, the current work illustrates a tendency for vortex-wing interaction to elicit unsteady fluid dynamics. While the phenomenon described here is not vortex breakdown in the strict sense defined by Leibovich and Stewartson[87], that is, requiring flow reversal or a stagnation point, axial pressure gradients are known to have a significant influence on the breakdown of columnar vortices. Sarpkaya[139] first subjected a streamwise vortex to an axial pressure gradient in a tube and observed a significant impact on vortex breakdown. Visbal[143] clarified the dominant role of the axial pressure-gradient for breakdown over delta wings. More severe conditions, perhaps at a higher Reynolds number or angle of attack, may lead to breakdown of the streamwise vortex in the present configuration upstream for a negative offset or above the wing for a positive offset. This may elicit behaviors reminiscent of the buffeting response of fins subject to a broken-down vortex emitted from delta wings presented by Mayori and Rockwell[1], Wolf *et al.*[144], Kandil *et al.*[145], Gordnier and Visbal[2], and more recently, Gursul and Xie [66] or Lambert and Gursul [67] to name a few.

6.3 Summary

In this chapter, a *rigid*, $\mathcal{AR} = 6$, flat plate wing operating at a Reynolds number of $\mathrm{Re} = 30,000$ and $\alpha = 5^\circ$ angle of attack was subjected to a stable, laminar q-vortex superimposed upstream of the leading-edge. The incident streamwise vortex was positioned $\Delta y/c = 0.25$ inboard from the wingtip. Exploration over a range of

vertical offsets, $-0.25 \leq \Delta z/c \leq +0.1$, provided a rich variation in the unsteady fluid dynamics and revealed several characteristic factors that influence vortex-wing interaction.

When the vortex was aligned with the leading-edge, the incident vortex core developed a helical instability upstream of the wing that wound in a sense opposite the rotation of the vortex swirl. Placing the vortex a small distance beneath the wing caused the instability to become much more pronounced and initiate further upstream. Moving the vortex slightly above the wing removed the upstream instability in the incident vortex.

The onset or lack of stability in the vortex was found to be related to the pressure gradients experienced at different vertical positions. Direct impingement and negative vertical offsets, in which vortex instability manifested, subjected the incident vortex to adverse pressure gradients that tended to enhance the axial velocity deficit in the incident vortex core. This effect reduced the swirl parameter of the initially stable, laminar q-vortex into its linearly unstable regime permitting the growth of short-wavelength perturbations. The onset of helical instability in each case became visible a short distance downstream from where the incident vortex entered the unstable regime. Placing the vortex slightly above the wing, which removed instability, aligned the vortex with the favorable pressure gradient provided by the acceleration of flow over the leading-edge. The axial velocity in the vortex core increased preserving a stable value for the swirl parameter. Adverse pressure gradients above the wing as the vortex approached the trailing-edge appeared to promote the growth of suction-side instabilities in the streamwise vortex for the positive vertical offset.

Incident vortex behavior was shown to provide a significant impact to the unsteady loads experienced by the wing. The more pronounced instability elicited by a negative offset increased the rolling moment fluctuations while the stabilizing effects of a small positive offset reduced the overall fluctuations of the rolling moment. The range of

vertical offsets explored produced fairly little change in the time-mean lift or drag suggesting the choice of vertical position is dictated by its unsteady characteristics rather than optimization of aerodynamic loads. If a streamwise vortex were to be intentionally encountered in the context of formation flight, a weaker interaction may be beneficial. For example, the $\Delta z/c = -0.25$ case produced comparable aerodynamic benefits to the closer positions with markedly diminished rolling moment fluctuations and trim penalty. A large negative offset would also ensure high aspect-ratio wings only deform away from the most unstable regimes.

Several implications for future research were also identified. Stronger adverse pressure gradients under more severe conditions, such as a higher Reynolds number or angle of attack, could evolve instabilities into breakdown of the streamwise vortex and elicit harsher buffeting loads. This could occur upstream for direct impingement/negative vertical offset cases or above the wing for a positive vertical offset. Incident vortex behavior could be modified by adjusting pressure gradient regimes using flow control or wing curvature. The taxonomy of flow regimes exhibited for the stationary vortices in this chapter are useful for better understanding the implications of relative motion between tandem wings or the outcomes of aeroelastic effects of large aspect-ratio wings.

Chapter 7

Isolation of dynamic aerolastic effects

Previous phases of the current research explored the impingement of a streamwise vortex on a wing, the development of vortex instability upstream of the leading-edge, and subsequent fluctuations in surface loading. Time-mean (static) bending deformations of flexible wings were shown to provide a significant influence to the unsteady behavior of the impinging vortex while the effect of vortex-induced oscillations of the flexible plates was shown to be secondary to the static displacement. The specific consequences of the dynamic component of aeroelasticity have not been explored in detail.

Past work in the context of vortex/fin interaction suggests the dynamic response can be important. For instance, Gursul and Xie[65] investigated the unsteady nature of vortex breakdown of a delta-wing leading-edge vortex impinging on a vertical fin. Measurements of the breakdown location revealed dominant frequencies that did not appear when the fin was absent suggesting feedback effect from the vertical fin. Gordnier and Visbal[2] demonstrated mutual interaction between unsteady separation on a plate and spiral breakdown of an impinging vortex from a delta wing. While both

of these experiments/computations only considered rigid wings, unsteady separation imposed by a deforming structure could produce similar feedback on the incident vortex. Later, Gursul and Xie[65] explored the feedback response imposed by forced oscillations of a fin on the location of vortex breakdown. They found that low frequency oscillations provided the greatest effect on the amplitude of the breakdown location and higher frequencies provided very little feedback. These observations motivate the present analysis of feedback effects imposed by forced wing oscillations on the unsteady fluid dynamics of an otherwise stable, laminar vortex impinging on a wing.

The objective of this work is to isolate the potential influence of dynamic aeroelastic response on the unsteady fluid dynamics in the presence of a streamwise vortex encounter. Wing oscillations are forced by prescribing deformations to follow the first mode shape of a fixed-free beam on the vortex encounter-side of the wing. The investigation in this chapter focuses primarily on characterization of the feedback response in the incident vortex instability upstream of the leading-edge. Specific aspects of the unsteady flow structure around the wing are described, but flow exploration is not intended to be as thorough as the previous chapters. Both bending amplitude and frequency are varied in this chapter in order to provide a more complete mapping of dynamic aeroelastic effects.

7.1 Problem setup

This chapter continues using the canonical setup and vortex definition provided in Section 5.1. Forced bending oscillations are now imposed on the vortex encounter-side of the wing, shown in Figure 7.1, in order to explore the feedback response of the vortex to a dynamic aeroelasticity. Bending deformations are actively imposed in the wing frame of reference (x_s, y_s, z_s) using the first bending mode shape for a fixed-free

beam where the vertical mid-plane deflections are given by

$$\hat{z}_s(y) = A/2 \sin(2\pi f_b F(\tau)\tau) \left[\cosh(\beta_n y) + \cos(\beta_n y) - \sigma_n(\sinh(\beta_n y) + \sin(\beta_n y))\right] \tag{7.1}$$

where

$$\sigma_n = \frac{\sinh(\beta_n s) - \sin(\beta_n s)}{\cosh(\beta_n s) + \cos(\beta_n s)} \tag{7.2}$$

s defines the wing semispan, A is the wingtip amplitude, $f_b = fc/U_\infty$ is the non-dimensional frequency of bending oscillations, and $\beta_n = 1.875$ for the first bending mode. $F(\tau) = 1 - e^{-9.2\tau}$ is a ramping function which provides a smooth transition from a stationary wing to the prescribed oscillations. Wing length is maintained constant by preserving arc length,

$$S(\hat{y}_s) = \int_0^s \sqrt{1 + (d\hat{z}_s/d\hat{y}_s)^2} dS \tag{7.3}$$

in order to account for horizontal mid-plane deflections at all phases of the deformation cycle where $\hat{y}_s$ and $\hat{z}_s$ describe the mid-plane shape of the deforming structure.

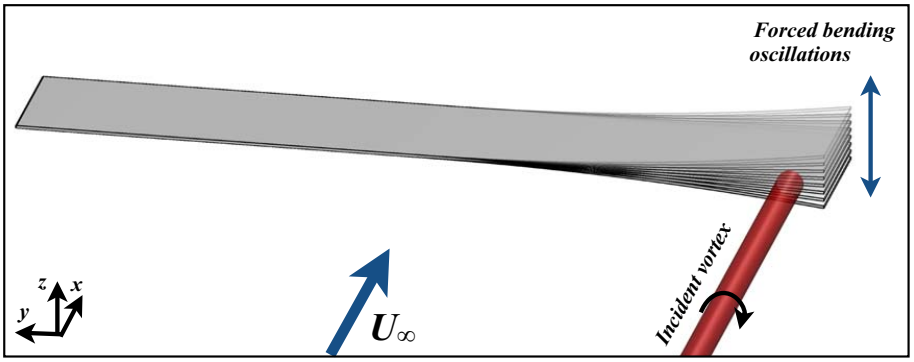

Figure 7.1: Demonstration of forced bending oscillations. Deflections are exaggerated for visual purposes.

Surface positions of the deformed plate are found by accounting for mid-plane

rotation in addition to the mid-plane deflections:

$$y_{s,\text{surf}} = \hat{y}_s - \left(\pm\frac{t}{2}\right)\sin(\theta) \tag{7.4}$$

$$z_{s,\text{surf}} = \hat{z}_s + \left(\pm\frac{t}{2}\right)\cos(\theta) \tag{7.5}$$

where $\theta = \tan^{-1}(d\hat{z}_s/d\hat{y}_s)$ is the mid-plane rotation, $y_{s,\text{surf}}$ and $z_{s,\text{surf}}$ are the deformed surface positions and $\pm$ refers to the upper/lower surface points, respectively.

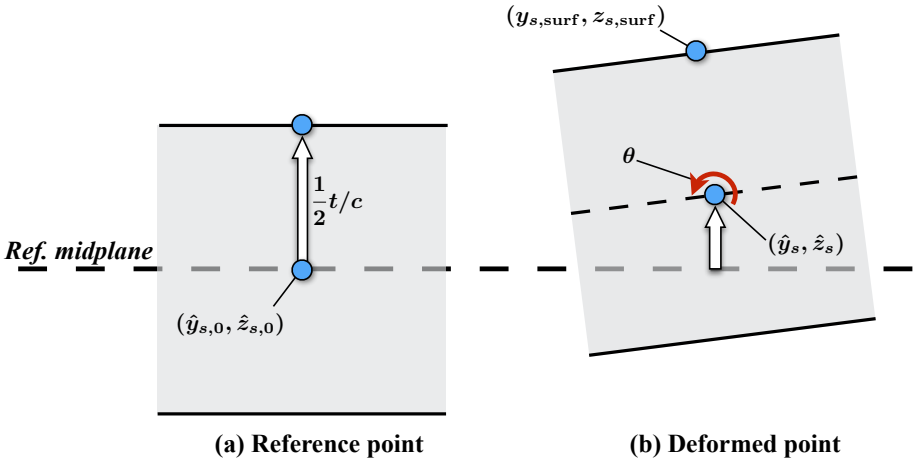

Figure 7.2: Mid-plane and surface point deflections (a) reference points for the undeformed wing and (b) mid-plane and surface deflections.

Instances of the bending cycle are described throughout this chapter using the phase angle, Φ. Typical phases of the motion described in this chapter include the maximum velocities during upward motion, $\Phi = 0°$, downward motion, $\Phi = 180°$, and maximum deflections at the top, $\Phi = 90°$, and bottom, $\Phi = 270°$, of the bending cycle. Each of these phases are depicted for the wingtip deflection, $\hat{y}_{s,\text{tip}}$, in Figure 7.3.

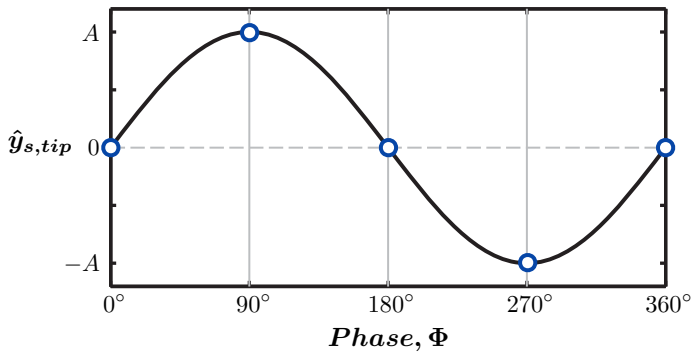

Figure 7.3: Phases of wingtip motion.

The non-dimensional frequency of the prescribed vibrations ranges from $f_b = 0.5, 1$, and 2 and the wingtip amplitude ranges from $A/c = 0.025$, 0.05, and 0.1 where the full parameter space covered in this chapter is provided in Table 7.1. The frequencies chosen closely coincide with the vortex-imposed bending oscillations found for the full aeroelastic cases in Chapter 5 and dominant frequencies of the vortex instability found in Chapter 6. The largest of the bending amplitudes used is intended to shift the vertical positioning between the most stable and least stable regimes described in Chapter 6 and the smallest amplitude approaches that of the dynamic oscillations of Chapter 5. Deformation of the fluid dynamics mesh for each of the prescribed motions is accommodated using the methods described in Ref. [129].

Table 7.1: Map of frequency and bending amplitudes

	$f_b = 0.5$	$f_b = 1.0$	$f_b = 2.0$
$A/c = 0.025$	x	x	x
$A/c = 0.050$	x	-	-
$A/c = 0.100$	x	-	-

While the final grid for the present case is identical to that used in Chapters 5 and 6, the decomposition to sub-blocks for parallel processing is reduced from 688 to 208 processors. This adjustment increases the implicit stencil in each decomposed grid block and helps preserve mesh quality for the highly dynamic deforming grids required by this investigation. Simulations of the forced bending cases were initialized

from the previously completed static wing simulation where the ramp function, $F(\tau)$, embedded in Eqn. 7.1 provides a smooth startup. All cases were run for an additional $\tau = 20$ at a non dimensional time step of $d\tau = 0.0001$.

7.2 Effect of bending amplitude

The effect of bending amplitude is explored first. This section compares the direct impingement of the streamwise vortex on the wing subject to oscillations at $f_b = 0.5$ with three amplitudes of $A/c = 0.025$, 0.05, and 0.1. Velocities were sampled within a $0.2c \times 0.2c$ window oriented normal to and centered on the vortex at two streamwise stations. Fourier analysis was applied to the kinetic energy and averaged within the sample window. The resulting frequency spectra is shown for streamwise stations of $x/c = -0.45$ and -0.25 below in Figures 7.4(a) and (b), respectively, for all three amplitudes alongside the stationary, rigid wing.

The $f_b = 0.5$, $A/c = 0.025$ case demonstrates a frequency signature at both streamwise stations that is nearly identical to that of the baseline static case with two small differences. Amplification is observed at the clearly defined frequencies indicating some degree of enhanced growth of instability due to the small amplitude, low frequency oscillations. A small clearly defined peak occurs at $\mathrm{St}_c = 0.5$ which matches the bending frequency. This is the dominant clearly defined peak at the more upstream location which indicates some degree of upstream wave propagation emanating from the oscillating wing.

The larger bending amplitudes of $A/c = 0.05$ and 0.1 exhibit increasingly higher peaks at $\mathrm{St}_c = 0.5$ due to the harsher dynamic behavior. Closer to the wing, at $x/c = -0.25$, the component matching the bending frequency is shown to remain the dominant component rather than that of the spiral instability, $\mathrm{St}_c = 0.9$. Interestingly, the frequency component closest to the vortex instability has shifted slightly to $\mathrm{St}_c = 1$

which is a harmonic of the bending oscillations. This observation suggests some modulation of the instability frequency is possible but, as will become apparent in the next section, the extent of this trend appears to be limited.

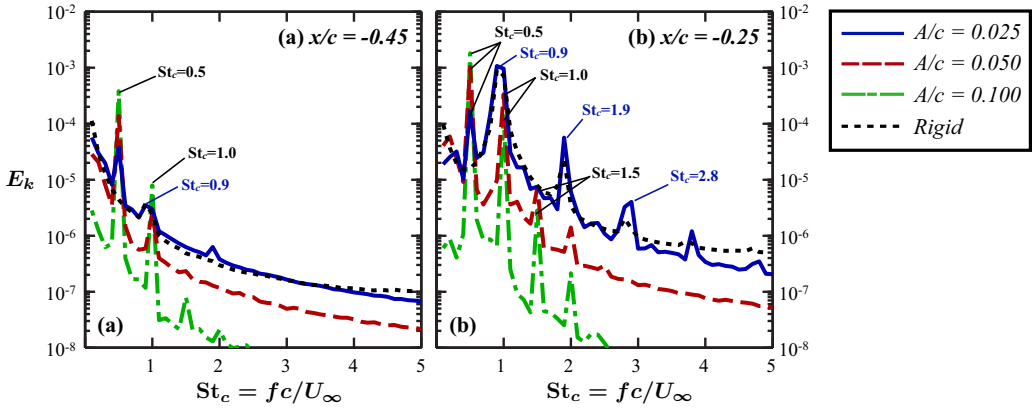

Figure 7.4: Turbulent kinetic energy spectra at (a) $x/c = -0.45$ and (b) $x/c = -0.25$ at $\mathrm{St}_c = 0.05$ for several amplitudes.

Some of the behavior indicated by the turbulent kinetic energy spectra is made clearer by observing the instantaneous flow. A top-down view of an instantaneous Q-criterion iso-surface for the $f_b = 0.5$, $A/c = 0.025$ case is shown in Figure 7.5 for several phases of a bending cycle. It is clear that the behavior of the helical instability is not dictated by the bending oscillations for this case in that the spiral has not demonstrated a major deviation from its behavior for the static wing.

Instead, the clearly defined peak at the bending oscillation frequency, $f_b = 0.5$, in Figure 7.4 appears to emanate from a disruption of the vortex spiral evolution. For instance, the vortex spiral completes nearly two revolutions for every bending cycle. This amounts to a shift in wing conditions roughly every other rotation of the helix and is best portrayed by comparing the flow structure between $\Phi = 0°$ and 180°. At $\Phi = 0°$, the wing is traveling upward while at $\Phi = 180°$ the wing is traveling downward. The vortex spiral is in comparable phases of its motion at both instances, but subjected to slightly different conditions in the two frames. The upward wing motion at $\Phi = 0°$ appears to inhibit the propagation of the spiral over the suction-side

while the downward motion at $\Phi = 180°$ appears to support a more coherent growth of the upper-surface component. These continuously changing flow conditions alter the spiral's ability to propagate over the wing which appears to be felt upstream in Figure 7.4. Ultimately, the spiral remains at the same frequency as the rigid case, $\mathrm{St}_c = 0.9$, and its behavior is largely unaffected by the low-frequency, low-amplitude bending vibrations. Because the incident spiral fails to adjust to a harmonic of the bending oscillations, the overall flow structure is somewhat aperiodic.

A top-down view of the instantaneous flow for the $f_b = 0.5$, $A/c = 0.05$ case is shown in Figure 7.6. The same behavior described for the $A/c = 0.025$ case becomes a bit more apparent where corresponding cycles of the vortex spiral between $\Phi = 0°$ and 180° or between $\Phi = 90°$ and 270° show comparatively greater differences due to the larger change in conditions provided by the higher amplitude oscillations. A second change in the unsteady flow structure begins to demonstrate the effect of increased bending amplitude. Here, the spiral structure appears less compact, but its rotation remains close to the primary frequency. This is most clearly portrayed at $\Phi = 180°$ where the spiral appears elongated compared to the lower-amplitude case in Figure 7.5. This is due to a stronger growth of the suction-side component when the vortex is bent downward between $\Phi = 180°$ and 360°. The larger bending amplitude case shifts the vortex further into the stabilizing regime when bent downward where the favorable pressure gradient provided by a positive vertical offset is enhanced during the downstroke motion. The spiral elongation is an indication of the spiral's tendency toward stabilization. The feedback response of larger amplitude oscillations is increasingly dictated by forcing the vortex between the stabilizing/destabilizing conditions provided by vertical offset. This effect becomes remarkably clear for the largest bending amplitude of $A/c = 0.1$ discussed next.

Snapshots of a top view of the instantaneous flow structure is shown for the $f_b = 0.5$, $A/c = 0.1$ case in Figure 7.7. This largest bending amplitude provides the

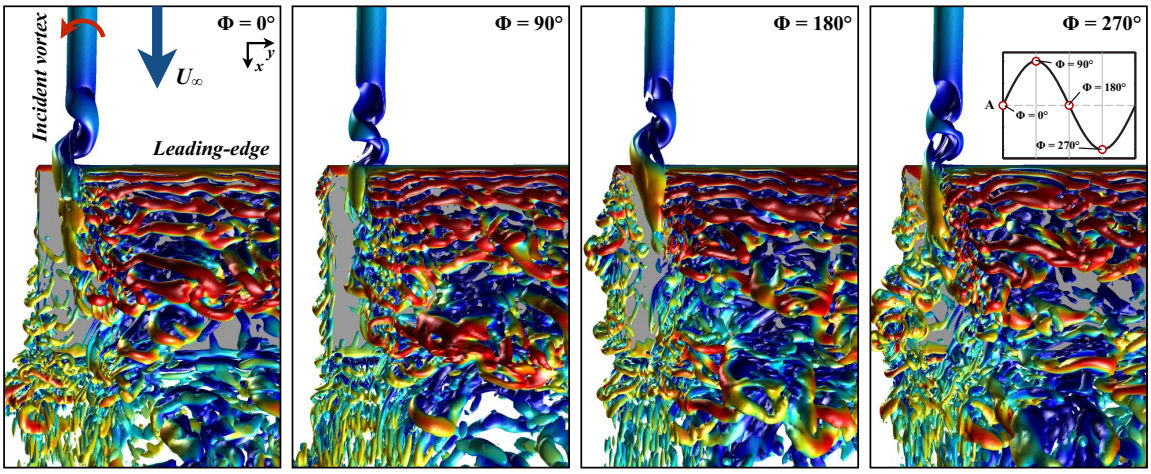

Figure 7.5: Top view of the flow structure over the $f_b = 0.50$, $A/c = 0.025$ case using an iso-surface of Q-criterion ($Q = 15$) for several phases of motion (inset). so-surfaces are colored by velocity magnitude.

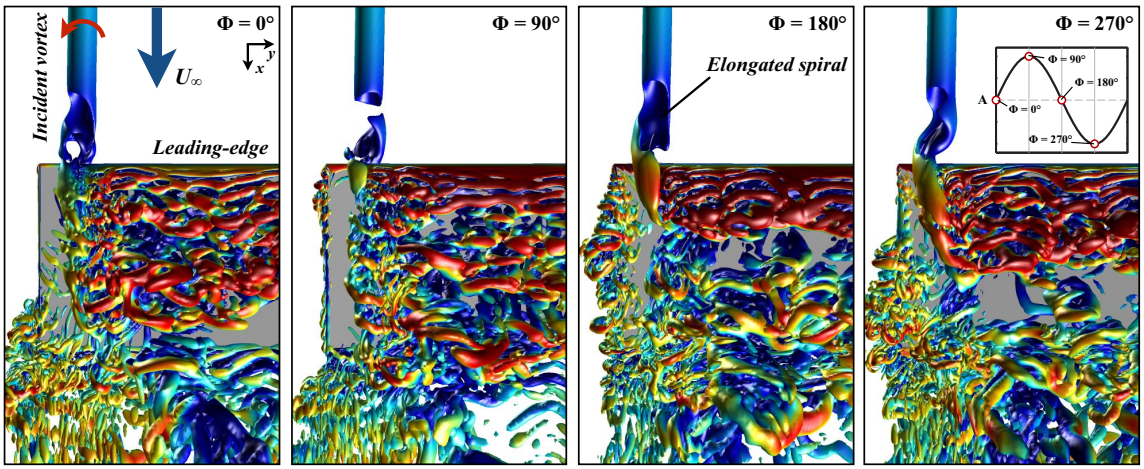

Figure 7.6: Top view of the flow structure over the $f_b = 0.50$, $A/c = 0.05$ case using an iso-surface of Q-criterion ($Q = 15$) for several phases of motion (inset). Iso-surfaces are colored by velocity magnitude.

most salient physics, and therefore, more detail is provided for this specific case in the following discussion. Upstream of the wing, the usual helical instability is visible during the downward phases of wing motion, $\Phi = 90°$ to $\Phi = 225°$. The spiral remains close to the leading-edge compared to both the static and lower-amplitude cases. Toward the bottom of the stroke, $\Phi = 225°$, the effective vertical offset provided by the bent-down wing places the vortex fully into the stabilizing regime. The favorable pressure gradient in conjunction with the time-scale of the low frequency oscillation is sufficient for the complete removal of upstream instability by $\Phi = 270°$. The vortex remains stable until around $\Phi = 0°$ where the plunging motion forces it to pinch-off from the upper-side and divert to the pressure-side. The bent-up wing provides an effectively negative vertical offset where the adverse pressure-gradient promotes a quick reemergence of unsteady behavior. The time-frame the vortex spends in the destabilizing regime is insufficient for it to evolve to the levels observed for the static and low-amplitude cases. In this case, a sufficiently large bending amplitude is capable of driving upstream behavior by providing a large-scale shift in flow conditions. This explains the dominance of the bending oscillations in the frequency content for $A/c = 0.1$ provided in Figure 7.4.

Compared to the lower amplitude oscillations, the flow structure above and below the wing for the $A/c = 0.1$ case is much more interesting. A detailed view of the instantaneous suction-side flow structure is shown in Figure 7.7 where phases corresponding with downward motion of the bending oscillation are shown on the left and the upward phases are portrayed on the right. An iso-surface of Q-criterion demonstrates a complex unsteady growth and destruction process of the incident vortex as it passes over the suction-side. By the middle of the downstroke, $\Phi = 45°$, the incident vortex has passed over the leading-edge and pinned to the upper surface. This anterior portion of the streamwise vortex is reoriented inboard due to spanwise flow provided by the growing leading-edge vortex, also pinned to the wing surface

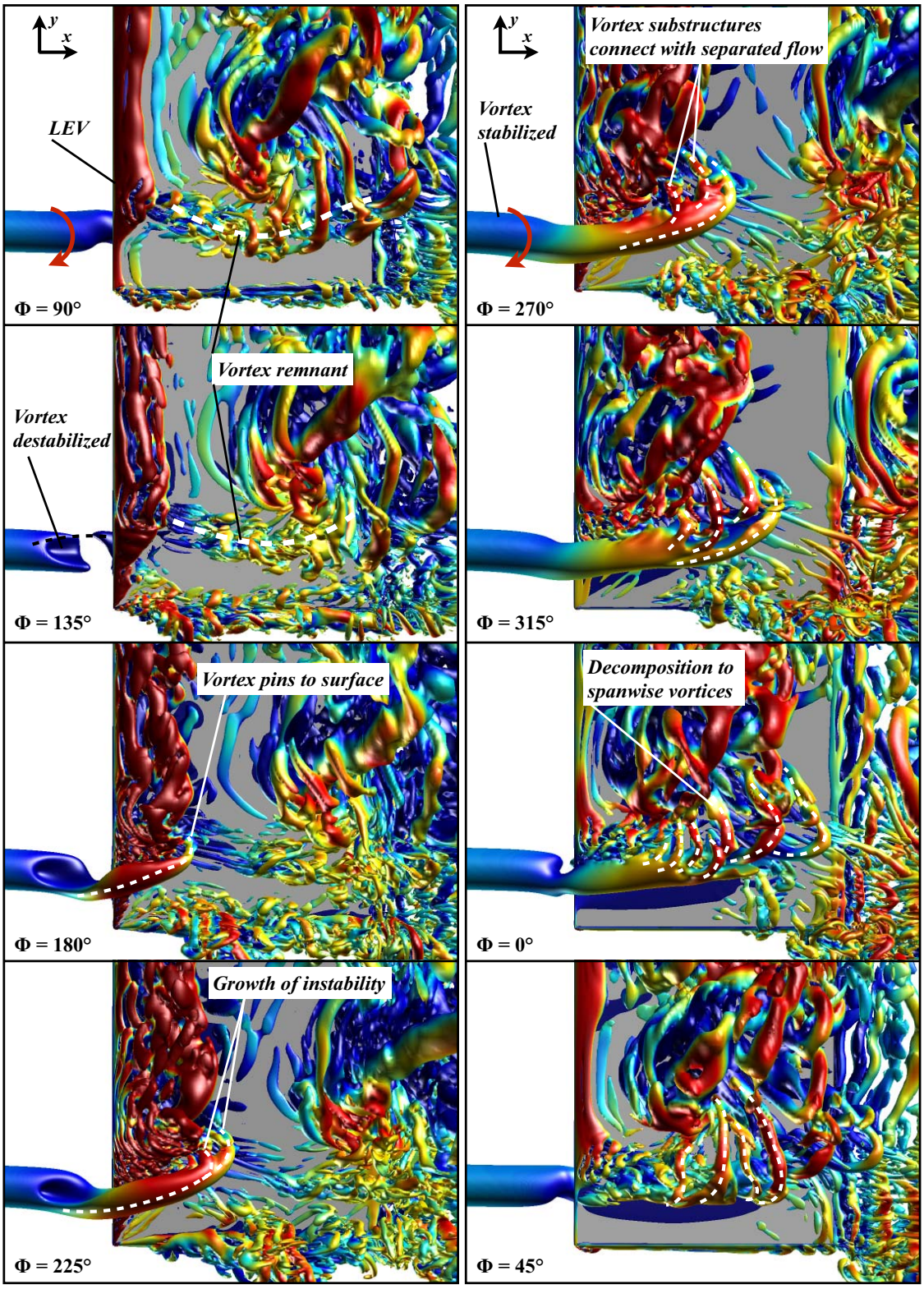

Figure 7.7: Top view of the instantaneous flow structure over the $f_b = 0.5$, $A/c = 0.1$ case using an iso-surface of Q-criterion ($Q = 15$); (a) shows the downward phases and (b) shows the upward phases of motion. Iso-surfaces are colored by velocity magnitude.

just inboard of vortex impingement. Toward the bottom of the bending oscillation, $\Phi = 225°$, streamwise instabilities in the initially coherent incident vortex begin to develop. Here, a second spanwise-oriented substructure appears near the front of the leading-edge vortex and is connected to the separated flow on the inboard side. At $\Phi = 270°$, the incident vortex is fully stabilized upstream of the leading-edge, but suction-side instabilities continue to grow where multiple spanwise-oriented substructures are now visible. This dynamic behavior appears to be supported by the same destabilizing physics that facilitate suction-side instability for a positive vertical offset, described previously in Chapter 6. In this case, low-frequency bending oscillations exacerbate the unsteady behavior and more clearly elucidate the decomposition process.

As the wing plunges upward, $\Phi = 315°$ to $\Phi = 45°$, the initially coherent swirling flow completely decomposes into a series of spanwise vortices. By $\Phi = 45°$, the incident vortex has diverted to the lower surface and the remaining suction-side component further decomposes as it reaches the trailing-edge. The remnant and subsequent destruction of the suction-side component is visible as the wing begins the next downward oscillation, $\Phi = 90°$ to $135°$.

A similar detailed view of the pressure-side is provided in Figure 7.8 where the left side again portrays downward bending phases and the right depicts the upward bending phases. This view portrays the unsteady processes in the streamwise vortex as it passes beneath the wing. The incident vortex is shown to divert to the pressure-side of the wing by $\Phi = 0°$. By $\Phi = 45°$, the vortex has clearly pinned to the lower surface and tends outboard as it advances toward the trailing-edge. As the wing plunges downward, $\Phi = 135°$, the incident vortex begins to pinch-off from the pressure-side at the leading-edge and the lower-surface component begins to develop streamwise instabilities. No longer supported by the incident flow, these spanwise-oriented substructures continue to grow, similar to the process observed on the suction-side, and

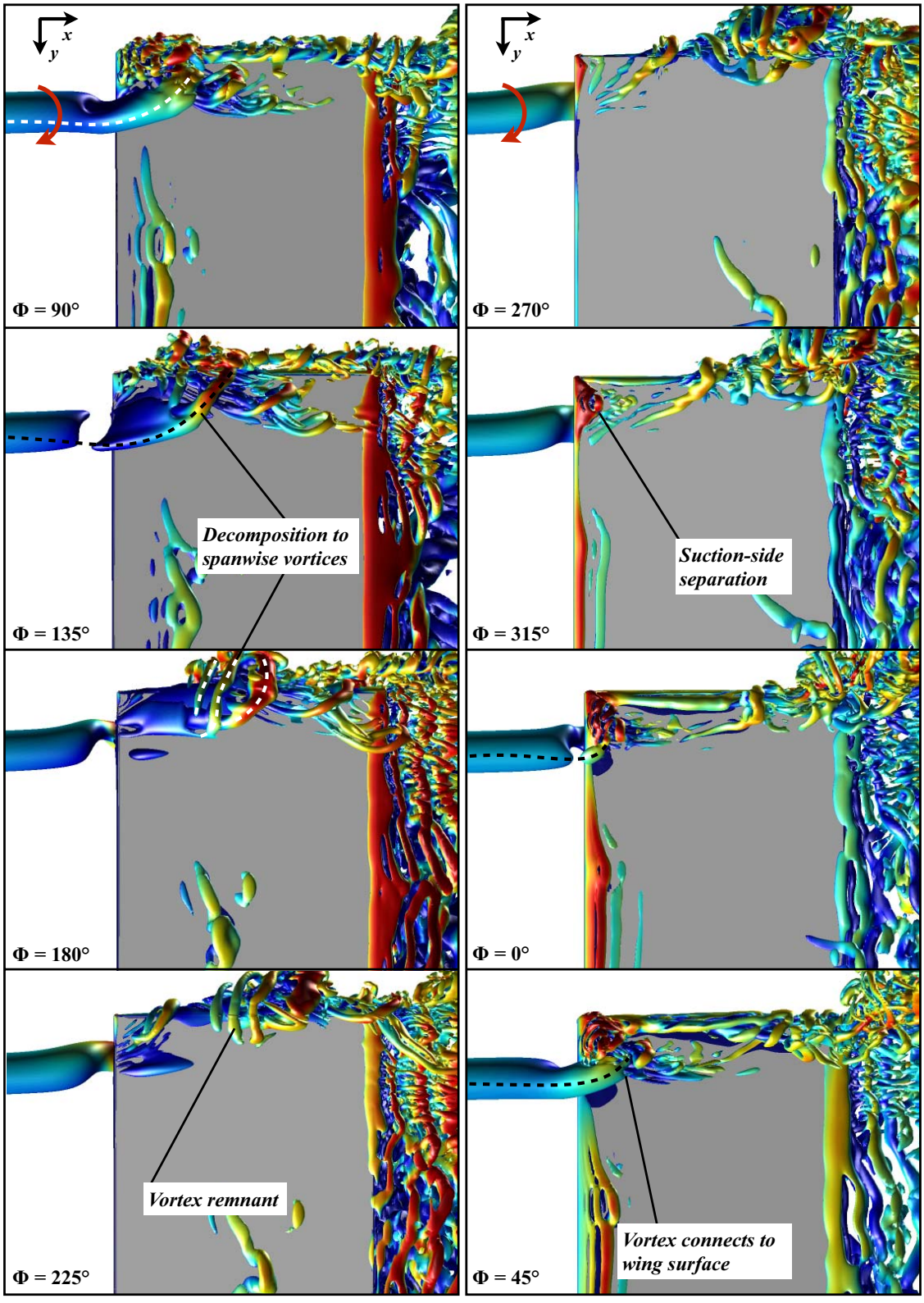

Figure 7.8: Bottom view of the instantaneous flow structure beneath the $f_b = 0.5$, $A/c = 0.1$ case using an iso-surface of Q-criterion ($Q = 15$); (a) shows the downward phases and (b) shows the upward phases of motion. Iso-surfaces are colored by velocity magnitude.

then divert over the wingtip through the remaining downward phases, $\Phi = 180°$ to $225°$.

7.3 Effect of bending frequency

This section describes the effects provided by varying the oscillation frequency between $f_b = 0.5$, 1, and 2 at the smallest bending amplitude of $A/c = 0.025$. Frequency spectra of turbulent kinetic energy, obtained in the same manner as previously described for Figure 7.4 above, is compared for several oscillation frequencies at a single bending amplitude of $A/c = 0.025$ in Figure 7.9. As discussed in the preceding section, the low frequency case exhibits little change from the rigid stationary wing with the exception of an additional peak that corresponds with the bending frequency.

At $x/c = -0.45$ in Figure 7.9(a), the $f_b = 1$ case portrays a single dominant peak at $\mathrm{St}_c = 1$ coinciding with the bending frequency. The $f_b = 1$ oscillations appear to enhance the upstream influence of the wing compared to both the rigid and low frequency, $f_b = 0.5$, cases. For $f_b = 1$, the dominant frequency component has shifted from its original value of $\mathrm{St}_c = 0.9$ to align with the bending oscillations at $\mathrm{St}_c = 1$. This frequency shift persists downstream at $x/c = -0.25$ and indicates the wing motion is capable of modulating vortex frequency to some degree.

The highest frequency case, $f_b = 2$, elicits two clearly defined peaks at $\mathrm{St}_c = 1$ and $\mathrm{St}_c = 2$ at $x/c = -0.45$ where the dominant component matches the bending frequency. Further downstream, $x/c = -0.25$, a subharmonic of the bending frequency, $\mathrm{St}_c = 1$, emerges as the primary component in the energy spectra which corresponds with the revolution of the vortex spiral. Similar to the $f_b = 1$ case, the highest frequency, $f_b = 2$, has also managed to shift the frequency of vortex instability a small amount. It is interesting to note that the vortex instability locks into the same frequency for both the $f_b = 1$ and $f_b = 2$ cases. When the wing vibrates at $f_b = 1$,

the vortex instability locks into the bending frequency. For $f_b = 2$, the vortex shifts to the subharmonic of the bending oscillations closest to its original frequency rather than adjust to the higher bending frequency or switch to a higher modal instability.

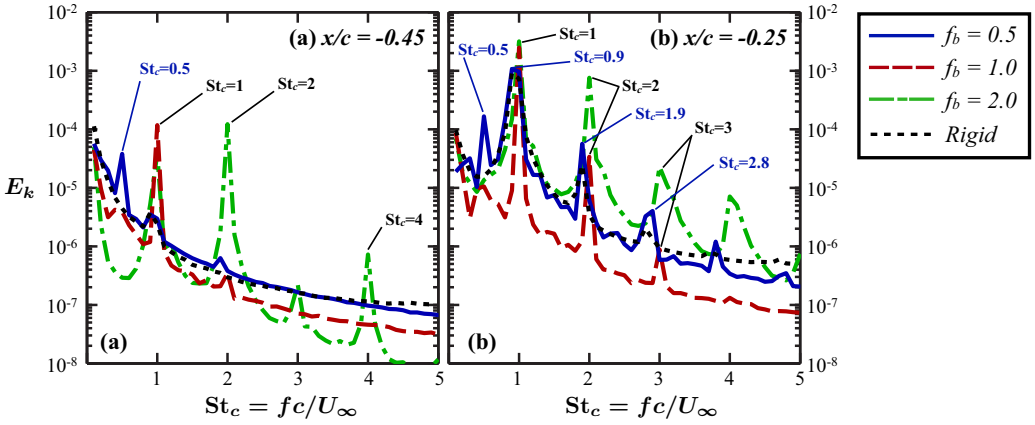

Figure 7.9: Turbulent kinetic energy spectra at (a) $x/c = -0.45$ and (b) $x/c = -0.25$ at $A/c = 0.025$ for several frequencies.

Figure 7.10 shows a top view of the instantaneous flow structure using an iso-surface of Q-criterion for the $f_b = 0.5$, 1, and 2 cases. These snapshots provide a close view of the vortex spiral and are captured at a sampling frequency of $f_s = 1$. The $f_b = 0.5$ case, Figure 7.10(a), demonstrates the vortex spiral, measured to revolve at $\mathrm{St}_c = 0.9$, is increasingly out of phase in each sequential snapshot, as should be expected. On the contrary, both the $f_b = 1$ and 2 cases, provided in Figures 7.10(b) and (c) respectively, produce an incident vortex that spirals in phase with the sampling frequency demonstrating a nearly identical helical flow structure upstream of the wing across all ten sampled frames. This observation confirms the dominant frequencies at $x/c = -0.25$ for the $f_b = 1$ and 2 cases, shown in Figure 7.9(b), are indeed caused by a frequency shift of the vortex spiral.

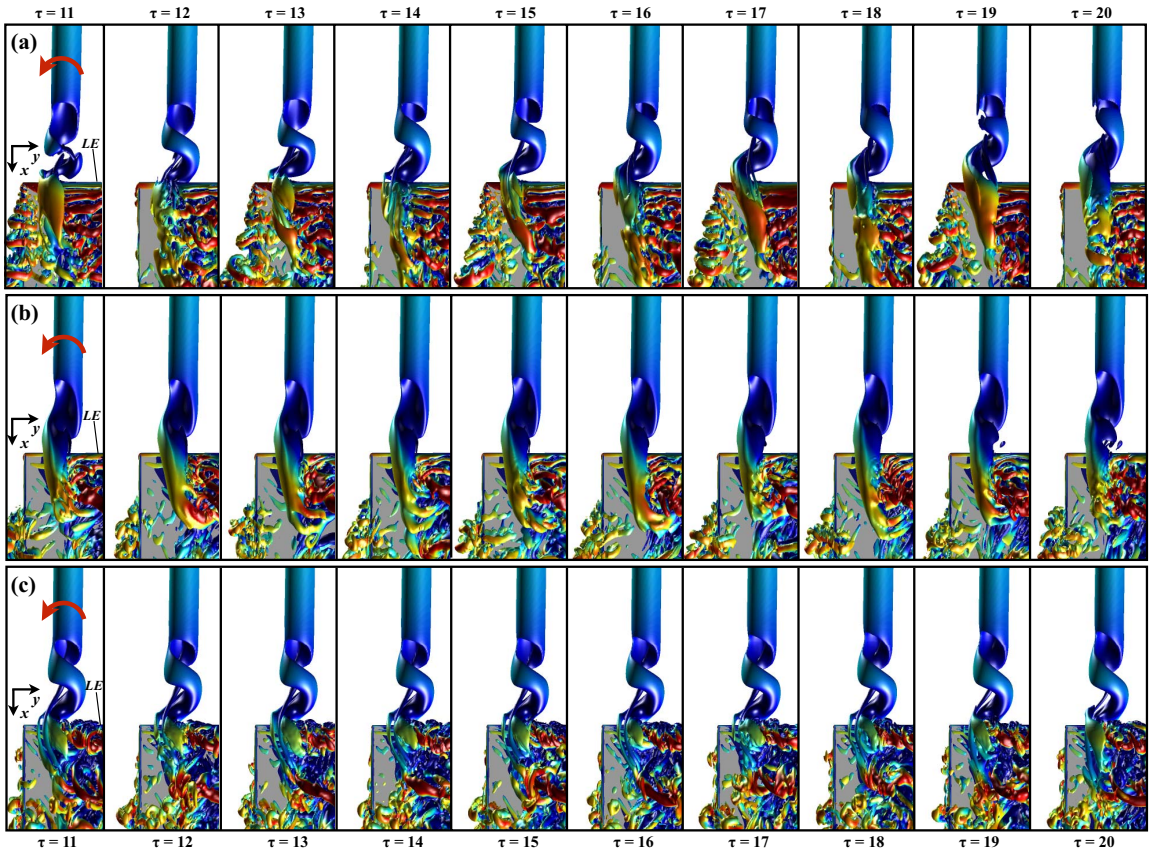

Figure 7.10: Top view of instantaneous flow structure using an iso-surface of Q-criterion ($Q = 15$) sampled every $\Delta\tau = 1$ beginning at $\tau = 11$: (a) $f_b = 0.5$, (b) $f_b = 1$, and (c) $f_b = 2$. $A/c = 0.025$ for each case. Iso-surfaces are colored by velocity magnitude.

Specific aspects of the unsteady flow structure for each case are discussed in more detail next. The unsteady flow structure for the $f_b = 0.5$, $A/c = 0.5$ case was covered in Figure 7.5 and discussed in Section 7.2. Therefore the low-frequency, low-amplitude case is not repeated in this section.

Several phases of the mid-frequency, $f_b = 1$, case is shown in Figure 7.11. At $\Phi = 0°$, the spiral instability traverses the upper-surface. Upstream of the leading-edge, the helical structure is less-compact compared to the rigid and low frequency cases and reminiscent of the flow structure for the $f_b = 0.5$, $A/c = 0.05$ case of Section 7.2. This spiral elongation appears to be related to vortex stretching provided by flow acceleration over the leading-edge during the preceding downward motion. Similar

to the $f_b = 0.5$, $A/c = 0.1$ case, the anterior portion of the vortex pins to the upper surface and is diverted inboard by the swirl of the leading-edge vortex followed by decomposition to spanwise sub-structures visible at $\Phi = 0°$. At $\Phi = 90°$, the spiral begins to pinch-off from the suction-side and briefly diverts to the pressure-side of the wing. From $\Phi = 90°$ to $180°$, the helix begins to contract and tends toward a more compact structure similar to that of the rigid and low-frequency cases. By $\Phi = 270°$ the spiral shifts back to the suction-side and returns to the more elongated form. The higher frequency oscillations of this case appear to support a forced shift between the stabilizing and destabilizing regimes provided by vertical offset as indicated by the extension and contraction of the vortex spiral. This behavior is reminiscent of the more severe effect shown for the $f_b = 0.5$, $A/c = 0.1$ case in Section 7.2.

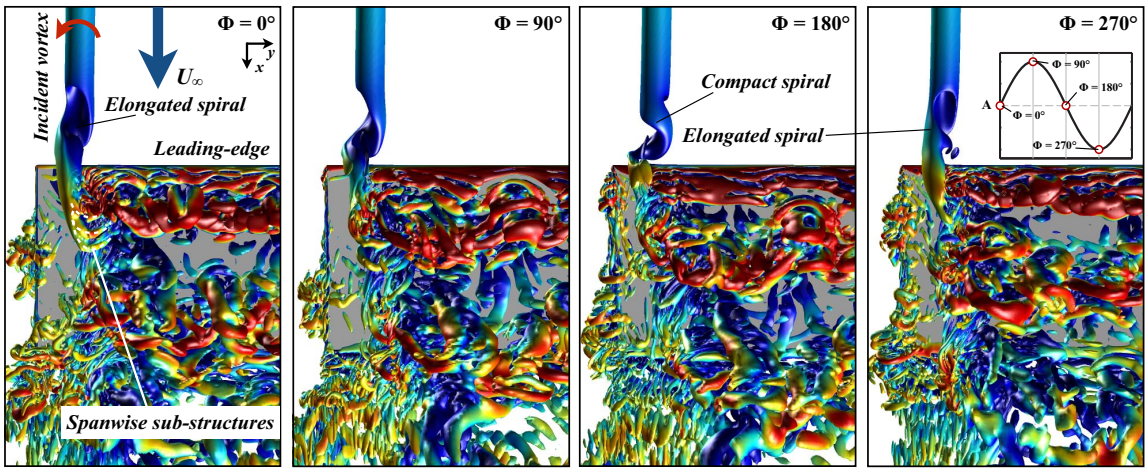

Figure 7.11: Top view of the flow structure over the $f_b = 1$, $A/c = 0.025$ case using an iso-surface of Q-criterion ($Q = 15$) for several phases of motion (inset). Iso-surfaces are colored by velocity magnitude.

The unsteady behavior for the highest frequency case, $f_b = 2$, becomes more complicated. Figure 7.12 shows a top view of the instantaneous flow structure using an iso-surface of Q-criterion. Upstream of the leading-edge, the higher frequency oscillations have failed to induce a switch to higher-mode instability. Instead, the fundamental behavior proves robust and the spiral takes on a form much like the low frequency and rigid cases. As indicated by Figures 7.9 and 7.10, the instability

has undergone a small frequency shift to $\mathrm{St}_c = 1$, a sub-harmonic of forced bending oscillations.

Because the wing completes two bending cycles for each revolution of the vortex spiral, two full cycles are necessary to describe the unsteady flow structure. The first cycle, shown in Figure 7.12(a), demonstrates the typical flow structure for a cycle when the vortex primarily traverses the pressure-side. Here, a train of leading-edge vortices, traced by white dashed lines, are visible and result from the higher frequency wing oscillations. Each of these vortical features remain pinned to the wing surface on the inboard side of the incident vortex.

At $\Phi = 270°$, the vortex has switched to the suction-side and begins to interact with the LEV. The progress of this interaction process is tracked through the next bending cycle, in Figure 7.12(b), which shows the flow structure when the incident spiral traverses the suction-side. Figure 7.12(c) shows a closer view of leading-edge wingtip for the second cycle. At $\Phi = 360°$, the front of the incident vortex is shown to be diverted inboard by the flow swirling around where the LEV is pinned to the wing surface. By $\Phi = 540°$, the interaction between the two vortical features becomes rather convoluted where the suction-side portion of the incident vortex has decomposed into a number of small-scale structures that envelop the LEV footprint. At $\Phi = 630°$ the suction-side component begins to attenuate as the incident vortex pinches off from the upper-surface. The remaining vortical feature continues to decompose into smaller-scale structures that wrap around the pinned location of a new LEV formed during the second cycle. Beyond $\Phi = 630°$, the flow returns to that shown in $\Phi = 0°$ and the unsteady process repeats.

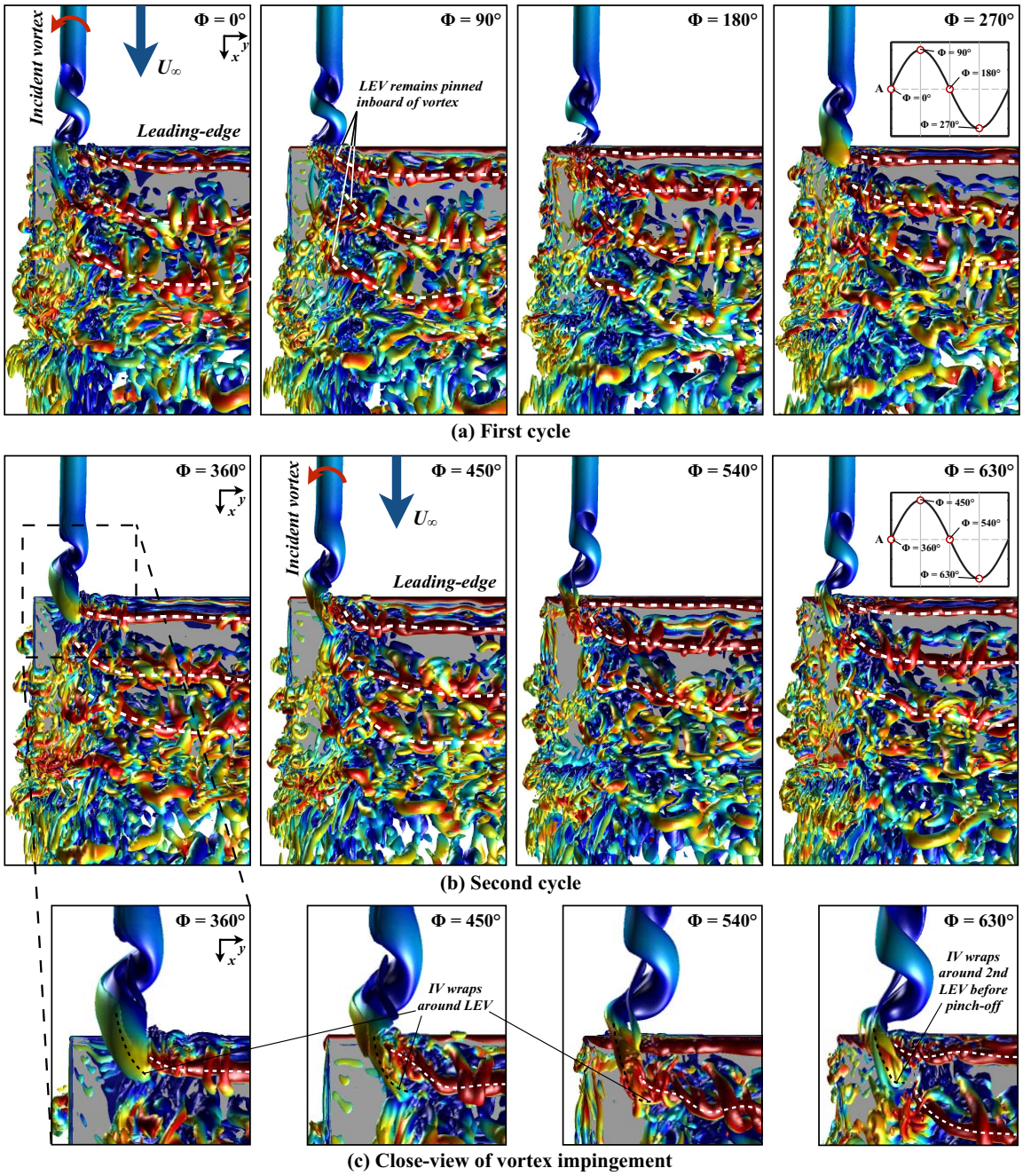

Figure 7.12: Top view of the flow structure over the $f_b = 2$, $A/c = 0.025$ case using an iso-surface of Q-criterion ($Q = 15$) for several phases of motion (inset). Two sequential cycles are shown in (a) and (b) while (c) provides a close view of the second cycle. Iso-surfaces are colored by velocity magnitude.

The combination of high-frequency bending and enhanced interaction between vortical features inhibits significant development of a coherent suction-side component that appeared for the lower-frequency cases. Higher frequency motion would likely

result in an increasingly rapid loss of coherent structure and dissipation of the incident vortex past the leading-edge. Further increases in bending frequency appear to be unlikely to provide a fundamental change in the unsteady behavior upstream of the wing, as the present behavior appears to be fairly resilient. This conclusion is further supported by the forced fin-oscillation work conducted by Gursul and Xie[66] where the feedback response on breakdown location was found to diminish with increasing frequency of fin oscillations.

7.4 Summary

The feedback response and unsteady flow structure due to a streamwise vortex impinging on a wing subject to forced bending oscillations is considered in this chapter. The oscillating wing operates at a chord-based Reynolds number of $\mathrm{Re} = 30,000$ and angle of attack of $\alpha = 5°$. The incident swirling flow is provided by a q-vortex imposed at the inflow boundary and initially positioned at $\Delta y/c = 0.25$ and $\Delta z/c = 0$. Several bending amplitudes of $A/c = 0.025$, 0.05, and 0.1 are considered along with several bending frequencies of $f_b = 0.5$, 1.0, and 2.0 which help to map a significant portion of the parameter space and are representative of the deformations/frequency content elicited during the full aeroelastic cases of Chapter 5. Analysis of forced bending oscillations helps to isolate and describe the potential influence of dynamic aeroelastic response on streamwise vortex interactions.

Low-frequency, low-amplitude ($f_b = 0.5$, $A/c = 0.025$) motion produced little change in the general flow structure. The frequency signature in the incident vortex of this case was markedly similar to that of the rigid wing with some enhancement of the dominant frequencies. While flow behavior remained much like the static wing, some degree of feedback response was observed. This appeared to be related to the a disruption of the spiral's evolution resulting from the periodic shift in the wing's

position during low-frequency oscillations. Significant changes to the unsteady fluid dynamics require an increase in either bending amplitude or frequency from this baseline case.

Increasing the bending amplitude at the low-frequency ($f_b = 0.5$) provided a large-scale change in the incident vortex behavior. A sufficiently high bending amplitude was shown to force the vortex between characteristic regimes that can occur with changes in static vertical positioning, described in Chapter 6, and drive the unsteady behavior of the incident vortex in a periodic fashion. This was best shown for the large amplitude case ($A/c = 0.1$) which supported both the complete stabilization of the incident vortex when bent down and rapid growth of helical instability when bent upward. This case demonstrates the time-frame to switch between stable and unstable regimes is relatively short and vortex behavior upstream of the wing can be driven by low frequency oscillations with sufficiently high amplitude.

Additionally, the high amplitude, low frequency case revealed a number of salient unsteady behaviors that more clearly elucidate some of the dynamic processes that occur in the static cases. Namely, the initially coherent suction-side vortex is shown to decompose into a series of spanwise sub-structures that emerge from and connect to the transitional flow-structure on the inboard side. This process more clearly depicts the unsteady mechanisms involved in suction-side instability. A similar process occurs for the pressure-side component in this case.

Two higher frequencies were explored at the lowest-amplitude ($A/c = 0.025$). At the mid-frequency ($f_b = 1$), the incident vortex experienced a small frequency shift from its initial value ($\mathrm{St}_c = 0.9$) and locked into that of the bending oscillations ($\mathrm{St}_c = 1$). The high-frequency bending oscillations ($f_b = 2$) failed to elicit a higher-modal helical instability upstream of the wing but did induce a small frequency shift in the spiral to a sub-harmonic of the bending motion ($St_c = 1$). This observation suggests that although some frequency modulation can be imposed on the incident

spiral, its basic nature is fairly robust. Lower bending frequencies are likely to tend toward a sweep through the behaviors of static positions mapped in Chapter 6. Higher bending frequencies would inhibit the coherent propagation of the incident vortex over the wing and appear to be unlikely to provide a major shift in unsteady behavior upstream of the leading-edge.

The ability of the vortex to be modulated to by bending oscillations appears to be limited to small shifts from its baseline value, but the implications could be important. This behavior demonstrates a tendency for an incident flow instability to adapt to a relatively close natural frequency of the aerodynamic structure potentially leading to a coupling of flow-structure dynamics. This resonance between fluid and structure could engender limit-cycle-oscillations dangerous to the life-cycle of airframes.

Chapter 8

Conclusions

8.1 Summary of research

Detailed three-dimensional, aeroelastic numerical simulations are presented in this dissertation in order to contribute to the fundamental understanding of the complex viscous and unsteady physics that arise in the context of streamwise-oriented vortex-surface interactions. Computations were performed using a high-fidelity, implicit large-eddy simulation technique coupled with a geometrically non-linear Reisner-Mindlin plate element. Several aspects of the general problem are explored in order to provide a targeted discovery and subsequent evaluation on several of the most interesting phenomena. Topics covered range from flow exploration in a tandem wing configuration, isolation of unsteady behavior in an incident streamwise vortex, and the influence of aeroelasticity through both passive and active deformations. A summary of the research conducted and the primary contributions are outlined in the following discussion.

General configuration

The general configuration consisted of an $\mathcal{R} = 6$ flat plate wing with uniform thickness of $t/c = 0.03$ and several different levels of stiffness. The follower wing operated at an $\alpha_F = 5^\circ$ angle of attack and a Reynolds number of $\mathrm{Re} = 30,000$ in every case investigated. Several different axial vortices were generated upstream of this wing at a number of lateral and vertical positions. This particular choice of parameters allowed for the investigation of streamwise vortex-surface interactions with transitional and separated flows while the simple configuration allowed for a reduction in the number of parameters of an otherwise very complex problem. Such simplifications are necessary to better elucidate the complex fluid physics and extends the basic understanding provided by detailed analysis to the broader class of perpendicular vortex interactions.

Comparison of streamwise vortices

The incident streamwise vortex was supplied using two different techniques, each with its own merits. The first approach employed an axial vortex generated by a leader wing operating in a close formation-like configuration. This setup provided a weaker but physical vortex that can be reproduced in an experimental investigation. Later, the swirling flow was provided by imposing a q-vortex at the inflow boundary in order to provide better control of the vortex properties and location as well as supply a more severe interaction. While not physically generated, the q-vortex is known to provide a good fit to trailing vortices at lower Reynolds numbers relevant to the current work and permits understanding of unsteady behaviors in the context of a number of theoretical studies.

Three incident vortices of differing size and strength were used in the course of this dissertation and are compared in Chapter 5. Two of the incident vortices were supplied by the tandem wing configuration with $\alpha_L = 5^\circ$ and 8° leader-wing an-

gles of attack while the strongest interaction was supplied by the imposed vortex case. This comparison suggested the main effects of vortex interaction tended towards those of the imposed vortex as the physically generated incident vortex was increased in strength. These trends included rapid attenuation of the upper-surface vortical component, growth of a surface normal recirculation region inboard of the vortex encounter, and increase in upwash induced lift enhancement. Most notably, the $\alpha_L = 8°$ tandem wing revealed an unsteady behavior just upstream of the leading-edge which is enhanced and more clearly evaluated in the imposed vortex case. This feature, not well portrayed in the tandem wing configuration, takes on a clear helical pattern in the imposed vortex case where the spiral revolves in a sense opposite the rotation of the incident swirling flow. The unsteady behavior, more thoroughly addressed in Chapter 6, permits a time-mean bifurcation of the incident vortex between the upper and lower surfaces by alternating between the two sides of the wing in the instantaneous flow.

Effects of lateral positioning

The effects of shifting the vortex position in the spanwise direction were revealed using the tandem wing configuration in Chapter 3. Several lateral positions were explored for wingtip offsets of $-0.15 \leq \Delta y/c \leq 0.30$ with no vertical offset between wings. Three distinct flow regimes were found to occur in the time-mean flow within a relatively small range of lateral positions for the impinging vortex. These behaviors were strongly influenced by mutual induction between the incident and tip vortices which determined the trajectory of the incident vortex and evolution of the wake behind the follower wing. This marked variation in flow structure provided a rich taxonomy of wake evolution which in turn would have significant implications for the impingement with subsequent aerodynamic surfaces downstream. These characteristic flow regimes were supported by qualitative comparison with a recent comparable

experiment that verified the same fundamental behaviors.

The effect of lateral positioning was found to produce equally interesting effects to the unsteady flow eliciting several unique phenomena that can significantly influence aerodynamic loads or interactions between aerodynamic surfaces in close proximity. A vortex placed outboard of the wingtip produced undulations in both the incident and follower wing trailing vortices similar to the cooperative instabilities found in trailing vortex pairs (see Section 1.3). Interactions between counter-rotating axial vortex pairs are known to have implications for wake dissipation and may accelerate trailing vortex destruction. Additionally, this behavior would supply an inherently transient encounter with a third aerodynamic surface downstream. The tip-aligned incident vortex generated a more vibrant unsteady response and a greater influence to the follower wing loads. A close interaction between the incident and tip vortices drove a highly unsteady tip vortex close to the wing surface and enhanced surface pressure fluctuations immediately beneath the flow instability. Attenuation of the inboard positioned vortex was shown to be related to an unsteady interaction with the transitional flow in the separation region which caused the swirling flow to reorient in the spanwise direction and then connect with the small-scale structures on its inboard side.

Evaluation of aerodynamic forces revealed significant lift enhancement compared to a single wing distributed over most of the span and a vortex-induced rolling moment for every case. Much of this improved lift was shown to be a consequence of the inviscid increase in effective angle of attack provided by the incident vortex upwash. Nonetheless, viscous effects were shown to be important in the wingtip region where rolling/bending moment is most sensitive. Interaction between the incident and tip vortices significantly altered the load distribution and influenced the time-mean rolling moment coefficient. While the fluctuations in the instantaneous loads were not very different from that of a single wing, much larger variations in rolling

moment and buffeting loads would be encountered if the vortex were to move through the various flow regimes that occur with changes to lateral positioning.

Effects of vertical positioning

The effects of vertical positioning were explored using the imposed vortex configuration in Chapter 6. Exploration at a single inboard position over a range of vertical offsets, $-0.25 \leq \Delta z/c \leq +0.1$, provided a rich variation in the unsteady fluid dynamics and revealed several characteristic factors that influence vortex-wing interaction.

When the vortex was aligned with the leading-edge, the incident vortex core resulted in helical instability upstream of the wing. Placing the vortex a small distance beneath the wing caused the instability to become much more pronounced and initiate further upstream. Conversely, moving the vortex slightly above the wing completely removed unsteadiness upstream of the leading-edge. The onset or lack of stability in the vortex was found to be related to the pressure gradients experienced at different vertical positions. Direct impingement and negative vertical offsets, in which vortex instability manifested, subjected the incident vortex to adverse pressure gradients that tended to enhance the axial velocity deficit in the incident vortex core. Should these trends persist for more severe conditions, such as higher angles of attack or Reynolds number, vortex-surface interaction could lead to more severe unsteady behaviors such as vortex breakdown.

The spiraling instability was connected to the growth of hydrodynamic instability (Section 1.3.3) through the swirl parameter. The enhanced velocity deficit provided by the adverse pressure gradient reduced the swirl parameter of the initially stable, laminar q-vortex into its linearly unstable regime permitting the growth of short-wavelength perturbations. The onset of helical instability in every case followed a drop beneath the linear stability threshold of the swirl parameter. Consistent with

this observation, placing the vortex slightly above the wing, which removed instability, aligned the vortex with the favorable pressure gradient provided by the acceleration of flow over the leading-edge. The axial velocity in the vortex core increased preserving a stable value for the swirl parameter. Adverse pressure gradients above the wing as the vortex approached the trailing-edge appeared to promote the growth of suction-side instabilities in the streamwise vortex for the positive vertical offset similar to the upstream instability, but this particular behavior was less severe.

In contrast to the effects of lateral positioning, vertical placement was shown be less important to the time-mean loads, but highly influential to the unsteady loading. The highly unsteady behavior provided by the small negative offset case was shown to increase rolling moment fluctuations while the stabilizing effects of the small positive offset reduced the overall fluctuations of the rolling moment. Little change in the lift enhancement or lift-to-drag ratio benefits occurred across the range of vertical positions considered.

Because of this lack of sensitivity between lift and drag, a weaker interaction may be beneficial in the context of formation flight. Although the largest vertical offset, $\Delta z/c = -0.25$, did result in helical instability it provided some aerodynamic benefits. While the larger offset quickly diminished the influence of instability on aerodynamic loading, the orientation of tangential flow of the vortex produced strong suction on the lower surface wingtip that helped to counteract the vortex-induced rolling moment. Despite the larger vertical positioning, time-mean lift and drag remained comparable to the optimal conditions. A large negative offset would be further beneficial for highly flexible wings where vortex-induced bending would tend to shift the wing away from the most unstable regimes whereas bending in a positive vertical offset might unintentionally destabilize a favorable interaction.

Effects of wing flexibility

The follower wing for both the tandem (Chapter 4) and isolated vortex (Chapter 5) configurations was subjected to rigid, moderate, and high levels of flexibility, all pinned at the midspan, in order to evaluate the effects of passive aeroelasticity on streamwise vortex-surface interactions placed inboard of the wingtip. For reference, the moderately flexible wing was comparable to a thin aluminum plate.

In both the tandem wing and isolated vortex cases, a significant time-mean bending deformation on the vortex encounter-side of the wing was produced by the asymmetric distribution of vortex-induced lift. The bending deformations in the tandem wing cases of Chapter 4 were predominantly static in nature due to a more stable incident vortex whereas surface pressure fluctuations provided by the unsteady flow structure upstream of the leading-edge produced a dynamic component in the more severe isolated vortex case of Chapter 5. Frequency content of the vortex-induced oscillations were found to be distributed at harmonics and sub-harmonics of the vortex instability frequency. The dominant component of bending oscillations was concentrated at roughly half the frequency of the vortex instability.

Twisting deformations were found to be highly dynamic for both the tandem wing and isolated vortex cases. These small amplitude oscillations where shown to clearly influence the unsteady flow structure and aerodynamic loads as revealed by the appearance of several unique modifications to the instantaneous flow in the tandem wing cases. Twisting mode vibrations of the moderately flexible wing coupled with instability in the lower-surface shear layer to generate enhanced pitching moment fluctuations which were more severe on the non-vortex encounter-side of the wing. Vortex-induced upwash provided a favorable effect that appeared to locally suppress the shear-layer instability and reduce pitching-moment oscillations on the vortex encounter-side for the tandem wing case in Chapter 4. This behavior persisted when the moderately flexible wing was subjected to the isolated q-vortex in Chap-

ter 5. The stronger upwash almost completely suppressed the pressure-side shear layer instability and removed the high frequency twisting oscillations on the vortex encounter-side of the wing. These were replaced by lower-frequency oscillations that matched the dominant bending frequency and appeared to be driven the surface pressure fluctuations imposed by the incident vortex.

The time-mean vortex-induced bending deformations provided an effective vertical offset relative to the incident vortex axis in both cases. This shift in static position resulted in mutual induction between the incident and tip vortices that tended outboard behind the follower wing for the tandem wing configuration in Chapter 4 and contributed an additional mode of wake-evolution to those discovered during exploration of lateral positioning. Increasing flexibility was found to quickly enhance the helical instability in the imposed vortex case in Chapter 5 providing an earlier onset and larger-scale fluctuations in the instantaneous flow which in turn influenced the buffeting response.

In general, wing flexibility demonstrated the potential for time-mean flow-induced deformations to shift vortex-surface interaction away from the intended regime by imposing a vertical offset. This behavior produced characteristic changes in the flow structure for both the tandem wing and isolated vortex configurations. Vortex-surface interaction provided a significant influence to the dynamic components of the structural deformations which could influence unsteady vortex behavior and would have implications for the fatigue-life of aerodynamic structures.

Separation of static and dynamic aeroelastic effects

Uncertainty as to whether the dynamic or static component of the aeroelastic response provided the greatest influence on vortex instability in Chapter 5 motivated the separation of the static deflection from the dynamic structural response in the isolated vortex case. To this end, the rigid wing was deformed to match the time-

mean deflections of both flexible plates providing only the static component of the deformations in Section 5.8. Observation of time mean-loading and the instantaneous flow structure revealed nearly identical solutions between the full aeroelastic and statically deformed counterparts. Comparison of the turbulent kinetic energy within the incident vortex suggested a minor influence of the dynamic component of aeroelasticity in both wings. This analysis demonstrated the primary contribution to the shift in unsteady response was due to the effective static vertical offset provided by vortex-induced loading. Feedback effects of the dynamic component contribute but are secondary to the static deflections. The prevalence of static deformations in the influence of wing flexibility motivated the more rigorous analysis on the effects of vertical positioning in Chapter 6 in order to better understand the implications of bending deformations on the unsteady fluid dynamics.

While static bending deformations were shown to provide the most significant influence, dynamic oscillations may be more influential under parameters not investigated in the current work and should not be neglected. The influence of bending oscillations was evaluated in order to explore the potential feedback effects of an oscillating or vibrating wing. Bending oscillations were actively imposed over a range of amplitudes of $0.025 \leq A/c \leq 0.1$ and frequencies of $0.5 \leq f_b \leq 2.0$ in order to map the potential effects of a dynamic response.

Low-frequency, low-amplitude motion produced little change in the general flow structure. Nonetheless, some degree of feedback response was observed and appeared to be related to a disruption of the spiral's evolution resulting from the periodic shift in the wing's position during low-frequency oscillations. Significant changes to the unsteady fluid dynamics require an increase in either bending amplitude or frequency from this baseline case. Low-frequency, high-amplitude oscillations forced the incident vortex between characteristic regimes that can occur with changes in static vertical positioning, described in Chapter 6, and consequently drove the unsteady vortex

behavior upstream of the wing. Furthermore, this case demonstrated rate of both growth and removal of instability is relatively quick and helped clarify some of the fine-scale features produced by suction-side instability.

The mid-frequency low-amplitude case, managed to provide a small frequency shift in the helical instability which locked into that of the bending oscillations. The high-frequency case failed elicit a higher-modal helical instability upstream of the wing but did induce a similar small frequency shift in the spiral to a sub-harmonic of the bending motion. This observation suggests that although some frequency modulation can be imposed on the incident spiral, its basic nature is fairly robust. Lower bending frequencies than those explored are likely to tend toward a sweep through the behaviors of static positions mapped in Chapter 6. Higher bending frequencies would inhibit the coherent propagation of the incident vortex over the wing and appear to be unlikely to provide a major shift in unsteady behavior upstream of the leading-edge. This observation is consistent with the low-pass behavior of fin oscillations on vortex breakdown suggested by Gursul and Xie[66].

The ability of the vortex to be modulated to by bending oscillations appears to be limited to small shifts from its baseline value, but the implications could be important. This behavior demonstrates a tendency for an incident flow instability to adapt to a relatively close natural frequency of the aerodynamic structure potentially leading to a coupling of flow-structure dynamics. This resonance between fluid and structure could engender limit-cycle-oscillations dangerous to the life-cycle of airframes.

8.2 Recommendations for future work

Significant insight on the unsteady physics and aeroelastic response related to streamwise vortex interactions with aerodynamic surfaces is presented in this dissertation. Nonetheless, the important contributions provided by this work only begin

to address a portion of a vast and complex field of study that remains a fertile topic for discovery and analysis. Recommendations and direction for future research can be made based upon the findings presented within this dissertation. These suggestions, intended to address yet unresolved issues, are described in the following and categorized by the proposed research direction.

Wider exploration of parameter space

The simple close-formation of Chapter 3 and canonical configuration of Chapter 5 were well-chosen for the purpose of simplifying problem complexity and providing versatility to systematically explore the parameter space. The effects of vertical positioning were explored in Chapters 3 and 6 while the effects of active and passive aeroelasticity were demonstrated in Chapters 4, 5, and 7. Many other parameters are very capable of significantly influencing perpendicular vortex-surface interactions.

Vortex size, r_v, may play an important role in selecting the frequency of vortex instability. Analysis of vertical positioning in Chapter 6 demonstrated the frequency of the primary unstable mode of the incident vortex is independent of the specific interaction while forced bending oscillations in Chapter 7 failed to drive mode selection of helical instability. These observations suggest the time scale of the primary frequency is fairly robust and a property of the vortex itself rather than the specific interaction. A similar instability appears for the smaller diameter vortex in the tandem wing cases of Chapter 3 at a much higher frequency. Therefore, vortex diameter is proposed as the main parameter driving the specific frequency. Exploration of several vortex diameters using the isolated vortex configuration employed in Chapter 5 would help to prove or disprove this speculation.

Vortex swirl, q, may prove an interesting topic for further study. The work in Chapter 6 demonstrated a consistent link between the swirl-ratio and onset of helical instability through the linear stability threshold. While the choice of swirl in

the present work falls well-within the stability threshold, the upstream influence of the wing provided by adverse pressure-gradients drives the swirl-ratio into a linearly unstable regime. Swirl attenuation due to natural viscous decay would likely tend to unsteady behavior preceding impingement unrelated to vortex-surface interaction in the case of a much lower initial swirl parameter. Therefore, efforts are better focused on vortex-surface interaction with higher swirl-ratio vortices. One potential outcome is that a more persistent vortex remains supercritical upstream of the wing precluding instability in favor of diverting to either the suction or pressure-side. A second prediction is contrary to the first in that a higher swirl vortex may actually develop a severe and abrupt breakdown upstream of the wing due to a more rapid change of flow conditions upon impingement.

Analysis of different axial flow profiles would further supplement the understanding of vortex-surface interactions. For instance, reversing the axial velocity profile would supply a jet-like vortex and permit analysis of a different class of vortex-surface interaction. This would be relevant to the trailing vortex emanating from a very high leader-wing angle of attack[146] or impingement of a delta-wing leading-edge vortex. A jet-like vortex will likely be more prone to vortex breakdown reminiscent of the previous works on vortex/fin interaction[147] described in Chapter 1.

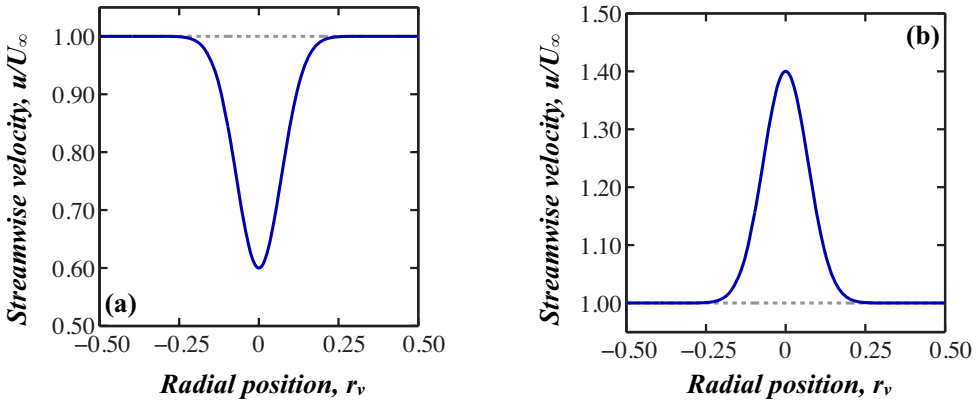

Figure 8.1: Axial velocity profiles for a (a) wake-like and (b) jet-like columnar vortex.

The operating conditions of the wing itself, such as Reynolds number and angle of attack, are likely to influence the nature of vortex-surface interactions. Spiral instability described in the work by Garmann and Visbal[5] at $\alpha = 4°$ and $\mathrm{Re} = 20,000$ is less severe than what occurs for a wing operating at $\alpha = 5°$ and $\mathrm{Re} = 30,000$ in Chapter 5. Another work by Garmann and Visbal[148] has recently emerged exploring vortex impingement on a NACA0012 wing at a much higher Reynolds number of $\mathrm{Re} = 200,000$. Remarkably similar behavior to the lower Reynolds number flat plate cases was demonstrated. In particular, spiral instability persists, at a comparable non-dimensional frequency, despite a large shift in Reynolds number and wing profile. These observations demonstrate the relevance of further study using the flat-plate configuration and suggests angle of attack may provide the most vibrant changes to the unsteady flow structure upstream of the wing.

Wing geometry

Chapter 6 specifically demonstrated the influence of pressure gradients on the unsteady characteristics of streamwise vortex-surface interaction. Wing geometry can have a significant influence on the pressure fields of the surrounding flow. Exploration of wing geometry will be necessary to understand the most favorable conditions for close vortex encounters. For example, careful choice of cambered wings, such as those shown in Figure 8.2, could be used to modify pressure gradients and better understand specific aspects of wing geometry. A reduction or prevention of vortex-induced separation over a streamlined wing, such as the NACA0012 airfoil in Figure 8.2, may lead to significant modification or removal of unsteady behaviors. The recent work by Garmann and Visbal[148] demonstrated direct impingement and outboard positioning of a streamwise vortex relative to a NACA0012 wing at $\mathrm{Re} = 200,000$ behaves much like the flat plate cases in many ways. However, vertical positing for this geometry has not been investigated. It would be interesting to see if a positive offset over a smooth

profile results in suction-side instability in the incident vortex. Suitable tailoring of the suction-side pressure gradient through a well-chosen or adaptive geometry could prevent suction-side instability/breakdown in a close vortex encounter.

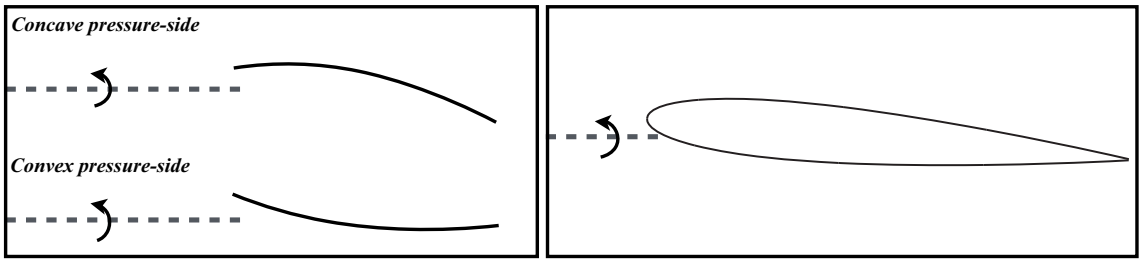

Figure 8.2: Wing geometry such as (a) wing camber or (b) smooth profiles may influence vortex-surface interaction.

Transient encounters

Chapter 3 found that unsteady loading provided by impingement of a stationary vortex was not nearly as important as the variation in loading that can occur over a small change in lateral positing. This suggests transient motion of the vortex is more likely to dominate buffeting loads. Such an unsteady impingement is feasible due to the natural motion from vortex meandering (Section 1.3.5), long wavelength instabilities (Section 1.3.1), or atmospheric turbulence. Motion of either aircraft during maneuvers, aeroelastic behavior and uncontrolled motion of either generator or follower wing can provide additional shifts in the relative positioning between aerodynamic surfaces and an impinging vortex. These findings motivate further study on transient streamwise vortex encounters and wing dynamics.

Wing motion has been addressed to some degree in the current work. Chapters 4 and 5 explored the aeroelastic response of streamwise vortex interaction with flexible wings and suggested some degree of influence due to small pitching or bending oscillations. Chapter 7 directly explored forced bending oscillations and demonstrated large-amplitude, low-frequency bending deflections can drive feedback response by

shifting the vortex between different stabilizing/destabilizing flow regimes. Further study on transient encounters due to aeroelastic behavior is merited. The effect of pitching oscillations of the follower wing on the incident vortex or behavior of a trailing vortex behind a bending/plunging or twisting/pitching leader would be interesting topics for study in this context. Further exploration on the effects of passive flexibility may be best addressed through a broad parametric exploration in a water tunnel study and then detailed through large-eddy simulations on the cases eliciting the most vibrant aeroelastic response.

Transience in the lateral direction is more likely to occur in the cases of natural motion of a streamwise vortex and uncertainty in the either generator or follower aircraft position. Unintentional motion of the leader or follower and maneuvering such as moving into or out of formation, both shown in Figure 8.3, are two possible sources unsteady vortex encounters that could be explored. To this end, at least one work has emerged on transient interactions during the course of this dissertation. Garmann and Visbal[149] imposed lateral oscillations in the incident vortex position in order to emulate meandering behavior. An initial lateral motion of the swirling flow was shown to incline to a more vertical motion as the wandering vortex evolves in the spatial direction shifting from the intended interaction. The time-scale of vortex motion prevented the growth of helical instability upstream of the wing suggesting transient encounters cannot be described as a simple extension of the stationary behavior. Further work is necessary to understand the spatial evolution of a wandering vortex, its subsequent interaction with aerodynamic surfaces, and the implications for wake-capture.

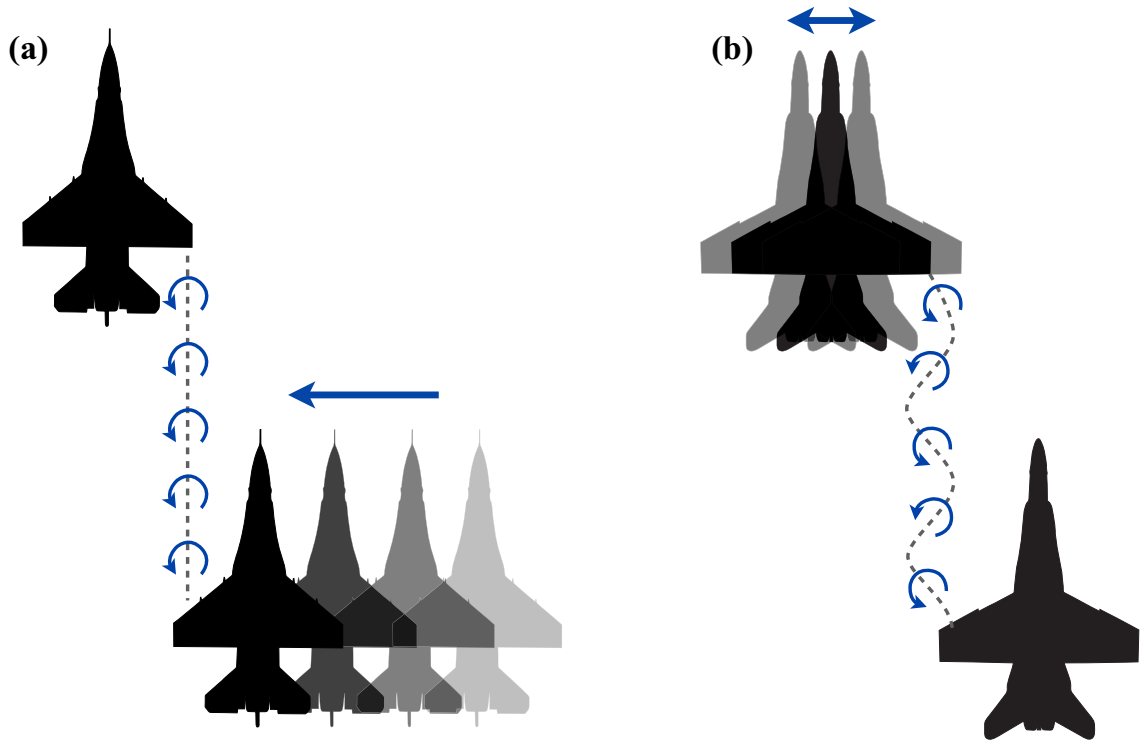

Figure 8.3: Transient encounters may encompass (a) wake crossings or moving into/out of formation and (b) meandering behavior due to relative motion between aircraft, atmospheric turbulence, or vortex instabilities.

Vortex-vortex interaction

Another unresolved topic is the mutual instability between the trailing vortices of tandem wings demonstrated in Chapter 3. Here, an outboard positioned incident vortex in conjunction with the counter-rotating tip vortex of the follower wing began to exhibit longer wave-length instabilities in both vortices. A detailed study on the evolution of the unsteady wake behavior is outside the scope of the current dissertation, but likely to influence interaction with a third aerodynamic surface or influence the destruction of wake vortices. Recently, Ryan *et al.*[77] conducted a more theoretical study on the stability characteristics of an unequal-strength Batchelor vortex pair using linear stability theory supplemented by direct numerical simulation. Instability growth was dominant in the weaker vortex, similar to that shown in Figure 8.4 below. Future work on mutual instabilities in wake interactions would be complimented well

by a similar theoretical component.

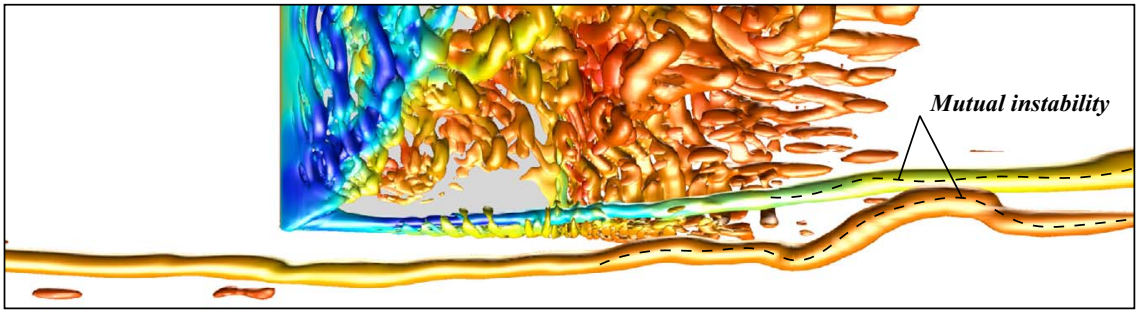

Figure 8.4: Cooperative instability between trailing vortices of a tandem wing configuration, see Chapter 3.

Stability analysis

A complimentary stability analysis would help provide some understanding of the general problem. If unsteady behavior does evolve from the non-linear growth of the linear instability modes, then frequencies associated with these instabilities should be comparable to those observed in the present work. Consistent frequency content throughout the isolated vortex cases in Chapter 6 suggests frequency of the spiral is a property of the vortex rather than unique to a particular interaction. Stability analysis on the specific vortex, perhaps using the techniques of Khorrami[150], would lend itself well to understanding the time-scales of unsteady behavior. If fruitful, this approach may provide a simpler tool for predicting frequencies of flow instability and could be useful in the aeroelastic tailoring of airframes for the prevention of flow/structure coupling.

Active and passive flow control

While the primary emphasis of this work is to contribute to the fundamental understanding of the viscous and unsteady physics related to streamwise/vortex surface interactions, a scientific understanding should ultimately lead to technological innovation. To this end, several recommendations can be derived from the content of this

article. First, the flexible plates in the tandem wing configuration of Chapter 4 appeared to alleviate the amplitude of surface pressure fluctuations due to the dynamic component of twisting oscillations. Further exploration on the potential to favorably tailor an aeroelastic structure is merited.

In addition to modifying wing geometry, favorable pressure gradients could be supported through simple flow control devices. One idea proposed here is swirl preservation through bleed-air or leading-edge suction as portrayed in Figure 8.5(b). The growth of unstable modes were shown in Chapter 6 to be strongly linked with the linear stability criterion proposed by Leibovich and Stewartson[80]. Flow control at the leading-edge could be used to alleviate the strong adverse pressure gradient upon stagnation with the leading edge and thus preserving swirl to remain within the stable regime, at least until reaching the follower wing's wake. Investigation in this topic would be best preceded by an exploration of a high swirl incident vortex. However, the most significant challenge with such an approach would be in reliably positioning the vortex at the correct location.

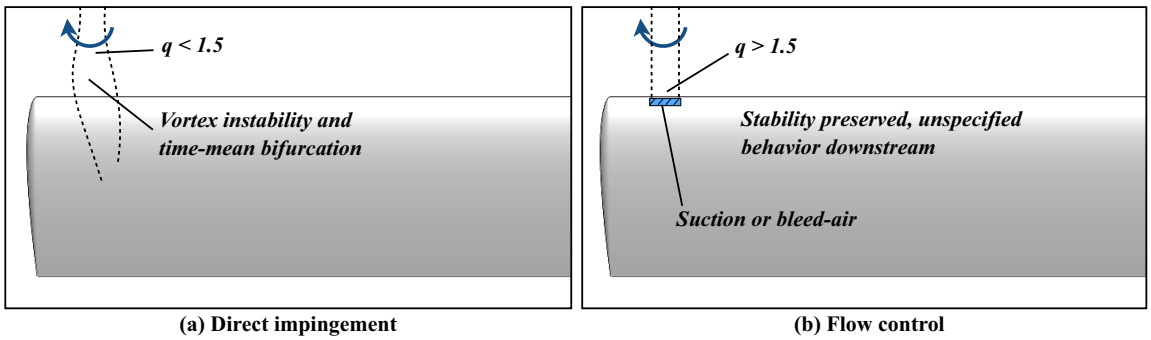

Figure 8.5: Direct impingement with the leading-edge engenders vortex instability upstream of the wing as shown in (a). Bleed air or suction at the leading-edge, shown in (b), could help preserve swirl and prevent instability.

Bibliography

[1] Mayori, A. and Rockwell, D., "Interaction of a streamwise vortex with a thin plate: a source of turbulent buffeting," *AIAA J.*, Vol. 32, No. 10, 1994, pp. 2022–2029.

[2] Gordnier, R. and Visbal, M., "Numerical simulation of the impingement of a streamwise vortex on a plate," *Int. J. Comput. Fluid D.*, Vol. 12, 1999.

[3] Lim, T. T. and Cui, Y. D., "On the generation of spiral-type vortex breakdown in an enclosed cylindrical container," *Phys. Fluids*, Vol. 17, 2005, pp. 044105.

[4] McKenna, C. and Rockwell, D., 2015, Private communication.

[5] Garmann, D. J. and Visbal, M. R., "Interaction of a streamwise-oriented vortex with a wing," *J. Fluid Mech.*, Vol. 767, 2015, pp. 782–810.

[6] Wieselsberger, C., "Beitrag zur Erklärung des Winkelfluges Eineger Zugvögel," *Z. Flugtechnik & Motorluftschiffahrt*, Vol. 5, 1914, pp. 225–229.

[7] Lissaman, S. and Shollenberger, C. A., "Formation flight of birds," *Science*, Vol. 168, 1970, pp. 1003–1005.

[8] Hummel, D., "Aerodynamic aspects of formation flight in birds," *J. Theor. Biol.*, Vol. 104, 1983, pp. 321–347.

[9] Hummel, D., "Formation flight as an energy-saving mechanism," *Israel J. Zool.*, Vol. 41, 1995, pp. 261–278.

[10] Badgerow, J. P. and Hainsworth, F. R., "Energy savings from formation flight? A re-examination of the vee formation," *J. Theor. Biol.*, Vol. 93, No. 41, 1981, pp. 41–52.

[11] Hainsworth, F. R., "Precision and dynamics of positioning by Canada geese flying in formation," *J. Exp. Biol.*, Vol. 128, 1987, pp. 445–462.

[12] Cutts, C., "Energy savings in formation flight of pink-footed geese," *J. Exp. Biol.*, Vol. 189, No. 1, 1994, pp. 251–261.

[13] Weimerskirch, H., Martin, J., Clerquin, Y., Alexandre, P., and Jiraskova, S., "Energy saving in flight formation," *Nature*, Vol. 413, No. 6857, 2001, pp. 697–698.

[14] Frazier, J. W. and Gopalarathnam, A., "Optimum downwash behind wings in formation flight," *J. Aircraft*, Vol. 40, No. 4, 2003, pp. 799–803.

[15] Pahle, J., Berger, D., Venti, M., Duggan, C., Faber, J., and Cardinal, K., "An initial flight investigation of formation flight for drag reduction on the C-17 aircraft," AIAA paper 2012-4802, AIAA, August 2012.

[16] Nangia, R. K. and Palmer, M. E., "Formation flying of commercial aircraft, variation in relative size/spacing: induced effects and control," AIAA paper 2007-4163, AIAA, 2007.

[17] Bower, G. C., Flanzer, C., and Kroo, I. M., "Formation geometries and route optimization for commercial formation flight," AIAA paper 2009-3615, AIAA, Jun. 2009.

[18] Bizinos, N. and Redelinghuys, C., "Tentative study of passenger comfort during formation flight within atmospheric turbulence," *J. Aircraft*, Vol. 50, No. 3, 2013, pp. 886–900.

[19] Magill, S. A., Schetz, J. A., and Mason, W. H., "Compound aircraft transport: a comparison of wingtop-docked and close-formation flight," AIAA paper 2003-607, AIAA, January 2003.

[20] Han, C. and Mason, W. H., "Inviscid wing-tip vortex behavior behind wings in close formation flight," *J. Aircraft*, Vol. 42, No. 3, 2005, pp. 787–788.

[21] Bramesfelt, G. and Maughmer, M. D., "Effects of wake rollup on formation-flight aerodynamics," *J. Aircraft*, Vol. 45, No. 4, 2008, pp. 1167–1173.

[22] Wagner, G., Jacques, D., Blake, B., and Pacher, M., "Flight test results of close formation flight for fuel savings," AIAA paper 2002-4490, AIAA, Aug. 2002.

[23] Cobleigh, B., "Capabilities and future applications of the NASA autonomous formation flight (AFF) aircraft," AIAA paper 2002-3443, AIAA, May 2002.

[24] Ray, R. J., Cobleigh, B., Vachon, M., and John, C. S., "Flight test techniques used to evaluate performance benefits during formation flight," AIAA paper 2002-4492, AIAA, August 2002.

[25] Hansen, J. L. and Cobleigh, B. R., "Induced moment effects of formation flight using two F/A-18 aircraft," AIAA paper 2002-4489, AIAA, 2002.

[26] Vachon, M., Ray, R., Walsh, K., and Ennix, K., "F/A-18 aircraft performance benefits measured during the autonomous formation flight project," AIAA paper 2002-4492, AIAA, August 2002.

[27] Ianotta, B., "Vortex draws flight research forward," *AIAA Aerospace America*, Vol. 40, No. 3, March 2012, pp. 26–30.

[28] Blake, W. B. and Gringas, D. R., "Comparison of predicted and measured formation flight," AIAA paper 2001-4136, AIAA, Aug. 2001.

[29] Iglesias, S. and Mason, W. H., "Optimum spanloads in formation flight," AIAA paper 2002-0258, AIAA, January 2002.

[30] Wang, Z. and Mook, D. T., "Numerical aerodynamic analysis of formation flight," AIAA paper 2003-0610, AIAA, January 2003.

[31] Ning, S. A., *Aircraft drag reduction through extended formation flight*, Ph.D. thesis, Dept. of Aeronautics and Astronautics, Stanford Univ., Stanford, CA, Aug. 2011.

[32] Gingras, D. R., "Experimental investigation of multi-aircraft formation," AIAA paper 1999-3143, AIAA, June 1999.

[33] Wagner, G., Jacques, D., Blake, B., and Pacher, M., "An analytical study of drag reduction in tight formation flight," AIAA paper 2001-4075, AIAA, Aug. 2001.

[34] Beukenberg, M. and Hummel, D., "Aerodynamics, performance and control of airplanes in formation flight," ICAS-90-5.9.3, 1990.

[35] Kless, J. E., Aftosmis, M. J., Ning, S. A., and Nemec, M., "Inviscid analysis of extended-formation flight," *AIAA J.*, Vol. 51, No. 7, 2013, pp. 1703–1715.

[36] McCamish, S., Pachter, M., and D'Azzo, J. J., "Optimal formation flight control," AIAA paper 96-3833, AIAA, 1996.

[37] Dargan, J. L., Pachter, M., and D'Azzo, J. J., "Automatic formation flight control," AIAA paper 92-4473, AIAA, 1992.

[38] Veth, M., Pacther, M., and D'Azzo, J. J., "Energy preserving formation flight control," AIAA paper 95-0335, AIAA, 1995.

[39] Wolfe, J. D., Chichka, D. F., and Speyer, J. L., "Decentralized controllers for unmanned aerial vehicle formation flight," AIAA paper 96-3833, AIAA, 1996.

[40] Binetti, P., Ariyur, K., Krstic, M., and Bernelli, F., "Formation flight optimization using extremum seeking feedback," *J Guid. Control Dynam.*, Vol. 26, No. 1, 2003, pp. 132–142.

[41] Rife, J., "Collaborative positioning for formation flight of cargo aircraft," *J. Guid. Control Dynam.*, Vol. 36, No. 1, 2013, pp. 304–307.

[42] Hemati, M. S., Eldredge, J. D., and Speyer, J. L., "Wake sensing for aircraft formation flight," AIAA paper 2012-4768, AIAA, August 2012.

[43] Schlichting, H., "Leistungsersparnis im verbandsflug," *Mitt. Deutsch. Akad. Luftfahrtforsh.*, Vol. No. 2, 1941, pp. 97–139.

[44] Blake, W. and Multhopp, D., "Design and performance and modeling considerations for close formation flight," AIAA paper 98-4343, AIAA, Aug. 1998.

[45] Blake, W. B., "An aerdynamic model for simulation of close formation flight," AIAA paper 2000-4304, AIAA, Aug. 2000.

[46] King, R. M. and Gopalarathnam, A., "Ideal aerodynamics of ground effect and formation flight," *J. Aircraft*, Vol. 42, No. 5, 2005, pp. 1188–1199.

[47] Blake, W. B. and Gingras, D. R., "Comparison of predicted and measured formation flight," *J. Aircraft*, Vol. 41, No. 2, 2004, pp. 201–207.

[48] Bangash, Z. A., Sanchez, R. P., and Ahmed, A., "Aerodynamics of formation flight," *J. Aircraft*, Vol. 43, No. 4, 2006, pp. 907–912.

[49] Inasawa, A., Mori, F., and Asai, M., "Detailed observations of interactions of wingtip vortices in close-formation Flight," *J. Aircraft*, Vol. 49, No. 1, 2012, pp. 206–213.

[50] Venkataramanan, S., Dogan, A., and Blake, W., "Vortex effect modeling in aircraft formation flight," AIAA paper 2003-5385, AIAA, 2003.

[51] Munk, M., "The minimum induced drag of aerofoils," NACA TR-121, 1979.

[52] Ning, S. A., Flanzer, T. C., and Kroo, I. M., "Aerodynamic performance of extended formation flight," *J. Aircraft*, Vol. 48, No. 3, 2011, pp. 855–865.

[53] Ning, S. A. and Kroo, I., "Compressibility effects of extended formation flight," AIAA paper 2011-3812, AIAA, June 2011.

[54] Slotnick, J. P., Clark, R. W., Friedmann, D. M., Yadlin, Y., Yeh, D. T., Carr, J. E., Czech, M. J., and Bieniawski, S. W., "Computational aerodynamic analysis for the formation flight for aerodynamic benefit program," AIAA paper 2014-1458, AIAA, 2014.

[55] Patel, M. H. and Hancock, G. J., "Some experimental results of the effect of a streamwise vortex and a vertical tail," *Aeronat. J.*, 1974, pp. 151–155.

[56] McAlister, K. W. and Tung, C., "Airfoil interaction with an impinging vortex," NASA Tech. Pap. 2273, NASA, 1984.

[57] Wittmer, K. S., Devenport, W. J., and Rife, M. C., "Perpendicular blade vortex interaction," *AIAA J.*, Vol. 33, No. 9, 1995, pp. 1667–1674.

[58] Wittmer, K. S. and Devenport, W. J., "Effects of perpendicular blade-vortex interaction, part 1: turbulence structure and development," *AIAA J.*, Vol. 37, No. 7, 1999, pp. 805–812.

[59] Zanotti, A., Ermacora, M., Campanardi, G., and Gibertini, G., "Stereo particle image velocimetry measurements of perpendicular blade-vortex interactino over an oscillating airfoil," *Exp. Fluids*, Vol. 55, No. 9, 2014, pp. 1–13.

[60] Bhagwat, M. J., Caradonna, F. X., and Ramasamy, M., "Wing-vortex interaction: unraveling the flowfield of a hovering rotor," *Exp. Fluids*, Vol. 56, No. 1, 2015, pp. 1–17.

[61] Wolfe, S., Lin, J.-C., and Rockwell, D., "Buffeting at the leading-edge of a flat plate due to a streamwise vortex: flow structure and surface pressure loading," *J. Fluid. Struc.*, Vol. 9, 1995, pp. 359–370.

[62] Shah, G. H., Grafton, S. B., Guynn, M. D., Brandon, J. M., Dansberry, B. E., and Patel, S. R., "Effect of vortex flow characteristics on tail buffet and high-angle-of-attack aerodynamics of a twin-tail fighter configuration," *Proceedings of the High-Angle-of-Attack Technology Conference*, 1990.

[63] Saffman, P. G., *Vortex Dynamics*, Cambridge University Press, 1992.

[64] Canbazoglu, S., Lin, J. C., Wolfe, S., and Rockwell, D., "Buffeting of a fin: streamwise evolution of flow structure," *J. Aircraft*, Vol. 33, 1995, pp. 185–190.

[65] Gursul, I. and Xie, W., "Buffeting flows over delta wings," *AIAA J.*, Vol. 37, No. 1, 1999, pp. 58–65.

[66] Gursul, I. and Xie, W., "Interaction of vortex breakdown with an oscillating fin," *AIAA J.*, Vol. 39, No. 3, Mar. 2001, pp. 438–446.

[67] Lambert, C. and Gursul, I., "Characteristics of fin buffeting over delta wings," *J. Fluid Struc.*, Vol. 19, 2004, pp. 307–319.

[68] Phillips, S., Lambert, C., and Gursul, I., "Effect of a trailing-edge jet on fin buffeting," *J. Aircraft*, Vol. 40, No. 3, 2003, pp. 590–599.

[69] Crow, S. C., "Stability theory of a pair of trailing vortices," *AIAA J.*, Vol. 8, 1970, pp. 2172–2179.

[70] Jiminez, J., "Stability of a pair of corotating vortices," *Phys. Fluids*, Vol. 18, 1975, pp. 1580–1581.

[71] Bristol, R. L., Ortega, J. M., Marcus, P. S., and Savaş, Ö., "On cooperative instabilities of parallel vortex pairs," *J. Fluid Mech.*, Vol. 517, 2004, pp. 331–358.

[72] Jacquin, L., Fabre, D., Sipp, D., and Coustols, E., "Unsteadiness, instability and turbulence in trailing vortices," *C. R. Physique*, Vol. 6, No. 4, 2005, pp. 399–414.

[73] Kerswell, R. R., "Elliptical instability," *Annu. Rev. Fluid Mech.*, Vol. 34, 2002, pp. 83–113.

[74] Leweke, T. and Williamson, C. H. K., "Cooperative elliptic instability of a vortex pair," *J. Fluid Mech.*, Vol. 360, 1998, pp. 85–119.

[75] Laporte, F. and Corjon, A., "Direct numerical simulations of the elliptic instability of a vortex pair," *Phys. Fluids*, Vol. 12, 2000, pp. 1016–1031.

[76] Meunier, P. and S. Le Dizes, T. L., "Physics of vortex merging," *C. R. Physique*, Vol. 6, No. 4, 2005, pp. 431–450.

[77] Ryan, K., Butler, C. J., and Sheard, G. J., "Stability characteristics of a counter-rotating unequal-strength Batchelor vortex pair," *J. Fluid Mech.*, Vol. 696, 2012, pp. 374–401.

[78] Batchelor, G., "Axial flow in trailing line vortices," *J. Fluid Mech.*, Vol. 20, No. 4, 1964, pp. 645–658.

[79] Ash, R. L. and Khorrami, M. R., "Vortex stability," *Fluid Vortices*, edited by S. I. Green, Dordrecht: Kluwer, 1995.

[80] Leibovich, S. and Stewartson, K., "A sufficient condition for the instability of columnar vortices," *J. Fluid Mech.*, Vol. 126, January 1983, pp. 335–356.

[81] Wu, J., Ma, H., and Zhou, M., *Vorticity and Vortex Dynamics*, Springer-Verlag, 2006.

[82] Khorrami, M. R., "On the viscous modes of instability of a trailing line vortex," *J. Fluid Mech.*, Vol. 225, 1991, pp. 197–212.

[83] Mayer, E. W. and Powell, K. G., "Viscous and inviscid instabilities of a trailing vortex," *J. Fluid Mech.*, Vol. 245, 1992, pp. 91–114.

[84] Fabre, D. and Jacquin, L., "Viscous instabilities in trailing vortices at large swirl numbers," *J. Fluid Mech.*, Vol. 500, 2002, pp. 239–262.

[85] Benjamin, T. B., "Theory of vortex breakdown phenomenon," *J. Fluid Mech.*, Vol. 14, 1962, pp. 593–629.

[86] Sarpkaya, T., "Vortex breakdown in swirling conical flows," *AIAA J.*, Vol. 9, 1971, pp. 1792–1799.

[87] Leibovich, S., "The structure of vortex breakdown," *Annu. Rev. Fluid Mech.*, Vol. 10, 1978, pp. 221246.

[88] Visbal, M. R., "Computational and Physical Aspects of Vortex Breakdown on Delta Wings," AIAA paper 95-0585, AIAA, 1995.

[89] Broadhurst, M. S., *Vortex stability and breakdown: direct numerical simulation and stability analysis using BiGlobal and parabolised formulations*, Ph.D. thesis, Department of Aeronautics, Imperial College London, 2007.

[90] Althaus, W., Brücker, C., and Weimer, M., "Breakdown of slender vortices," *Fluid Vortices*, edited by S. I. Green, Dordrecht: Kluwer, 1995.

[91] Liu, H.-T., "Effects of ambient turbulence on the decay of a trailing vortex wake," *J. Aircraft*, Vol. 29, No. 2, 1992, pp. 255–263.

[92] Moet, H., Laporte, F., Chevalier, G., and Poinsot, T., "Wave propagation in vortices and vortex bursting," *Phys. Fluids*, Vol. 17, 2005, pp. 054109.

[93] Garmann, D. J., Visbal, M. R., and Orkwis, P. D., "Three-dimensional flow structure and aerodynamic loading on a revolving wing," *Phys. Fluids*, Vol. 25, No. 3, 2013, pp. 034101.

[94] Devenport, W. J., Rife, M. C., Liapis, S. I., and Follin, G. J., "The structure and development of a wing-tip vortex," *J. Fluid Mech.*, Vol. 312, 1996, pp. 67–106.

[95] Corsiglia, V. R., Schwind, R. G., and Chigier, N. A., "Rapid scanning, three-dimensional, hot-wire anemometer surveys for wing tip vortices in the Ames 40- by 80-foot wind tunnel," AIAA paper 1973-681, AIAA, July 1973.

[96] Rokhsaz, K., Foster, S. R., and Miller, L. S., "Exploratory study of aircraft wake vortex filaments in a water tunnel," *J. Aircraft*, Vol. 37, No. 6, 2000, pp. 1022–1027.

[97] Gursul, I. and Xie, W., "Origin of vortex wandering over delta wings," *J. Aircraft*, Vol. 37, No. 2, 2000, pp. 348–350.

[98] del Pino, C., López-Alonso, J. M., Parras, L., and Fernandez-Feria, R., "Dynamics of the wing-tip vortex in the near field of a NACA 0012 aerofoil," *Aeronat. J.*, Vol. 115, No. 1164, 2011.

[99] Bailey, S. C. C. and Tavoularis, S., "Measurements of the velocity field of a wing-tip vortex, wandering in grid turbulence," *J. Fluid Mech.*, Vol. 601, 2008, pp. 281–315.

[100] McAlister, K. W. and Tung, C., "Interaction between an airfoil and a streamwise vortex," AIAA paper 84-1626, AIAA, June 1984.

[101] Bodstein, G. C. R., George, A. R., and Hui, C. Y., "The three-dimensional interaction of a streamwise vortex with a large-chord lifting surface: theory and experiment," *J. Fluid Mech.*, Vol. 322, 1996, pp. 51–79.

[102] Garmann, D. J. and Visbal, M. R., "Interaction of a streamwise-oriented vortex with a wing," AIAA paper 2014-1282, AIAA, January 2014.

[103] Vinokur, M., "Conservation equations of gasdynamics in curvilinear coordinate systems," *J. Comput. Phys.*, Vol. 14, 1974, pp. 105–125.

[104] Steger, J. L., "Implicit finite-difference simulation of flow about arbitrary two-dimensional Geometries," *AIAA J.*, Vol. 16, No. 7, 1978, pp. 679–686.

[105] Tannehill, J. C., Anderson, D. A., and Pletcher, R. H., *Computational Fluid Mechanics and Heat Transfer*, McGraw-Hill Book Company, 1997.

[106] Beam, R. and Warming, R., "An implicit factored scheme for the compressible Navier-Stokes equations," *AIAA J.*, Vol. 16, 1978, pp. 393–402.

[107] Jameson, A., Schmidt, W., and Turkel, E., "Numerical solutions of the Euler equations by finite volume methods using Runge-Kutta time stepping schemes." AIAA paper 1981-1259, AIAA, 1981.

[108] Pulliam, T., "Artificial dissipation models for the euler equations," *AIAA J.*, Vol. 24, No. 12, 1986, pp. 1931–1940.

[109] Pulliam, T. and Chaussee, D., "A diagonal form of an implicit approximate-factorization algorithm," *J. Comput. Phys.*, Vol. 17, No. 10, 1981, pp. 347–363.

[110] Lele, S., "Compact finite difference schemes with sectral-like resolution," *J. Comput. Phys.*, Vol. 103, 1992, pp. 16–42.

[111] Visbal, M. R. and Gaitonde, D. V., "High-order-accurate methods for complex unsteady subsonic flows," *AIAA J.*, Vol. 37, No. 10, 1999, pp. 1231–1239.

[112] Visbal, M. R. and Gaitonde, D. V., "On the use of high-order finite-difference schemes on curvilinear and Deforming Meshes," *J. Comput. Phys.*, Vol. 181, 2002, pp. 155–185.

[113] Gaitonde, D. and Visbal, M., "Further development of a Navier-Stokes solution procedure based on higher-order formulas," AIAA paper 1999-0557, AIAA, 1999.

[114] Gaitonde, D. V. and Visbal, M. R., "Padé-type higher-order boundary filters for the Navier-Stokes Equations," *AIAA J.*, Vol. 38, No. 11, 2000, pp. 2103–2112.

[115] Visbal, M. R. and Rizzetta, D. P., "Large-eddy simulation on curvilinear grids using compact differencing and Filtering Schemes," *J. Fluid. Eng.*, Vol. 124, 2002, pp. 836–847.

[116] Visbal, M. R., Morgan, P. E., and Rizzetta, D. P., "An implicit LES approach based on high-order compact differencing and Filtering Schemes," AIAA paper 2003-4098, AIAA, June 2003.

[117] Garmann, D. J., Visbal, M. R., and Orkwis, P. D., "Comparative study of implicit and subgrid-scale model large-eddy simulation techniques for low-reynolds number airfoil applications," *Int. J. Numer. Methods Fluids*, Vol. 71, No. 12, 2012, pp. 1546–1565.

[118] Mathew, J., Lechner, R., Foysi, H., Sesterhenn, J., and Friedrich, R., "An explicit filtering method for large eddy simulation of compressible Flows," *Phys. Fluids*, Vol. 15, No. 8, 2003, pp. 2279–2289.

[119] Stolz, S. and Adams, N., "An approximate deconvolution procedure for large-eddy simulation," *Phys. Fluids*, Vol. 11, No. 7, 1999, pp. 1699–1701.

[120] Attar, P. J., "Some results for approximate strain and rotation tensor formulations in geometrically non-linear Reissner-Mindlin plate theory," *Int. J. Nonlinear Mech.*, Vol. 43, 2008, pp. 81–99.

[121] Oñate, E., *Structural Analysis with the Finite Element Method. Linear Statics: Volume 2, Beams, Plates and Shells*, Springer Netherlands, 2013.

[122] Attar, P. J. and Gordnier, R. E., "Aeroelastic modeling using a geometrically nonlinear p-version mixed Reissner-Mindlin plate element," AIAA paper 2007-2318, AIAA, Apr. 2007.

[123] Crisfield, M., *Non-linear Finite Element Analysis*, Vol. 2, Wiley, 1st ed., 1997.

[124] Reddy, J., *Energy Principles and Variational Methods in Applied Mechanics*, Wiley, 2nd ed., 2002.

[125] Szabó, B. and Babŭska, I., *Finite Element Analysis*, John Wiley and Sons, New York, 1991.

[126] Borst, R., Crisfield, M. A., Remmers, J. J. C., and Verhoosel, C. V., *Non-Linear Finite Element Analysis*, Wiley, 2nd ed., 2012.

[127] Cook, R. D., Malkus, D. S., Plesha, M. E., and Witt, R. J., *Concepts and Applications of Finite Element Analysis*, John Wiley & Sons, 4th ed., 2002.

[128] Gordnier, R. and Visbal, M., "Development of a three-dimensional viscous aeroelastic solver for nonlinear panel flutter," *J. Fluid Struc.*, Vol. 16, No. 4, 2002, pp. 497–527.

[129] Melville, R., "Dynamic aeroelastic simulation of complex configurations using overset Grid Systems," AIAA paper 2000-2341, AIAA, June 2000.

[130] Gordnier, R. E. and Attar, P. J., "Impact of flexibility on the aerodynamics of an aspect ratio two membrane wing," *J. Fluid Struc.*, Vol. 45, 2014, pp. 138–152.

[131] Wall, W. A. and Ramm, E., "Fluid-structure interaction based upon a stabilized (ALE) finite element method," *Computational Mechanics: New Trends and Applications*, edited by S. Idelson, E. Oñate, and E. Dvorkin, CIMNE, Barcelona, 1998.

[132] Steger, J., Dougherty, F., and Benek, J., "A chimera grid scheme," *Advances in Grid Generation*, edited by K. Ghia and U. Ghia, Vol. 5, American Society of Mechanical Engineers, 1983, pp. 59–69.

[133] Sherer, S. E. and Scott, J. N., "High-order compact finite-difference methods on general overset grids," *J. Comput. Phys.*, Vol. 210, 2005, pp. 459–496.

[134] Visbal, M. and Gaitonde, D., "Very high-order spatially implicit schemes for computational acoustics on Curvilinear Meshes," *J. Comput. Accoust.*, Vol. 9, No. 4, 2001, pp. 1259–1286.

[135] Jeong, J. and Hussain, F., "On the identification of a vortex," *J. Fluid Mech.*, Vol. 285, 1995, pp. 69–94.

[136] Ramaprian, B. R. and Zheng, Y., "Measurements in rollup region of the tip vortex from a rectangular wing," *AIAA J.*, Vol. 35, No. 12, 1997, pp. 1837–1843.

[137] Visbal, M. and Gordnier, R., "On the structure of the shear layer emanating from a swept leading edge at angle of attack," AIAA paper 2003-4016, AIAA, 2003.

[138] Delisi, D. P., "Turbulence measurements in the wakes of aircraft and model laboratory wings," AIAA paper 2012-0427, AIAA, 2012.

[139] Sarpkaya, T., "Effect of the adverse pressure gradient on vortex breakdown," *AIAA J.*, Vol. 12, No. 5, 1974, pp. 602–607.

[140] Visbal, M. R. and Garmann, D. J., "Flow structure above stationary and oscillating low-aspect-ratio wings," *Proceedings of the ASME 2012 Fluids Engineering Division Summer Meeting*, Vol. FEDSM2012-72405, ASME, 2012, pp. 1593–1605.

[141] Jacquin, L. and Pantano, C., "On the persistence of trailing vortices," *J. Fluid Mech.*, Vol. 471, 2002, pp. 159–168.

[142] Spalart, P. R., Shur, M. L., Strelets, M. K., and Travin, A. K., "Direct simulation and RANS modeling of a vortex generator flow," 10th ERCOFTAC Symposium on Engineering Tubulence Modelling and Measurements, Marbella, Spain, 17-19 Sep 2014, ERCOFTAC, 2015.

[143] Visbal, M. R., "Onset of vortex breakdown about a pitching delta wing," *AIAA J.*, Vol. 38, No. 8, 1994, pp. 1568–1575.

[144] Wolfe, S., Canbazoglu, S., Lin, J. C., and Rockwell, D., "Buffeting of fins: assessment of surface pressure loading," *AIAA J.*, Vol. 33, 1995, pp. 2232–2235.

[145] Kandil, O. A., Sheta, E. F., and Massey, S. J., "Buffet responses of a vertical tail in vortex breakdown flows," AIAA paper 95-3464, AIAA, 1995.

[146] Lee, T. and Pereira, J., "Nature of wakelike and jetlike axial tip vortex flows," *J. Aircraft*, Vol. 47, No. 6, 2010, pp. 1946–1954.

[147] Rockwell, D., "Vortex-body interactions," *Annu. Rev. Fluid Mech.*, Vol. 30, 1998, pp. 199–229.

[148] Garmann, D. J. and Visbal, M. R., "Streamwise-oriented vortex interactions with a NACA0012 wing," AIAA paper 2015-1066, AIAA, January 2015.

[149] Garmann, D. J. and Visbal, M. R., "Unsteady interactions of a wandering streamwise-oriented vortex with a wing," AIAA paper 2014-2105, AIAA, June 2014.

[150] Khorrami, M. R., "A Chebyshev spectral collocation method using a staggered grid for the stability of cylindrical flows," *Int. J. Numer. Methods Fluids*, Vol. 12, 1991, pp. 825–833.